



The  
University  
Of  
Sheffield.

*Department of Mechanical Engineering*

**Effect of Surface Traction and Non-Metallic Inclusions  
on the Premature Failure of Wind Turbine Gearbox  
Bearings**

**Author:**

Hamza Abdulrasool Al-Tameemi

Registration No: 130249562

December 2017

**Supervisors:**

*Dr. Hui Long*

*Prof. Rob Dwyer-Joyce*

Thesis submitted to the Department of Mechanical Engineering, University  
of Sheffield in partial fulfilment of the requirements for the degree of

**Doctor of Philosophy**

## Abstract

The reliability of offshore Wind Turbine (WT) operation has been affected by costly maintenance and replacement of critical mechanical components such as bearings in the gearbox which often fail prematurely much earlier than the designed life-time of 20~25 years. It has been observed that irregular microstructural changes known as the White Etching Area (WEA), which could appear as butterfly wings, and the cracks associated with it, termed as White Etching Cracks (WECs), are present in most of the prematurely failed WT bearings. Currently no agreed theories regarding their causes and failure mechanisms, nor an effective solution have been established. In this research, two failed planetary bearings from WT gearboxes were destructively investigated to develop an in-depth understanding on the characteristics of the irregular microstructural changes and damages initiated from defects such as non-metallic Inclusions. One of the investigated bearings had a Black Oxide (BO) coating. The characterisation of the BO coating layer was performed to assess its effectiveness in preventing and delaying the premature WT gearbox bearings failure. To investigate the effect of various tribological parameters on surface and subsurface initiated damage, Rolling Sliding Tests (RSTs) using bearing steel specimens were conducted on a benchtop twin-disc machine. To understand the subsurface initiated damage, the stress distribution around an inclusion was investigated using Finite Element (FE) analysis and the results were correlated to the experimental observations.

The investigation of the failed bearings consisted of metallurgical examinations to categorise the key characteristics of surface and subsurface initiated cracks, with a focus on those cracks initiated from non-metallic inclusions. The examinations were conducted using optical microscopy, Scanning Electron Microscope (SEM), Atomic Force Microscopy (AFM) and Energy Dispersive X-ray spectroscopy (EDX). The micro- and Nano-indentation were also used to investigate the mechanical properties of the inclusions, WEA, BO layer and the steel matrix. The RSTs were conducted using the tribometer and rolling contact fatigue testing system (SUROS), the Sheffield University Rolling Sliding twin disc machine; and metallurgical examinations were conducted for the specimens. The FE analysis software ABAQUS was used to model a part of a WT bearing under various loading conditions. The models were 2D with an imbedded Manganese Sulphide inclusion (MnS) of a micro-scale with consideration of the debonding between the inclusion and the steel matrix.

It was found that the MnS inclusion was the dominating defect in the uncoated bearing, and those inclusions which are not perfectly bonded to the steel matrix initiated most micro cracks and WEAs. It was also found that the depth of these inclusions from the contact surface was not within the zone of the maximum principal shear stress  $\tau_{1(\max)}$  which could imply they were affected by surface traction since surface traction and subsurface shear stress are linked. In the BO coated bearing, oxide inclusions initiated most

of the subsurface microstructural damage. The examination of both bearings in the axial direction showed a direct relationship between the length of initiating inclusions with the total length of WEA (butterfly wings) or micro-cracks. In addition, surface initiated cracks with similar appearance to the WECs were found to propagate to form surface pitting and spalling of the examined bearings, similar features were observed on some of the RSTs specimens with high surface traction. The RST results confirmed that micro-cracks were initiated by the inclusions and by the effects of non-perfect bonding between the inclusion and the steel matrix. These test results also showed the effect of high surface traction at rotation direction reversed. This work also demonstrated the effect of the sequence of applying different loading conditions on the surface and subsurface initiated damage in certain degrees. The FE modelling results showed that surface traction and the non-perfect bonding between inclusion and steel matrix had a significant effect on initiation of localised ratcheting and tensile stress around an inclusion due to high loads as well as loading-unloading cycles after each roller pass. The stress distribution around inclusion tips showed a similar pattern of butterfly wings at certain surface traction direction.

This research identified a number of types of microstructural damage in WT gearbox bearings, some of which had not been reported before. The damage observations were correlated with the findings from the completed RSTs, and the FE modelling showed the effect of non-metallic inclusions and surface traction. Another contribution of this research was the characterisation of the BO coating layer based on hardness measurements, showing that premature WT bearing failure still occurred in spite of employing this coating technique currently recommended by manufacturers.

# Contents

Abstract .....	I
Contents .....	III
List of Tables .....	VI
List of Figures.....	VII
Publications and Presentations .....	XVIII
Acknowledgments .....	XIX
Abbreviations.....	XX
Nomenclature.....	XXII
1 Introduction.....	1
1.1 Background .....	1
1.2 Aims and Objectives.....	2
1.3 Thesis Outlines.....	3
1.4 Contributions to Knowledge .....	5
2 Literature review.....	7
2.1 Failure of Wind Turbine Gearbox Bearings.....	7
2.1.1 Bearings Failure Modes .....	7
2.1.2 Normal and Tangential Loading on WTGBs.....	9
2.1.3 RCF Cracks and Shakedown .....	12
2.1.4 WECs and WEAs Characterization and Initiation .....	13
2.1.5 Steel Cleanliness and Butterflies .....	16
2.1.6 Bearing Life Assessment .....	19
2.2 Experimental Investigation of Bearing Failure.....	20
2.3 Black Oxide Coating and Other Surface Treatment.....	22
2.4 Tribological and Stress Analysis in Rolling Contact Fatigue.....	24
2.4.1 Bearing Load Calculations.....	24
2.4.2 Hertzian Contact Pressure .....	25
2.4.3 Elasto-hydrodynamic Lubrication Theory (EHL) .....	26
2.4.4 Subsurface Stress Analysis.....	29
2.5 Modelling of Inclusions Initiated Damage .....	31
2.6 Identification of Current Research Gaps .....	33
2.7 Summary .....	34

3	Destructive Investigation on the Failed Bearings .....	36
3.1	Investigated Bearings.....	36
3.2	Sample Preparation for Subsurface Metallography .....	39
3.2.1	Sectioning .....	39
3.2.2	Mounting .....	41
3.2.3	Grinding .....	42
3.2.4	Polishing.....	43
3.2.5	Etching .....	43
3.3	Inspection Techniques .....	44
3.3.1	Optical, Scanning Electron and Atomic-Force Microscopic Imaging.....	44
3.3.2	Micro and Nano Indentation Hardness Testing .....	47
3.4	Characterization of Inclusions and Damages.....	53
3.4.1	Damage terminology .....	53
3.4.2	Cleanliness analysis .....	57
3.4.3	Energy Dispersive X-ray Spectroscopy (EDX).....	59
4	Experimental Investigation of Damage Initiation Using Twin Disc Testing .....	61
4.1	Twin Disc Test Equipment and Test Procedure .....	61
4.2	Design of Specimens and Properties of Oil.....	64
4.3	Surface Characterisation and Subsurface Metallography .....	68
5	Results and Discussion on Investigation of a Non-coated Bearing.....	71
5.1	Characterisation of damage initiating inclusions .....	71
5.1.1	Types of Inclusion .....	71
5.1.2	The Debonding of Inclusions .....	72
5.1.3	WEA (Butterfly Wings).....	73
5.1.4	Cracked Inclusions and Inclusion Initiated Cracks.....	75
5.1.5	Mechanical Properties of Inclusions, WEA and the Interface.....	78
5.2	Statistical Analysis of Subsurface Damage .....	82
5.3	Discussion of Surface Traction Effect on Subsurface Initiated Damage.....	88
5.4	Summary .....	91
6	Results and Discussion of Investigation of Black Oxide Coated Bearing .....	93
6.1	BO bearing steel cleanliness .....	93
6.2	Butterflies.....	94
6.3	Subsurface cracks.....	101

6.4	Cracks linked to surface .....	105
6.5	Analysis of Black Oxide Coating .....	110
6.6	Summary .....	114
7	Results and Discussion of the Experimental Investigation Using the Twin Disc Machine .....	116
7.1	Experimental Design of RSTs .....	116
7.2	Coefficient of Friction at Different Testing Conditions .....	121
7.3	Effects of Tested variables on Surface Damage and Wear .....	124
7.4	Effects of Tested Variables on Subsurface Damage and Hardness .....	133
7.5	Comparing Damage between Specimens and Failed Bearings .....	138
7.6	The Development of Surface and Subsurface Initiated Damage .....	143
7.7	Summary .....	145
8	Results and Discussion of Load Calculation and Stress Analysis .....	147
8.1	Results and Discussion of Surface and Subsurface Stress Analysis .....	147
8.1.1	Validation of load calculation .....	147
8.1.2	Contact Pressure and Lubricant Film Thickness .....	148
8.1.3	Surface Traction Effect on Subsurface Stresses .....	151
8.1.4	Surface Traction Effect on Damage Accumulation .....	152
8.2	Results and Discussion of FE Modelling .....	155
8.2.1	General description .....	155
8.2.2	Validation .....	159
8.2.3	Local Effect of Inclusion for different steel matrix bonding .....	165
8.2.4	Effect of normal and tangential loading-unloading on residual stress .....	168
8.2.5	Effect of Surface Traction Direction .....	174
8.3	Summary .....	178
9	Conclusions and Future Work .....	180
9.1	Conclusions .....	180
9.2	Future work .....	183
	References .....	185

## List of Tables

Table 2.1.1: Some types of failure observed in WT bearings [26][29][33][34][35] .....	9
Table 2.1.2: Properties of non-metallic inclusions [11][68][76][79][83][84] .....	18
Table 3.2.1: Specifications for the grinding and polishing process .....	43
Table 3.4.1: Definitions of the damage types observed.....	55
Table 4.2.1: Chemical composition for the steel used in the specimens of the RSTs.....	66
Table 4.2.2: Average cleanliness for the steel used in the specimens of the RSTs.....	66
Table 4.2.3: Properties of lubricants used for RSTs with SP 320 for comparison .....	67
Table 6.1.1: Cleanliness of BO coated bearing for axial sections (F= Fine and T= Thick)....	94
Table 7.1.1: The settings for the COT measurement tests.....	117
Table 7.1.2: Specifications of RSTs .....	119
Table 7.1.3: Investigated variables by RSTs.....	120
Table 7.3.1: Effects of investigated variables on surface observations from RSTs 1 to 9 where LS and HS are the low and high speed steps, respectively .....	132
Table 7.4.1: Effects of investigated variables on subsurface observations from RSTs 1 to 9 .....	136
Table 8.1.1: Gear dimensions of NREL 750 kW WT planetary stage [30] .....	148
Table 8.1.2: Comparison of steadily transmitted load in planetary stage of NREL 750 kW WT.....	148

## List of Figures

Figure 1.1.1: Global cumulative installed wind capacity 2001-2016 [1] .....	1
Figure 2.1.1: Main components of wind turbine drive train (Courtesy of Olympus) [36] ..	10
Figure 2.1.2: WTGBs in planetary stage (Courtesy of Olympus) [36].....	10
Figure 2.1.3: Generic WT planetary stage illustrates the unidirectional load on the inner raceway of the planetary bearings and the loaded zone.....	11
Figure 2.1.4: WECs observed in the inner ring of a failed case hardened bearing (adopted from [57]).....	14
Figure 2.1.5: SEM image of a butterfly initiated on an MnS inclusion (adopted from [56], Courtesy of Jürgen Gegner).....	15
Figure 2.4.1: The EHL theory (Courtesy of Robert Errichello) [110].....	27
Figure 2.4.2: The Stribeck diagram (adopted from [49]) .....	29
Figure 2.4.3: Hertzian pressure distribution (Top); subsurface stresses along the axis of symmetry (Left); contours of principal shear stress $\tau_1/p_0$ (Right). (adopted from [50]) ..	30
Figure 3.1.1: Dimensions of the examined bearings (a) uncoated and (b) BO coated .....	37
Figure 3.1.2: The part of the inner raceway of the uncoated failed bearing which was not examined in this research (Courtesy of Tom Bruce [19]).....	38
Figure 3.1.3: Inner raceway of the uncoated failed bearing examined in this study.....	38
Figure 3.1.4: Inner raceway of the BO failed bearing .....	39
Figure 3.2.1: Sectioning of the inner raceway of the uncoated bearing. The samples are shown as red blocks, 6 in the axial direction and 11 in the circumferential direction which grouped in 5 regions (yellow borders) numbered from 1 to 5. ORD is from right to left...	40
Figure 3.2.2: Sectioning of the inner raceway of the BO coated bearing. The samples are shown as red blocks, 8 in the axial direction and 8 in the circumferential direction which grouped in 6 regions (yellow borders) numbered from 1 to 6. White arrows are the observation direction. ORD is from right to left.....	40
Figure 3.2.3: (a) Abrasive cut-off wheel BUEHLER AbrasiMet 250 (b) Linear precision saw BUEHLER IsoMet 5000.....	41

Figure 3.2.4: (a) the hot mounting machine BUEHLER SimpliMet 1000 (b) three samples mounted in conductive Bakelite.....	42
Figure 3.2.5: The automated grinding and polishing machine BUEHLER Automet 250 .....	42
Figure 3.3.1: Optical microscope Nikon ECLIPSE LV150.....	45
Figure 3.3.2: Scanning electron microscopes (a) Camscan Series II (b) FEI/Philips XL-30 (c) HITACHI TM3030 plus.....	45
Figure 3.3.3: Illustration of the difference between images of the same feature taken by different microscopic techniques (a) optical microscopic (b) SEM (c) AFM .....	46
Figure 3.3.4: AFM Bruker's Dimension 3100.....	47
Figure 3.3.5: Schematic of the system used in AFM (Courtesy of Nicholas Geisse [125])..	47
Figure 3.3.6: Automated indentation machine (Struers Micro/Macro Hardness tester DuraScan).....	48
Figure 3.3.7: Adopted micro-indentation pattern to measure hardness under the surface of rolling contact.....	49
Figure 3.3.8: Nano-indentation system Hysitron Triboscope .....	49
Figure 3.3.9: Force-displacement curve from the Nano-indentation of the uncoated failed bearing steel .....	50
Figure 3.3.10: Schematic representation of an indentation showing quantities used for analysis [129][131] .....	51
Figure 3.3.11: Loading-partial unloading curve from the Nano-indentation test to measure the thickness of the undamaged BO layer in the failed BO coated bearing. It shows 50% unloading after each loading cycle. This test revealed that a higher load is needed to measure the whole thickness of the undamaged BO layer .....	52
Figure 3.3.12: The Nano-indentation hardness for the undamaged BO layer measured at 25 steps of loading-partial unloading (see Section 6.5 for full details).....	52
Figure 3.3.13: Nano-indentation system Hysitron TI Premier .....	53
Figure 3.4.1: Illustration of surface and subsurface initiated damage in axial section.....	54
Figure 3.4.2: Examples for the damages defined in Table 3.4.1 (a) Debonded inclusion (b) Cracked inclusion with micro-cracks initiated by inclusions (c) Butterfly (d) WEC (e) Subsurface cracks in the axial section (f) Surface-linked RCF cracks .....	56

Figure 3.4.3: Illustration of samples prepared from axial and circumferential sections with a three dimensional representation of two inclusions viewed in circumferential and axial directions .....	57
Figure 3.4.4: Definition for the angles of inclusion and butterfly right and left wings .....	57
Figure 3.4.5: Example for the fields used in cleanliness analysis. Red and yellow circles show examples for inclusions Type A and Type D.....	58
Figure 3.4.6: EDX analysis (spectrum 1) point identification of a MnS inclusion and (spectrum 2) area identification of a WEA .....	59
Figure 3.4.7: EDX mapping of inclusion attached to a butterfly wing in the BO coated bearing. The distribution of three chemical elements are shown for the inside area marked.....	60
Figure 4.1.1: Schematic representation of SUROS machine adopted from [133] ( Courtesy of Dr. David Fletcher).....	63
Figure 4.1.2: The manufactured oil path used for the SUROS machine .....	63
Figure 4.1.3: The lubrication of the contact area .....	64
Figure 4.1.4: Measuring the flash temperature between specimens using non-contact Infrared thermocouple .....	64
Figure 4.2.1: Specimens used for the RSTs (a) Flat (b) crowned surface of contact.....	65
Figure 4.2.2: Specimens contact configuration (a) illustration for the flat and slot sides (I) and (II) respectively (b) illustration for the contact width and the half width of non-crowned specimen .....	65
Figure 4.2.3: IR Spectra of three grades of oils .....	68
Figure 4.2.4: Illustration for finding oil viscosity at variable temperature using ASTM standard viscosity temperature charts.....	68
Figure 4.3.1: The non-contact profilometer (InfiniteFocus Alicona) which was used for measuring the surface roughness of the RSTs specimens .....	69
Figure 4.3.2: Example for the roughness measurement pattern applied on the specimens of the RSTs. ....	70
Figure 5.1.1: (Left) AFM 3D image and (Right) SEM image of debonded inclusions at 1300 $\mu\text{m}$ from the contact surface.....	72

Figure 5.1.2: AFM analysis shows the debonding between a MnS inclusion and WEA (butterfly wing).....	73
Figure 5.1.3: (Left) optical images for debonded MnS inclusions attached to WEA. The highlighted parts are the 3D AFM images to show the discontinuity of the WEA, and the debonding at the boundaries between the WEA and the steel matrix. The images in (a) to (d) are from axial sections; and (e) and (f) are from circumferential section with ORD from left to right.....	74
Figure 5.1.4: Images showing cracked inclusions with cracks propagated into the steel matrix.....	75
Figure 5.1.5: Micro-cracks initiated from non-cracked inclusions in axial sections.....	75
Figure 5.1.6: Non-MnS inclusion initiated cracks without internal cracking of inclusion...	76
Figure 5.1.7: WEC propagated almost vertically toward the surface and linked two butterflies .....	77
Figure 5.1.8: Nano-indentations across (a) MnS inclusion and (b) WEA for the butterfly in Figure 5.1.3 (c) .....	79
Figure 5.1.9: Nano indentation hardness measured across a MnS inclusion and WEA in a butterfly .....	80
Figure 5.1.10: Modulus of elasticity measured across a MnS inclusion and WEA in a butterfly .....	80
Figure 5.1.11: The average value and standard deviation of Nano-indentation hardness for a MnS inclusion, WEA and attached steel matrix in an etched sample and a MnS inclusion and attached steel matrix in un-etched sample .....	81
Figure 5.1.12: The average value and standard deviation of modulus of elasticity for a MnS inclusion, WEA and attached steel matrix in an etched sample and a MnS inclusion and attached steel matrix in un-etched sample.....	82
Figure 5.2.1: Percentage of catalogued inclusions (a) out of the total catalogued inclusions (b) out of the inclusions that initiated damage only with the <i>red</i> and <i>green</i> percentage refer to the debonded and cracked inclusions respectively .....	83
Figure 5.2.2: Characteristics of catalogued inclusions (average values with the error bars show $\pm$ one standard deviation).....	84
Figure 5.2.3: Characteristics of micro-cracks initiated by inclusions with their initiating inclusions (the number above each characteristic refers to the average value) .....	85

Figure 5.2.4: Characteristics of butterflies' wings with their initiating inclusions (the number above each characteristic refers to the average value) .....	85
Figure 5.2.5: Inclusion length vs total length with the depth of inclusions (a) cracks initiated from inclusion in circumferential sections (b) cracks initiated from inclusion in axial sections (c) butterflies in circumferential sections (d) butterflies in axial sections ...	87
Figure 5.3.1: Depth of inclusions initiating micro-cracks and butterflies in axial and circumferential sections (the number above each characteristic refers to the average value) .....	89
Figure 5.3.2: Depth of micro-cracks in axial and circumferential sections compared with the depth of subsurface maximum shear stress $\tau_1(max)$ at various levels of contact pressure .....	90
Figure 5.3.3: Hardness variation with depth below the surface for the uncoated bearing	91
Figure 6.2.1: Characteristics for butterfly wings and their initiating inclusions (the number above each characteristic refers to the average value) .....	95
Figure 6.2.2: Depth of butterflies (the number above each characteristic refers to the average value) .....	95
Figure 6.2.3: Sample 6A2 at exit to loaded zone with white arrow represents the observation direction .....	97
Figure 6.2.4: Observations from axial sample 6A2 (Depth is shown in the upper left corner) .....	98
Figure 6.2.5: EDX analysis of the inclusion which initiated the longest butterfly in circumferential direction .....	99
Figure 6.2.6: Mg-Al-O inclusion .....	100
Figure 6.2.7: Inclusion length vs total length with the depth of inclusions (a) butterflies in axial sections; and (b) butterflies in circumferential sections.....	101
Figure 6.3.1: Irregurare subsurface crack network in circumferential section .....	102
Figure 6.3.2: Subsurface crack network initiated from deep inclusion at more than 1500 $\mu\text{m}$ in circumferential section.....	102
Figure 6.3.3: EDX analysis of highlighted inclusion in Figure 6.3.2 .....	103

Figure 6.3.4: Characteristics of subsurface cracks in axial sections (a) depth and length (the number above each characteristic refers to the average value) (b) angle (average values with the error bars show $\pm$ one standard deviation) .....	104
Figure 6.3.5: Subsurface WECs in axial section .....	104
Figure 6.3.6: Hardness variation with depth below the surface for BO coated bearing ..	105
Figure 6.4.1: Surface-linked RCF cracks (a) and (c) in circumferential sections and (b) in axial section .....	106
Figure 6.4.2: Surface-linked RCF cracks appears similar to WECs (a) from circumferential section and (b) WEC from axial section.....	107
Figure 6.4.3: Characteristics of surface-linked RCF cracks (a) length (the number above each characteristic refers to the average value) (b) angle (average values with the error bars show $\pm$ one standard deviation) .....	107
Figure 6.4.4: Surface cracks change direction toward the surface .....	108
Figure 6.4.5: Spall created by surface-linked RCF cracks in circumferential sections (ORD from left to right).....	108
Figure 6.4.6: Vertical surface cracks passing through an inclusion.....	109
Figure 6.5.1: EDX analysis of the BO layer.....	110
Figure 6.5.2: BO regions used for EDX and Nano-indentation analyses .....	111
Figure 6.5.3: AFM image of partially removed BO layer shows the adopted pattern off the Nano-indentation measurements using Hysitron Triboscope .....	112
Figure 6.5.4: Nano-indentation hardness of partially removed and undamaged BO layer using Hysitron Triboscope .....	112
Figure 6.5.5: Modulus of elasticity of partially removed and undamaged BO layer using Hysitron Triboscope.....	113
Figure 6.5.6: Nano-indentation hardness of undamaged BO layer using Hysitron TI Premier .....	114
Figure 6.5.7: Modulus of elasticity of undamaged BO layer using Hysitron TI Premier ...	114
Figure 7.1.1: Illustration of surface traction direction relative to the rolling direction and tangential velocity. This configuration was used for tests COT1 to COT3 (in Table 7.1.1) and RSTs 2 to 8 (in Table 7.1.2) .....	117

Figure 7.1.2: Illustration of rotation directions used for the RST1 in Table 7.1.2 (a) for RST 1a and 1c and (b) for RST 1b.....	120
Figure 7.2.1: COT variation with number of cycles according to Table 7.1.1 (a) COT1 (b) COT2 .....	121
Figure 7.2.2: (a) COT variation with number of cycles for dry contact (COT3) according to Table 7.1.1 (b) applied load (c) slip ratio .....	122
Figure 7.2.3: The surface after the COT measurement tests in Figures 7.2.1 and 7.2.2 (a) F1S after lubricated tests; (b) F1S after high speed dry test; and (c) C1 after high speed dry test.....	123
Figure 7.2.4: COT during reversed rotation according to testing conditions in Table 7.1.2. ....	123
Figure 7.2.5: COT of RSTs 1 to 9 at High Speed (HS) and Low Speed (LS) steps.....	124
Figure 7.2.6: Overall average for RSTs at High Speed (HS) and Low Speed (LS) steps.....	124
Figure 7.3.1: Non-crowned specimen surfaces at the middle of the contact width after each step of RSTs 1 to 9 (continue from previous page) .....	126
Figure 7.3.2: Specimen surfaces after RSTs and COT measurement tests.....	127
Figure 7.3.3: Surface damages measurement.....	128
Figure 7.3.4: Maximum size of surface cracks and pits after each step of RSTs 1 to 9.....	128
Figure 7.3.5: Surface roughness of specimens before and after RSTs 1 to 9. The under-scroll sign 1 and 2 refer to the measurement inside the central band of the wear scar or outside it, respectively .....	129
Figure 7.3.6: Lambda ratio ( $\lambda$ ) after RSTs 1 to 9 .....	130
Figure 7.3.7: Percentage change of surface roughness after RSTs 1 to 9.....	130
Figure 7.3.8: Specimen weight loss after each step of the RSTs 1 to 9 (each of the labels of the x-axis refers to the test number, steps and specimen used for the test separated by an under-scroll).....	131
Figure 7.4.1: Observations from metallurgical examination of RSTs specimens: (a) - (c) Surface-linked RCF cracks, (d) and (e) Pits and spalls (f) Debonded and cracked inclusion (g) and (h) Cracked inclusions initiated micro crack and (i) Possible butterfly.....	133

Figure 7.4.2: Surface-linked RCF cracks in circumferential direction: (a) Length and (b) Angle .....	134
Figure 7.4.3: Micro-cracks initiated by inclusions: (a) Depth in axial and circumferential direction (b) Length in circumferential direction .....	134
Figure 7.4.4: Number of inclusion initiated micro-cracks in axial and circumferential sections .....	135
Figure 7.4.5: Variation in subsurface hardness after RSTs .....	137
Figure 7.5.1: Surface-linked RCF cracks in circumferential sections (a), (b), (c) and (d) cracks start from surface spall; (e) and (f) cracks start from the surface; and (g) and (h) stair-like cracks .....	139
Figure 7.5.2: Inclusion initiated micro-crack (a) and (b) debonded inclusions in axial sections; (c) cracked inclusion in axial section; (d) cracked and debonded inclusion in axial section; and (e) and (f) undamaged inclusions in circumferential section .....	140
Figure 7.5.3: Debonded inclusion (a) and (b) debonding expanded to micro cracks in circumferential section; and (c) and (d) debonded and cracked inclusions in circumferential and axial sections, respectively .....	141
Figure 7.5.4: Possible WEA and butterfly wings in circumferential sections (a) and (b) debonded inclusions and butterfly wings; and (c), (d), (e) and (f) butterfly wings and micro-cracks.....	142
Figure 7.6.1: Development of surface-linked RCF cracks (specimen F1F for RST 1 with higher magnification to show propagation of crack) .....	143
Figure 7.6.2: Pits and spalls formation in circumferential sections (a) surface-linked RCF cracks propagate close to each other; (b) and (c) surface-linked RCF cracks interact to form a spall; (d) and (e) spall with cracks extending to form bigger spalls; and (f) crack network in axial section.....	144
Figure 7.6.3: Percentage of cracked and debonded inclusions in inclusions that initiated micro-cracks.....	145
Figure 8.1.1: Torque on LSS for NREL 750 kW WTG .....	149
Figure 8.1.2: Maximum contact pressure at inner ring of upwind planetary bearing (points 1 and 2 are the minimum and maximum point during torque reversal) .....	149
Figure 8.1.3: Minimum lubricant film thickness between rollers and inner race of upwind planetary bearing (points 1 and 2 are the equivalent to those in Figure 8.1.2) .....	150

Figure 8.1.4: Pressure spike $p_s$ at inner ring of upwind planetary bearing .....	150
Figure 8.1.5: Subsurface $\tau_1$ at different COT under $x=0$ and $x=0.9b$ at $p_{\max}=1700$ MPa ...	152
Figure 8.1.6: Subsurface $\sigma_v$ at different COT under $x=0$ and $x=0.9b$ at $p_{\max}=1700$ MPa ...	152
Figure 8.1.7: $\tau_1(\max)$ and $\sigma_v(\max)$ with and without surface traction at different operation conditions (a) and (c) are for point 1 ( $x=0, z=0.78$ ); and (b) and (d) are for point 2 ( $x=0.9b, z=0.5$ ). Blue and black arrows show maximum value with and without surface traction. ....	153
Figure 8.1.8: Damage accumulation ratio at different operation events with and without surface traction (COT=0.08) .....	155
Figure 8.2.1: Illustration of M1-2D models .....	156
Figure 8.2.2: Illustration of M2-2D models .....	157
Figure 8.2.3: Illustration of M1-3D models (all the sides are unconstrained) .....	157
Figure 8.2.4: True stress-strain curve for bearing steel [149] .....	158
Figure 8.2.5: (a) Comparison of subsurface stresses at $x=0$ under $p_{\max}=1466$ MPa and no surface traction using FE models M1-2D and M2-2D, and analytical solution (Figure 8.2.3 shows the axes) (b) the uncertainty of M1-2D and M2-2D.....	160
Figure 8.2.6: Validating results of M1-2D models at different values of surface traction and under $p_{\max}=1700$ MPa .....	162
Figure 8.2.7: Validating results of 2D FE modelling with MnS inclusion (a) schematic illustrates the inclusion and points A and B are where the stress concentration calculated (b) comparing the stress concentration calculated analytically with that from FE modelling .....	162
Figure 8.2.8: Comparison between results from 2D model with circular gap and 3D model with spherical gap (a) and (c) M1-2D model, and (b) and (d) M1-3D model (the highlighted values are not related to the stress around the gap).....	164
Figure 8.2.9: Comparison between results from 2D model (on left) and from 3D model (on right), the load at (a) and (e) is maximum and all others are at unloading (the highlighted values are not related to the stress around the gap).....	165
Figure 8.2.10: Lines measuring variation of $\sigma_v$ at $p_{\max}=1700$ MPa (a) across inclusion, and (b) at tip of inclusion (contact surface being $80 \mu m$ below inclusion).....	166
Figure 8.2.11: Local effect of inclusion on the variation of $\sigma_v$ under $p_{\max}=1700$ MPa .....	167

Figure 8.2.12: Load amplitude representing loading/unloading on bearing raceways ....	168
Figure 8.2.13: Stress contours at $p_{max}=1700$ MPa (a) matrix and inclusion (b) inside the inclusion.....	169
Figure 8.2.14: Yielding of elements at tips of MnS inclusion under $p_{max}=1700$ MPa.....	169
Figure 8.2.15: Stress contours and Yielding of elements at tips of MnS inclusion under $p_{max}=1700$ MPa and $q_{max}=600$ MPa (a) stress contours (b) yielded elements .....	169
Figure 8.2.16: Compression stress at tips of MnS inclusion (a) under $p_{max}=1700$ MPa (b) under $p_{max}=1700$ MPa and $q_{max}=600$ MPa.....	169
Figure 8.2.17: Residual tensile stresses (a) and (c) after $p_{max}=1700$ MPa; and (b) and (d) after $p_{max}=1700$ MPa and $q_{max}=600$ MPa .....	170
Figure 8.2.18: Stresses resulting from $p_{max}=3000$ MPa (a) equivalent stress at maximum loading; and (b) and (c) residual tensile stresses .....	171
Figure 8.2.19: Cyclic amplitude of normal and tangential load, representing cyclic loading on bearing raceways.....	172
Figure 8.2.20: Stress variation at inclusion tip due to load amplitude variation shown in Figure 8.2.19 with $p_{max}=1700$ MPa and $q_{max}=340$ MPa. A: No load and no residual stress; C: Maximum load and maximum equivalent stress; D: ( $p_{max}/2$ ) Start of build-up of residual stress in this cycle; E: No load and maximum residual stress in this cycle; and F: ( $p_{max}/2$ ) overcoming the residual stress from previous cycles and starting the compression stress .....	172
Figure 8.2.21: Equivalent plastic strain at inclusion tip due to the load amplitude variation shown in Figure 8.2.19 with normal load of $p_{max}=1700$ MPa and surface traction of $q_{max}=340$ MPa (letters have similar representation in Figure 8.2.20).....	173
Figure 8.2.22: Stress variation at inclusion tip during cyclic loading with the peaks and valleys have similar representation as in Figure 8.2.20 (the load amplitude applied is shown in Figure 8.2.19 and $p_{max}=1700$ MPa) .....	173
Figure 8.2.23: Equivalent plastic strain at inclusion tip without surface traction during cyclic loading with highlighting the stepwise increase of the PEEQ as in Figure 8.2.21 but with smaller rate (the load amplitude applied is shown in Figure 8.2.19 and $p_{max}=1700$ MPa).....	174
Figure 8.2.24: Models (A and B) used to investigate effect of surface traction direction on stress and strain at inclusion tips .....	175

Figure 8.2.25: Stress at maximum load (time=0.2 sec) from models in Figure 8.2.24 ((a) and (b) for model (A) and (c) and (d) for model (B)) .....	175
Figure 8.2.26: Residual stress and equivalent plastic strain at unloading (time=0.4 sec) from models in Figure 8.2.24 ((a) to (c) for model A and (d) to (f) for model B) .....	176
Figure 8.2.27: Illustrations of stress around 2 $\mu\text{m}$ circular gap under different directions of surface traction, shown in Figure 8.2.24 ((a) corresponding to model A; and (b) corresponding to model B) .....	176
Figure 8.2.28: Butterfly wing angle relative to rolling direction (surface of contact is below the butterflies and rolling direction from left to right) .....	177

## Publications and Presentations

*"Wind turbine gearbox bearings surface and subsurface damages due to impact and overloading conditions"* a poster presented in the conference of TriboUK 2014, in Sheffield

*"Experimental investigation of wind turbine bearing subsurface initiated damage"* a poster presented in the SUPERGEN Wind General Assembly in Glasgow UK

*"Experimental and FE modelling of wind turbine bearing subsurface initiated damage"* a poster presented in the Doctoral Academy Conference, and the PhD Poster Event and won the 2nd prize for the best poster

*"Investigation of wind turbine gearbox bearing subsurface damage considering transient loading"* a conference paper and a poster presented in the Conference of Wind Europe Summit 2016 in Germany, Hamburg

*"Initiation of sub-surface micro-cracks and white etching areas from debonding at non-metallic inclusions in wind turbine gearbox bearings"* a journal paper accepted to be published in the journal of Wear

*"Analysis for the white etching cracks and butterflies observed in wind turbine black oxide coated bearing"* a journal paper to be submitted to a journal

## Acknowledgments

### Allah

First and foremost, all praises to *Allah* for the strengths and blessing in completing this thesis.

### Supervisors

- My gratitude to my first supervisor *Dr Hui Long* for the guidance and support throughout the PhD study.
- Thank you to my second supervisor *Prof. Rob Dwyer-Joyce*.

### Family

- Thank you to my well and sincere wishers ever my beloved *parents* and my steadfast supporters my *brothers*.
- Only deep love can acknowledge my patient and ever faithful *wife* and my darling *daughter* and *son*.

### Sponsor

Grateful feelings go to my ever beloved country *Iraq* and its representatives the *Iraqi ministry of higher education and scientific research* and the *University of Baghdad* to sponsor my PhD study.

### Industrial Sponsors

- *Vestas Wind Systems A/S* for the provision of the failed Black Oxide coated bearings and technical support.
- An *anonymous partner* for the provision of the failed non-coated bearings and technical information.
- The *National Renewable Energy Laboratory* for the provision of their 750 kW wind turbine gearbox test data.

### Technical support

- Sincere thank you to *Dr Thomas M Bruce* for the directions provided at the beginning of my PhD study.
- The continuous technical support and willing to help shown by *Mr. David G Butcher* and *Mr. Luke R Callaghan* are highly appreciated and never forgettable.
- Sincere thank you to *Miss Dawn Bussey* for the training on the AFM and Nano-indentation techniques, and for the help in conducting some of the tests.
- Thank you to the friendly helper and trainer in the samples preparation laboratory *Mr. Michael Bell*.
- Thank you to *Mr. Robert J Hanson* for help in conducting the Infra-Red spectroscopy tests.

### Friends

- Thank you to all *my friends* all over the world for the kind wishes and emotional support.
- Special thanks to fellows and friends *Haider RD Al-Hamadani, Jasim H AL-Bedhany, Sheng Ai* and *Zhaohua Li* and I wish them all the best for their PhD.

## Abbreviations

AFM	Atomic Force Microscopy
ASB	Adiabatic Shear band
BO	Black Oxide
COT	Coefficient Of Traction
CRB	Cylindrical Roller Bearing
EDX	Energy Dispersive X-ray spectroscopy
EHL	Elasto-hydrodynamic Lubrication
EVA	Extreme Value Analysis
FE	Finite Element
GRC	Gearbox Reliability Collaborative
HSS	High Speed Shaft
irWEA	irregular White Etching Area
LSS	Low Speed Shaft
MBS	Multi Body System
MnS	Manganese Sulphide
NREL	National Renewable Energy Laboratory
ORD	Over Rolling Direction
RCF	Rolling Contact Fatigue
RSTs	Rolling Sliding Tests
SEM	Scanning Electron Microscope
SPM	Scanning Probe Microscopy
SUROS	Sheffield University Rolling Sliding twin disc machine
WEA	White Etching Area
WEC	White Etching Cracks

WSF	White Structure Flaking
WT	Wind Turbine
WTG	Wind Turbine Gearbox
WTGB	Wind Turbine Gearbox Bearing

## Nomenclature

$\alpha$	Pressure viscosity coefficient
$\eta$	Dynamic viscosity of lubricant
$\nu_1$	Poisson's ratio of rolling elements
$\nu_2$	Poisson's ratio of bearing race
$\sigma_a$	Stress amplitude
$\sigma_f'$	The fatigue strength coefficient in the Palmgren-Miner rule
$\sigma_m$	Stress mean
$\sigma_v$	von Mises stress
$\sigma_{v(\max)}$	The maximum von Mises stress along the subsurface stress distribution under certain point on the surface
$\tau_1$	Principle shear stress
$\tau_{1(\max)}$	The maximum principle shear stress along the subsurface stress distribution under certain point on the surface
$\tau_{xz}$	Alternative orthogonal shear stress
$\tau_{xz(\max)}$	Maximum orthogonal shear stress along the subsurface stress distribution under certain point on the surface
$b$	Half width of contact
$B$	The exponent for the Palmgren-Miner rule
$D_i$	Damage due to specific stress and number of cycles
$E^*/E_r$	The reduced (or equivalent) elastic modulus
$E_1$	Elastic modulus of rolling elements
$E_2$	Elastic modulus of bearing races
$F_p^r$	Unidirectional force on each planetary bearing
$G$	Non-dimensional material parameter
$h_{min}$	Minimum lubricant film thickness

L	Length of the rolling element
M1-2D	Two dimensional FE models represent a section of the inner raceway with Hertzian pressure distribution on the surface to represent the contact with the roller of maximum rolling element load $Q_0$ (these models could include a MnS embedded inclusion with certain interaction with the steel matrix)
M1-3D	Three dimensional FE model represents an extension of the M1-2D to three dimension but with an ellipsoidal gap instead of the inclusion
M2-2D	Two dimensional FE models represent section of the roller, inner raceway and outer raceway
N	Number of cycles
$N_{fi}$	the number of cycles to failure at specific stress
$N_i$	the applied number of cycles at specific stress
$p_{max}$	Maximum contact pressure
$p_s$	Pressure spike due to the EHL effect
$Q_0$	Maximum load of rolling element
R	Reduced radius (or the sum curvature)
$T_{LS}$	Low speed shaft torque
u	Average tangential velocity
U	Non-dimensional speed parameter
W	Non-dimensional load parameter
Z	Number of rolling elements

# 1 Introduction

In this chapter the importance of wind energy production is introduced in the context of both the dramatic growth in the global deployment of wind turbine technology, and the essential reliability issues. Any mechanical systems that involve moving parts present reliability challenges, and in Wind Turbines (WTs) the gearbox components and particularly their bearings are critically important to the overall reliability of these turbines.

Premature failure in Wind Turbine Gearbox Bearings (WTGBs) has been a cause for concern in recent years, and the aim of this research is to investigate the root-causes of this unexpected behaviour. Despite this problem is thoroughly investigated in the published research literature, it is still not fully understood, and further investigations are essential in order to identify the causes of these failures. The aims and objectives of this research are presented in the following sections together with a brief outline of the content of each chapter in the thesis.

## 1.1 Background

Globally, the production of wind power increases every year as shown in Figure 1.1.1 [1] and in the last fifteen years the global wind capacity has grown by a factor of 20, from about 25000 MW to almost 500000 MW. The European Commission has set the 2030 Energy Strategy to achieve a target of at least 27% of the overall electricity consumption to be provided from renewable energy [2], with individual plans for the European countries, such as Germany who plans to achieve 40 to 45% of the energy consumption from renewable sources by 2025 and 80% by 2050 [3]. Although the cost of wind energy is very competitive with other types of renewable energies, and sometimes with conventional energy [4][5], reducing the maintenance and downtime of this technology is essential to keep up with future demands [6]. The trend toward multi-Megawatt offshore wind turbines and the associated accessibility challenges highlight the importance of component reliability. Thus, extending the lifetime to failure of the most challenging parts to be replaced is a key factor in sustaining this technology and maintaining a financially competitive edge.

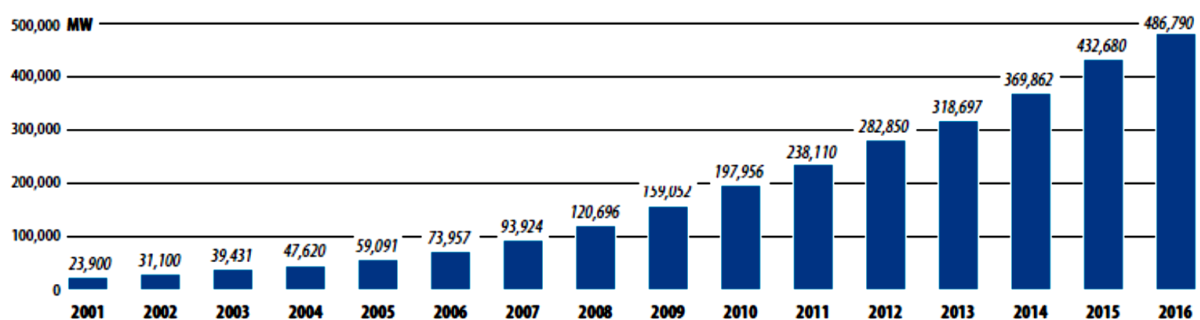


Figure 1.1.1: Global cumulative installed wind capacity 2001-2016 [1]

The costs of the downtime due to maintenance clearly influences this technology with regard to the reliability of wind energy. Premature bearing failures have been frequently

observed in Wind Turbine Gearboxes (WTGs) which makes their reliability a top priority among other components [7][8][9]. One of the many studies on the reliability of wind turbine components is based on the operational data of 26 wind farms in the UK in which components with the highest rate of failures were studied [10]. The bearings in these turbines failed before the expected operating life-time of normally 20 years. The most common premature failure was due to White Etching Cracks (WECs) which cause pieces of material to be flaked from the surface (White Structure Flaking (WSF)) [11][12][13]. The root causes of the premature failure for WTGBs are not fully understood and further investigation is necessary followed by corrective action before satisfactory operating life-times can be achieved.

Bearings failures may initiate either on the surface or under the surface of contact in the bearing raceways. The surface initiation hypothesis suggests that cracks could be caused by surface flaws which become worsened under loading conditions [13][14][15][16]. Another possible cause is material defects such as non-metallic inclusions which could serve as WECs initiators by forming butterflies, and this is described as the subsurface damage initiation hypothesis [17][18][19]. Other damage initiation hypotheses have been proposed, including the effect of hydrogen, plastic deformation, brittle fracture due to high traction on the surface, and unconsidered loadings, such as impact load, causing lubrication failure [20][21][22][23]. However, a clear explanation supported by sufficient evidence by investigating the critical factors, such as high loads during transient operation events, and the observed subsurface damages, such as the WECs and the attaching White Etching Areas (WEAs), has not been established.

## 1.2 Aims and Objectives

The aim of this research is to provide an explanation for the mechanism of the premature failure of WT planetary bearings taking into account steel cleanliness (non-metallic inclusions), the surface traction and the loading sequence representing WT operational conditions involving torque reversal and severe transient loading. In addition, this study also aims to investigate if a special bearing surface coating technique, namely Black Oxide (BO) coating, is effective as one of the currently used means to prevent the premature failure and to prolong the bearing life. This study aimed to achieve the following objectives:

1. To examine the surface and subsurface damage of a failed WT planetary bearing removed from service after premature failure. To characterise key features of surface damage and subsurface microstructural damage initiated at non-metallic inclusions to provide a database to analyse the damage initiation mechanism.
2. To evaluate the functionality of the BO coating against the premature failure and the damage observed in the uncoated failed bearing by metallurgical examination of a failed BO coated planetary bearing.
3. To identify the effect of surface traction value and sequence on the surface and subsurface damage initiation by designing and executing a set of experimental

tests. To replicate the observed surface and subsurface damages in the aforementioned bearings and to validate the explanations based on the examination of the failed bearings.

4. To investigate the effect of surface traction on damage accumulation in the planetary bearing of a case study wind turbine by calculating the load, contact pressure and subsurface stress distribution.
5. To determine the mechanism of the subsurface damage caused by inclusions and to determine the key factors affecting this damage by developing Finite Element (FE) models of the inner raceway of the planetary bearing in a case study wind turbine considering the non-metallic inclusions.

### 1.3 Thesis Outlines

The following provides an overview of the structure of the thesis and the contents of each chapter. An overview for the key findings of investigation results, presented in Chapters 5 to 8, is also presented at the end of each of these chapters.

#### **Chapter 2: Literature review**

This chapter starts with an overview of the key bearings failure modes which have been found in WTGBs, and then discusses in more detail, some of the causes of premature failure such as WECs, and the effect of bearing cleanliness. Next, a review of published research in the field of premature bearing failure is presented together with a discussion on current methods for improving the bearing lifetime to failure. This is followed by an outline of the analytical calculations conducted in Chapter 8 for the load and tribological aspects of WT planetary bearings. Then, a review of the studies that modelled the effect of non-metallic inclusions is presented and discussed. Lastly, the findings from the previous investigation of the subsurface initiated damage are correlated to the reviewed modelling methods and the unconsidered parameters were highlighted.

#### **Chapter 3: Destructive Investigation on the Failed Bearings**

This chapter explains the steps and techniques adopted to examine the failed bearings described in Chapter 5 and 6, and the tested specimens of the Rolling Sliding Tests (RSTs) in Chapter 7. Firstly, the preparation of samples for the metallurgical examination is presented including the sectioning patterns used for each bearing raceway. Then the inspection of the prepared samples is presented, where different imaging and hardness measurement techniques on the micro and nano scales are explained with reference to the investigations in this research. The last section of this chapter introduces the observations from the metallurgical examinations and clarifies the terms used for these observations of damage throughout this thesis. The last section also explains the method used to evaluate the cleanliness of the bearing steel, and to identify the types and chemical elements of the non-metallic inclusions.

#### **Chapter 4: Experimental Investigation of Damage Initiation Using Twin Disc Testing**

This chapter describes the procedure adopted to conduct the RSTs and the results obtained will be presented in Chapter 7. It starts with a general description of the test equipment, SUROS (Sheffield University Rolling Sliding) twin disc machine, which is used to conduct Rolling Contact Fatigue (RCF) under different loads and slipping ratios. This is followed by a description of the modifications made to this machine to meet the requirements of this research in order to providing constantly lubricated tests. It presents the design and manufacturing details for the specimens and lubricants properties used for the Coefficient Of Traction (COT) measurements, and the RSTs as well as the test conditions, and the selected parameters for each test. Lastly, the methods and procedures used to investigate the specimens' surface and subsurface damage are presented.

#### **Chapter 5: Results and Discussion on Investigation of a Non-coated Bearing**

This chapter presents the examination results of a failed non-coated planetary bearing retrieved from a sub-Megawatt WT. The chapter starts by presenting the observations from the metallurgical examination of the most dominant type of non-metallic inclusions, Manganese Sulphide (MnS), and their associated defects such as the debonding from the steel matrix. The focus was on those that are cracked, and those that caused subsurface initiated damage, micro-cracks and WEAs in the form of butterflies. A database of the properties of the inclusions and damage were developed and analysed. Also, the Nano-indentation was conducted across a butterfly to show the variation of the hardness across the interface between the WEA and the steel matrix. To show specifications for the butterfly wing which has not been reported before, the AFM was used. Lastly, the distribution of micro-cracks and butterflies along the depth was correlated with the distribution of the principal shear stress  $\tau_1$  in order to highlight the role of surface traction.

#### **Chapter 6: Results and Discussion of Investigation of Black Oxide Coated Bearing**

This chapter describes the examination results of the failed BO coated planetary bearing retrieved from a Multi-Megawatt WT. The investigation involved metallurgical examination and BO layer characterisation. The chapter starts by evaluating the steel cleanliness. The results of analysing the butterflies, subsurface cracks and cracks linked to the surface were used to explain the initiation of surface and subsurface damage. The following part of this chapter presents the characterisation of the BO layer. In this examination Nano-indentation was used to measure the hardness and Young's modulus for this layer at two regions, damaged and undamaged, on the raceway surface. The measurement was conducted in a specific way to find the depth of the BO at these two regions.

## **Chapter 7: Results and Discussion of the Experimental Investigation Using the Twin Disc Machine**

This chapter presents the results of investigations of a number of parameters on the surface and subsurface initiated damage of the RSTs. It begins with the results for the COT at different operating conditions including dry contact and reverse rotation. Then the surface examination of the specimens is presented, followed by the subsurface metallurgical examination. Accordingly, the effects of the investigated parameters on the initiation surface and subsurface damage are compared. This chapter also includes a comparison between the observed surface linked cracks, micro-cracks initiated by inclusion and possible butterflies with those found in the examined failed bearings described in Chapters 5 and 6. Lastly, based on the observation and statistics of surface and subsurface damage, taking the investigated parameters into consideration, predictions for damage initiation mechanisms are presented.

## **Chapter 8: Results and Discussion of Load Calculation and Stress Analysis**

This chapter is divided into two main parts in which tribological calculations and FE modelling are used to explain the observations from the failed bearings and the tested specifications. The first part includes a validation for the load calculation method and this is followed by calculations of maximum contact pressure  $p_{max}$  and minimum lubricant film thickness  $h_{min}$  during three operation events. Following this the maximum subsurface stress at different surface traction is investigated, and the accumulated damage presented. The second part of this chapter begins with a description and validation of the FE models of the inner raceway of the planetary bearing of the NREL 750 kW. The models were used to investigate the stress and strain developed at the MnS inclusion under various normal and tangential loading. The effect of the inclusion-matrix interface and cyclic loading were also investigated. Lastly, the results obtained were correlated with the observations from the examined failed bearings in order to investigate the direction effect of surface traction.

## **Chapter 9: Conclusions and Future Work**

This final chapter firstly presents the overall conclusions of this research based on the results and analysis in Chapters 5 to 8. The second part of this chapter includes suggestions for future work and recommendations for improving the lifetime of WTs, based on the findings from this thesis.

### **1.4 Contributions to Knowledge**

The study identified seven types of surface and subsurface damage initiated from non-metallic inclusions and the important role of surface traction. Destructive examination of a failed WT bearing confirmed the initiation of damage from MnS inclusions that were mostly debonded from the steel matrix, identified the occurrence of high surface traction and characterised the distortion of the material inside the butterfly wing using AFM.

Examination of a failed BO coated bearing and measuring the properties of the BO layer showed that this coating does not prevent surface and subsurface initiated damages of surface initiated cracks, WECs, WEA and butterflies in the loaded zone of the WT planetary bearing. The RSTs identified the effect of tribological conditions sequence and reverse rotation on the initiation of surface and subsurface damage, and the tested specimens showed similarity with the observations from failed bearings. The FE models confirmed the role of surface traction and inclusion debonding from the steel matrix on the stress state around the MnS inclusion, and also revealed the effect of surface traction direction on the generation of tensile stress and thus the subsurface initiated damage. This study showed the occurrence of high surface traction in WT planetary bearings and provided a hypothesis to explain the mechanism of subsurface initiated damage with emphasizing the importance of bearing steel cleanliness and inclusions debonding.

## 2 Literature review

A review of the premature failure of WTGBs is presented in this chapter. Various bearing damage types are overviewed, with a focus on the WECs. To investigate the factors affecting the deterioration of bearings, WT operational conditions and bearing steel cleanliness are discussed, highlighting the detrimental effect of high surface traction (severe tribological conditions) and non-metallic inclusions in bearing steel. The experimental investigations reported in the literature are discussed and classified to develop the objectives of this research and the design of the experiment. Different surface treatment methods used in WTGBs are discussed. In addition to the experimental investigations, studies that modelled subsurface damage initiation are reviewed.

### 2.1 Failure of Wind Turbine Gearbox Bearings

In this section, the main types of failure modes of roller bearings are presented with a focus on those reported in the WTG. Then the WECs, which is one of the focused areas in this research, and the RCF, which is the classic failure mode for roller bearings, are discussed in more details. The configuration of the WTG design and load transmitted to the bearings are introduced with a review of the studies in this area. Since the effect of non-metallic inclusions on subsurface initiated damage is investigated in this research, steel cleanliness and non-metallic inclusions types are presented and discussed. Lastly, the fundamentals of bearing life assessment methods are discussed.

#### 2.1.1 Bearings Failure Modes

Many failure modes are reported for wind turbine bearings and they are presented briefly in this section. The premature failure by WECs is the main failure mode investigated in this thesis and it is discussed separately in Section 2.1.4. Also, the subsurface initiated spalling due to the RCF process is presented in Section 2.1.3 to be discussed in correlation to the initiation of WECs. The root causes of WECs are currently under investigation by many theories. On the other hand, the failure modes presented in the current section are included in the international standards with their main features and causes. Reviewing these modes provides an understanding for the main driving factors that could be involved in the initiation or propagation of the WECs. The classification of different types of failures modes in rolling bearings is mainly based on either the feature of the failures or their cause and mechanism. The international standard (ISO 15243:2017) [24] provides a list of failure modes that have been observed in different applications. Lists based on other classification of modes are suggested by bearing manufacturers such as SKF [25], or some tribology books such as [26]. However, in advanced stages of failure, it is not straightforward to decide the cause or mechanism based on the observed surface.

The factors affecting the bearing life can be named as incorrect handling, assembly or mounting (misalignment); inadequate lubricant film thickness due to overheating or inappropriate lubricant; contamination due to poor filtering and sealing; transient loading

and vibration; and electrical current [27]. In addition, even with avoiding all these factors, the expected lifespan of any bearing is still limited due to the failure by RCF [28]. The possible causes and key features for some types of failure observed in WT bearings are presented in Table 2.1.1. Most of the damage in this table is initiated due to high stress concentrations on the surface and/or high frictional force. Other factor controlling the failure of bearings is the steel cleanliness since the strength of the bearing steel varies due to defects such as non-metallic inclusions. Therefore, the metallurgical examination, or non-destructive techniques, can be used to differentiate between surface and subsurface damage initiation.

Previous studies, such as the NREL report [29], provide surface observations from damaged wind turbine bearings but without operation history. Therefore, trials to replicate the damage observed in the bearings from the field are useful to better understand the key factors of wind turbine bearing deterioration. Although the surface examination can indicate the possible causes of damage, it provides less information about the initiation stage when the damage is advanced. In the wind turbine, bearings of different types, such as ball, roller, spherical and tapered bearings are deployed in different components, such as the generator, gearbox, the main shaft, and yawing and pitching systems [30]. In addition to the failure modes listed in Table 2.1.1, the premature failure of WTGBs have been reported to be mainly caused by WSF and WECs [31][32].

**Table 2.1.1: Some types of failure observed in WT bearings [26][29][33][34][35]**

Damage	Cause
Smearing (skidding): Mechanical removal of material from a surface, usually involving plastic shear deformation	The rolling elements are lightly loaded and subjected to severe acceleration on their re-entry into the load zone.
(surface initiated) Pitting: A form of material removal involving the separation of particles from a surface, generally less extensive than spalling	<ul style="list-style-type: none"> <li>• The surface stress due to the frictional shear stress and asperities interaction</li> <li>• Insufficient lubricant film thickness</li> </ul>
Surface distress: micro-cracks and micro-spalls	<ul style="list-style-type: none"> <li>• Reduced lubrication regime and a certain percentage of sliding motion</li> <li>• Indentations caused either by contaminant particles or by handling</li> </ul>
Spalls: separation of particles from a surface in the form of flakes or chips	<ul style="list-style-type: none"> <li>• Material removal, resulting from the separation of macroscopic particles from a surface</li> <li>• increase in geometric stress concentrations</li> <li>• may also result from impact</li> </ul>
Abrasion wear: displacement of material caused by hard particles or hard protuberances	Contaminated lubricant causing wear of the bearing contacting surfaces
False brinelling marks: a combination of corrosion and wear which forms shallow depressions in the raceways	Vibrations transfer from an outside source to a stationary bearing, leading to oscillating movements between raceways and rolling elements
Brinelling: plastic deformation of the surface recognised by equidistance indents	Overloading (shock) while the bearing is at stationary state

### 2.1.2 Normal and Tangential Loading on WTGBs

The WT experience a broad range of operational and severe loading conditions: for instance, unsteady winds, potential grid faults and torque reversal during transient events. The major components of wind turbine drive train depicted in Figure 2.1.1 show the connection of the gearbox with the rotor from one side, by the Low Speed Shaft (LSS), and

the generator from the other side, by the High Speed Shaft (HSS). The configuration of a generic three stage WTG is shown in Figure 2.1.2. The figure shows how the planetary gears are supported by the planetary bearings.

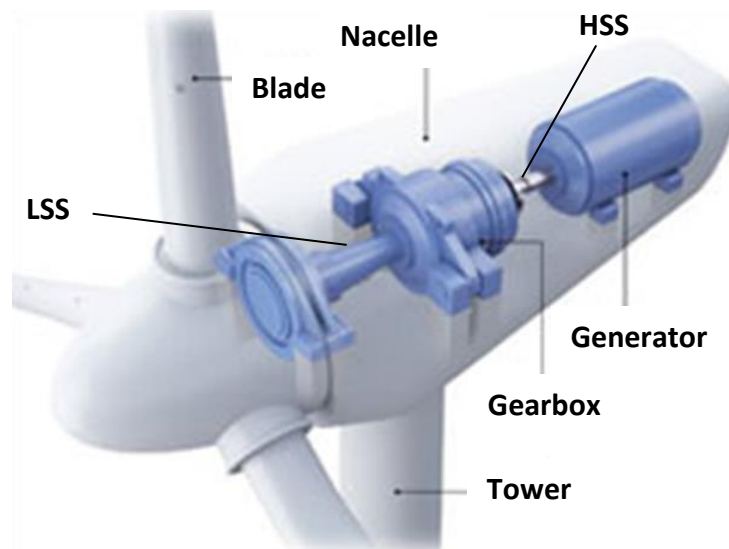


**Figure 2.1.1: Main components of wind turbine drive train (Courtesy of Olympus) [36]**

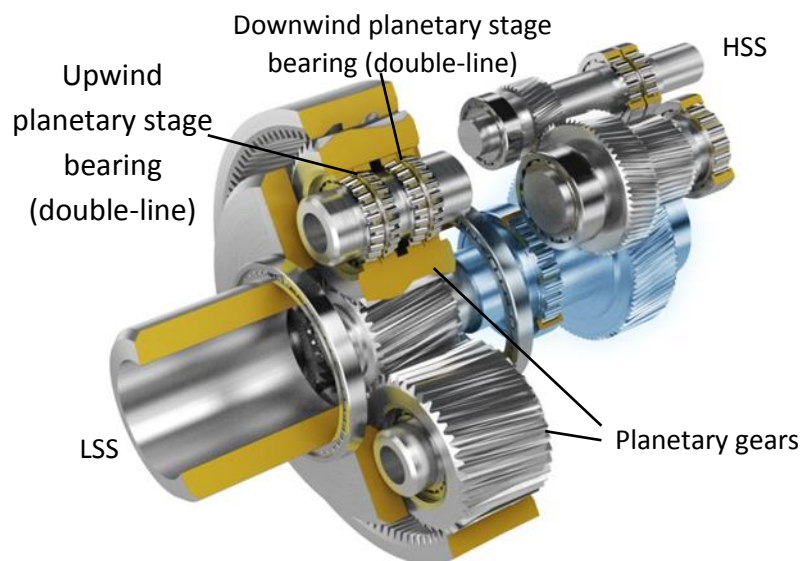


**Figure 2.1.2: WTGBs in planetary stage (Courtesy of Olympus) [36]**

In this research, the damage of the planetary bearings was investigated, which have been observed in previous studies to be one of the WTGB that are vulnerable to premature failure [31][37]. Figure 2.1.3 shows how the inner raceway of the planetary bearing is mounted to the pin which is not rotating, while the outer raceway rotates with the planetary gear. This configuration transfers the load from the low speed shaft to the planet carrier in a unidirectional way which exposes the loaded zone of the inner raceway to greater damage.

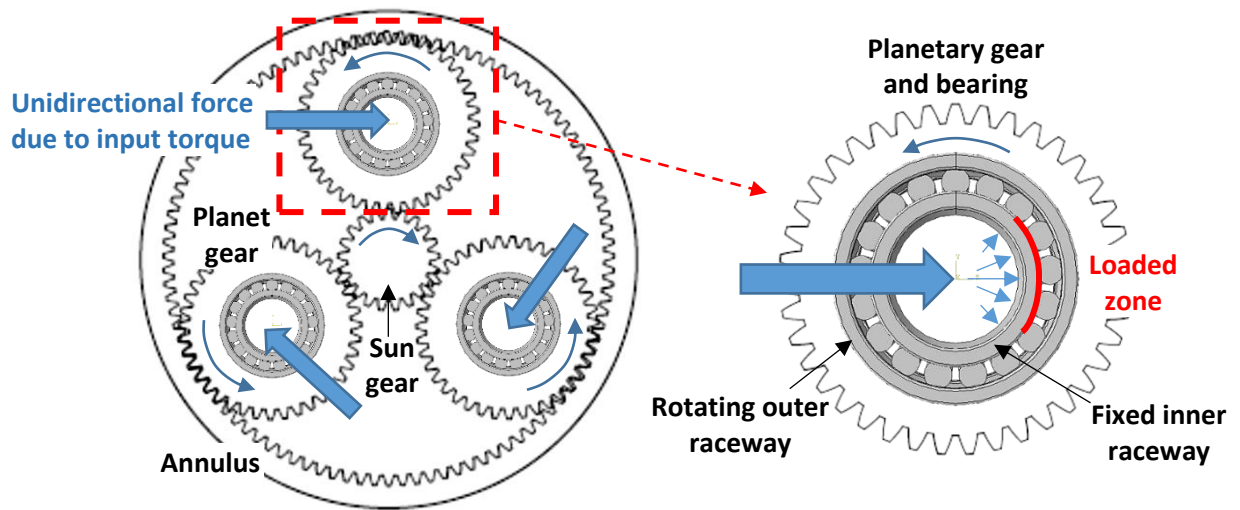


**Figure 2.1.3: Generic WT planetary stage illustrates the unidirectional load on the inner raceway of the planetary bearings and the loaded zone**

The operation of wind turbines consists of different events, such as start-up, normal operation and shutdown. The load at each of these events represents a spectrum of different load variations. Accordingly, gearbox bearings, as one of the most vulnerable machine elements to failure, work under highly variable loading conditions. This leads to different contact pressure and lubricant film thickness, which sometimes exceeds the designed load limit. In addition, the lubricant, which is one of the most important factors for alleviating the tribological effects on the bearing surface, may not work in the most efficient way because the same lubricant is used for the whole gearbox, which consists of machine elements operating under different speed, load and temperature. Above all, of the aforementioned transient events, misalignment and harsh environments, such as variable temperature and high moisture, worsen the working condition of the mechanical components [10][12][38].

In this research the effect of two transient events, shutdown and start up, on damage accumulation is investigated in Chapter 8. Previous studies, such as [10][30][39][40][41], investigated the load on bearings in different stages of the wind turbine drive train through models of different complexity. Most of those models show that during transient events, such as emergency shutdown, the load on some bearings reaches a high level, exceeding the recommended limit. The stress caused by this load may increase to a much higher value when some cases of misalignment such as truncating occurs where only a part of the full length of the roller is in contact with the races [39]. Although, this may not cause yielding or fatigue of the very hard bearing steel, during some of the transient events, such as the emergency stopping of the wind turbine, the normal force decays relative to the tangential force, causing the onset of skidding [39]. A recent study investigated the effect of torque reversal, which occurs during the transient event of grid loss, on the slipping of the HSS

tapered roller bearings [42]. The study was conducted through a full-scale 750 kW wind turbine drivetrain of the Gearbox Reliability Collaborative (GRC). During grid loss, the reversed torque caused a speed increase and the counter torque resulted in a braking effect. This resulted in an impact effect at each torque reversal and a possible lubricant film failure. On the HSS, the results of the experimental investigation in [42] shows that, during torque reversal, excessive slipping may occur. Other studies, such as [43][44], were conducted to investigate the load sharing between the upwind and downwind planetary bearings, and revealed a higher load on the upwind bearing at the rated torque. It is also shown that skidding can occur in planetary bearings, according to [45][46][47].

Slipping could happen for the roller due to the acceleration and deceleration during entering and exiting the loaded zone. Also, the sudden change in the loaded zone during the transient event, the torque reversal, increases the risk of excessive slipping, and thence skidding [48]. In addition to all this, during the transient events the heavy components of the wind turbine may cause the shafts of the gearbox to be elastically displaced more than the clearance, causing misalignment, which may have a considerable effect on machine elements of high sensitivity to misalignment, such as bearings [34].

### 2.1.3 RCF Cracks and Shakedown

The deformation developed during the rolling contact is determined by the contact pressure and surface traction. When the surface and subsurface stresses are below the yield limit, elastic deformation occurs, and plastic deformation occurs above this limit. When the applied load exceeds the yield limit during the early loading cycles, some plastic deformation and residual stress develop. The residual stress will increase the limit for the applied load to cause plastic deformation and this is called the shakedown limit. During the following cycles, no more plastic deformation occurs if the load is below the shakedown limit. At even higher load, ratchetting occurs which is a plastic deformation accumulation that arises at a threshold value higher than the shakedown limit and it leads to failure [49]. The introducing of surface traction reduces the shakedown limit and drag the damage initiation point toward the surface [50]. On the other hand, due to the strain hardening and under repeated plastic deformation, the material shear strength may rise and more load is allowed without exceeding the shakedown limit [49].

In rolling bearings, the occurrence of shakedown as the first stage of surface and subsurface damage is shown by the X-ray diffraction (XRD) measurements of macro- and micro-residual stresses [18]. The rapid increase in the compressive residual stress, as well as the observation of the micro-plastic deformation, characterises the shakedown which represents the first stage in subsurface initiated RCF [18]. The second stage is a steady-state elastic response with insignificant damage. The third stage of instable deterioration is represented by micro-plastic deformation and microstructure changes due to carbon diffusion and eventually material softening [18][51]. In addition to the subsurface initiated RCF, micro-pitting caused by surface initiated RCF also occurs in rolling bearings [16][52].

There are two types of surface initiated micro-cracks. The first is due to surface stress concentration caused by machining defects or indents by solid contaminations. The propagation of this type can occur due to pure rolling or rolling plus sliding. The second type initiates at high surface traction and propagates opposite to the sliding direction, mainly due to mode II crack openings [16]. Some studies show that controlled elastic-plastic deformation to cause elastic shakedown can improve a bearing's lifespan [53]. However, in applications with severe transient loading, such as wind turbines, shakedown can be followed by ratcheting and a deterioration in the bearing's life. In this research, the observations from the examination of failed bearings and the rolling sliding tests revealed surface as well as subsurface initiated cracks, as discussed in Chapters 5, 6 and 7. Moreover, for coated surfaces, the shakedown limit is shown to be affected by the coating and substrate properties [54][55]. In Chapter 6, the effect of BO coating on surface and subsurface damage in WT bearing is investigated.

#### 2.1.4 WECs and WEAs Characterization and Initiation

##### Characterization:

The WSF is considered to be the main cause of premature failure of WTGBs. The WSF is the final stage of WECs, which are micro-cracks surrounded by the microstructure change of WEA [19][56][57], as shown in Figure 2.1.4. The WEA can be seen under optical microscope after etching with nital (~ 2% nitric acid in ethanol) or picral [14][58][59]. In addition to conventional destructive methods, a non-destructive method using ultrasound and Barkhausen noise analysis techniques can also detect the subsurface WECs and microstructural changes [60]. The microstructure changes shown in premature bearing failure due to WSF are not uniform in shape or distribution, which is why it is often called a irregular White Etching Area (irWEA) [15][23]. For all the types for bearing steel [11], the microstructure of WEA is Nano-recrystallized carbide-free ferrite grains of sizes, ranging from 10 to 100 nm, supersaturated with carbon [56][61]. It is also found that there are two regions within the WEA in the WECs, one with a Nano-crystalline body-centred cubic (bcc) structure, and the other with a mixture of the Nano-crystalline bcc and newly formed metastable carbide M<sub>2</sub>C structures [62].

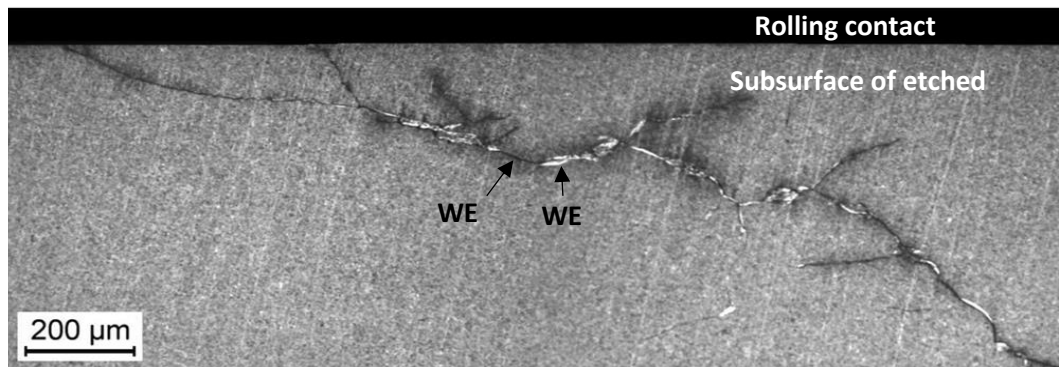


**Figure 2.1.4: WECs observed in the inner ring of a failed case hardened bearing (adopted from [57])**

#### Effecting Factors:

The relation and the sequence of WEA and WECs are not fully understood. Also, there is no consensus about the root causes of the WEC/WEA initiated failure. However, a number of hypotheses exist, including the influence of a number of parameters such as non-metallic inclusions [19][56][63][64], the amount of retained austenite [65], the type of lubricant used in operation and consequently the amount of hydrogen generated [14][58], the level of Hertzian contact stress induced by loading [18][64], transient loading and impact effect [66], surface traction in mixed lubrication regime [18] and stray current [21][67]. The theories developed to explain the WECs are divided according to the initiation of these cracks into surface initiation and subsurface initiation.

#### Subsurface Initiation:

The subsurface initiation of WECs is one of the theories to explain this damage, where the WEA could be initiated around non-metallic inclusions and develop to WECs [19][61]. According to this theory, the initiation started by forming features which are called 'butterflies' that consist of inclusions (cracked or not) and WEAs attached to them with or without microcracks propagated from the inclusions as shown the Scanning Electron Microscope (SEM) image in Figure 2.1.5. These inclusions, such as MnS or aluminium oxides,  $Al_2O_3$ , could be softer or harder than the bearing steel matrix [68]. Hydrogen embrittlement is widely accepted as a main source for worsening and propagating the WECs. Hydrogen can be released from the dissociation of water drops in the lubricant, the degradation of organic lubricants and/or oxidation [11]. Nevertheless, the harmful atomic hydrogen, absorbed into the steel, could only be generated when the formation of molecular hydrogen is suppressed, which is caused by hydrogen poisons, such as sulphur, where its source could be the base oil, additives in the lubricant or the steel [12][69]. Despite the role of hydrogen, a recent study by Diederichs et al. [58] shows that WEA and WECs can be found in vacuum pump bearings working in a hydrogen-free environment. One theory suggests that the butterfly forms by the rubbing between the steel matrix and the debonded inclusions due to the repeated loading and unloading which causes material

transfers from the steel matrix to the inclusion to form the WEA [70]. A hypothesis to explain the subsurface initiation of the WECs assumes an impact loading which could result high strain rate and localized heat that develop Adiabatic Shear Band (ASB) and initiate stepped WECs from the subsurface inclusions [66][71]. The impact loading is expected to be caused by the spike pressure due to the Elasto-hydrodynamic Lubrication theory (EHL) under variable loading and slipping conditions [66][71]. The impact loading also reported to occur in WT bearings due to the transient events such as gusts, braking, load reversals, grid loss and start-up that is expected to cause about 15000 overload cycles per year [72]. However, it is found by some researchers [18][57] that the strain rates occur in WT bearing due to the impact loading are much less than the strain rate required to cause ASB in bearing steel.

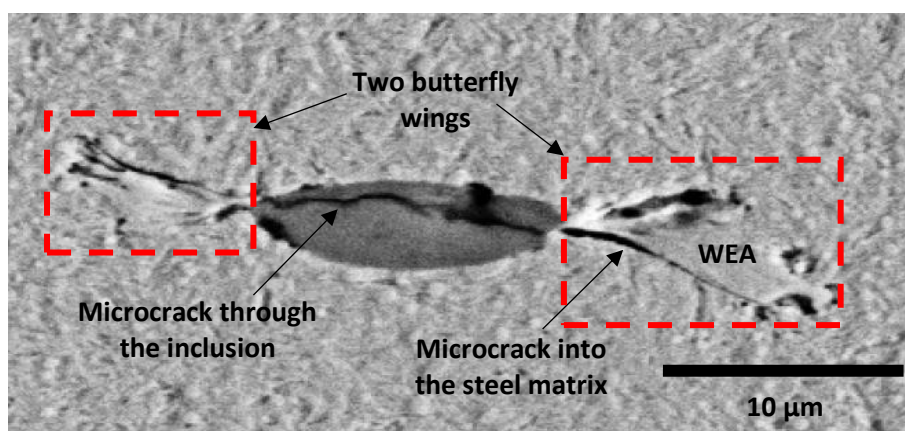


**Figure 2.1.5: SEM image of a butterfly initiated on an MnS inclusion (adopted from [56], Courtesy of Jürgen Gegner)**

#### Surface Initiation:

Some researchers believe that WECs are surface initiated [18] and their propagation is influenced by chemical factors such as oxygen ageing components of the lubricants and hydrogen, combined with loading and environmental factors [13]. Other propagation factors could be the impact loading or vibration-related conditions [69]. The initiation mechanism is explained by tensile stress due to high traction on the surface, which initiates a brittle fracture on the surface then propagates due to corrosion-fatigue cracking, due to hydrogen penetrating into the initiated crack. This mechanism suggests top-down crack propagation [12][13][18][59].

The initiation of the cracks (cleavage) on the surface due to frictional force and surface tensile stress is followed by propagation downward. Some theories explain the WEA in the WECs initiated from the surface by the rubbing occurs between the crack faces and the atomic transferring of the material from one side of the crack to the other side of the crack [70][73]. Another explanation using the rubbing mechanism is the deformation of the ferrite in the vicinity of the crack due to the rubbing between the crack sides and the recrystallisation to form the nano-ferrite where this process followed the stress induced

transformation of retained austenite in the vicinity of the crack to untempered martensite [73][74]. Other studies propose the formation of the WEA by the dissolving of the temper carbide [73]. In this research the effect of non-metallic inclusions and high surface traction on the surface and subsurface damage initiation are investigated.

### 2.1.5 Steel Cleanliness and Butterflies

The mechanical properties of bearing steel, such as the yield limit 1400-2200 MPa, the ultimate strength 2150-2450 MPa and hardness 59-66 HRC [68] are considered to be high compared to other types of steel. However, the impurities, such as inclusions, inevitably reduce the strength (fatigue strength) of the bearing steel [75][76]. The source of inclusion could be the erosion of the furnace lining material, dirt entrapped during steel manufacturing process or the deoxidation process [75]. During deoxidation, elements such as Mn, Si and Al, or rarely Cr, V, Ti, Zr and B are added to the molten steel to remove the excess oxygen by forming oxides of these elements as slags [77]. The size, shape and number of inclusions in the manufactured steel illustrate its cleanliness. A number of systematic methods are available for studying the cleanliness of steel, as documented and explained in the standards such as ASTM E45 [78], ISO 4967 [79] and ASTM E2283 [80]. The procedure of measuring steel cleanliness is to prepare samples from rolled or forged steel products through specific procedures, including sectioning in the inclusion elongation direction to prepare a number of samples, then preparing the samples for optical microscopy by grinding and polishing and sometimes etching with chemical composition. The scanning procedure varies according to the adopted standard, but in general fields of specific size and number are scanned and the size and number of inclusions are recorded. Next, in each field, the sum of the inclusions size, the number or maximum size for each type of inclusion, are recorded and processed to give the measure for cleanliness. More details are provided in Chapter 3. Inclusions of different chemical composition and mechanical properties have different shapes and colours when they are observed under an optical microscope. For rating steel cleanliness, non-metallic inclusions are classified according to their morphology and composition into sulphides, aluminates, silicates, oxides and sometimes nitrides [75]. These inclusions are classified into Types A to D, according to the ASTM E45 [78] and ISO 4967 [79] standards or Types A to C according to the Japanese standard JIS [76]. The morphologies, composition and mechanical properties of these non-metallic inclusions are shown in Table 2.1.2. It can be seen that some inclusions of specific chemical composition could be classified as type B or D, depending on their appearance as single, for type D, or group, for type B. Also, different chemical compositions, and thus different mechanical properties, can be found from the same type of inclusion. Thereby, the bonding between inclusions and steel matrix, as well as the resulted stress concentration caused by these inclusions, may vary significantly, with inclusions of different morphology and properties which are not fully represented by the standards. In addition, the methods recommended in the standards to determine the size or the number of inclusions neglect the distribution of the inclusions relative to the location of maximum

shear stresses under the surface, such as  $\tau_{1(\max)}$ . However, among other standards, the ASTM E2283 [80] seems to correlate better with the fatigue behaviour of the rolling bearings, according to industrial experts [81]. This standard is based on the Extreme Value Analysis (EVA), which relies on the size of individual inclusions rather than the total size or the number of inclusions in a number of fields as in the ASTM E45 and the ISO 4967. However, the cleanliness analysis based on the number of inclusions is used in this research to evaluate the cleanliness of the BO coated bearing, since it provides cleanliness that is comparable to the required cleanliness for roller bearings, which is given in ISO 683-17 [82]. This method provides an index from 0.5 to 3 to show the cleanliness level, as explained in detail in Section 3.4.2.

The relation between the inclusion content or type and the subsurface initiated cracks has been investigated in a number of studies. Murakami developed a relation between the fatigue limit and inclusion square root of the area and showed how the life of the component could be affected significantly by the inclusion content [76]. Other researchers have shown experimentally the initiation of microstructure alteration, in the form of butterflies around the hard inclusions of  $\text{Al}_2\text{O}_3$ , which is assumed to cause tensile stress due to the non-deformable nature of these inclusions [56]. For the more malleable inclusions, such as MnS, the deformability made it more favourable to cause less damage due to the assumption of perfect inclusion-matrix bonding and the compression stress around it. They are also thought to act as a cocoon to encapsulate the harder and sharper inclusions and improve machinability [75]. However, for the WT bearing of high MnS inclusion content, the subsurface initiated damage of butterfly formations and WECs mainly initiates from these inclusions [19][56]. Chapters 5 and 6 present observations of various types of damage initiated by different inclusions in sub-Megawatt and multi-Megawatt WTGBs.

**Table 2.1.2: Properties of non-metallic inclusions** [11][68][76][79][83][84]

Inclusion group	Morphology	Possible chemical composition	Hardness HV	Modulus of elasticity (GPa)	Thermal expansion ( $10^{-6} \text{ K}^{-1}$ )	Yield limit *1960 MPa (matrix)
A (sulphide)	grey particles, a wide range of aspect ratios (length/width); generally rounded ends	MnS, CaS	3.4 GPa	69-147	18.1	1/5
B (aluminate)	black or bluish particles (at least three) aligned in the deformation direction; low aspect ratio (generally < 3)	$\text{Al}_2\text{O}_3$ , $\text{CaO} \cdot 6\text{Al}_2\text{O}_3$ $\text{CaO} \cdot \text{Al}_2\text{O}_3$	$\approx 2200\text{HV}$ $\approx 1900\text{HV}$	387-389	8.0	3
C (silicate)	individual black or dark grey particles; a wide range of aspect ratios (generally > 3); generally sharp ends	$\text{MnO-SiO}_2$	> 1100HV	73	5.0	-
D (globular oxide)	black or bluish, angular or circular; low aspect ratio (generally < 3); randomly distributed particles	$\text{CaO} \cdot 2\text{Al}_2\text{O}_3$ $\text{CaO} \cdot \text{Al}_2\text{O}_3$	900–2500HV	113–350	5.0	3
DS (single globular)	circular, or nearly circular; single particle with a diameter > 13 $\mu\text{m}$	Same as type B or D but oversized	Not available	Not available	Not available	Not available

### 2.1.6 Bearing Life Assessment

Bearing life calculation is based on fatigue calculation, as conducted initially by Lundberg & Palmgren [75]. The development of this calculation method assumes subsurface damage initiation induced by the maximum alternating orthogonal shear stress  $\tau_{xz(max)}$  [49][75]. The lifespan is defined as the operation millions of revolutions until the first spall [75]. According to the reliability of the bearing life, different names can be used to describe it. The widely used version is the  $L_{10}$  basic rating life, which means 90% reliability or 10% of a group of bearing operating under the same condition are expected to fail by the end of their  $L_{10}$  rating life. Equation 2.1.6.1 can be applied for ball or roller bearings by using the empirically found load life exponent  $n=3$  or  $n=10/3$ , respectively [28]. The basic dynamic radial load rating  $C_r$  represents the radial load that the bearing can endure for one million cycles and it is calculated according to the specifications and arrangement of the bearing, while the dynamic equivalent radial load  $P_r$  represents the actual radial and axial load acting on the bearing [28].

$$L_{10} = \left( \frac{C_r}{P_r} \right)^n \quad 2.1.6.1$$

This equation predicts the life of bearing working under conditions of adequately clean lubrication, good alignment and standard bearing steel cleanliness. These conditions may not always be met. Accordingly, the modified rating life,  $L_{nm}$ , as shown in Equation 2.1.6.2, is used [28]. The modification factor for reliability  $a_1$ , facilitates calculating the bearing life for different reliability levels, which is 1 for reliability of 90%. The life modification factor is  $a_{ISO}$  introduced in the BS ISO standard 281: 2007 [28] to consider the exceeding of the fatigue stress limit  $\sigma_u$  from the SN curve for bearing steel. This fatigue stress limit is reached at  $p_{max}$  of approximately 1500 MPa [28], which is the maximum allowable contact stress for planetary bearings in WTG, according to the BS EN 61400-4:2013 [85] or IEC 61400-4 [86]. The life modification factor  $a_{ISO}$  is less than 1 when total induced stress  $\sigma$  exceeds  $\sigma_u$  due to the applied load and the additional stresses induced through various factors, such as mounting, contaminant particles and inadequate lubrication. Detailed descriptions of the calculation of  $a_{ISO}$  and the bearing internal load distribution are presented in BS ISO 281: 2007 [28] and ISO 16281: 2008 [87], respectively. For wind turbine design, the basic rating life described in BS ISO 281: 2007 [28] is adopted for the preliminary selection of bearings, although it is represented by hours instead of millions of revolutions [85].

$$L_{nm} = a_1 a_{ISO} L_{10} \quad 2.1.6.2$$

For advanced WT bearing rating life calculations, a detailed load analysis should be conducted according to BS EN 61400-4:2013 [85] or IEC 61400-4 [86]. The bearings in a wind turbine application is designed to last approximately 20 years [85]. However, the

actual lifespan of different WTGBs does not reach this requirement, as discussed in Chapter 1. For subsurface initiated damage, bigger bearings with bigger volume of material and thus more material impurities can be more vulnerable because of the higher probability of these material impurities being located in the high stress zone. In addition, surface and subsurface initiated failure can be affected by the extreme loading conditions during transient events, such as the shutdown and start-up of WT, as discussed in Chapter 8. During these events, loads such as impact and high surface traction are not counted in the current rating life calculation. The combined effect of these kinds of loading with the subsurface stress riser, such as non-metallic inclusions, can exceed the yield or strength limit of the material and thus result in a shorter life. In this research, the effect of non-metallic inclusions and surface traction on the premature failure in WTGBs is investigated, as presented in the results chapters. Finally, as a fatigue calculation, the  $L_{10}$  life neglects the effect of load sequence, which could have an effect on the initiation and propagation of surface and subsurface damage, as discussed in Chapter 7.

## 2.2 Experimental Investigation of Bearing Failure

Premature bearing failure has been investigated experimentally using different machines considering various testing parameters. Common procedures and issues were investigated by many studies. Most of these studies use bench-top machines, which simplify the real geometry of roller bearings. The non-conformal contact between the inner or outer raceways and the rollers in the bearings can be represented but it may not be exactly the same in term of the size of contact and the surface and subsurface stress distributions. In addition, the operational conditions such as load and lubricant viscosity and cleanliness, as well as the specifications of the specimens used, such as steel cleanliness and manufacturing techniques, can be more difficult to represent exactly in bench-top tests. The bench-top tests enable better controlled parameters but at the same time they neglect other factors that could interact with the considered ones. Accordingly, some tests were conducted at component level by using full scale roller bearings as the testing specimens. Although the real applications, such as the WTG, may still not be fully tested at the component level, these bench-top tests are likely to be the most affordable. Some tests on a full scale WTG have been conducted in research hubs such as NREL [88] or CATAPULT [89] but they are mostly for developing new designs. Despite the limitations of the bench-top and the component level tests, many were successful in replicating some of the damages observed in failed bearings retrieved from the field. Since the WSF is considered to be the most common mode of failure of WTGBs, most of the tests have focused on replicating this failure mode and the related damage to WECs and WEA, observed in the form of butterflies. Others have investigated micro-pitting and the surface initiation of spalling. From the author's point of view, both surface and subsurface initiated damage are important, since they are both observed in the examined bearings retrieved from the field.

### **Methodologies:**

The tests can be classified based on the machine used in bench-top testing, such as a twin disc machine [90][91], a three ring on roller [14], a ball-on-rod testing [56][63]; and component level testing, such as a ball or roller thrust-bearing tester [60][92][93], and a tapered, cylindrical or spherical roller bearing tester [61][70][94]. The common testing condition among most of the tests was the high number of cycles, which reaches tens or hundreds of millions [92][94], and sometime reaches 130% of the  $L_{10}$  life [61]. Normally, to achieve this high number of cycles within a reasonable time, the tests were run at high speed, which may not be representative of the real application. The parameters investigated in these tests include the maximum contact pressure [56][63][91], the rolling-sliding ratio [91], the non-metallic inclusions types and intensity [61], lubricant additives [91], vibration and transient loading [61], sliding to an over-rolling direction [14], and the number of cycles [14][92][94]. In addition to these parameters, the effect of charging the specimens/bearings with hydrogen on the premature failure, and mainly the generation of WECs and WEA (butterflies) was investigated, along with the aforementioned parameters [70][90][93]. Some studies focus on the role of friction in the absorption of hydrogen by investigating the effect of the asperity friction energy accumulation [92].

### **Findings:**

The metallography examinations, and the ultrasonic examinations in some of these studies, show the range of damage including WECs and butterflies initiated from inclusions, surface initiated cracks and spalling. Some of the main findings from the studies in the literature are presented here. It was found that, in addition to the contact pressure and sliding ratio, the number of load cycles and friction between the contacted surface in a mixed lubrication affect the formation of WECs [92]. Their research also hypothesises a measurement, friction energy accumulation, to predict the occurrence of WECs in roller-thrust bearings. One of the recent studies investigated the effect of a number of tribochemical factors, such as sliding kinematics, water contamination, and electrical potential and lubricant additives, on initiation and driving the WECs [91]. It has been found that specific lubricant additives, metal sulphonate detergent, can have a significant effect, triggering surface-initiation cracks that were similar to the WECs. Their study also proposes a criterion to predict the WECs, based on friction power dissipation. It is also emphasised that the formation of WECs was mainly surface affected by local embrittlement, associated with a hydrogen effect. Although the proposed criteria are important steps toward developing new bearing life predictions, considering the WECs or brittle fracture, the relying of these criteria on surface roughness is not practical, from the author's point of view. This opinion is based on the observed reduction in the specimens' surface roughness during the testing. Also, the effect of extreme pressure additives may change the expected friction between asperities but this effect is neglected in these models. Chapter 7 in this thesis show that the COT barely change during changing the  $h_{\min}$ , which is expected to be due to the extreme pressure

additives, and thus estimating the friction energy approach will not be accurate. One of the studies that believe in subsurface initiation of WECs proposes subsurface initiation from non-metallic inclusions with or without butterflies formation [61], which has been confirmed in this thesis. The authors also suggested that steel cleanliness in term of inclusions density was more relevant to the subsurface WEC initiated damage than maximum inclusion size, which is partially proven in this thesis, since the examined orientations of specimen sections in axial or circumferential direction was found to affect this conclusion regarding the effect of inclusion size.

### **Summary and conclusions on bearing tests:**

Despite the wide range of parameters investigated and different complexity levels of the testing, some issues have not been addressed. In WT planetary bearings the tangential speed is much lower than that considered in most previous studies. Also, the values of the COT or surface traction have not been reported in some of the tests, or have been reported to be a very small value, smaller than expected for roller bearings. Although the torque reversal is frequently reported in WT, no experimental investigation has been conducted to identify the value and the effect of the COT in the bearings during this reversing of the torque or any other transient event. Although some tests have investigated the effect of vibration or regular variation of the load, no test was found to consider the effect of the variable sequence of the load or tribological conditions on damage initiation and propagation.

## **2.3 Black Oxide Coating and Other Surface Treatment**

Surface treatments are proposed by bearing manufacturers to protect the roller bearings from surface initiated damage due to running in the mixed or boundary lubrication regime [95][96][97]. Another advantage claimed for some surface coating is to reduce hydrogen absorption and thus subsurface initiated embrittlement cracks / WECs [98], which could be specifically useful for WT bearings [97]. In this section, the most commonly used type of coating, black oxide (BO), is discussed and compared with two other types of surface treatments: Diamond-Like Carbon (WC/a-C:H) and case hardening or case carburizing. Black oxide is a chemical conversion of the bearing steel surface and it is normally applied on the rollers and the raceways. This layer, which is used for roller bearings, is formed by immersing the part in chemical solutions, mainly an alkaline aqueous salt solution, for specific time at temperature between 130 and 150 °c within 15 steps of immersion according to SKF [97]. The resulted black layer is  $Fe_3O_4$  (a blend of FeO and  $Fe_2O_3$ ), which was reported to have lower hardness than the bearing steel matrix and a thickness of approximately 1-2  $\mu m$  [97]. This technology was reported to reduce friction in 1978 [99], and it is well known for reducing corrosion. The WC/ a-C:H is tungsten carbide–reinforced diamond-like carbon deposited on the rollers only. The process is conducted in a vacuum equipment using reactive physical vapour deposition [96][100]. This layer is harder than the bearing steel, and it is about 1  $\mu m$  thickness [96]. This technology, developed in 1985

[101] began to be used for roller bearings in the 1990s [102]. In large bearings, the highly loaded region is the layer close to the surface and one of the solutions to improve the life of the bearings is to make this layer harder. This process is called case-hardening (or case carburising), where a larger concentration of carbon is diffused into the surface of the low carbon steel, which transfers into hard steel of about 750 HV [68]. It was also reported that this technique results in beneficial compressive stress on the surface, reducing surface fatigue [68].

A test using a ring-on-ring tribometer tester was conducted by Evans, et al. [96] to investigate the adhesive wear resistance of the BO layer and the Diamond-Like Carbon coating WC/a-C:H. The BO layer in this study was formed by using a single-bath process. The test shows that BO layer provides lower adhesive wear protection compared to the WC/a-C:H. Another test conducted by the same group used tapered roller bearings of 82.55 mm outer diameter, 41.28 mm bore, and 26.54 mm overall bearing width. These bearings were made of case-carburized bearing-quality low-alloy steel. Two groups of bearings were prepared with four bearings in each group. Again, one group of the bearings was coated with BO and the other group with WC/a-C:H. The fatigue life of these groups were tested using a first-in-four life test procedure, where the life was measured by the time to the occurrence of first spall of more than 6 mm<sup>2</sup>, which was detected by a vibration sensor. The contact pressure between roller and inner raceway during the tests were ~2.4 GPa with a lambda ratio  $\lambda=0.5-1$ , based on the initial roughness of the contacted elements. The results show very high improvements in the bearings life, almost eight times of those without a coating, due to the use of WC/a-C:H, while a very slight extension in bearings life occurs due to the BO coating. From the author's point of view two issues mean that these results should be used with caution. Firstly, the single bath process to form the BO in this study may not result in a similar specifications for the BO layer as that formed by the 15 steps of immersion adopted by the BO layer bearings manufacturers. Secondly, the bearings used in the tests were case-carburized, while most of the bearings used in WTG are through hardened, and it is expected that the results will not be valid (or exactly the same) for through hardened bearings. Despite reservations about the results in this study, these results emphasise the need for further investigation of BO coating.

Another study compares the failure by WECs among bearings with case carburizing and BO coating [66]. The study was based on observing a number of bearings in WTGs in the field for 14 months, and it showed that the failure by WECs dropped from 40% to 2.7% after replacing the bearings without surface treatment with case carburized bearings [66]. The same study reported further reduction of the WECs failure to zero percent when bearings with BO coating were used for two years. From the author point of view, the slim difference between the performances of the two groups of bearings could be due to the stochastic operation conditions in the field, which may not be identical for both groups of bearings. Also, according to this study, zero percentage of failure by WECs was reported after 26 months of operation in the field, when the bearings assembled at 130 °c. Although this

study shows three promising solutions to the WECs, the one most often adopted is the BO coating, one reason for this being that it is economical, since it is less expensive than other surface treatments. Despite using BO coated bearings the failure by WECs is still reported in WTGs, as shown in the examined BO bearing in Chapter 6. In this thesis, the BO layer on a large WTGB was investigated, as discussed in Chapters 3 and 6.

## 2.4 Tribological and Stress Analysis in Rolling Contact Fatigue

This section presents the analytical calculations used to determine the load, contact pressure, lubricant film thickness and subsurface stresses due to normal and tangential surface load on WT planetary bearings. These calculations are used in Section 8.1 and applied to the gearbox configuration and load spectrum of the NREL 750 kW wind turbine [40], which is used as a case study to investigate the surface and subsurface stresses, as well as damage accumulation on the planetary bearings.

### 2.4.1 Bearing Load Calculations

The level of complexity or accuracy of the models used to calculate the load on the WTG components is determined by the considered external load, flexibility of the machine elements and the stiffness and damping between the elements. The conditions of wind, marine and electrical power network represent the external load, such as the variable wind speed on the rotor, the waves on the tower and the resistant torque on the high speed shaft [85]. Studies in this field have shown that the simplified calculations that consider only the torque on the low speed shaft directly and assume other components being rigid bodies and rigid contacts without damping still provide fairly close results to the more complicated calculation methods, such as the Multi Body System (MBS) modelling [103][104]. According to the simplified method for a gearbox with six single-line planetary bearings, the unidirectional force on each planetary bearing  $F_p^r(t)$ , as shown in Figure 2.1.3, can be calculated from the torque on the low speed shaft  $T_{LS}(t)$  as a time series, according to equation 2.4.1.1 [44].

$$F_p^r(t) = \frac{T_{LS}(t)}{6 * (Radius_{sun} + Radius_{planet})} \quad 2.4.1.1$$

Many factors, such as flexible components and inertial loads, cause unequal load sharing between the planetary bearings supporting each planetary gear. Software such as SIMPACK can be used to develop detailed dynamic modelling of WT drive train under various loading conditions using MBS and FEM [44][47][105]. These kinds of models and the experimental measurement provide a range of load-sharing factors for the planetary bearings. When there are two planetary bearings for each planetary gear, it is found that 30 to 60% more load is carried by the bearing at the rotor side (upwind bearing) than the

bearing at the generator side (downwind bearing) [43][44]. The calculations in Chapter 8 adopted 50% more load on the upwind bearing.

#### 2.4.2 Hertzian Contact Pressure

Contact mechanics was firstly developed by Heinrich Hertz [50]. Hertz analysed the stresses at the contact of two non-conformal bodies. He used Newton's optical interference fringes of two glass lenses to correlate their deformation to the contact pressure between them. Accordingly, equations were developed for three shapes of the contact area, point or circular, line or rectangular, and elliptical. These equations correlate the applied load, the elastic properties and the contact radii of the contacted bodies to the contact pressure between the bodies and the stress distribution on the area of contact and underneath it. The theory is still valid, and is widely used in many industrial applications, such as roller bearings. However, the assumptions of the Hertz theory should be considered when applying it to applications where the bodies are non-conformal; that the size of the contact area is much smaller than the radii of the bodies; that the strains are small; and that the bodies are elastic and their surfaces are frictionless [50]. For roller bearing of Z rolling elements, each of the rollers in the loaded zone supports different values of load normal to the surface of contact. The load on each rolling element varies according to the clearance and the angle relative to the direction of the applied load with the maximum rolling element load  $Q_0$  acts in line with the unidirectional force, as shown in Figure 2.1.3. For nominal clearance, a valid approximation for  $Q_0$  can be calculated from Equation 2.4.2.1 [75]. The maximum contact pressure  $p_{max}$  for line contact can be calculated by Equation 2.4.2.2, according to Hertzian contact theory [75]. This equation is used in this thesis to calculate the maximum contact pressure  $p_{max}$  on the inner raceway of the cylindrical roller bearings in Chapter 5, for the examined uncoated bearing, and in Chapter 8 for the case study of NREL 750 kW WT. Also, Equation 2.4.2.3 for elliptical contact is used to calculate the maximum contact pressure between the specimens of the RSTs in Chapter 7 [75]. In these equations, R is the reduced radius (or the sum curvature),  $E^*$  is the reduced (or equivalent) elastic modulus and  $\nu$  is the Poisson's ratios of the contacted bodies 1 and 2, where x is the rolling direction and y is the axial direction. For line contact, the contact area is a rectangle of  $2b_l$  width and L length; and for elliptical contact, it is an ellipse of semi-major and semi-minor radii of a and b. These radii are calculated using formulas with contact coefficients that can be found from charts. However, approximations to calculate a and b as shown in Equations 2.4.2.8 and 2.4.2.9 were developed using simplified expressions for the elliptic integrals in Equations 2.4.2.10 and 2.4.2.11 [75].

$$Q_0 = \frac{5 * F_p^r}{Z} \quad 2.4.2.1$$

$$p_{max} = \frac{2 * Q_0}{\pi * L * b_l} \quad 2.4.2.2$$

$$p_{max} = \frac{3 * Q_0}{2 * \pi * a * b} \quad 2.4.2.3$$

$$\frac{1}{R} = \frac{1}{R_x} + \frac{1}{R_y} = \frac{1}{R_{1x}} + \frac{1}{R_{2x}} + \frac{1}{R_{1y}} + \frac{1}{R_{2y}} \quad 2.4.2.4$$

$$\frac{1}{R_l} = \frac{1}{R_1} - \frac{1}{R_2} \quad 2.4.2.5$$

$$\frac{1}{E^*} = \frac{1 - \nu_1^2}{E_1} + \frac{1 - \nu_2^2}{E_2} \quad 2.4.2.6$$

$$b_l = \sqrt{\frac{4 * Q_0 * R_l}{\pi * E^* * L}} \quad 2.4.2.7$$

$$a = \sqrt[3]{\frac{3 * k^2 * E * Q * R}{\pi * E^*}} \quad 2.4.2.8$$

$$b = \sqrt[3]{\frac{3 * E * Q_0 * R}{\pi * k * E^*}} \quad 2.4.2.9$$

$$k = 1.0339 \left( \frac{R_y}{R_x} \right)^{0.636} \quad 2.4.2.10$$

$$E = 1.003 + \frac{0.5968 * R_x}{R_y} \quad 2.4.2.11$$

### 2.4.3 Elasto-hydrodynamic Lubrication Theory (EHL)

It is essential to use a lubricant film to separate the contacted bodies, in order to ensure no metal-on-metal contact. The Reynolds equation is used to calculate the lubricant film thickness for conformal bodies but when it is used for non-conformal surfaces it results in

very low film thickness that should cause surface damage for many applications that do not show this damage. This is why the Elasto-hydrodynamic Lubrication theory (EHL) has been developed. This theory considers the elastic deformation of the contacted surfaces and the change of oil viscosity with pressure at the contact area. The first approximate solution for the EHL to line contact, including the elastic deformation of the surfaces and the piezo-viscous behaviour of the lubricant, was presented by Grubin when the contact was for a cylinder on flat surface [106]. Later, the solution for point and elliptical contact was introduced by Hamrock and Dowson [107][108].

According to EHL theory, elastic deformation is represented by a contraction in the contact area that results in a pressure spike, as can be seen in Figure 2.4.1. For roller bearing, a formula was developed by Dowson and Higginson to calculate the minimum film thickness  $h_{\min}$  for line contact, as shown in Equation 2.4.3.1 [27][49], This will be used in Chapter 8 of this thesis. Another formula developed by Hamrock and Dowson for general contact, as shown in Equation 2.4.3.2 [27], is used for the RSTs in Chapter 7 in this thesis. The non-dimensional parameters  $U$ ,  $W$  and  $G$  representing speed, load and material respectively and are calculated from Equations 2.4.3.3 to 2.4.3.5, where  $\alpha$  is the viscosity pressure coefficient for the lubricant; and  $u$  is the average tangential velocity. Another essential feature of the EHL is the pressure spike  $p_s$  before the exit of the contact area, which makes the pressure distribution deviate from the Hertzian distribution, as shown in Figure 2.4.1. Pan and Hamrock [109] derived a formula to calculate the amplitude of the pressure spike, as shown in Equation 2.4.3.6 and this is used in Chapter 8 of this thesis.

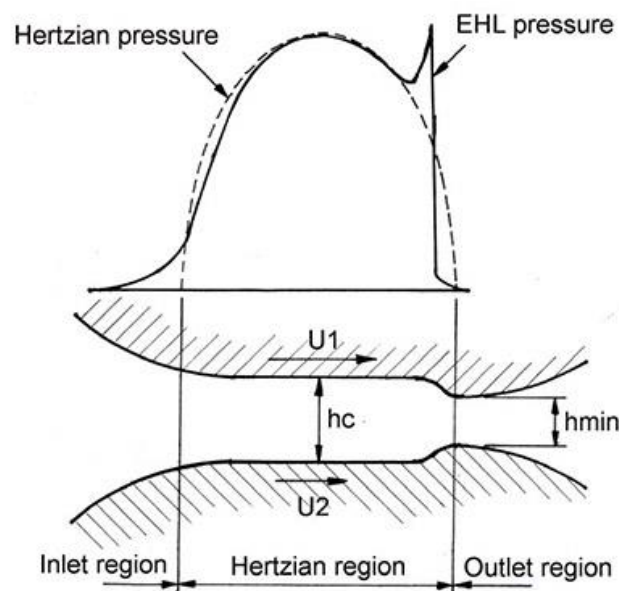


Figure 2.4.1: The EHL theory (Courtesy of Robert Errichello) [110]

$$h_{min} = 2.65 * R_x * U^{0.7} * G^{0.54} * W^{-0.13} \quad 2.4.3.1$$

$$h_{min} = 3.63 * R_x * U^{0.68} * G^{0.49} * W^{-0.073} (1 - e^{-0.68k}) \quad 2.4.3.2$$

$$U_i = \frac{\eta * u}{2 * E^* * R_x} \quad 2.4.3.3$$

$$W_i = \frac{Q_0}{L * 2 * E^* * R_x} \quad 2.4.3.4$$

$$G = 2 * \alpha * E^* \quad 2.4.3.5$$

$$p_s = 0.648 * 2 * E * U^{0.275} * G^{0.391} * W^{0.185} \quad 2.4.3.6$$

The thickness of the lubricant film generated relative to the roughness of the contacted surfaces determines the asperities contact and degree of contact, defined as the lubrication regime. These regimes are divided into a boundary regime with high contact between the asperities, a mixed regime with partial contact between asperities and a full lubrication regime, where the asperities are fully separated [111]. These regimes are described by the Stribeck diagram as shown in Figure 2.4.2. According to this diagram, the coefficient of friction  $\mu$  is reversely proportional to the  $h_{min}$  in the mixed lubrication regime. This is due to there being less contact between asperities, which is described by the  $\lambda$  ratio between the  $h_{min}$  and the composite surface roughness, as shown in Equation 2.4.3.7. In this equation,  $R_a$  is the arithmetical mean roughness for the contacted surfaces, which could also be replaced by the root mean square roughness  $R_q$  where large peaks increase  $R_q$  more than  $R_a$  [111]. On the other hand, in the full lubrication regime,  $\mu$  is proportional to the  $h_{min}$  due to the higher resistance caused by shearing thicker film of lubricant. It is agreed that  $\lambda$  ratio of more than four is consider to be representative for the full separation (EHL or Hydrodynamic);  $1 < \lambda < 3$  results in mixed lubrication regime; and  $\lambda$  ratio of less than one, such as 0.1 [112], causes boundary lubrication regime [113][111]. Estimating the lubrication regime could help to explain the surface traction generated and thus the surface and subsurface damage generated.

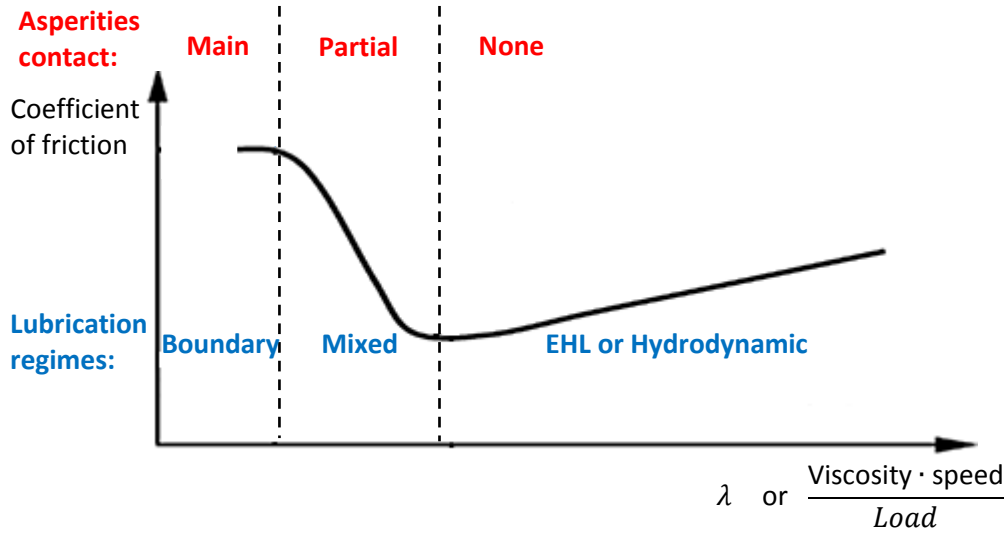


Figure 2.4.2: The Stribeck diagram (adopted from [49])

$$\lambda = \frac{h_{min}}{\sqrt{Ra_1^2 + Ra_2^2}} \quad 2.4.3.7$$

#### 2.4.4 Subsurface Stress Analysis

The subsurface stress in non-conformal contact, which is the case for rolling bearing, is multiaxial and the distribution is derived from the Hertzian pressure distribution on the surface. Figure 2.4.3 shows the subsurface stress distribution under the surface along the axis of symmetry  $x=0$  due to normal load. For line contact, the distribution of subsurface stresses due to the Hertzian contact pressure is derived by McEwen for any point  $(x,z)$  under the contact area [114]. The surface traction could also be considered through the coefficient of friction  $\mu$ , which is also called the Coefficient Of Traction (COT), as shown in Equations 2.4.4.1 to 2.4.4.6. Under normal load only with zero traction, at  $x=0$ , the maximum shear stress  $\tau_{1(max)} = 0.3p_{max}$  and it is located at  $z=0.78b$  [115]. While at  $x=\pm(0.87-0.9)b$ , the maximum orthogonal shear stress  $\tau_{xz(max)} = 0.25p_{max}$ , and it is located at  $z=(0.49-0.5)b$  [75]. Also, the maximum equivalent von Mises stress  $\sigma_{von(max)} = 0.55p_{max}$  and it is located at  $x=0$  and  $z=(0.7-0.8)b$  [75]. These maximum stresses could be used for the fatigue analysis. The fatigue life of bearings that derived by Lundberg–Palmgren is based on  $\tau_{xz(max)}$  [75]. However, the depth of subsurface material alteration observed in previous studies is greater than the depth of  $\tau_{xz(max)}$  and is closer to the depth of  $\tau_{1(max)}$  [75]. The subsurface stresses calculations are given in Section 8.1, where they were used to investigate the variation of  $\sigma_{v(max)}$  and  $\tau_{1(max)}$  due to different levels of contact pressure and surface traction.

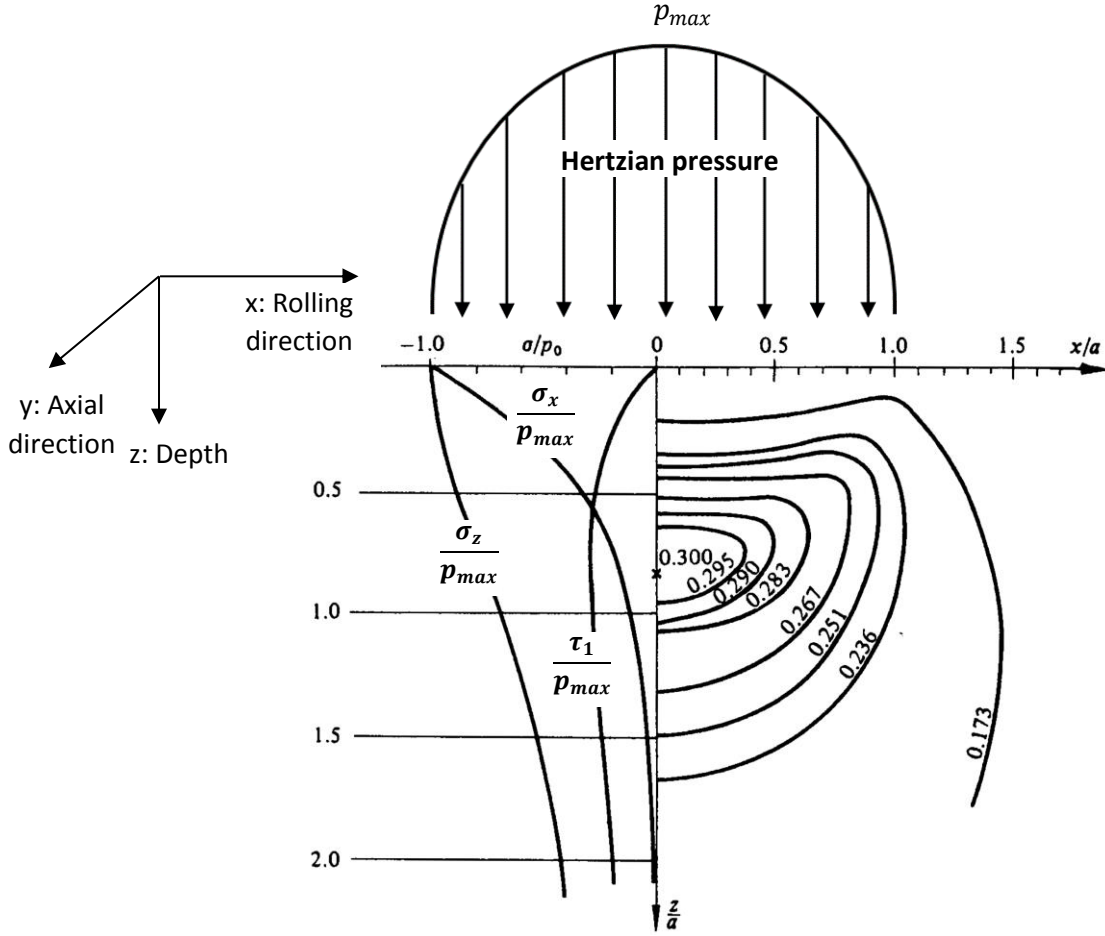


Figure 2.4.3: Hertzian pressure distribution (Top); subsurface stresses along the axis of symmetry (Left); contours of principal shear stress  $\tau_1/p_0$  (Right). (adopted from [50])

$$\sigma_x = -\frac{p_{max}}{b} \left\{ m \left( 1 + \frac{z^2 + n^2}{m^2 + n^2} \right) - 2 * z \right\} - COT * \frac{p_{max}}{b} \left\{ n \left( 2 - \frac{z^2 - m^2}{m^2 + n^2} \right) - 2x \right\} \quad 2.4.4.1$$

$$\sigma_y = 2\nu \frac{p_{max}}{b} \left( z - m - m \frac{z^2 + n^2}{m^2 + n^2} \right) + 2\nu * COT * \frac{\nu p_{max}}{b} \left( x - n - n \left( \frac{m^2 - z^2}{m^2 + n^2} \right) \right) \quad 2.4.4.2$$

$$\sigma_z = -m \frac{p_{max}}{b} \left( 1 - \frac{z^2 + n^2}{m^2 + n^2} \right) - COT * n \frac{p_{max}}{b} \left( \frac{m^2 - z^2}{m^2 + n^2} \right) \quad 2.4.4.3$$

$$\tau_{xz} = -\frac{p_{max}}{b} n \left( \frac{m^2 - z^2}{m^2 + n^2} \right) - COT * \frac{p_{max}}{b} \left\{ m \left( 1 + \frac{z^2 + n^2}{m^2 + n^2} \right) - 2 * z \right\} \quad 2.4.4.4$$

$$m^2 = \frac{1}{2} [\sqrt{(b^2 - x^2 + z^2)^2 + 4x^2 z^2} + (b^2 - x^2 + z^2)] \quad 2.4.4.5$$

$$n^2 = \frac{1}{2} [\sqrt{(b^2 - x^2 + z^2)^2 + 4x^2 z^2} - (b^2 - x^2 + z^2)] \quad 2.4.4.6$$

The motion of the roller over the raceway can be described as rolling or sliding. Sliding occurs when there is a relative tangential velocity between the contacted bodies. In roller bearings, such as WTGBs, rolling and sliding could occur simultaneously. The normal force acting on the contacted surfaces results in a contact area that can be found using the Hertz theory when the friction force is neglected. The surface and subsurface stresses should not be affected when frictionless bodies slide over each other, however, sliding motion of real surfaces introduces friction force opposes the motion and influences the contact stresses. For steady sliding between the bodies, the tractive force represents kinetic friction; and when the tangential force try to cause sliding between the bodies, the tractive force represents static friction with its maximum value 'limiting friction' before starting sliding [50]. Since the elastic deformation of the same material contacted bodies are conformal with each other, neither the contact area nor the contact pressure due to normal load should be disturbed by the tangential frictional force [50].

When the tangential force is less than the limiting friction, partial slip occurs and the contact area is divided into two regions 'stick' and 'slip' [50]. The stick region is located adjacent to the leading edge of the contact area and the slip region is located adjacent to the trailing edge. When the tangential force equals the limiting friction, the slip zone expands to reach the leading edge and a complete sliding occurs. The slip ratio, which represents the relative velocity between the contact bodies, determines the tangential force and thus decides whether the slip is partial or complete. According to the reported high slip ratio in WTGBs, complete sliding is expected and the Hertzian distribution of surface traction is assumed. When the tangential force is less than the limiting friction, the distribution of surface traction deviates from that given by the Hertz theory and becomes lower in the stick region and higher in the slip region [50]. In this case, when the point of first yield locates under the surface, it is not influenced by the change of the traction distribution [50]. On the other hand, when the point of first yield occurs on the surface, it locates at the boundary between the stick and slip region [50].

## 2.5 Modelling of Inclusions Initiated Damage

The computational modelling, usually FEM in this case, of non-metallic inclusions inside bearing steel provides viable solution to the problem of investigating the stress state around inclusions. Many studies have developed models to determine the parameters affecting the stress concentration and crack initiation due to defects such as voids and inclusions. Some other models have tried to correlate the damage observed from experimental examination with the stress distribution due to stress risers. In general, the models simulate parts of the contacted bodies, the roller and the raceways, representing the contact zone. The models are two dimensional (2D) in plain strain or three dimensional (3D). In some of the models, the bearing steel is modelled as one phase homogenous material with elastic-plastic properties [116]. In more advanced models, the material is modelled as multi-phase, with different specifications [117]; and in further advanced

models, a phase transformation is also modelled [118][119]. The load could be represented by a roller moving on the contact surface. Many models represent the load between the roller and the raceways by Hertzian pressure distribution and sometimes with surface traction. The inclusion is normally represented by either a void or a partition of perfect bonding to the steel matrix. In this section, three FE models are presented and discussed, in order to cover the range of methodologies used to investigate the subsurface initiated damage from inclusions and voids.

Hiraoka et al. developed a 2D model and presented the inclusion at 1.2 mm from the surface, which is the depth of the maximum shear stress, as a circular void of 5  $\mu\text{m}$  diameter with and without 5  $\mu\text{m}$  cracks extending at 45° from the void [116]. The load is applied as a roller moving on the contact surface with maximum contact pressure of 3920 MPa. They compare the stress distribution around the void with a butterfly inclined at 45°, as found in an RCF test on a thrust bearing. It is shown in this study that there is better matching when the void is attached to the cracks. Accordingly, it is assumed that cracks initiate from inclusions before the formation of WEA (butterfly wings). However, in this thesis, it is found that for some butterflies there are no micro-cracks initiated by the inclusion, and thus the assumption of pre-existing cracks is not fully representative of the butterfly formation.

Another 2D model was developed by M. Cerullo [120] to predict crack growth from alumina inclusion in bearing steel. This model utilized the stress history from an inner raceway model [121] to represent the boundary conditions of a sub model. In this model, the repeated Hertzian contact pressure with maximum value of  $\sim 1$  GPa was used to represent the load of the equivalent roller passing over the inner raceway. In the sub model, a circular alumina inclusion or a void of 5  $\mu\text{m}$  in radius is embedded with a crack of 1.5  $\mu\text{m}$  length initiates from the inclusion or the void. The sub model is placed at the location of the maximum Dang Van damage factor. This model also investigated the effect of different interaction between the inclusion and the steel matrix, as well as different crack directions. The interface between the inclusion and the matrix were modelled either as a perfect bonding or by using cohesive elements that are not allowed to fail. The irreversible fatigue cohesive elements were used to model the crack growth, where they aligned in the crack direction which allows the crack to grow in a straight direction only. It is found that the crack grows slower when the inclusion is perfectly bonded to the steel matrix. It is also found that cracks grow faster when they start at an angle between 0 and 45° with the vertical axis. This study highlights the role of the interface between an inclusion and the steel matrix, however, without investigating the debonding between inclusion and the steel matrix, which is observed in the examined bearings in Chapter 5 and 6 in this thesis. Also, it is expected that considering the effect of surface traction could provide new insights into the crack growth rate.

Another study modelled the microstructure alteration that forms butterfly wings [119] in three dimensions. In this study the microstructure of the material was modelled as

polycrystalline using a 3D Voronoi tessellation [117], where each cell in this tessellation represents a distinct material grain to be meshed separately. The gains geometry was set randomly by the ordinary Poisson–Voronoi diagram to represent the microstructure of the bearings steel. The load applied is a Hertzian pressure distribution with a maximum value of 2 GPa and contact width of  $b=50\ \mu\text{m}$  [119]. This pressure moves repetitively over the contact area [119]. In this study surface traction due to  $\mu=0.05$  is also considered [119]. The FE software ABAQUS was used as a solver and postprocessor [119]. A spherical inclusion of  $16\ \mu\text{m}$  diameter and  $E=300\ \text{GPa}$  is embedded at a distance of  $0.5b$  from the surface [119]. The inclusion is considered to be perfectly bonded to the steel matrix [119]. A damage model based on the continuum damage mechanics (CDM) used in previous work to simulate the formation of the butterfly wings in 2D [118] was extended, in order to be used in the 3D simulation [119]. This formation occurs by transforming the martensite to ferrite, according to the damage, which evolves as a function of the number of cycles, the orthogonal shear stress, and two material constants from the S-N curve [119]. This work also included an experimental investigation of butterfly formation using the three balls on a rod bench-top tester, where the biggest butterfly was found using ultrasonic measurement. Serial sectioning was conducted to verify the simulation. The main finding of this study is the lateral expansion of the butterfly wing after reaching a certain length, which could explain the experimental observation of some butterfly wings without inclusions. Although this model considers many variables, it does not explain the crack formation and neglects the debonding between the inclusion and the steel matrix, which is widely observed.

The studies reviewed here show different views and levels of sophistication for modelling damage initiation from non-metallic inclusions. However, it is found that three important issues have not been considered. Firstly, modelling the elongated inclusions, such as MnS, is less common; secondly, the debonding between the inclusion and the steel matrix is not considered, although it is frequently observed; and thirdly, the extreme loading, such as high surface traction, has not been investigated, although it may be a main factor in the premature failure of WTGBs. In this thesis, less sophisticated 2D FE models were developed to address these issues and provide an understanding for the stress state that could initiate cracking due to elongated MnS inclusion.

## 2.6 Identification of Current Research Gaps

The metallurgical examination of the failed bearings could be a highly important method for revealing the key factors for this failure. However, not many failed bearings retrieved from the field were investigated with detailed statistical analysis for damage initiation. Accordingly this kind of study is conducted in this thesis to provide a database for further analysis.

The theories developed to explain the WECs were either based on surface or subsurface initiation. It is found that surface initiation is affected by specific lubricant additives, friction

power dissipation and local embrittlement, associated with the hydrogen effect; and the subsurface initiated cracks with or without butterflies are affected by contact pressure, the sliding ratio, the number of load cycles and the density of the non-metallic inclusions. It is found that the tests in the literature are commonly accelerated by high speed, which sometimes makes the entraining speed of the lubricant entering the contact zone much higher than that in the WTGBs, resulting in different tribological conditions. Also, no test was conducted to investigate the effect of high surface traction and measuring the COT during the test. In addition, applying different sequences of loading has not been investigated, although the initiation and propagation of the damage are expected to be affected by it. Thus, this thesis addresses the unconsidered factors in the literature, through COT tests and RSTs.

Many studies have shown the positive effect of different kinds of surface treatments, such as BO coating, diamond-like carbon and case carburizing on premature failure, and WECs during accelerated tests or in uncontrolled environments. However, the premature failure of WTGBs are still being reported, which shows the limited effectiveness of these measures to make these bearings meet the designed lifespan. To find out if there is any difference between the damage in the uncoated bearings and those with coating, it is important to examine some of the surface treated bearings which failed prematurely. Accordingly, a failed BO coated WTGB is examined in this thesis.

The subsurface damage initiation from inclusions reported in the literature has also been investigated using FE modelling. The main findings from these models are that the stress concentration around the inclusions and the interface with the steel matrix could form the 3D geometry of the butterfly wings by phase transformation. Other research focuses on the crack growth assuming different initial crack lengths. However, some of these models did not consider important features, such as the debonding between the inclusions and the steel matrix, which is observed from the metallurgical examinations of the failed bearings. It is also found that the elongated inclusions, such as MnS, were not considered in those models, although the experimental investigations showed the initiation of cracks and WEA from these inclusions. In this thesis, the modelling of elongated MnS with and without debonding from the steel matrix is developed to investigate damage initiation under high surface traction.

## 2.7 Summary

The premature failure of WTGBs has been reviewed through a number of studies that have investigated this issue experimentally and numerically. It has been found that external factors such as extreme or unconsidered loading, as well as internal factors, such as bearing steel non-metallic inclusions and defects, have been reported as contributors to the short life of these bearings. Different modes of failures have been reported. However, the WECs and WSF are considered to be the main damaging mode, which has not been fully understood and cured, despite the considerable number of studies in this area. It is

observed from the studies reviewed that no overall view of the problem is available. The preliminary conclusion at the current time is that the combined effect of external and internal factors leads to the failure. The unidirectional load on the planetary bearings is a specific feature of these bearings. However, this should not cause a premature failure of the bearing steel without additional loading, such as surface traction at sufficiently high levels of contact pressure. It has been found that many studies highlighted the high level of slipping in these bearings but with the assumption of less slipping inside the loaded zone. However, during transient events such as torque reversals, the loading condition becomes more complicated and thus further investigation is required. This also shows that the current bearing life assessment methods are not appropriate.

### 3 Destructive Investigation on the Failed Bearings

This chapter presents the methods that were used to obtain the results described in Chapters 5 and 6 and some of these are also applicable to the metallurgical examination of the specimens in Chapter 7. Firstly, the details of the bearings investigated are provided of the two inner raceway rings of the failed planet bearings that were under examination. This was followed by descriptions of the procedure for preparing the samples cut from these rings, and the metallurgical examination applied to these samples.

#### 3.1 Investigated Bearings

The bearings under investigation are both single row Cylindrical Roller Bearing (CRB) used as an upwind bearing of three planetary gears in planetary stage of a WTGB. The two bearings which came from different WTGBs, were also different with regard to their size, their surface treatment and their state of bearing steel cleanliness. The inner raceway of the first examined bearing, as shown in Figure 3.1.1 (a), was uncoated and was used in a gearbox in which each planetary gear is supported by two single row CRB. This bearing was used in an on-shore wind turbine with a 600 kW power rating. It is through hardened bearing steel, grade is not available, without any surface coating. The inner raceway of the second examined bearing, as shown in Figure 3.1.1 (b), was used in a gearbox in which the upwind planetary bearing is a single row CRB and the downwind is a double row CRB. It was used in a wind turbine of 2 MW power rating. This bearing was through hardened with a Black Oxide (BO) coating. The dimensions of each bearing are shown in Figure 3.1.1 along with the Over Rolling Direction (ORD) which refers to the direction of the rollers whilst orbiting round the inner raceway. The details of the BO coated bearing are confidential and the dimensions of the rollers are not presented. For the uncoated bearing, the dimensions of the cylindrical rollers are the radius of 23.5 mm and length of 43.5 mm.

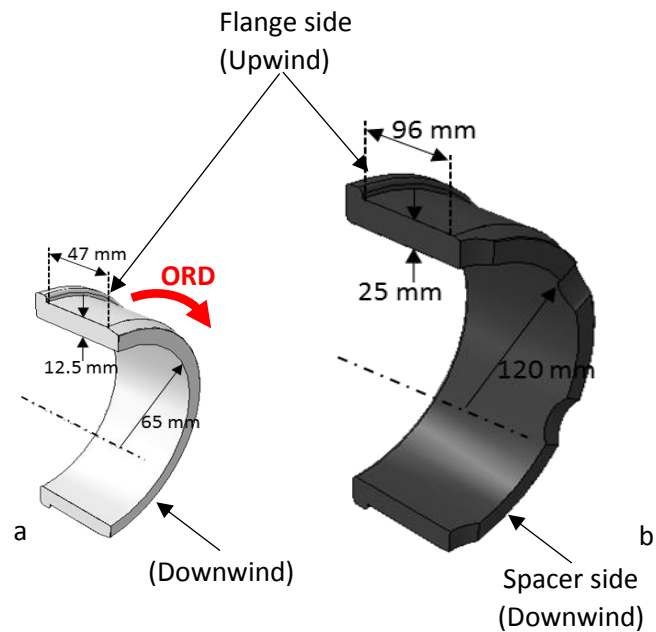


**Figure 3.1.1: Dimensions of the examined bearings (a) uncoated and (b) BO coated**

Only half of the inner raceway of the uncoated failed bearing was available for examination in this research, and the results obtained refer only to that half. The other half, shown in Figure 3.1.2 was used in another study [19]. The uncoated bearing was in service for five years before it was replaced after a site inspection due to abnormal noise during operation. The visual inspection showed extreme surface damage on the inner race compared with the outer raceway. The damaged area was in the loaded-zone where the unidirectional load is applied in a planetary bearing as shown in Figure 2.1.3. Three regions can be identified on the surface of the examined part of this bearing as shown in Figure 3.1.3. The first region consists of big spalls (more than 3 mm maximum dimension) spread on the downwind side of the raceway. The width of this region was about 20 mm. At the entrance to the loaded zone, less damage (spalling) was observed with the largest spalls in this region located on the flange side. The red dotted line in Figure 3.1.3 shows that the wear trace was not parallel to the axial axis of the raceway. This could be due to skewing of the rollers at the entrance to the loaded zone. Outside these two regions, no spalling was observed although an optical microscopic examination of the surface showed some micro-indentations. The examined part was sectioned in the circumferential and axial directions in order to prepare samples for the subsurface examination.



**Figure 3.1.2: The part of the inner raceway of the uncoated failed bearing which was not examined in this research (Courtesy of Tom Bruce [19])**

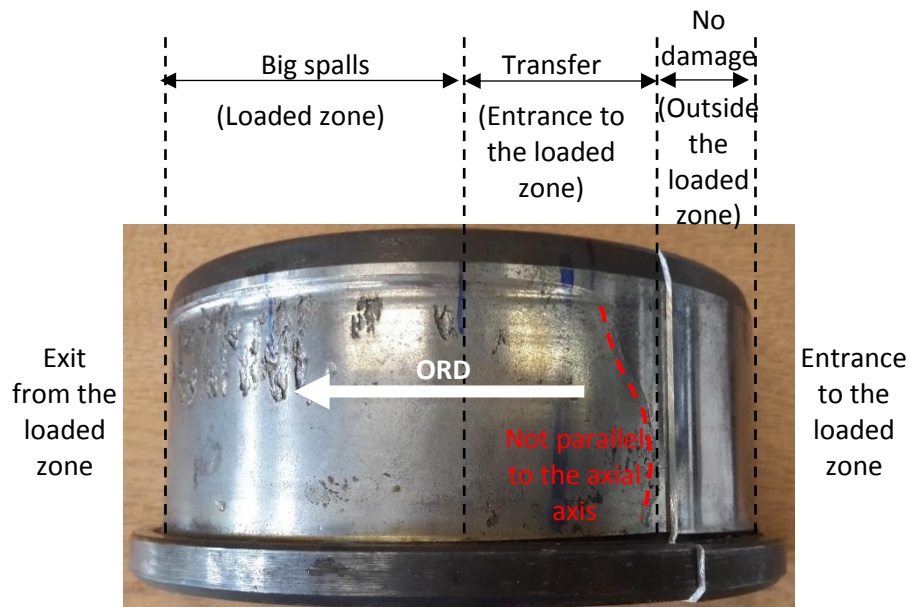


**Figure 3.1.3: Inner raceway of the uncoated failed bearing examined in this study**

The examined upwind BO coated bearing was in service for around 6.5 years and failed without previous gearbox interventions. It exhibits severe surface damage in the loaded zone seen as a band covering the whole width of the raceway, except the edges under the cage, and extending to 220 mm in length as shown in Figure 3.1.4. Along this band, the BO coating has been clearly removed, but the severity of the damage was distinguished by two regions. The first region was in the transition between the severely damaged zone and the area outside the loaded zone. It was an area extending over 90 mm in length at the entrance to the loaded zone with less number of big spalls (more than 3 mm maximum dimension). This area was followed by the second region of the damaged band shows almost evenly distributed big spalls. Outside the damaged regions, the visual examination showed that the BO layer was slightly removed, close to the entrance and the exit of the loaded zone, and intact far from the loaded zone. Indents of variable sizes, which could be

caused by the debris carried from the damaged region, have been observed along almost the whole circumference of the raceway outside the loaded zone. However, the indents show higher density and greater size (more than 3 mm maximum dimension) at the exit from the loaded zone compared with those at the entrance to it.

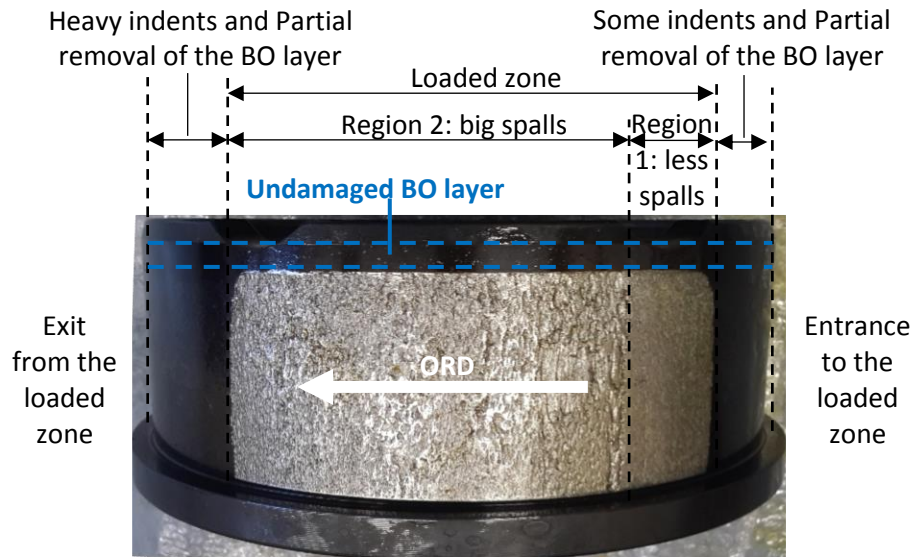


**Figure 3.1.4: Inner raceway of the BO failed bearing**

## 3.2 Sample Preparation for Subsurface Metallography

This section outlines the procedures and stages adopted for preparing samples from the failed bearings investigated. These procedures were also followed in the metallurgical examination of the specimens of Rolling Sliding Tests (RST). Subsurface metallurgical examinations are essential for revealing non-metallic defects, such as inclusions and voids, and the damage caused by them, such as cracks and WEAs.

### 3.2.1 Sectioning

The first step in sample preparation was to section the inner raceway into smaller parts where circumferential and axial subsurface sections can be examined individually. Figures 3.2.1 and 3.2.2 show the sectioning pattern adopted for the uncoated and the coated bearings. The reason for observing the subsurface in two directions - axial and circumferential - was in order to investigate the variation of the metallurgical properties of the bearing steel between the rolling and the axial directions that resulted from the manufacturing process.

For the uncoated bearing, the focus was on the severely damaged area and so cutting was made through the area of surface spalling. However, to investigate the stages of damage development, some sections were taken from areas where the surface does not show big spalls. The sectioning pattern for the BO coated bearing aimed to investigate areas covering the entrance to, and the exit from, the loaded zone as well as the severely damaged region in the middle, close to the flange side and close to the spacer side. This

enabled an exploration in regions which could be under different loading and sliding conditions.

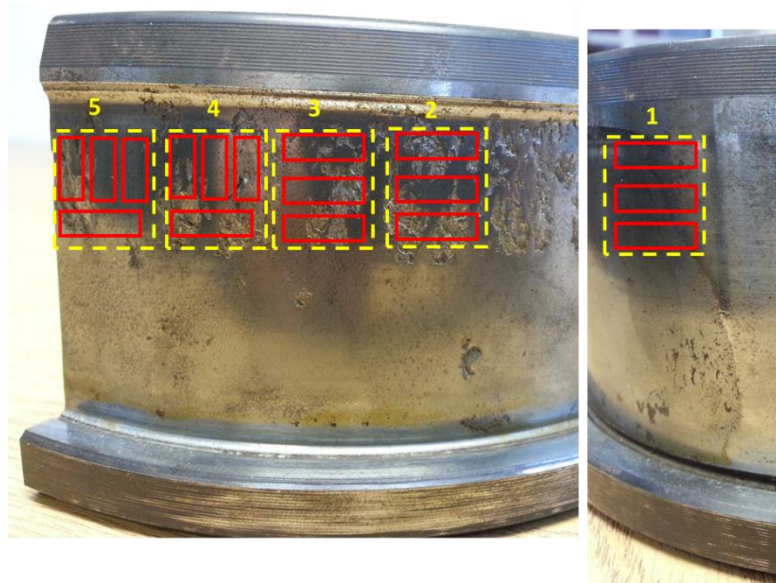


**Figure 3.2.1: Sectioning of the inner raceway of the uncoated bearing. The samples are shown as red blocks, 6 in the axial direction and 11 in the circumferential direction which grouped in 5 regions (yellow borders) numbered from 1 to 5. ORD is from right to left.**

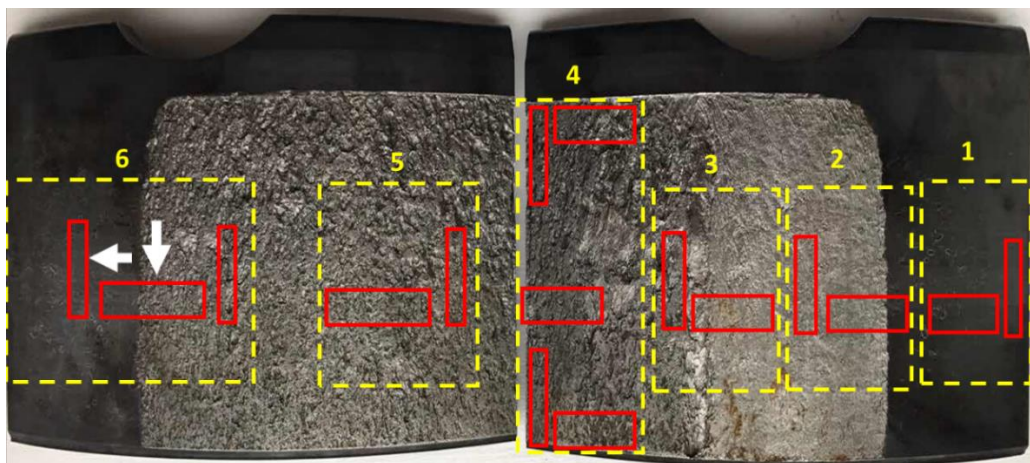


**Figure 3.2.2: Sectioning of the inner raceway of the BO coated bearing. The samples are shown as red blocks, 8 in the axial direction and 8 in the circumferential direction which grouped in 6 regions (yellow borders) numbered from 1 to 6. White arrows are the observation direction. ORD is from right to left.**

Three cutting machines were used to prepare the appropriate size of samples for the next stages of samples preparation. A wire erosion machine was used to separate the sections, that is to say the whole sections in Figures 3.2.1 and 3.2.2, from the rest of the inner raceways. This made it possible to fit it in other cutting machines in order to prepare the required size of the samples. This machine was also used to reduce the thickness of the

inner raceway of the BO bearing to 10 mm. The cut sections were then sectioned using an abrasive cut-off wheel (BUEHLER AbrasiMet 250), shown in Figure 3.2.3 (a). This manual abrasive machine removes about a 2 mm thickness of the material during the cutting which needs to be allowed for when cutting through the surface feature of interest. Also, an automatic cutter (BUEHLER IsoMet 5000), shown in Figure 3.2.3 (b), of blade thickness less than 0.8 mm has been used when more accurate and smaller sections were needed.

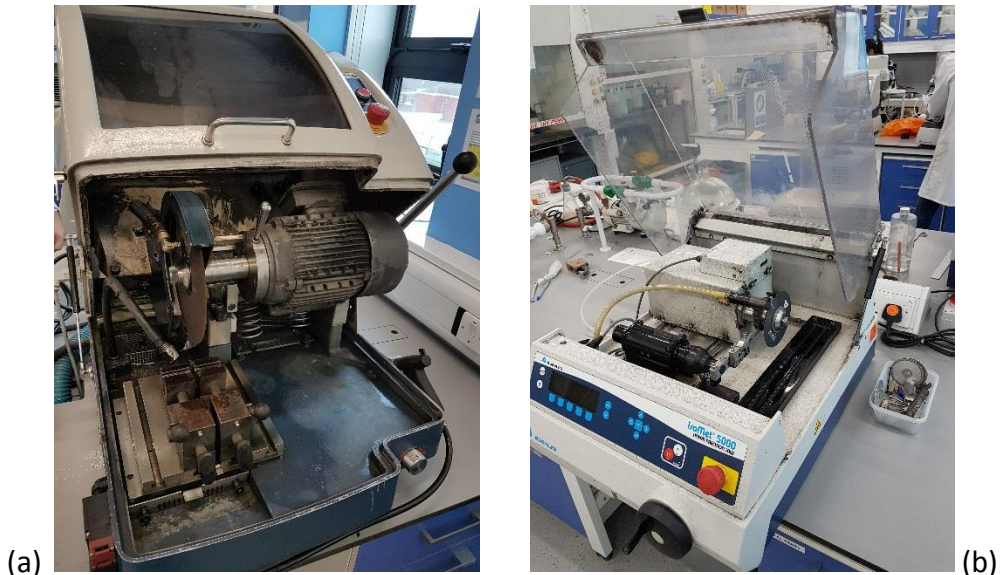


**Figure 3.2.3: (a) Abrasive cut-off wheel BUEHLER AbrasiMet 250 (b) Linear precision saw BUEHLER IsoMet 5000**

### 3.2.2 Mounting

To perform the next steps of sample preparation, the samples needed to be mounted in a specific mounting material. The mounting machine used was BUEHLER SimpliMet 1000 shown in Figure 3.2.4 (a), to carry out hot mounting in which a high temperature is applied to form the mould of the sample using Bakelite as shown in Figure 3.2.4 (b). The mounting material can be general purpose Bakelite which is sufficient for optical microscopy, or conductive Bakelite, which is required for Scanning Electron Microscope (SEM). On the back side of each mounted samples, codes have been carved to identify the location of each sample in the original part before sectioning.

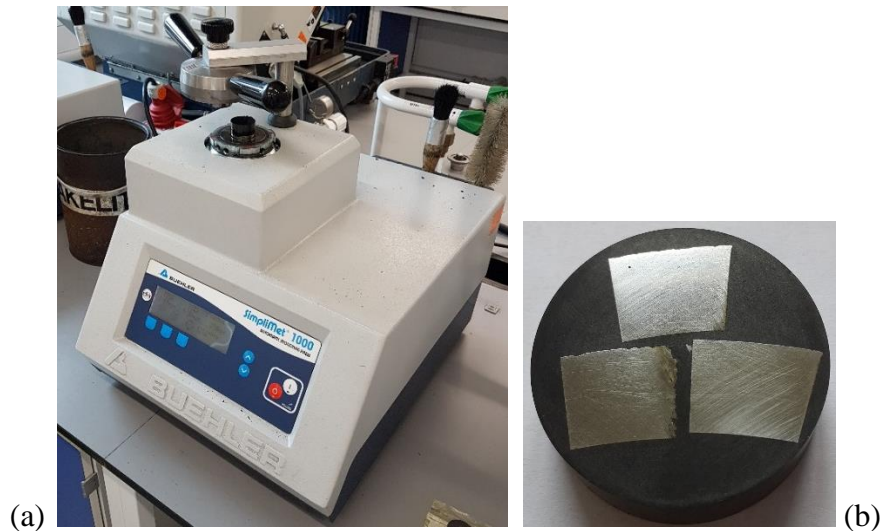


**Figure 3.2.4: (a) the hot mounting machine BUEHLER SimpliMet 1000 (b) three samples mounted in conductive Bakelite**

### 3.2.3 Grinding

The sectioning of samples leaves the cut surfaces very rough and the scars on those surfaces make it very difficult to recognize the features of interest under microscopic examination. Therefore automated grinding was carried out using silicon carbide SiC abrasive grinding papers with three levels of roughness using an automated grinding and polishing machine (BUEHLER Automet 250) shown in Figure 2.2.5. The grit specifications were 240, 600 and 1200 of median grain size of 58.5, 25.8 and 15.3  $\mu\text{m}$  respectively [122]. The force used at each grinding stage was 20 N and the grinding time was 2 minutes and water was applied during the process. The base speed used for the base was 200 rpm and the head speed was 60 rpm respectively as shown in Table 3.2.1.



**Figure 3.2.5: The automated grinding and polishing machine BUEHLER Automet 250**

**Table 3.2.1: Specifications for the grinding and polishing process**

Process	Grit / Cloth	grain size ( $\mu\text{m}$ )	Suspension	Time (min)	Force (N)	Head speed (rpm)	Base speed (rpm)
Grinding	240	58.5	Water	2	20	60	200
Grinding	600	25.8	Water	2	20	60	200
Grinding	1200	15.3	Water	2	20	60	200
Polishing	Cashmere (from MetPrep)		Diamond 3 ( $\mu\text{m}$ )	3	15	60	150
Polishing	Chemcloth m (from MetPrep)		Silica, 0.06 ( $\mu\text{m}$ )	3	15	60 counter	150

### 3.2.4 Polishing

The same machine used for grinding (BUEHLER Automet 250) which is shown in Figure 3.2.5, was also used for polishing, but special suspensions with polishing cloths were used instead of water and grinding papers. The abrasive grinding grits could not produce the final surface finishing needed for the microscopy and polishing cloths with suspensions of a few microns in size were used instead. In this research, a mono-crystalline diamond water base suspension of 3  $\mu\text{m}$  particles size was used for the initial polishing stage. The final polished surface was achieved with a non-crystallising colloidal silica suspension of 0.06  $\mu\text{m}$  particle size. The polishing disc speed, head speed, time and load applied with the diamond and silica suspensions are shown in Table 3.2.1.

### 3.2.5 Etching

The micro-structural features of a metallic material, such as the grain boundary, can be revealed by exposing it to specific chemical solvents known as etchants [123]. Different regions on the etched surface react differently to chemical materials resulting contrast under the microscopic light. In previous studies, bearing steel AISI 52100 has been etched with nital based on a solution of 2% nitric acid in ethanol in order to show the WEA [11][61]. Because the structure of the WEA differs from the non-altered area, the WEA have a lighter colour appearance. In this research, the immersion time used to etch the bearing steel was about 5 to 10 seconds using the aforementioned solution of nital.

### 3.3 Inspection Techniques

After preparing the samples, imaging was performed using optical microscopy, SEM and Atomic Force Microscopy (AFM). These instruments provide a wide range of magnifications and diagnostic techniques for studies on the different features of interest including cracks, inclusions, WEA and the debonding between inclusions and the steel matrix. In addition to imaging techniques, the mechanical properties of the inclusions, WEA and the steel matrix were examined by measurements of the hardness and the modulus of elasticity on both the micro- and Nano-scale. From the information gathered from these measurements, it helps to develop an in-depth understanding of the loading conditions in the examined bearings. The imaging techniques presented in this chapter were also used for the inspection of the specimens of the RSTs. However, special details related only to the RSTs are presented in Chapter 4.

#### 3.3.1 Optical, Scanning Electron and Atomic-Force Microscopic Imaging

A range of optical, electron and probe microscopy techniques were used for scanning the surface on the micro- and Nano-level. The samples, prepared using the techniques described in section 3.2, were inspected in order to acquire statistical and comprehensive details of the subsurface metallurgical features and damage. The procedures applied on the samples prepared from the failed bearings, and those prepared from the specimens of the RSTs, are described below.

Optical microscopy was performed by using a computerized Nikon ECLIPSE LV150 microscope, with a magnification power from 50 to 1000 times, as shown in Figure 3.3.1. After the final polishing stage, each sample was scanned at 100 times magnification to cover a depth of up to 1 mm below the surface. This preliminary scanning was used to perform the steel cleanliness analysis which will be further discussed in Section 3.4.2. The scan was repeated using 200 times magnification over a range of 500 microns below the surface, and focusing on features which could be less obvious to be seen after etching, such as cracks and debondings. Occasionally a higher magnification up to 1000 times was used when smaller features needed to be examined. The software associated with the optical microscope enabled measurements of the dimensions and angles of imaged features which was used extensively in order to collect a data-base for characterizing the damaged inclusions.



**Figure 3.3.1: Optical microscope Nikon ECLIPSE LV150**

After identifying the location of the features that needed to be investigated at a greater magnification than 1000 times, SEM imaging was performed using a camscan Series II, FEI/Philips XL-30, and the tabletop HITACHI TM3030 plus, as shown in Figure 3.3.2. Both the Secondary electron (SE) and the Back-scattered Electron (BSE) detectors were used with accelerating voltages in the range of 15 - 20 kV. The BSE was mainly used to clearly differentiate between materials of different atomic number such as the non-metallic inclusions in the steel matrix. In this case the inclusions were darker because their atoms caused fewer backscattered electrons to reach the detector. The opposite effect applied to the heavier atoms of the iron.



**Figure 3.3.2: Scanning electron microscopes (a) Camscan Series II (b) FEI/Philips XL-30 (c) HITACHI TM3030 plus**

The AFM provided measurements of the topography (characterization in three dimensions) of the surface at the nanometer scale and these measurements were used to obtain detailed mapping images of some of the damaged inclusions. These images also helped in characterising the possible debonding between inclusions and the steel matrix as well as the debonding between the MnS inclusions and the WEAs as shown in Figure 3.3.3. Further details on these observations will be presented in Section 3.4.1. The AFM revealed more details on the deformations in the WEA that could not be revealed by the optical microscope or SEM, where only two dimensional images are produced. This technique was used for the samples of the uncoated bearing and the results are presented in Chapter 5.

The AFM used in this research, Bruker's Dimension 3100, as shown in Figure 3.3.4, has a very high resolution of better than 1 Angstrom ( $1e^{-10}$  m) in the vertical direction and a lateral scanning range is a square of  $90\ \mu\text{m} \times 90\ \mu\text{m}$  with a maximum of  $6.1\ \mu\text{m}$  in the z-direction [124]. This technique uses a mechanical probe rather than light or electrons as that used in conventional microscopy methods. The probe sits on a small cantilever beam with a conical tip at its free end which is controlled accurately and precisely by a piezoelectric element as shown in Figure 3.3.5 [125][126]. The tip at the free end of the cantilever of the AFM has a radius  $\approx 10$  nm. The tip touches the surface either by dragging on the surface which is known as 'Contact mode' or by tapping the surface (Tapping mode). The tapping mode was used here because it gave better quality images.

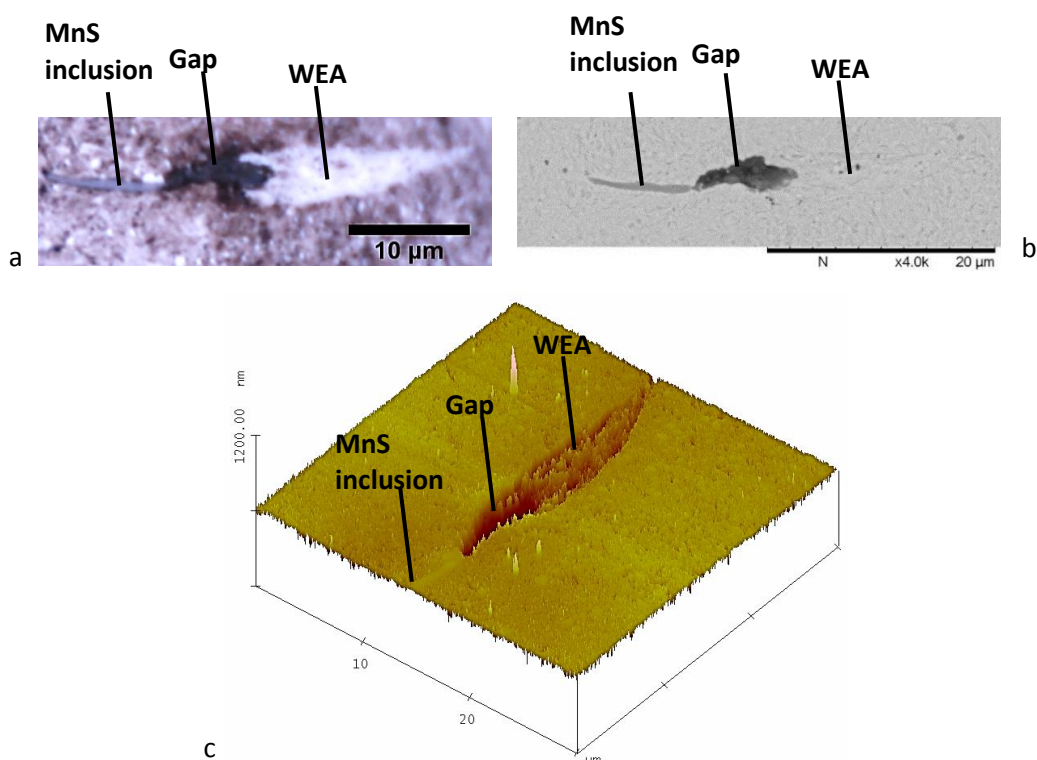


**Figure 3.3.3: Illustration of the difference between images of the same feature taken by different microscopic techniques (a) optical microscopic (b) SEM (c) AFM**

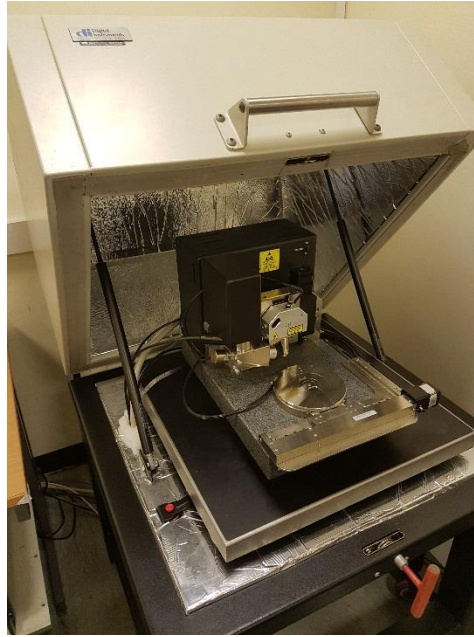


Figure 3.3.4: AFM Bruker's Dimension 3100

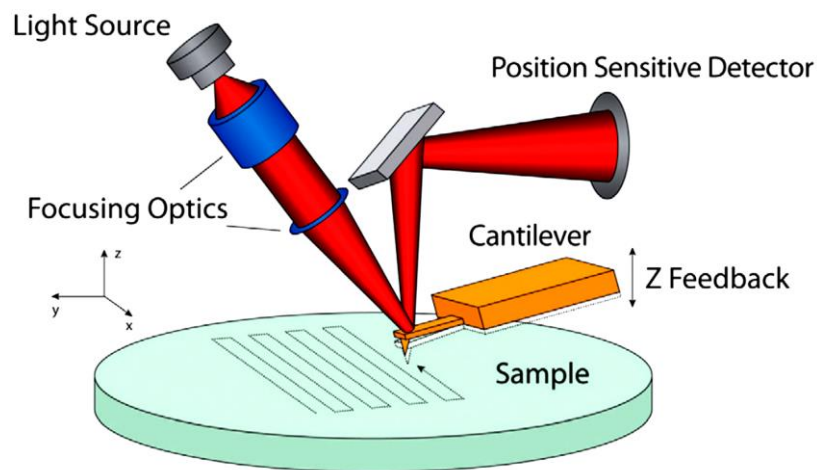


Figure 3.3.5: Schematic of the system used in AFM (Courtesy of Nicholas Geisse [125])

### 3.3.2 Micro and Nano Indentation Hardness Testing

Micro and Nano-indentation were used to measure the hardness of the bearing steel, inclusions, microstructure alteration of WEA (butterflies) and the black oxide layer in the BO coated bearing. Also, the Nano-indentation technique was used to measure the thickness of the BO layer. In this section, only the procedure is presented and supported by some of the results, but the full results and specific sample selection are presented in the related results in Chapters 5 and 6.

The variation of the hardness under the surface was measured for polished samples prepared from the uncoated bearing, the BO coated bearing and the samples of the RSTs. These measurements were made using the Struers Micro/Macro Hardness tester

(DuraScan) shown in Figure 3.3.6. Although this machine is automated; a different approach was needed to manually measure the out-of-focus indents, or discard the outliers of the measurements. The adopted pattern of indentation was a matrix of  $6 \times 3$  indents with the first row positioned at  $70 \mu\text{m}$  from the contact surface, and the distance between the centre of the indents in the horizontal and vertical direction at  $100 \mu\text{m}$ , as shown in Figure 3.3.7. The distance from the contact surface and between indents were chosen to avoid edge effects. This distance should be more than 2.5 to 3 times of the mean diagonal length of the indentation [127]. The mean value and the standard deviation were calculated for indents at the same depth, the three in each row in Figure 3.3.7. The Vickers hardness test was conducted with a load of 0.3 kgf and a holding time of 15 seconds. The size of the indents' diagonals did not exceed  $25 \mu\text{m}$ . This size for the distance from the edge (surface) and between the centre of the indents meets the manufacturers' recommendations and the ISO standard [127][128]. By selecting this load and indentation pattern, it ensured to capture the variation of hardness where higher load causes bigger distance between indents and thus only allows less number of indents. The results of the hardness measurements are presented in Chapter 6, 7 and 8.



**Figure 3.3.6: Automated indentation machine (Struers Micro/Macro Hardness tester DuraScan)**

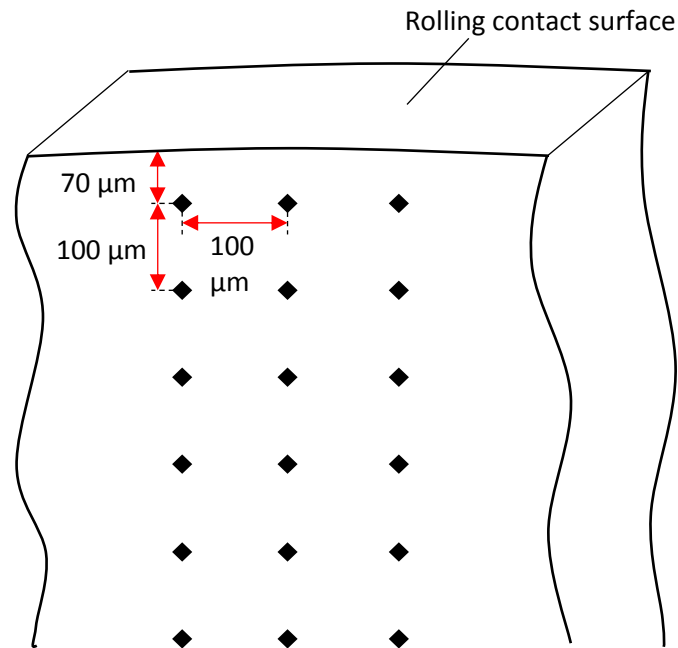


**Figure 3.3.7: Adopted micro-indentation pattern to measure hardness under the surface of rolling contact**

The Nano-mechanical characterization of inclusions, WEA, BO layer and the bearing steel as well as the thickness of the BO layer, were performed using the Hysitron Triboscope Nano-mechanical test system attached to a Bruker Dimension 3100 AFM. With this system, the standard AFM scanner and probe holder was replaced with a Hysitron Tribo-scanner and transducer, as shown in Figure 3.3.8, which enables the Nano-indentation, using a three-sided 120 degree Berkovich indenter tip and by applying a load and simultaneously measuring the displacement. The transducer's maximum displacement and load are 5 μm and 10 mN respectively. The resolution of the displacement and load varies with the environment, and is typically  $4 \times 10^{-4}$  nm at a noise of 0.2 nm, and 1 nN at a noise of 100 nN respectively [124].

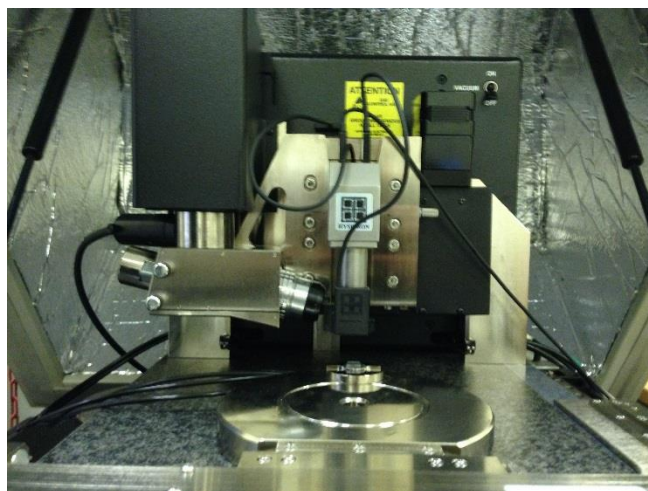


**Figure 3.3.8: Nano-indentation system Hysitron Triboscope**

The Nano-indentation test was performed by applying and removing the load as shown in Figure 3.3.9. The unloading part of the load-displacement curve is used to find the hardness  $H$  and the reduced modulus of elasticity  $E_r$ . The slope  $S$  of the elastic unloading is used to calculate  $E_r$  from equation 3.3.2.1, and the  $H$  is calculated from Equation 3.3.2.2. The variables in these equations and in Figure 3.3.10 are the maximum applied load ( $P_{max}$ ), the final depth ( $h_f$ ) and the resultant projected contact area ( $A$ ) which is a function of the contact depth ( $h_c$ ) [129][130][131]. To account for any variation in the geometry of the indenter, an advanced integrated analysis software was used to calculate the probe area function  $A$ , and to modify the constants in Equation 3.3.2.3 [129]. The  $E_{indenter}$  and  $\nu_{indenter}$  of the diamond indenter are 1120 GPa and 0.07 respectively and are used to calculate the  $E$  of the indented material from Equation 3.3.2.4. The Berkovich indenter used in this machine has a tip radius around 150 nm. This is not as sharp as the tip at the free end of the cantilever of the AFM which has a radius around 10 nm, but it can still be used as an in-situ Scanning Probe Microscopy (SPM) imaging or AFM.

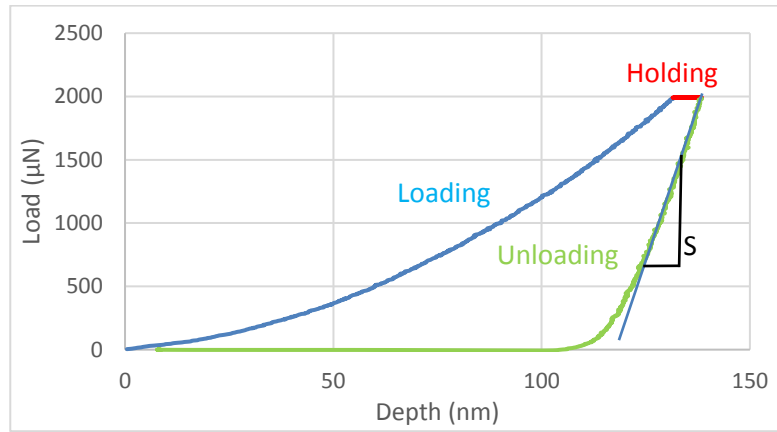


**Figure 3.3.9: Force-displacement curve from the Nano-indentation of the uncoated failed bearing steel**

$$E_r = \frac{S\sqrt{\pi}}{2\sqrt{A}} \quad 3.3.2.1$$

$$H = \frac{P_{max}}{A} \quad 3.3.2.2$$

$$A = C_0h^2 + C_1h_c + C_2h_c^{1/2} + C_3h_c^{1/4} + C_4h_c^{1/8} + C_4h_c^{1/16} \quad 3.3.2.3$$



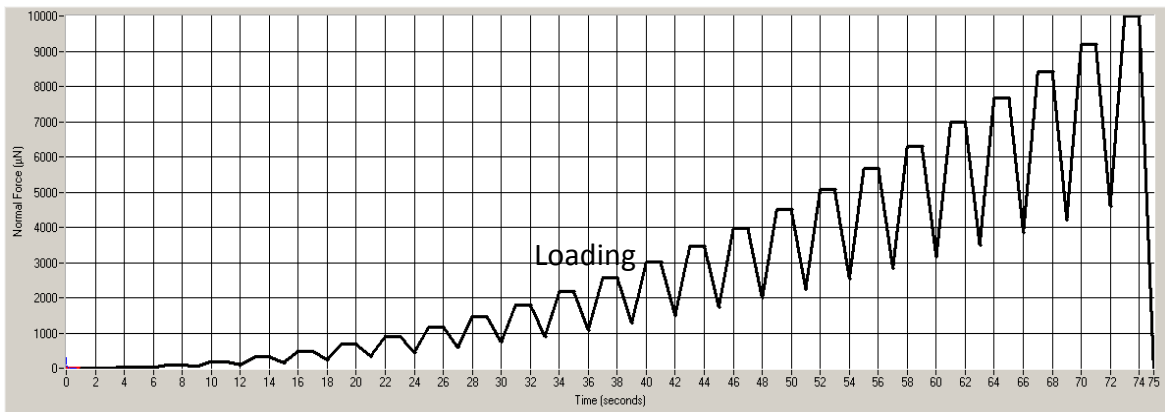


**Figure 3.3.11: Loading-partial unloading curve from the Nano-indentation test to measure the thickness of the undamaged BO layer in the failed BO coated bearing. It shows 50% unloading after each loading cycle. This test revealed that a higher load is needed to measure the whole thickness of the undamaged BO layer**

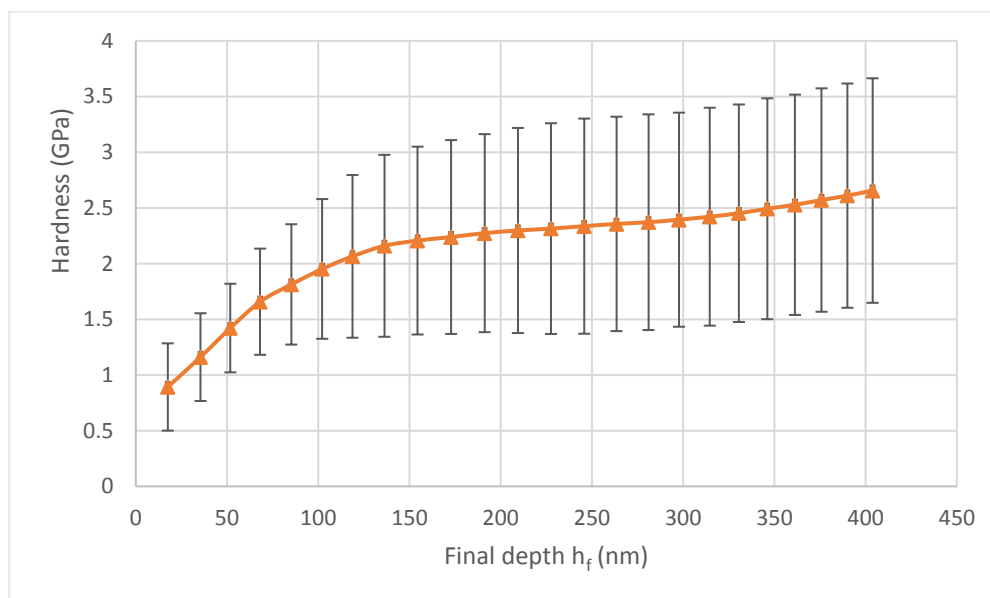


**Figure 3.3.12: The Nano-indentation hardness for the undamaged BO layer measured at 25 steps of loading-partial unloading (see Section 6.5 for full details)**

As it will be discussed in Section 6.5, it was found that measuring the full thickness of the undamaged BO layer was not possible even with the maximum load capacity of the Hysitron Triboscope Nano-mechanical transducer because higher load was needed. To achieve this another Nano-indentation system, the Hysitron TI Premier was used and this is shown in Figure 3.3.13. In this system the maximum load is 1368 mN and the maximum z displacement is 91.863  $\mu\text{m}$ . The measurement of the Nano-mechanical properties using this system was conducted in the same way as discussed earlier; however, different number of indents, loading-partial unloading steps and maximum load were used as discussed in Section 6.5. In addition to measuring the thickness of the BO layer and characterising its mechanical properties, the hardness of damaged inclusions and associated WEA were also measured and will be presented in Chapter 5.



**Figure 3.3.13: Nano-indentation system Hysitron TI Premier**

### 3.4 Characterization of Inclusions and Damages

This section describes the damage that was observed and analysed in Chapter 5, 6 and 7. The definition of each damage type is given and examples are shown for illustration. The observations from the uncoated bearing, BO coated bearing and the specimens of the RSTs are not exactly the same, therefore the definitions and descriptions given in this section are general. The methods used to identify inclusions are explained in Section 3.4.2 and 3.4.3. Also, the methods used to assess the cleanliness of the steel of the examined bearings are presented in Section 3.4.2.

#### 3.4.1 Damage terminology

Bearing failure is defined by the stage of damage which prevents the bearing from meeting its designed performance [33]. For bearings, spalling, and in more severe situations flaking of material from the surface of the rolling contact, is one of most common failure modes and this is referred to as White Structure Flaking (WSF). In wind turbine applications, GB bearings, and more frequently the planetary bearings, are failing earlier than their designed  $L_{10}$  life, by WSF. In this research the initiation of the damage that eventually causes the premature failure was investigated, and it is defined in this thesis as a discontinuity in the material (steel matrix or inclusions) in the form of cracks of few microns to a few millimetres, or microstructure alterations in the form of WEA. The damage could be initiated by a defect on the surface, or a defect in the subsurface such as voids (gaps) or inclusions as shown in Figure 3.4.1. The types of inclusions and their bonding with the steel matrix is discussed in Chapter 2. The definition of all the types of damage observed during the examination of the failed bearings, and the specimens of the RSTs are presented in Table 3.4.1. It should be noted that more than one type of damage could exist at the same time such as debonded and cracked inclusions. Figure 3.4.2 shows examples of different

types of damage defined in Table 3.4.1. Figure 3.4.3 illustrates the observation of an elongated inclusion in the axial and circumferential sectioned specimens, and how their characteristics, length and angle, vary. A database was created by recording the length, angle and depth for observed cracks, inclusions and WEA in the axial and circumferential sections. Figure 3.4.4 depicts the procedure adopted to measure the angle of inclusion and the butterfly wings. This figure shows the definition of the right and left wings of the butterfly, relatively to the ORD. The length of the inclusion represents the distance between the two pointed tips, or the radius for globular inclusions while the width is the maximum dimension normal to the length. The depth is measured from the surface to the centre of the inclusion. The measurement results reported in Chapter 5, 6 and 7 are all based on the definitions given in this section unless otherwise stated.

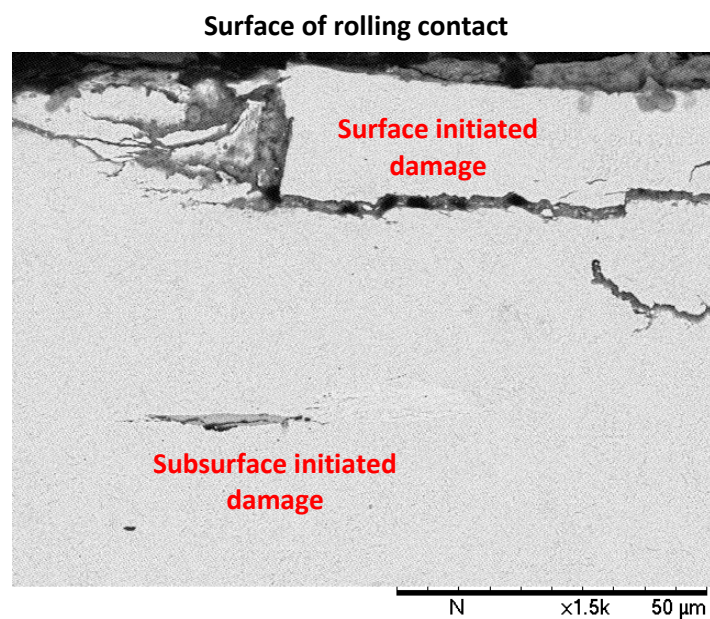


**Figure 3.4.1: Illustration of surface and subsurface initiated damage in axial section**

**Table 3.4.1: Definitions of the damage types observed**

Damage Type	Definition
Inclusions initiated damage	Inclusion cracked or debonded from the steel matrix by a gap or non-perfect bonding; inclusion initiated cracks into the matrix or inclusion formed WEA; or inclusion linked to any surface or subsurface initiated crack or WEC.
Debonded inclusion	Inclusion not perfectly bonded with the steel matrix, a line of debonding can be seen in the interface, or a gap separating part of the inclusion from the steel matrix.
Cracked inclusion	Inclusion that has one or more micro-cracks across it which may or may not extend to the steel matrix.
Micro-crack initiated by inclusions	Crack initiated from an inclusion or a debonding of the inclusion and propagating into the steel matrix. It may or may not attach to WEA (butterfly wing).
WEA	A microstructure change which appears white under optical microscopy and shows dissolution of the spheroidal carbide which are normally observed in the martensitic bearing steel. The WEA could be observed around an inclusion or a void to form a butterfly or along a crack to form WEC.
Butterflies	Inclusion with one or two wing(s) of WEA, with or without micro-crack(s). The wings have specific inclination angles relative to the surface, or the Over Rolling Direction (ORD), and length within the range of few microns to 90 microns per wing as found from the examination of the uncoated and BO coated bearings.
WECs	Single crack or network of cracks which is normally longer than the total length of a butterfly (inclusion+wing(s)) with WEA along the whole or part of the crack or network of cracks. The WECs could be connected to the surface of contact or completely under the surface with no specific inclination angle. The WECs could be linked to inclusion(s).
Subsurface cracks	Not connected to the surface, without WEA and could be linked to inclusion(s). <ul style="list-style-type: none"> <li>• In circumferential sections: single crack or network with no specific inclination.</li> <li>• In axial sections: single crack with specific inclination at one or both of its ends.</li> </ul>
Surface-linked RCF cracks	Cracks which are connected to the surface with specific inclination and are not linked to inclusions. Sometimes cracked steel particles are confined between the two sides of the crack. When these particles are very small, these cracks have similar appearance to the WECs. These cracks could be continuous at certain angle or a series of cracks in the shape of steps.

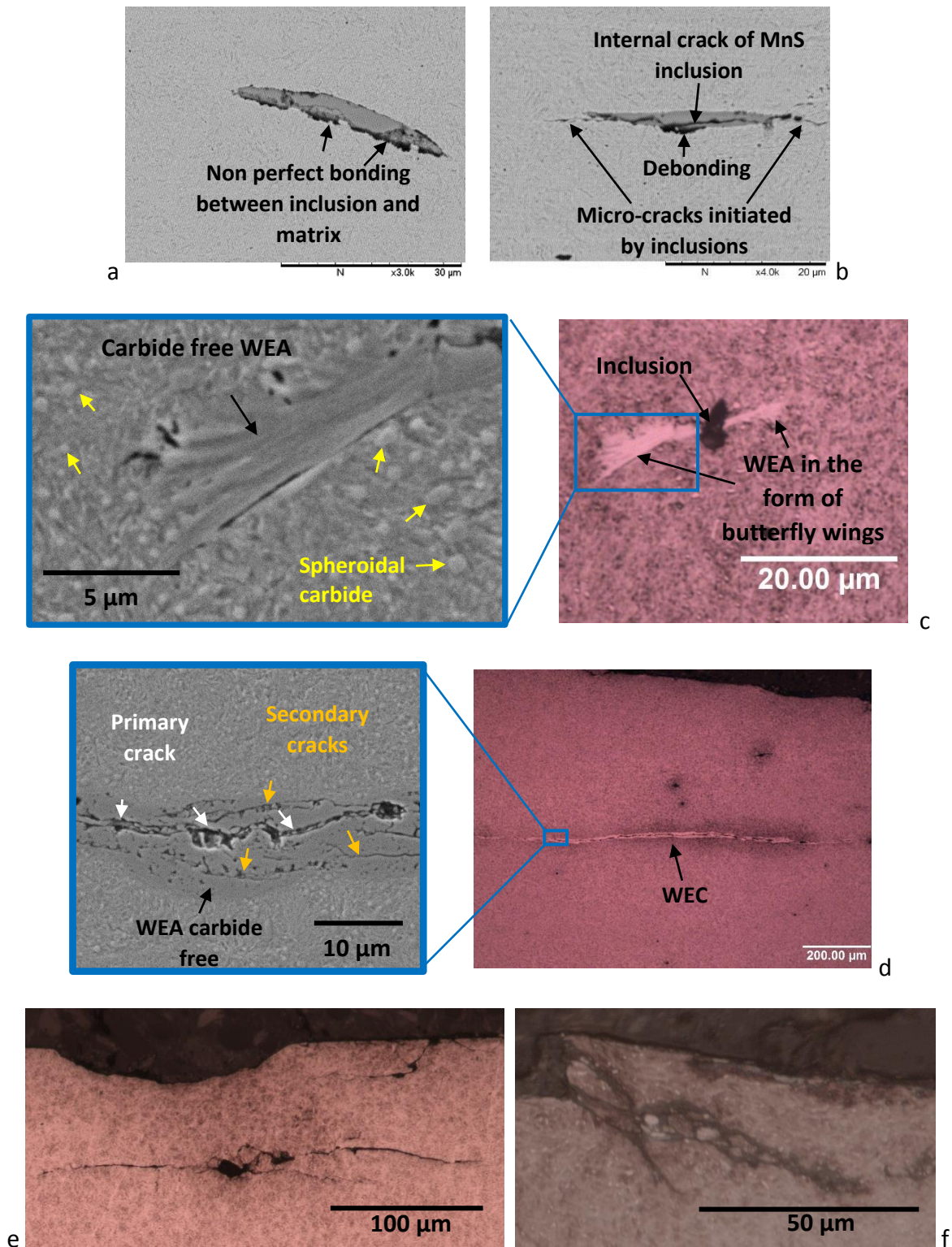
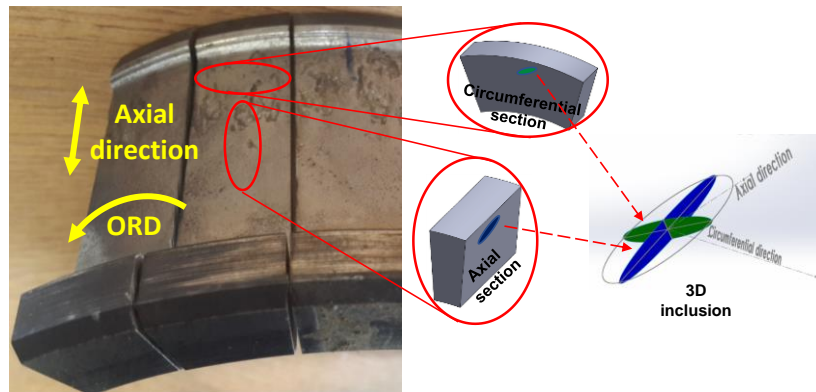
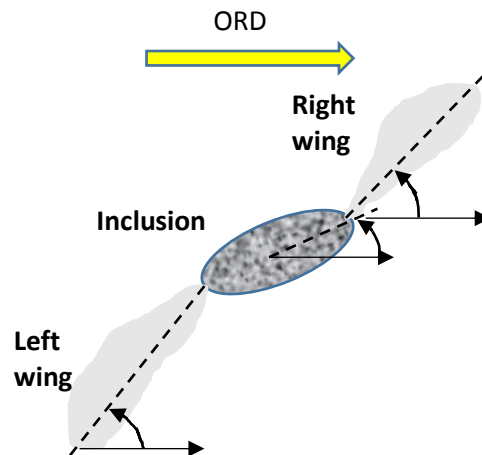


Figure 3.4.2: Examples for the damages defined in Table 3.4.1 (a) Debonded inclusion (b) Cracked inclusion with micro-cracks initiated by inclusions (c) Butterfly (d) WEC (e) Subsurface cracks in the axial section (f) Surface-linked RCF cracks



**Figure 3.4.3: Illustration of samples prepared from axial and circumferential sections with a three dimensional representation of two inclusions viewed in circumferential and axial directions**



**Figure 3.4.4: Definition for the angles of inclusion and butterfly right and left wings**

### 3.4.2 Cleanliness analysis

As discussed in Section 2.1.5, different types of inclusions could exist in bearing steel, and the cleanliness can be assessed by the methods recommended by the international standard. In this section the cleanliness method used in this research is presented and explained. The examination of the failed bearings revealed that the predominant type of inclusions was Type A in the steel of uncoated bearing, while a range of inclusions types were observed in the BO coated bearing with the majority being of Type D. Only the cleanliness of the BO coated bearing was assessed, and that is just to check if the technology of the BO coating had cleaner or dirtier steel than that for the uncoated bearings and thereby providing some insight into the effectiveness of the BO coating. The ISO-4967 [79] cleanliness standard was used to characterize the inclusions observed from the subsurface examination. In addition the Energy Dispersive X-ray spectroscopy analysis (EDX) was used to confirm the chemical composition for some inclusions as presented in Section 3.4.3. As discussed in Section 2.1.5, the EVA method could be more representative

for the effect of inclusion length on the fatigue behaviour. However, this method provides the results in term of maximum expected length for each type of inclusion which cannot be used for measuring the cleanliness for the steel of the BO coated bearing since there is no typical inclusions length available to compare with. On the other hand, the results obtained by applying ISO-4967 provides a fair insight on the steel cleanliness, and a comparison with the requirements in ISO 683-17 [82] to conclude if the investigated roller bearings had the accepted level of steel cleanliness. The method adopted for the cleanliness rating starts with the preparation of polished samples from axial sections since it was found to be the elongation direction for malleable inclusions. Then a number of fields, that showed the worst cleanliness (highest number and biggest size of inclusions), with an area of  $710 \times 710 \mu\text{m}$ , that forms number of fields which covers the requested scanned area according to [79], were measured. These fields were scanned with 100x magnification to record the size and number of each inclusion type in each field. Each inclusion is classified into fine or thick series according to limits provided in ISO 4967. For inclusions Type A, B and C, the length of inclusions from the same type and thickness series were summed up and the total length recorded for each field. For inclusion Type D of the same thickness series, the total number in each field were calculated. The total length was converted to an index number (rating limits) from 0.5 to 3 with a step size of 0.5 according to a table, or equations provided in ISO 4967. Another method to find the index is by comparing each field with standard chart diagrams in ISO 4967 for each inclusion type to find the best match where each diagram carries an index number. After finding the index of each inclusion type in each field, a table was constructed to list these values and to find the average of each index or take the maximum. Figure 3.4.5 shows an example for one of the fields analysed. For this field, the total length of inclusion Type A is fine =  $8.275 \mu\text{m}$  and thick =  $63.71 \mu\text{m}$ ; and the total number of inclusions Type D was 10. This field is equivalent to a cleanliness rating (index) of A: 0.5F/ 0.5T and D: 1.5F where F and T refer to fine and thick inclusions. The cleanliness from the five worst fields are presented in Chapter 6.

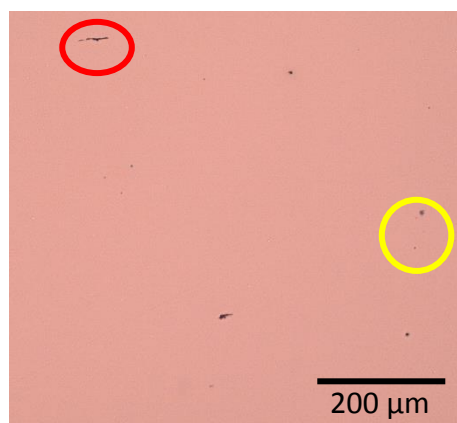


**Figure 3.4.5: Example for the fields used in cleanliness analysis. Red and yellow circles show examples for inclusions Type A and Type D**

### 3.4.3 Energy Dispersive X-ray Spectroscopy (EDX)

The EDX technique was used to identify the chemical elements of a specific point or scanned area on the steel matrix, inclusions and the BO layer. In this research, the EDX was used to identify the inclusion types through recognizing their chemical elements. The FEI/Philips XL-30 shown in Figure 3.3.2 (b), was used to conduct the EDX analysis on polished and etched samples of the failed bearings. Specific inclusions, mainly attached to butterflies or initiated micro-cracks, were analysed by this technique. The procedure involved scanning the samples with an optical microscope first. The location of the feature of interest, such as an inclusion, was then marked with silver ink or by putting indents close to it. After that, the SEM was conducted using the marks as a reference point to identify the feature of interest. To start the EDX, the working distance was set to 5  $\mu\text{m}$  and the accelerating voltages to 15 or 20 kV. For point identification, a single point or area can be selected, and one overall spectrum generated as shown in Figure 3.4.6. The area identification does not show the location of each element over the scanned area which can only be shown by mapping scanning. Mapping scanning takes more time than the point or area identification, however, it was used to reveal the compound inclusions which consist of more than one type of standard inclusions as show in Figure 3.4.7. In each of the dark fields, the bright dots show the chemical element at certain location in the scanned field and the density of the dots reflect the amount of this chemical element. The compound inclusions were mainly observed in the BO coated bearing and more results will be presented in Chapter 6.

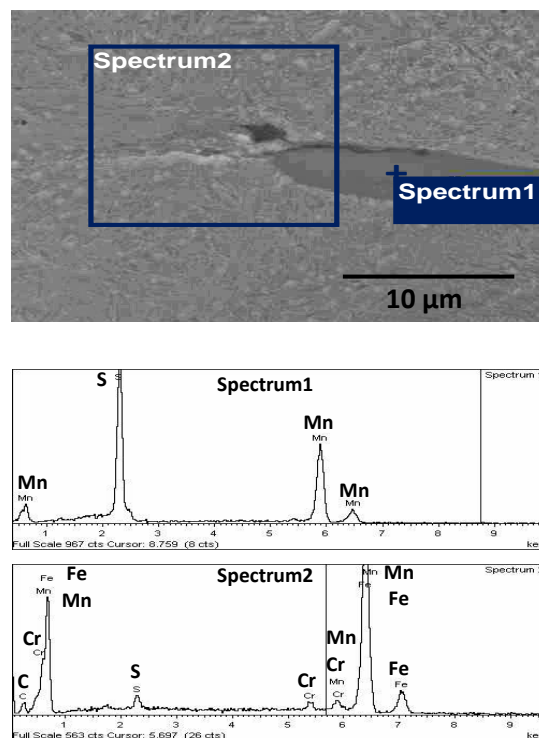


**Figure 3.4.6: EDX analysis (spectrum 1) point identification of a MnS inclusion and (spectrum 2) area identification of a WEA**

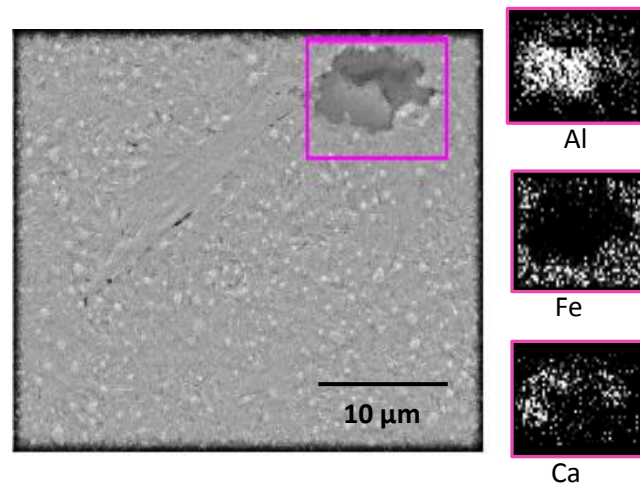


**Figure 3.4.7: EDX mapping of inclusion attached to a butterfly wing in the BO coated bearing. The distribution of three chemical elements are shown for the inside area marked.**

## 4 Experimental Investigation of Damage Initiation Using Twin Disc Testing

This chapter provides a description of the procedure, equipment, devices, specimens and lubricant used to obtain the results of experimentally identify the key parameters that affect the surface and sub-surface initiated damage observed from the examination of the failed bearings as presented in Chapter 7. The focus is on the role of surface traction and the sequence of various tribological conditions. In the literature, as discussed in Chapter 2, many studies were made on the generated alterations of the steel microstructure in the form of butterflies and WECs by specimen testing after millions of cycles under different loading conditions. However, these tests were conducted at high speed, which may not be representative of the operating conditions of the planetary bearings. On the other hand, to investigate the effect of low lambda value (ratio of lubricant film thickness to composite surface roughness), low speed is needed which was used in this research. In addition, the lower number of cycles could represent the initiation of the damage rather than its propagation before the cracks interact with each other and cause spalling.

### 4.1 Twin Disc Test Equipment and Test Procedure

The machine used to perform rolling and sliding contact was the SUROS system which was mainly designed for railway engineering tests and a sketch of the equipment is shown in Figure 4.1.1 [132][133]. The main body of the machine is a Colchester Mascot lathe with the upper specimen attached to its main shaft that is driven by the lathe motor and gearbox. The lower specimen is attached to a shaft that is driven by an AC motor and a gearbox. The lathe speed is set manually while the controller sets the motor speed based on the instantaneous slip ( $S_i$ ) required, as shown in Equation 4.1.1 where  $R$  is the radius of the specimens and  $N$  is the speed in RPM. The load is applied by a hydraulic piston pushing the lower specimen toward the upper one with a load cell measuring the applied load. The specimens were fixed on the arbours which have parallel axes. The LabVIEW program on a Pentium computer was designed to log and show the load, speed, number of revolutions, torque and COT at rates of 1/min or 60/min. The machine is designed to run using a dry contact or lubricated contact by dripping the lubricant or feeding it to the contact area at a specific rate either by automatic Syringe pumping or manually. For long duration lubricated tests, it was necessary to improve the control of the lubrication. Accordingly, one of the main modifications to the equipment was designing and making the oil bath, shown in Figure 4.1.2. This was designed to fit in the very small available space between the cases of the pivoted bearing and the fixed bearing, as shown in Figure 4.1.1. Only the lower specimen was submerged in the oil, but the oil was dragged into the contact area as shown in Figure 4.1.3. The double lips seal in the oil bath allowed the rotation of the shaft, and prevented leakage of the oil towards the pivot bearing.

The operation and monitoring of this machine were conducted according to a standard procedure. However, in this research, this procedure was slightly different because one of

the contacted specimens has a crowned contact surface and this represented a departure from the standard way of calculating the contact pressure. Also, the sequence of mounting the specimens is different because an oil bath was used. The procedure began by cleaning the specimens by immersing them in Acetone in an ultrasonic bath for 5 minutes. They were left to dry before weighing them using a digital scale (Sartorius Entris224-1S of 0.0001 gram increment). After that the upper specimen was mounted on the arbor with a bolt as shown in Figure 4.1.2. Then the oil bath without the transparent screen was mounted on the pivoted bearing case with six bolts, before mounting the lower specimen and the transparent screen. The oil can be added at this stage to a level below the edge of the oil bath to reduce splashing. The lower specimen and the whole pivoted bearing case can slide over the lathe bed in the axial direction. This gives some choice in the contact location between the specimens before starting the test. After deciding the location of contact between the upper and lower specimen, the pivoted bearing case was locked to the lathe bed by a designated screw. The rotating speed for the upper specimen was set on the lathe gearbox by rotating the control lever to the required speed.

Equation 2.4.2.3 in Chapter 2 was used to calculate the required load to achieve specific  $p_{\max}$  for elliptical contact. Then the slip ratio, speed of the lathe and required load were entered into the software menus on the computer. The speed of the lower specimen was calculated automatically by the equipment. To calibrate the machine before starting the test, the specimens were prevented from being in contact by a restraining bolt which pushed the pivoted bearing case downward. At this stage, the machine was started and the load was calibrated to read the required value, and the torque was zeroed as the specimens were not in contact. After calibration, the load was put to zero and the restraining bolt was released and the test was started by applying the load. During the test, the user interface screen showed the rotating speed and number of revolutions for the specimens, the slip ratio, applied load, COT and the resistant torque, which were all recorded in a log file. As discussed in Section 7.1, each test lasted for more than one day, and the tests were stopped and resumed several times in order to achieve the required number of cycles. The same oil was used during each test step, at low or high speed (see Table 7.1.1). The running track temperature close to the point of contact was measured using an Infrared thermocouple as shown in Figure 4.1.4. This temperature was clearly higher than that of the oil inside the oil bath, which was measured using wire probe thermocouple. The temperature was measured every 30 minutes during the tests and a record was made in which the average was applied for calculating the lubricant film thickness between the specimens at each test as discussed in Chapter 7. At the beginning of each test the temperature was increased quickly until it settled, usually after the first 30-60 minutes. At the end of each test, when the required number of cycles had been reached, the machine was stopped and the specimens were cleaned in the ultrasonic bath before weighing them again to check the weight loss.

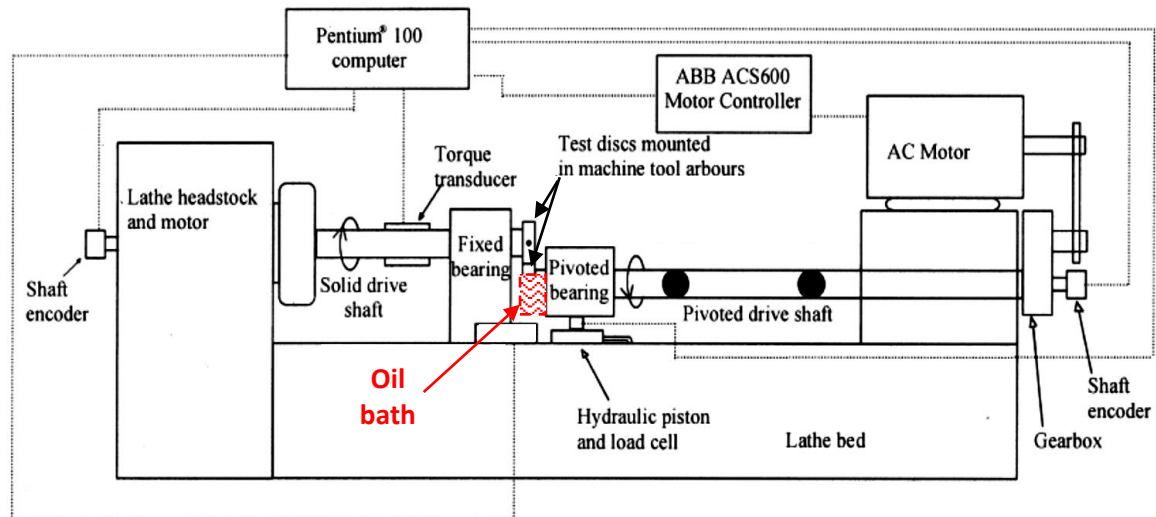


Figure 4.1.1: Schematic representation of SUROS machine adopted from [133] ( Courtesy of Dr. David Fletcher)

$$S_i(\%) = 200 * \left( \frac{R_{Upper} * N_{Upper} - R_{Lower} * N_{Lower}}{R_{Upper} * N_{Upper} + R_{Lower} * N_{Lower}} \right) \quad 4.1.1$$

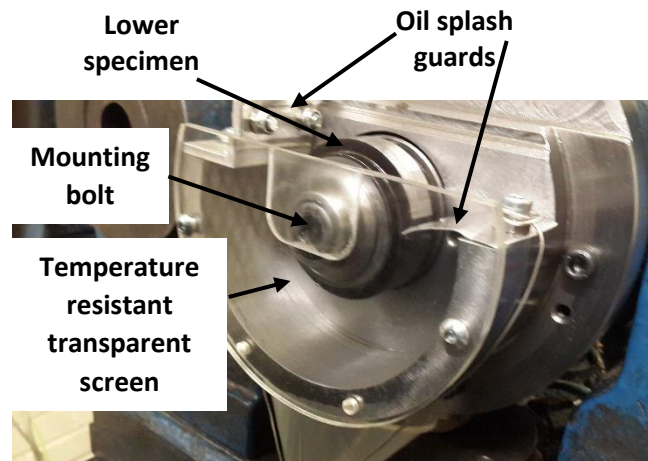
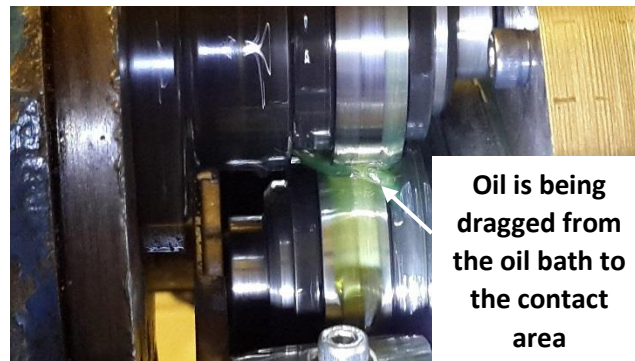


Figure 4.1.2: The manufactured oil path used for the SUROS machine

The measurement of the COT in the SUROS machine takes into consideration the friction in the fixed bearing supporting the shaft of the upper disc [134]. The torque transducer measures the total torque from the friction in the bearing, which always acts opposite the rotation of the shaft, and the torque due to the traction at the contact. The latter changes direction according to the sign of the slip ratio that could be positive or negative due to the speed of the discs, as shown in Equation 4.1.1. The bearing torque was calculated using the measured torque in lubricated tests at both  $\pm$  slip ratio [134]. A relation was found between

the normal load and the bearing torque which was utilized to find the COT caused by the bearing friction and this was considered in the measured COT [134].



**Figure 4.1.3: The lubrication of the contact area**

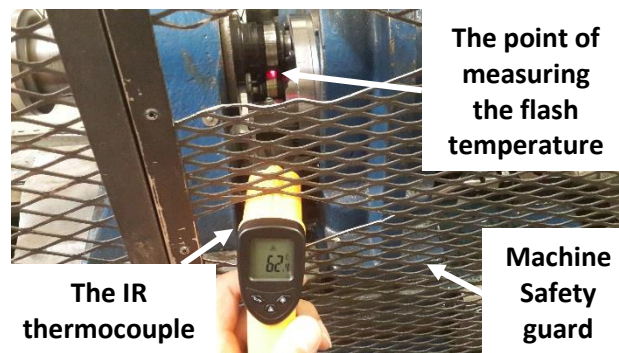


**Figure 4.1.4: Measuring the flash temperature between specimens using non-contact Infrared thermocouple**

## 4.2 Design of Specimens and Properties of Oil

Two types of specimens were designed as shown in Figure 4.2.1 and they represent the pair used for testing. The first type, Figure 4.2.1 (a), has a flat contact surface, non-crowned, and it is normally used for the SUROS machine in the railway research. The second type, Figure 4.2.1 (b), has a crowned surface, which allows higher contact pressure. In this research, the non-crowned specimen represents the inner raceway of the bearing, and the crowned specimen represents the roller of the bearing. Accordingly, the contact area between these specimens was elliptical instead of rectangle, which is the usual contact area for the SUROS machine. This configuration allows higher contact pressure within the load limit of the SUROS machine. Another advantage of this specimen modification is to use each non-crowned specimen for two tests, since the width of contact zone under the maximum load did not exceed the half width of the non-crowned specimen, as illustrated in Figure 4.2.2. In this research, the notation used to identify specimens used for each test are termed such as C1 on F2S. This means crowned specimen number 1 was

used on flat (non-crowned) specimen number 2. F refers to the flat surface, and the test is conducted on the half width of the non-crowned specimen, which is close to the slot side as shown in Figure 4.2.2. Three crowned and 5 flat specimens are used to conduct 9 tests as presented in Section 7.1.

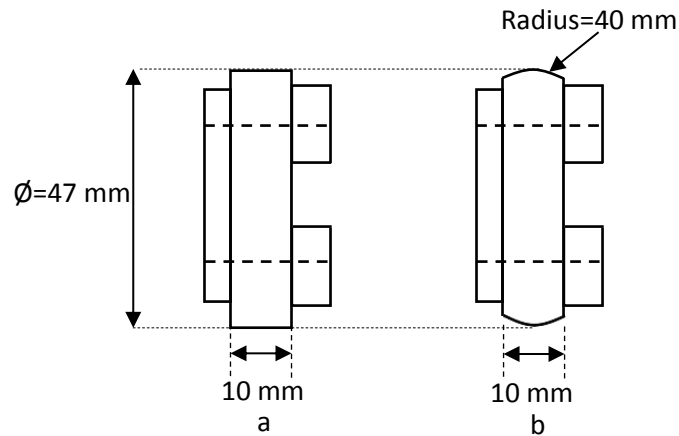


**Figure 4.2.1: Specimens used for the RSTs (a) Flat (b) crowned surface of contact**

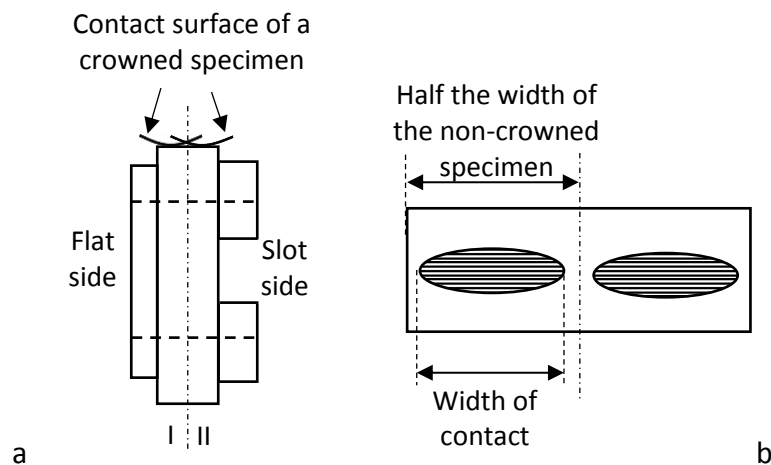


**Figure 4.2.2: Specimens contact configuration (a) illustration for the flat and slot sides (I) and (II) respectively (b) illustration for the contact width and the half width of non-crowned specimen**

Bearing steel of 100CrMo7-3 according to EN 10027 B825 [135] was provided by the steel manufacturer OVAKO to manufacture the specimens. According to OVAKO, this steel is used in medium and big bearings. The steel was provided as a bar of 50 mm diameter in the tempered state. This state allowed the bar to be machined to the required specimen geometry. Then heat treatment was carried out according to a process provided by OVAKO to achieve through hardened Martensitic steel for the specimens. This process involves stress relief annealing with two hours of air-cooling from a temperature of 550 - 650°C. This is followed by oil quenching for 20-60 minutes from a temperature of 830 - 870°C. Within two hours of the oil quenching, tempering should be achieved in cool air starting at a temperature of 160 - 500°C. After the heat treatment, all the specimens were grounded

to a surface finishing close to the actual bearing roughness. The variation and analysis of surface roughness before and after each test will be discussed in Section 4.3 and Chapter 7. The chemical composition of this steel is presented in Table 4.2.1 [136]. The manufacturer adopted a similar process as discussed in Section 3.4.2 to find the average cleanliness for this steel as shown in Table 4.2.2 [136]. The dominating inclusion in this steel is type A, which is similar to what has been observed in the examined uncoated failed WTGB, and this is discussed in Chapter 5. Some of these inclusions also show debonding, similar to that in the failed bearings, which is found to affect the damage initiation more than other factors, as it will be discussed in Chapters 5, 6 and 7. These similarities make the differences due to the manufacturing process, such as the length of inclusions in axial direction, are less significant. Also, duplicating the manufacturing process of a WT bearing is complicated and it is beyond the scope of this research.

**Table 4.2.1: Chemical composition for the steel used in the specimens of the RSTs**

	C%	Si%	Mn%	P%	S%	Cr%	Ni%	Mo%
Min.	0.93	0.20	0.60			1.65		0.20
Max.	1.05	0.40	0.80	0.025	0.015	1.95	0.25	0.35

**Table 4.2.2: Average cleanliness for the steel used in the specimens of the RSTs**

Inclusion type							
A		B		C		D	
Fine	Thick	Fine	Thick	Fine	Thick	Fine	Thick
2.0	1.5	0.5	0.1	0	0	0.2	0.1

The properties of the lubricant used in the mechanical systems, such as the WTG, plays a decisive role in minimizing the friction and wear between the contacted surfaces, as well as removing the generated heat [85]. The lubricant used for wind turbine applications varies with the variation of the gearbox design configuration and the operating environment, such as ambient temperature, operating temperature, viscosity index and operating speed range [85]. In this research, two types of lubricants, Castrol Alpha SP 46 and 68, were used to investigate the effect of different viscosities of the lubricant. Most of the tests that generated WECs without hydrogen charging, as discussed in section 7.1, were performed using Castrol Alpha SP 68 [14]. The properties of these lubricants and one of the most common lubricant used for wind turbine, Castrol Alpha SP 320, are shown in Table 4.2.3 [137]. Although the viscosities are different, considering the operation speed, temperature and load results in close  $h_{\min}$ . To investigate the variation of chemical

elements in these oils an Infra-Red spectrometry test was needed. This test was kindly performed by Mr Rob Hanson in the Department of Chemistry – CCIAS/ University of Sheffield. Although the viscosities are different, the Infra-Red spectrometry test showed that almost the same additives are used for these oils as shown in Figure 4.2.3. The peaks in these spectra show the additives but these cannot be identified without a comparison with a standard reference, which is not provided by the manufacturers. However, the additive could be oxidation inhibitors, corrosion inhibitors, anti-wear additives, extreme-pressure additives, detergents, etc. [111]. It has been found in previous studies that the additives can play an important role in the development of the WSF [69], however it is not within the scope of this research to study this further. Allowance for the variation of oil viscosity during RSTs was made by taking the average temperature and calculating the viscosity at this temperature. This was conducted by using the properties in Table 4.2.3 and by plotting a temperature-viscosity relation line on ASTM standard viscosity-temperature charts, and finding the viscosity at any temperature as shown in Figure 4.2.4. The calculations in Chapter 7 used the viscosities at different temperatures during the RSTs to find the minimum lubricant film thickness and the  $\lambda$  ratio to determine the lubrication regime.

**Table 4.2.3: Properties of lubricants used for RSTs with SP 320 for comparison**

Lubricant	SP 46	SP 68	SP 320
Density @ 15°C (kg/m <sup>3</sup> )	880	880	900
Kinematic Viscosity @ 40°C (mm <sup>2</sup> /s)	46	68	320
Kinematic Viscosity @ 100°C (mm <sup>2</sup> /s)	6.65	8.53	24
Viscosity Index	>95	>95	>95

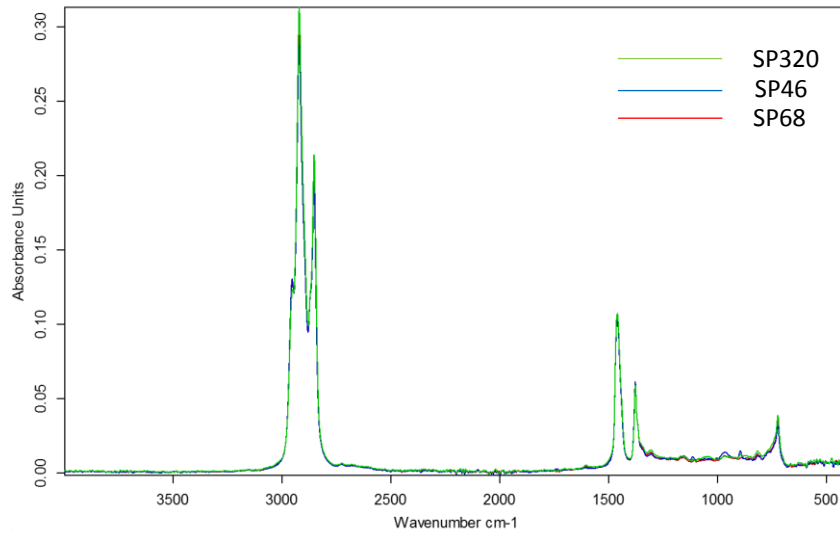


**Figure 4.2.3: IR Spectra of three grades of oils**

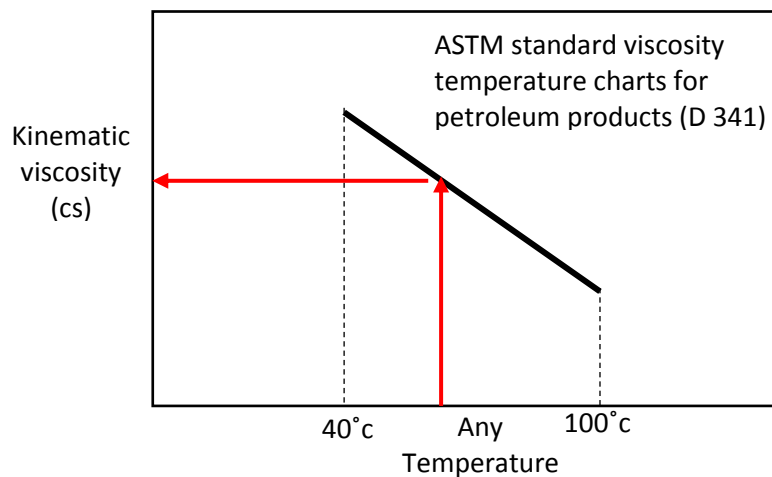


**Figure 4.2.4: Illustration for finding oil viscosity at variable temperature using ASTM standard viscosity temperature charts**

### 4.3 Surface Characterisation and Subsurface Metallography

The surface roughness variation was examined using the non-contact profilometer (INFINITEFOCUS Alicona) shown in Figure 4.3.1. This system uses the optical focus variation method to create 3D measurements. The main parts in this measurement system are: the Laboratory Measurement Module which is the interface to operate the machine and set the parameters; and the control or the processor unit which analyses the surface after taking the measurements. The machine has a stage on which the sample is placed and this can be moved in the x and y direction while the objective is moving in the z direction. To start the measurement, the extent of the surface area to be examined needs to be specified

as well as the maximum expected distance between the deepest and the highest points on the surface which can be estimated by a pre-measurement process. The machine scans the specified area and captures images at different depths by automatically changing the distance between the surface and the object in the z direction. The focused image at each scanned plane corresponds to a certain depth or height [138]. The vertical resolution of the objective used for all the measurements was 50 nm. After acquiring the data at each point, a line or area can be specified to measure the roughness using the interface software.

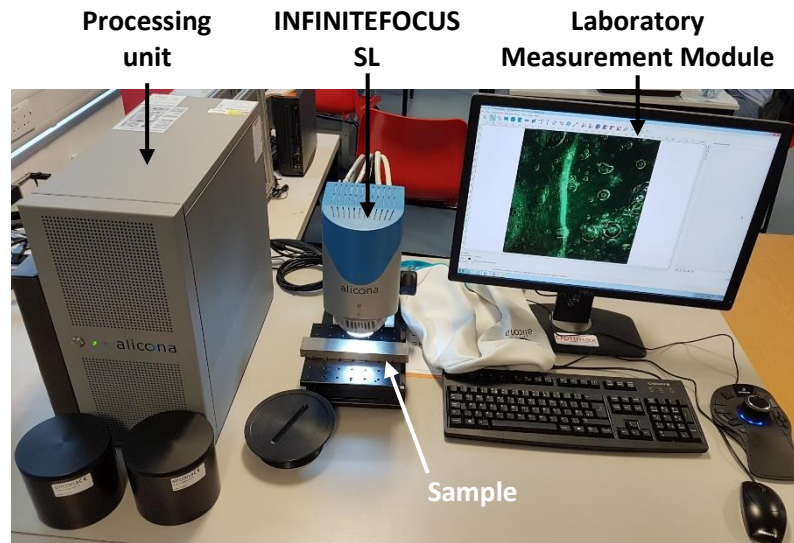


**Figure 4.3.1: The non-contact profilometer (InfiniteFocus Alicona) which was used for measuring the surface roughness of the RSTs specimens**

Each non-crowned specimen has two wear scars from two RSTs. The arithmetical mean roughness ( $R_a$ ) was measured for the surface of each specimen outside and inside wear scars in the axial and circumferential directions with at least three lines at different locations, as shown in Figure 4.3.2. Then, the average and standard deviation were calculated to find the  $R_a$  inside and outside the wear scars in the axial and circumferential directions. The wear scar roughness for each RST was compared with the original roughness of the specimens in order to find the percentage difference as discussed in Chapter 7.

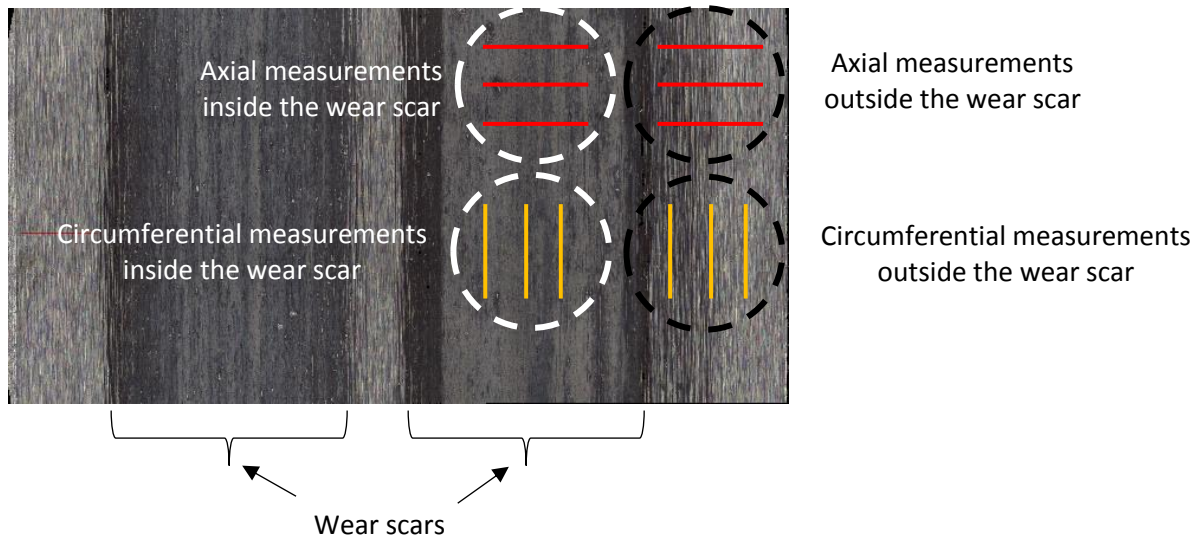


**Figure 4.3.2: Example for the roughness measurement pattern applied on the specimens of the RSTs.**

For measuring the hardness variation under the surface of the RSTs specimens, the same micro-indentation technique and procedure described in Section 3.3.2 were used. In this measurement, a pattern of 18 indents into the side of the cross-section were adopted to find 6 values of hardness starting from 70  $\mu\text{m}$  to 570  $\mu\text{m}$  under the centre of the wear scar on the surface. An axial section was taken from each specimen in order to prepare samples for the hardness measurement.

## 5 Results and Discussion on Investigation of a Non-coated Bearing

This chapter presents and discusses the results of an examination of the uncoated failed bearing using the methodologies presented in Chapter 3. After preparing samples from the inner raceway of this bearing, they were scanned for the damages defined in Section 3.4.1 using a range of optical, electron and probe microscopy. The emphasis here was on identifying the subsurface damage initiation at inclusions. In this chapter, four types of these inclusions that initiated damage were observed and they are defined as: debonded inclusion, cracked inclusion, inclusion initiated micro-crack, and a butterfly inclusion. The characterisation of these inclusions, and the associated micro-cracks or micro-structure changes (WEA) were analysed. The damage initiated by these inclusions was correlated with the subsurface stress distribution, and conclusions were drawn on the effect of surface traction.

### 5.1 Characterisation of damage initiating inclusions

After preparing samples from the inner raceway of the uncoated bearing according to the procedures described in Section 3.2, they were inspected using optical, SEM, AFM, and micro and Nano-indentation as described in Section 3.3. The results are presented in this section and categorised into groups representing the characteristics of observed damage initiating inclusions.

#### 5.1.1 Types of Inclusion

The most common inclusions found in this bearing were light grey elongated inclusions. Inclusions of these features are classified as Type A-Sulfide which could be manganese sulphides [78] or aluminates embedded in manganese sulphide [75], according to the standards ASTM-E45-13 and ISO-4967, as discussed in Section 2.1.5. Determining the exact components of these inclusions was performed using EDX, which revealed the presence of Manganese (Mn) and Sulphur (S), as shown in Figure 3.4.6. No Aluminium (Al) was found at the dark tips of some of the inclusions that were identified using AFM and SEM as shown in Figure 5.1.1, and observed as gaps/debondings. These inclusions show the debondings at the tips and sides of MnS inclusions, which could be mistaken for encapsulated oxide.

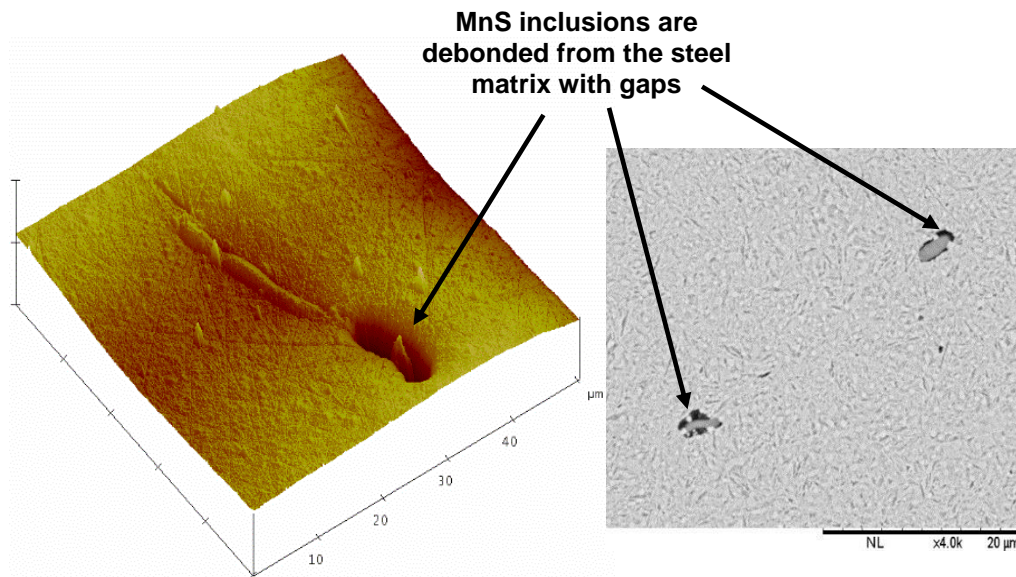


**Figure 5.1.1: (Left) AFM 3D image and (Right) SEM image of debonded inclusions at 1300  $\mu\text{m}$  from the contact surface**

### 5.1.2 The Debonding of Inclusions

Debondings or gaps were found with different shapes around the inclusions at different depths from the contact surface. Sometimes these debonded inclusions were found far from the zone of high subsurface stresses, which was calculated by the Hertzian contact theory. Accordingly, the debondings could be manufacturing defects which has been reported in manufacturing studies ([139][140][141]). It is important to investigate the occurrence of debonded inclusions far from the effects of loading and to confirm that it is mostly a material defect rather than a result of loading. Many inclusions were observed to be located at some distance from the surface, deeper than 1 mm, an example is shown in the right image in Figure 5.1.1, and they show similar debonding features as those observed for debonded inclusions close to the surface. These deep inclusions were not included in the database of the catalogued inclusions.

It was observed that WEAs, butterfly wings, are mostly attached to the debondings at inclusion tips rather than to the inclusions directly. This could be due to the higher stress concentration factor at debondings around the inclusion tips [142][143]. To gain an insight on the size of the inclusion as well as examining the topography of the WEA, AFM analysis was conducted for an inclusion that initiated damage at 207  $\mu\text{m}$  under the surface as shown in Figure 3.3.3. This Figure shows a MnS inclusion with a debonding at one of its tips, and a single butterfly wing attached to the debonding. After an AFM scan, the depth along two lines crossing the debonding was characterised as shown in Figure 5.1.2. The WEA is found to be lower than the steel matrix, and the discontinuity between the inclusion and the WEA is clearly shown by the relative depth. The maximum dimensions for this debonding were found to be 0.58  $\mu\text{m}$  in depth, 9.6  $\mu\text{m}$  in length and 3.3  $\mu\text{m}$  in width. The characters of the debondings could be important for fracture mechanics analysis by

considering the size of the debonding as the initial crack length. Such an analysis was not within the scope of this research, but it is suggested for future work.

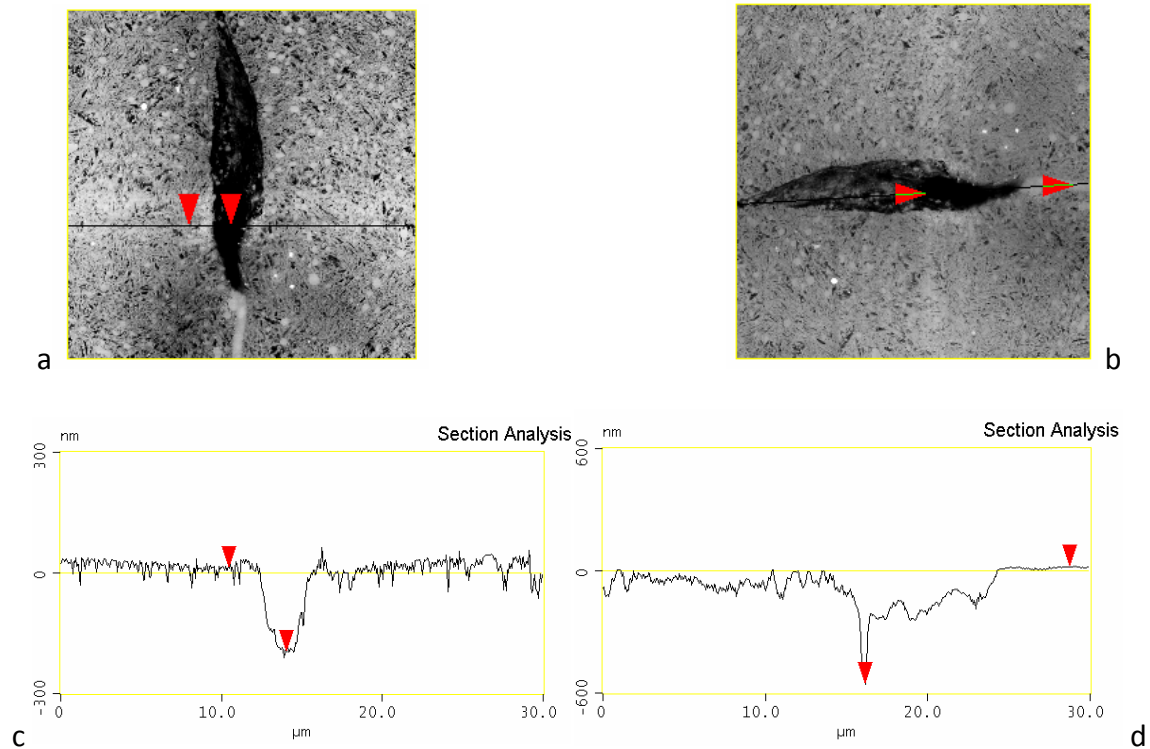


**Figure 5.1.2: AFM analysis shows the debonding between a MnS inclusion and WEA (butterfly wing)**

### 5.1.3 WEA (Butterfly Wings)

The 3D AFM imaging measurements also showed that the WEA is not a dense material, and it resembles a damaged material extending from the debonding or inclusion tips. Figure 5.1.3 shows three butterfly wings observed in the axial and circumferential sections with 3D AFM images for the WEAs. To the author's knowledge, AFM images of WEA have not been investigated in studies conducted on the initiation or the occurring mechanisms of WEA. These images show clearly the features of the WEAs that are not available by 2D optical or SEM images. The borders of the WEA show a sudden transition from the dense steel matrix to the discontinuous material inside the WEA. This could be due to a local tensile stress concentration that pulls aside the edges of the WEA (ie the interface with the steel matrix). Chapter 8 investigates the stress developed around an inclusion under different loading conditions, and highlights the occurrence of tensile stress. The hardness of the WEA is reported to be higher than the steel matrix as presented and measured in this research in Section 5.1.5. This could be an indication of the material hardening for the bearing steel at the WEA. In a similar way, the formation of a WEA may be due to the localized strain hardening around a debonding where the stress exceeded the yield limit of the bearing steel.

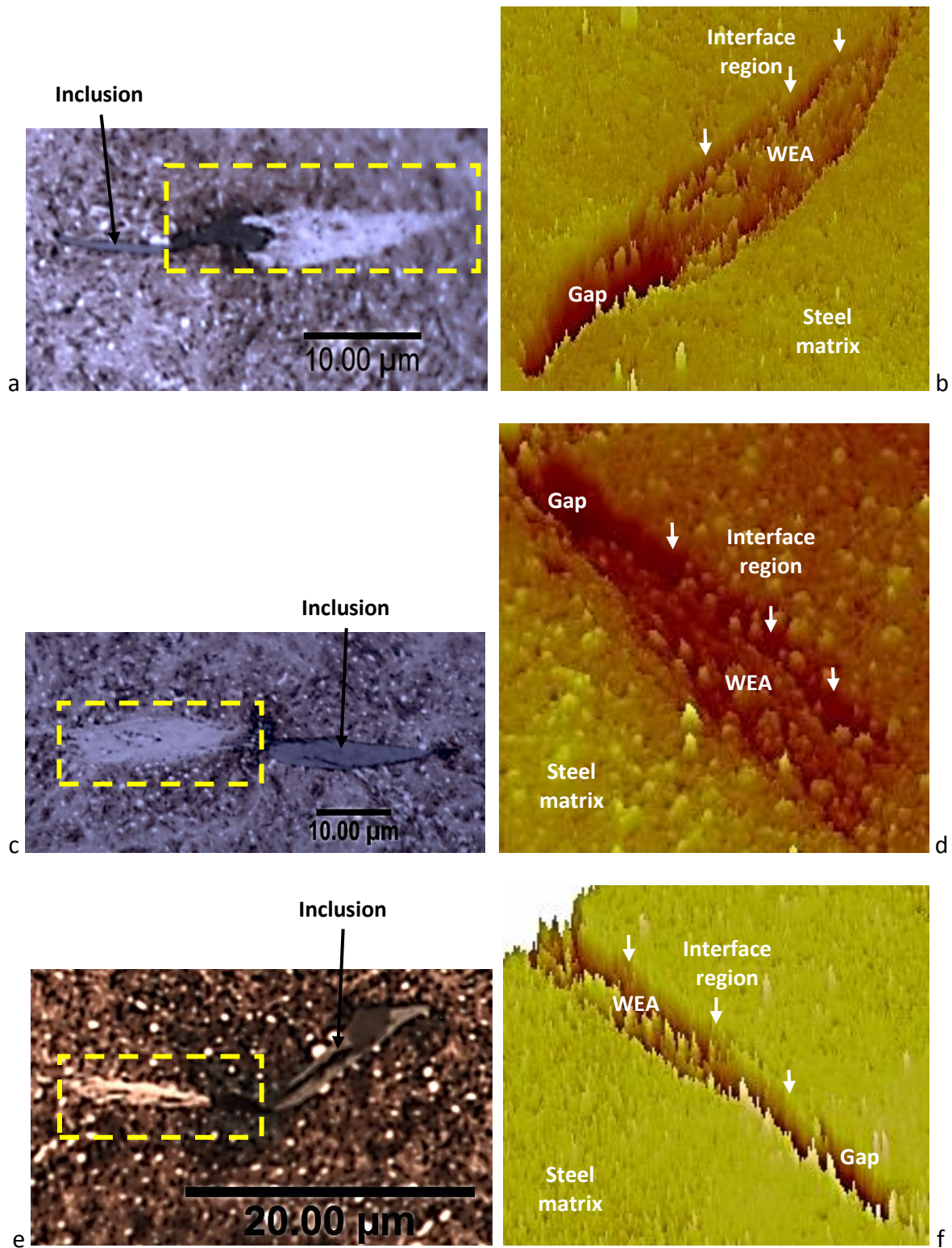


Figure 5.1.3: (Left) optical images for debonded MnS inclusions attached to WEA. The highlighted parts are the 3D AFM images to show the discontinuity of the WEA, and the debonding at the boundaries between the WEA and the steel matrix. The images in (a) to (d) are from axial sections; and (e) and (f) are from circumferential section with ORD from left to right

#### 5.1.4 Cracked Inclusions and Inclusion Initiated Cracks

Some of the observed micro-cracks and WEA (butterfly wings) were initiated by inclusions combined with a crack into the inclusion as shown in Figure 5.1.4. Because the MnS inclusions are weaker than the hardened bearing steel, it is expected for these inclusions to be damaged first when there is the same stress acting on the inclusion and the steel matrix. It is more likely that the micro-cracks would be started from the interface between the inclusion and the steel matrix, since no inclusions were found for having a micro-crack completely contained inside the inclusion without interacting with this interface. It is also observed that micro-cracks propagated into the steel matrix or the butterfly wings could initiate from the debonding between the inclusion and the steel matrix where the inclusions are not cracked themselves. An example of this is the non-cracked inclusion and the debonding which formed a butterfly as shown in Figure 5.1.3 (a). In other cases, micro-cracks into the steel matrix were initiated from inclusions tips without debonding or inclusion internal cracking as shown in Figure 5.1.5. Accordingly, the sequence of inclusion cracking followed by micro-cracks into the steel matrix followed by WEA formation, as suggested in a previous study [18], cannot be confirmed by this study to be the only mechanism. The sequence appears to be more related to depth, geometry and bonding of the inclusion to the steel matrix, which determine the stress field around the inclusions and the material property changes due to local plastic deformation that affects ductility leading to different modes of fracture.

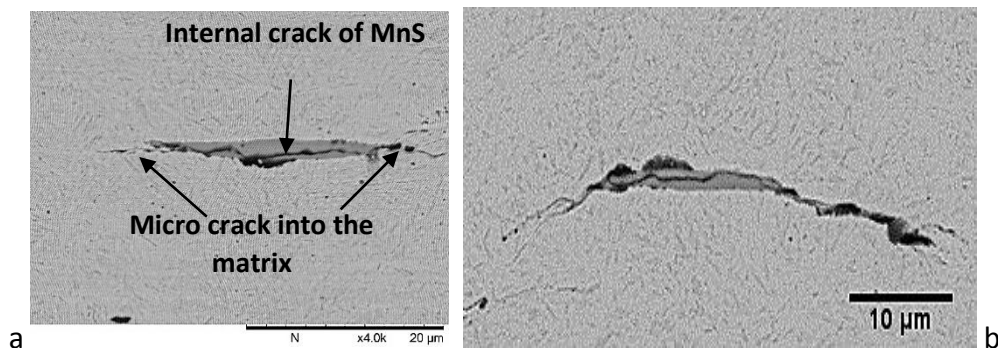


Figure 5.1.4: Images showing cracked inclusions with cracks propagated into the steel matrix

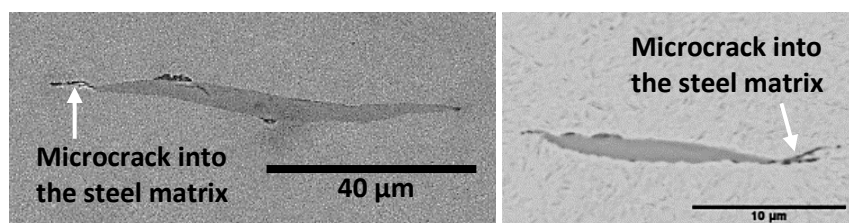
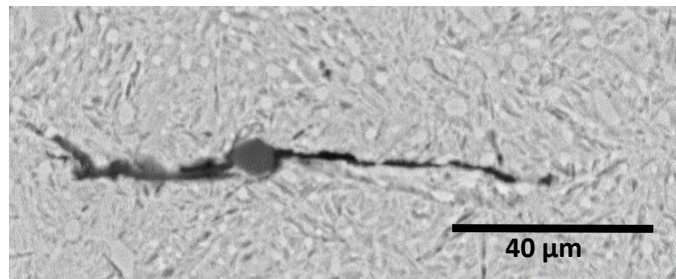


Figure 5.1.5: Micro-cracks initiated from non-cracked inclusions in axial sections

Other types of inclusions that could be harder than a MnS inclusion show relatively long cracks into the steel matrix without self-cracking as shown in Figure 5.1.6. However, only one crack was found while all other cracks were initiated from MnS inclusions. In addition to the micro-cracks, one fully developed crack linking the surface with two butterflies was found as shown in Figure 5.1.7. In this figure, no inclusions could be found in the butterflies, which may have been removed due to the sample preparation process. Although the cracks are three-dimensional, the plane examination can still reveal general features of these cracks and their interaction with inclusions and voids as shown in the cracks in Figure 5.1.7. In this figure, since no damage (spalling) is linked to the WEC, it appears most likely that this crack propagated from the butterflies and it is not surface initiated. The lower butterfly is around  $210\ \mu\text{m}$  from the surface which is closer to the surface than the location of  $\tau_{1(max)}$ , which will be discussed in Section 5.3. The image in Figure 5.1.7 shows that a crack could start as a WEC close to the butterfly, as shown in the lower left of this image, and then propagate without WEA as shown by the yellow arrows. It also shows that cracks/WECs could initiate from the inclusions, or the interface between WEA and the steel matrix. These cracks propagate in a vertical direction towards the surface or deeper down without following the extension direction of the butterfly wings, which suggests a different mechanism for the initiation and propagation. This research focussed on the initiation rather than the propagation. Statistical analysis was conducted in order to investigate the initiation by analysing the inclusions that initiated damage and the characteristics of subsurface initiated damage as described in Section 5.2.



**Figure 5.1.6: Non-MnS inclusion initiated cracks without internal cracking of inclusion**

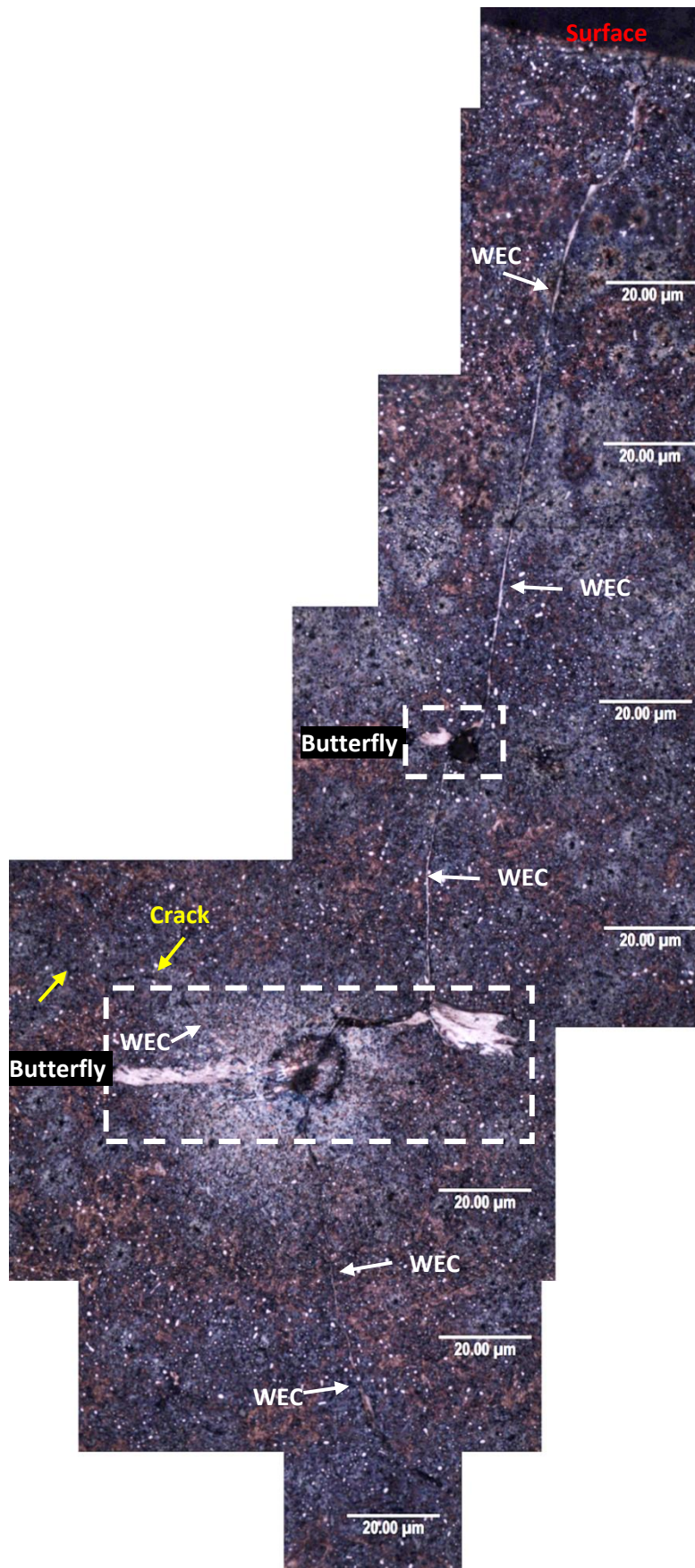
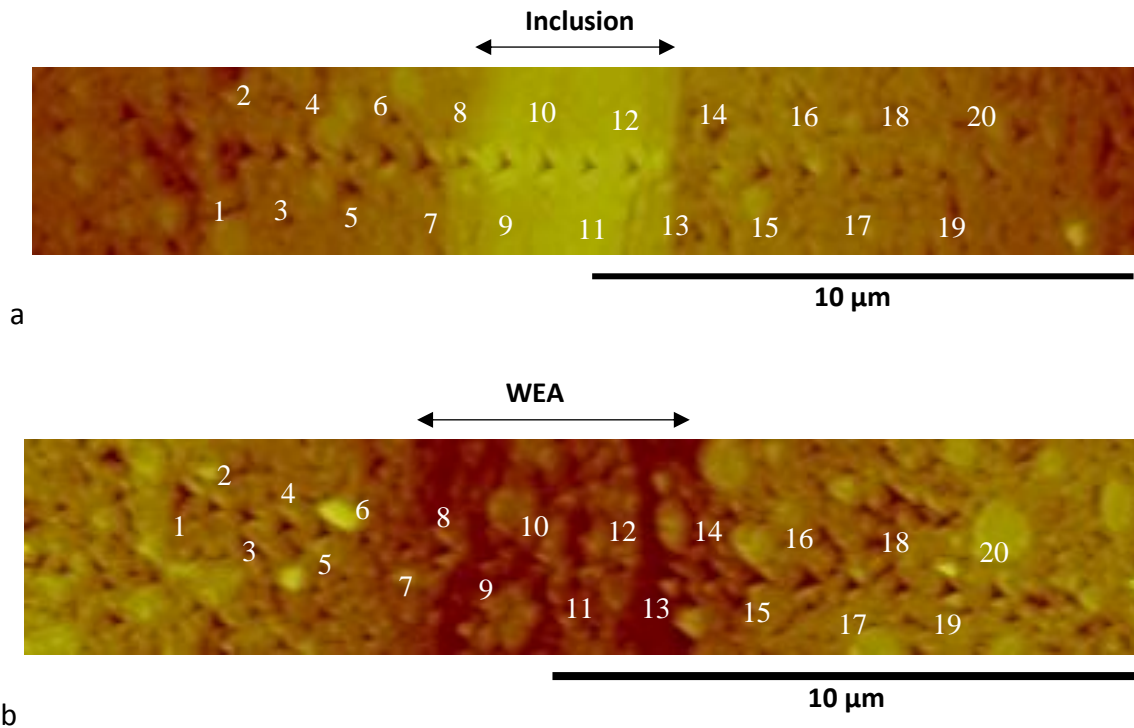


Figure 5.1.7: WEC propagated almost vertically toward the surface and linked two butterflies

### 5.1.5 Mechanical Properties of Inclusions, WEA and the Interface

The Nano-indentation technique employing a three sided 120 degree Berkovich indenter tip in the Hysitron Triboscope system, as described in Section 3.3.2, was used to measure the mechanical properties, hardness  $H$  and modulus of elasticity  $E$ , of MnS inclusions and WEA in a butterfly. An etched sample was needed to conduct this measurement since the WEA cannot be observed without etching. However, a polished sample that was un-etched, was also used to measure  $E$  and  $H$  for MnS inclusion and the steel matrix as a reference to compare with the measurement from the etched sample. For the un-etched sample, the measurement was applied on the inclusion shown in the left of the image in Figure 5.1.1 which is 75  $\mu\text{m}$  from the surface. The scanning area was  $2 \times 2 \mu\text{m}$  with a distance of 0.8  $\mu\text{m}$  between the centres of adjacent indents, and the maximum load applied was 2000  $\mu\text{N}$ . The same level of load was applied for the measurements of the steel matrix close to the inclusion in the un-etched sample, with a scanning area of  $10 \times 10 \mu\text{m}$  and 6  $\mu\text{m}$  distance between the centres of adjacent indents. The results are presented in the final paragraph of this section together with those from the etched sample, in order to provide a comparison. For the etched sample, the hardness measurement was carried out across an inclusion and a WEA (butterfly wing), to show the variation across these features and the interface with the steel matrix.

The measurement applied to both the inclusion and the WEA of the butterfly in Figure 5.1.3 (c) which is 63  $\mu\text{m}$  from the surface. The pattern of indents used was a line of 20 with a single cycle of loading-unloading for each indent, as discussed in Section 3.3.2. A spacing of 0.5  $\mu\text{m}$  between indents and load of 800  $\mu\text{N}$  were used in the measurements. These values of load and spacing were decided after testing the indent size required to ensure sufficient spacing between indents and with a sufficient number of indents across the width of the inclusion and WEA. The arrays of indents across the inclusion and the WEA are shown in the AFM images in Figure 5.1.8 where the indents are the dark triangles above or below the numbers. It can be seen that not all the indents had the same size, specifically in the steel matrix and the WEA. Generally, the reason for this was the small size of the Nano-indents, due to the relatively small load, which makes the measurements very local and very susceptible to the different phases of material. Accordingly, some of the variation in the measurements was related to the multi-phase of steel on the Nano scale which is also true for the WEA [62].



**Figure 5.1.8: Nano-indentations across (a) MnS inclusion and (b) WEA for the butterfly in Figure 5.1.3 (c)**

The curves in Figure 5.1.9 and 5.1.10 show the variation of hardness  $H$  and modulus of elasticity  $E$  across the inclusion, and the WEA with the indents numbers refer to those in Figure 5.1.8. The results from the first indent in the WEA-steel matrix curves, and the third and the fifteenth in the inclusion-steel matrix curves were excluded and deleted because they were clear outliers according to Dawn Bussey (the expert technician responsible for the Nano-indentation at the Material Department) and this happens when the indenter slips over asperity instead of indenting. The high values of  $E$  and  $H$  for indent No. three and six in the WEA-steel matrix curves could be due to indent on a hard particle of carbide. In Figures 5.1.9 and 5.1.10, the variation is clear across the WEA and the steel matrix, however, the higher hardness of the WEA was revealed. Despite the variation, indents number 9 and 13 show potential drop in the hardness of the WEA which can indicate the weak interface between the WEA and the steel matrix which could justify the observed butterfly micro-cracks at the side edges of the WEA. Also, the WEA was normally observed at one side of the WECs. As shown in Figure 5.1.8, seven indents, number 8 to number 14, could be considered within the WEA and six indents, number 8 to number 13, could be considered within the inclusions.

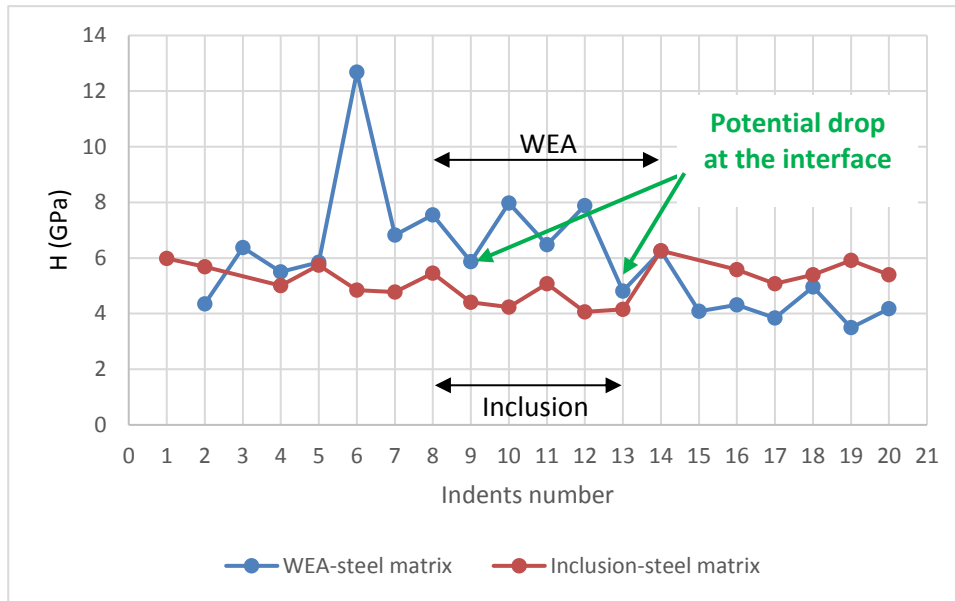


**Figure 5.1.9: Nano indentation hardness measured across a MnS inclusion and WEA in a butterfly**

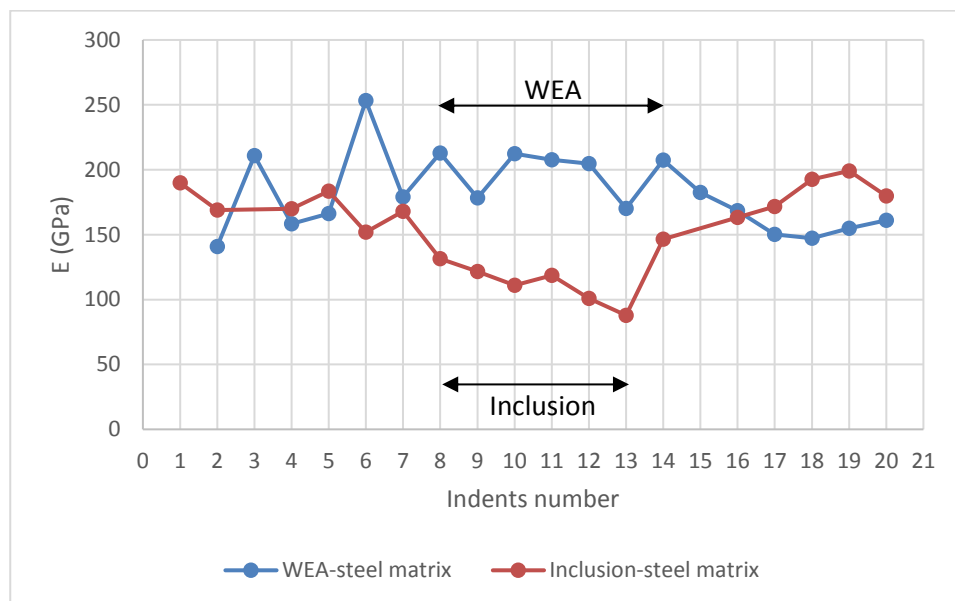


**Figure 5.1.10: Modulus of elasticity measured across a MnS inclusion and WEA in a butterfly**

To discuss the accuracy of the measurements, the mean values and standard deviations for the results from the etched and un-etched samples are shown in Figures 5.1.11 and 5.1.12. For the etched sample, H and E are calculated from the indents within the inclusion and the WEA, and the steel matrix attached to each of them with the exception of indents number three and six in the WEA-steel matrix measurements. It was observed that the average values of H and E for the steel matrix attached to the inclusion and the WEA were less than that measured from the un-etched sample. The reason for this could be due to

the distance between indents. Since the first indent should not be affected by adjacent indents this value could be used to investigate the effect of the distance between indents on the lower values of H and E in the etched sample. The H and E values for the first indent in the inclusion- steel matrix curve of Figures 5.1.9 and 5.1.10 are not significantly different from those in the steel matrix. This confirms that there was no effect for the distance between indents on the measured values of E and H in the etched sample. Accordingly, the deviation between the measurement of H and E for the steel matrix in the un-etched and the etched sample could be due to either to the etching, or the effect of the butterfly on the steel matrix. It is more likely to be the effect of etching, at least for the inclusion, since the measured hardness for the MnS inclusion from the un-etched sample is very close to that reported in the literature. Referring to Table 2.1.2 and the difference between the measured value and that in the literature, this could be due to the measurement method used and the different load applied. For the WEA hardness, a wide range of values were reported in the literature, such as 1000 HV [11] and 1200 HV [18]. The measured value in this research however, was less than these values, which confirms the effect of etching. According to the values reported in the literature, the ratio of WEA hardness to the bearing steel hardness is around 1.3 to 1.6. Despite the effect of etching, the relative hardness of WEA to the steel matrix, which was found to be 1.41 in this study, is still within the range reported in the literature. To the author's knowledge, no E value for the WEA has been reported in the literature; therefore, no comparisons could be made with that found in this research.

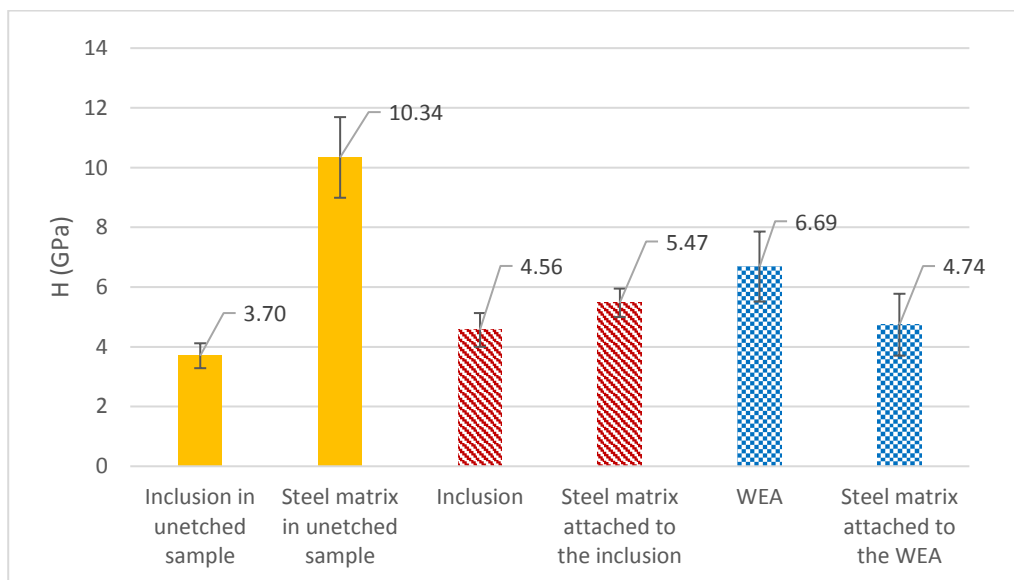


**Figure 5.1.11: The average value and standard deviation of Nano-indentation hardness for a MnS inclusion, WEA and attached steel matrix in an etched sample and a MnS inclusion and attached steel matrix in un-etched sample**

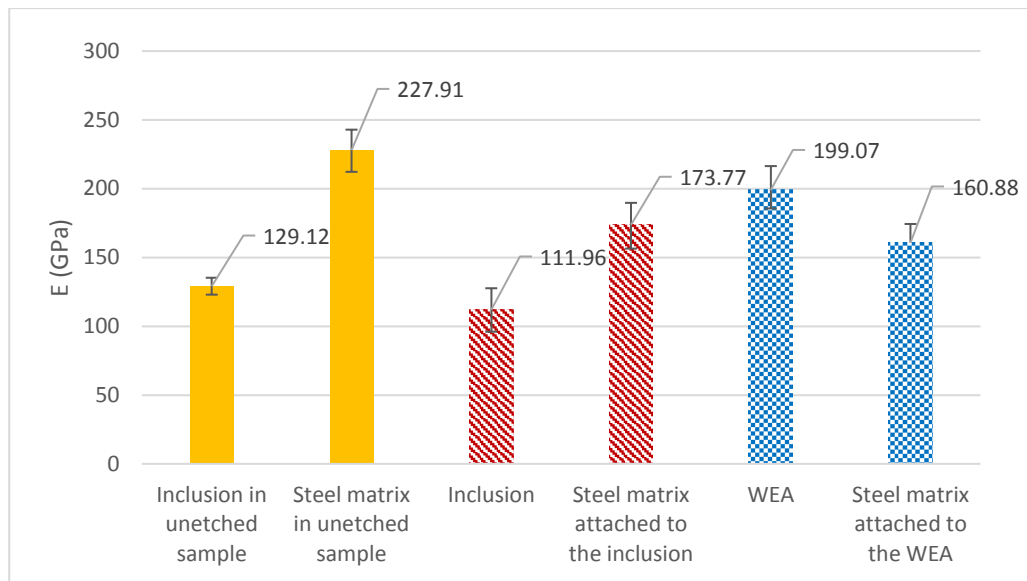


**Figure 5.1.12: The average value and standard deviation of modulus of elasticity for a MnS inclusion, WEA and attached steel matrix in an etched sample and a MnS inclusion and attached steel matrix in un-etched sample**

## 5.2 Statistical Analysis of Subsurface Damage

The inclusions observed consist of the inclusions that initiated damage and inclusions that did not initiate damage and these are catalogued according to the definitions given in Table 3.4.1. The selection of inclusions that did not initiate damage was not according to their size or depth but they were selected from locations close to the inclusions that initiated damage. Categorization of these inclusions were performed to characterise the subsurface damage that was initiated from inclusions in the examined bearing, and to identify the effects of this damage. In total 153 inclusions in the axial and circumferential sections were recorded, however some of them showed more than one type of damage, and were therefore classified in more than one damage category. The total number of catalogued inclusions, that initiated one or more types of damage and that did not initiate damage, was therefore 208. Figure 5.2.1 shows the number of each type of catalogued inclusion as a percentage of the total of 208. Although debonded inclusions were not the largest group among the inclusions that initiated damage, it was observed that all the types of subsurface damage were related to debonded inclusions more than other types of damages. As shown in Figure 5.2.1 (a), it was found that almost 60% of the inclusions exhibited debonding from the steel matrix and one or more of the other three types of subsurface initiated damage, namely cracked inclusions, inclusion initiated micro-cracks and butterflies. The percentage of the debonded inclusions in each of the other groups of inclusions is shown in Figure 5.2.1 (b). For the inclusions initiated micro-cracks, 52% of them were debonded inclusions. For the butterflies, 80% of the inclusions were debonded. Moreover, almost all the cracked inclusions were debonded inclusions. For the cracked inclusions in other groups of inclusions, they were 21% in the group of inclusion initiated micro crack and 50% in the

group of the butterflies. These statistics highlights the role of inclusion debonding in subsurface damage initiation.

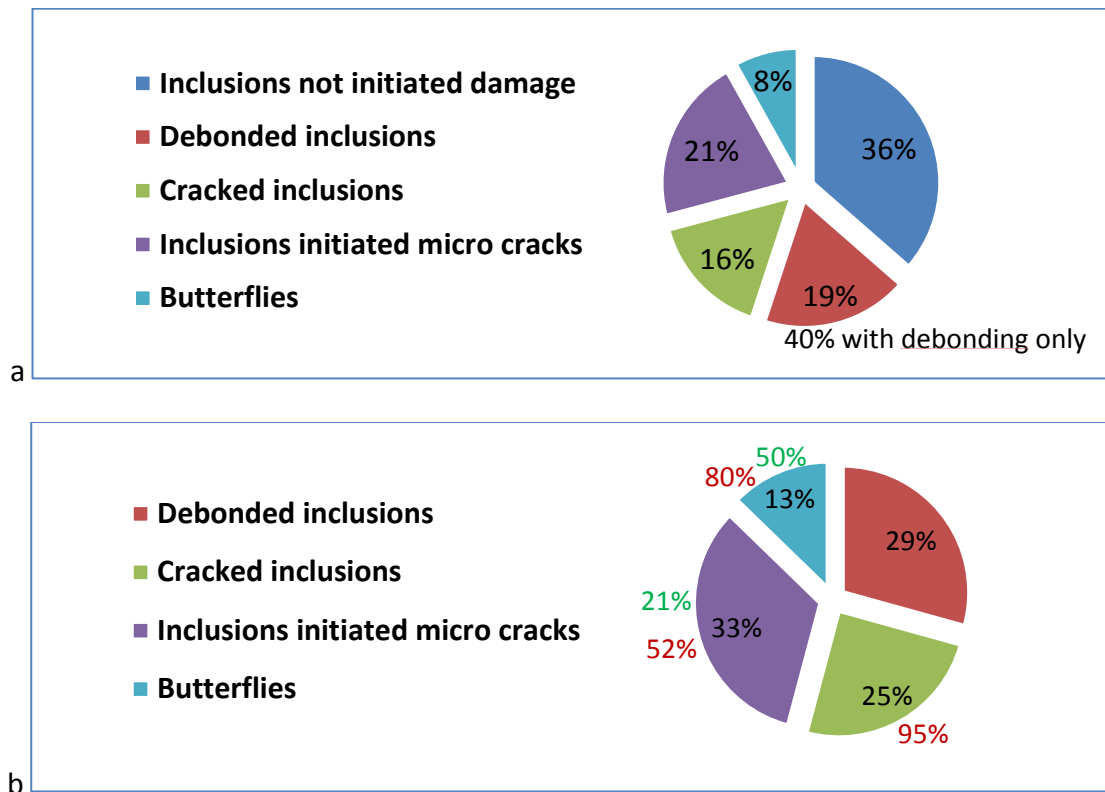


**Figure 5.2.1: Percentage of catalogued inclusions (a) out of the total catalogued inclusions (b) out of the inclusions that initiated damage only with the red and green percentage refer to the debonded and cracked inclusions respectively**

The characteristics of each catalogued inclusion include: length, width, inclination angle and depth from the surface. The measurements were made according to the definition given in Figure 3.4.4. The results for the inclusions observed in the axial and circumferential sections are shown in Figure 5.2.2. It can be seen from Figure 5.2.2 (a) that the depth of inclusions that did not initiate damage is very close to that of the inclusions that initiated damage. This makes the comparison between the two groups valid, since the characteristics of inclusions may vary with depth. The first observation was that inclusions that initiated damage are bigger in size, length and width, than the inclusions that did not initiate damage. The difference between the inclusion angles in the axial and circumferential sections was very clear in both groups. Although the difference between the angles of these two inclusion groups is not significant, inclusions that initiated damage show consistently shallower angles in the axial and circumferential sections.

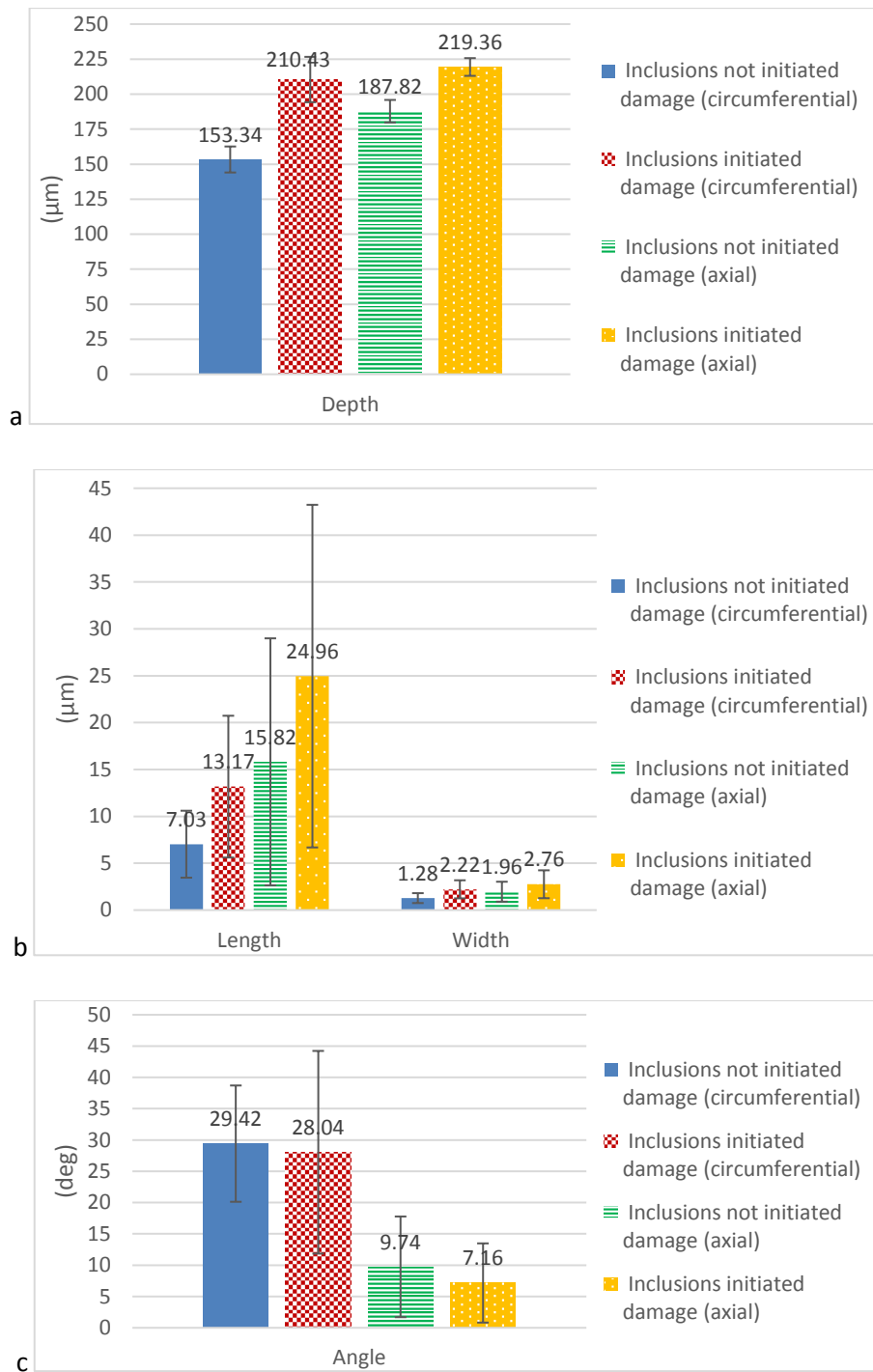


**Figure 5.2.2: Characteristics of catalogued inclusions (average values with the error bars show  $\pm$  one standard deviation)**

In Figure 5.2.3 and Figure 5.2.4, the characteristics of micro-cracks initiated by inclusion and butterflies are presented separately in order to investigate the characteristics of the inclusions that initiated them. These figures show the mean values and standard deviations for length, width and angle of inclusions initiated micro-cracks into the matrix and those inclusions initiated butterflies.

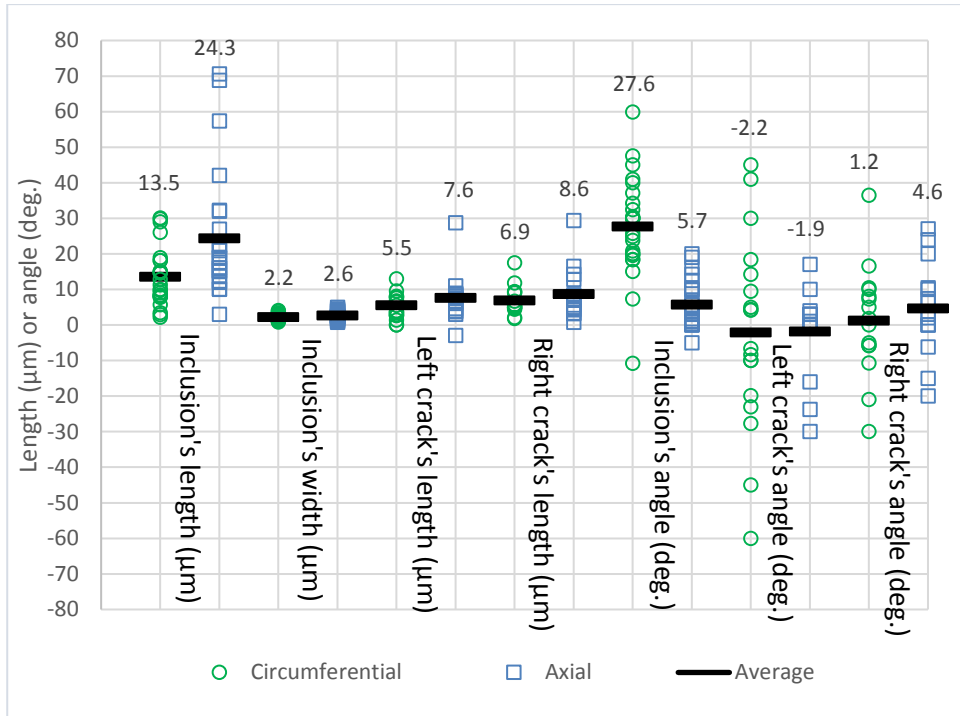


Figure 5.2.3: Characteristics of micro-cracks initiated by inclusions with their initiating inclusions (the number above each characteristic refers to the average value)

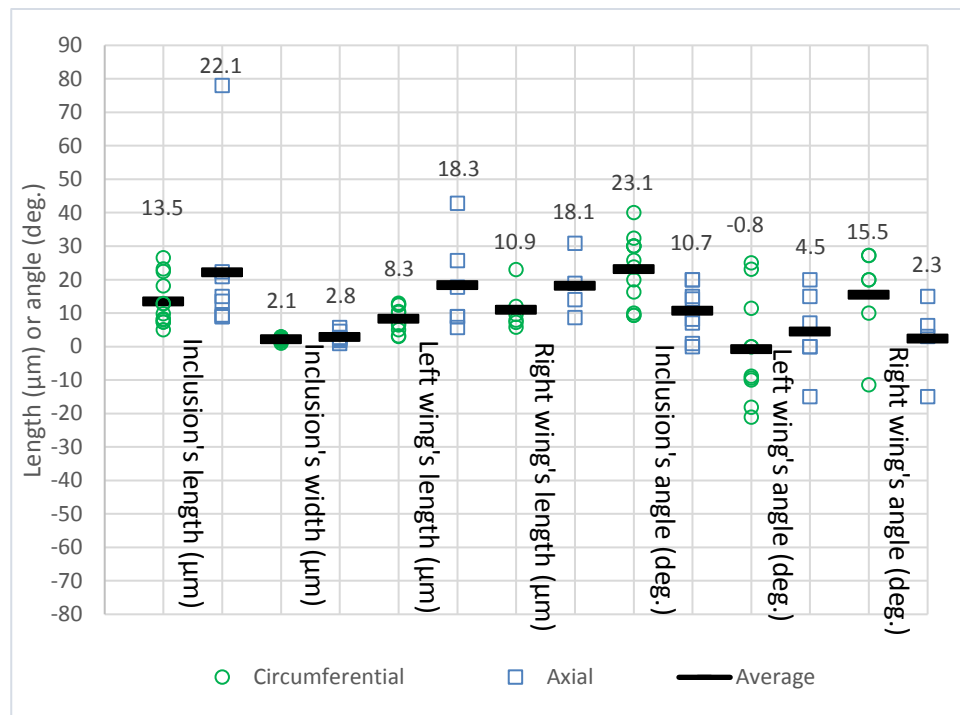


Figure 5.2.4: Characteristics of butterflies' wings with their initiating inclusions (the number above each characteristic refers to the average value)

The average values of the length and width of these inclusions were close to the overall average length and width of inclusions that initiated damage in Figure 5.2.2 (b), but those inclusions formed butterflies in the axial sections were slightly shorter. If the average angle of inclusion initiated micro-cracks in Figure 5.2.3 is compared with that in Figure 5.2.2 (c), the average inclusion angle is in line in the circumferential sections, but has a lower value in the axial sections. On the other hand, the inclusion that initiated butterflies were inclined with a lower angle in the circumferential sections and a greater angle in the axial sections, comparing Figures 5.2.4 and 5.2.2 (c). The left and right cracks in Figure 5.2.3 follow the definitions of right and left wings in Figure 3.4.4. The common observations from the length of micro-cracks and butterfly wings initiated from inclusions are: a) They are longer in the axial sections than that in the circumferential sections. b) In the axial sections, their length on both right and left sides are almost the same, while for the circumferential sections the length of micro-cracks is slightly longer on the right hand side than on the left hand side.

One of the main differences is that the butterfly wings are longer than micro-cracks in both of the circumferential and axial sections. The most recognisable feature regarding the angles of the micro-cracks and butterfly wings, presented in Figures 5.2.3 and 5.2.4, is the positive and greater angle of the butterfly wings on the right hand side in the circumferential sections compared with micro-cracks on the same side and circumferential section, with the angle direction varying through a range of positive and negative values. The small average angles of the micro-cracks in axial and circumferential sections are due to the fact that the angle values vary between positive and negative values at almost the same absolute value. However, the range of angles for the micro-cracks and butterfly wings is lower than  $45^\circ$  and this is the angle for  $\tau_{1(max)}$  at the point  $x=0$  due to normal loading. The angle and depth of  $\tau_{1(max)}$  can be changed due to the effects of surface traction, which could be the reason for the observations of the angles for the butterflies and the cracks in Figures 5.2.3 and 5.2.4. The effects of inclusion depth and the relationships with the load on the surface will be discussed further in Section 5.3.

No clear relationship could be found between the size of the inclusions and the length of butterfly wings or micro-cracks initiated from inclusions in circumferential sections. However, it was found that the total length of the inclusions and their associated cracks or butterfly wings showed a clear and direct relationship with inclusion length regardless of their depth as shown in Figure 5.2.5, where the length of butterfly wings and micro-cracks on both the left and right side of the inclusions were measured. Accordingly, if the inclusion was considered a weakening point of similar effect as a subsurface micro-crack, the trend lines shown in Figure 5.2.5 demonstrated that greater damage was created from bigger inclusions. The results in Figure 5.2.5, and specifically (a) and (b), are in agreement with the expectation stated in the cleanliness standards such as ASTM E2283 [80] that the biggest inclusion is the most important on damage initiation. In the same context, Murakami derived relationships to describe the effect of inclusion size ( $\sqrt{Area}$ ), on the fatigue limit of bearing steel, based on the assumption that a non-metallic inclusion acts like the initial

crack length [76]. Although the number of butterflies found is less than that of the micro-cracks propagated from inclusions, the trend lines for the butterflies in Figure 5.2.5 (c) and (d) are similar to that of the micro-cracks in Figure 5.2.5 (a) and (b). Accordingly, inclusion size affects butterflies and micro-cracks initiated from inclusions in the same way. Figure 5.2.5 also shows that no consistent relationships can be recognized from the depth of butterflies or micro-cracks and the size of the initiating inclusions.

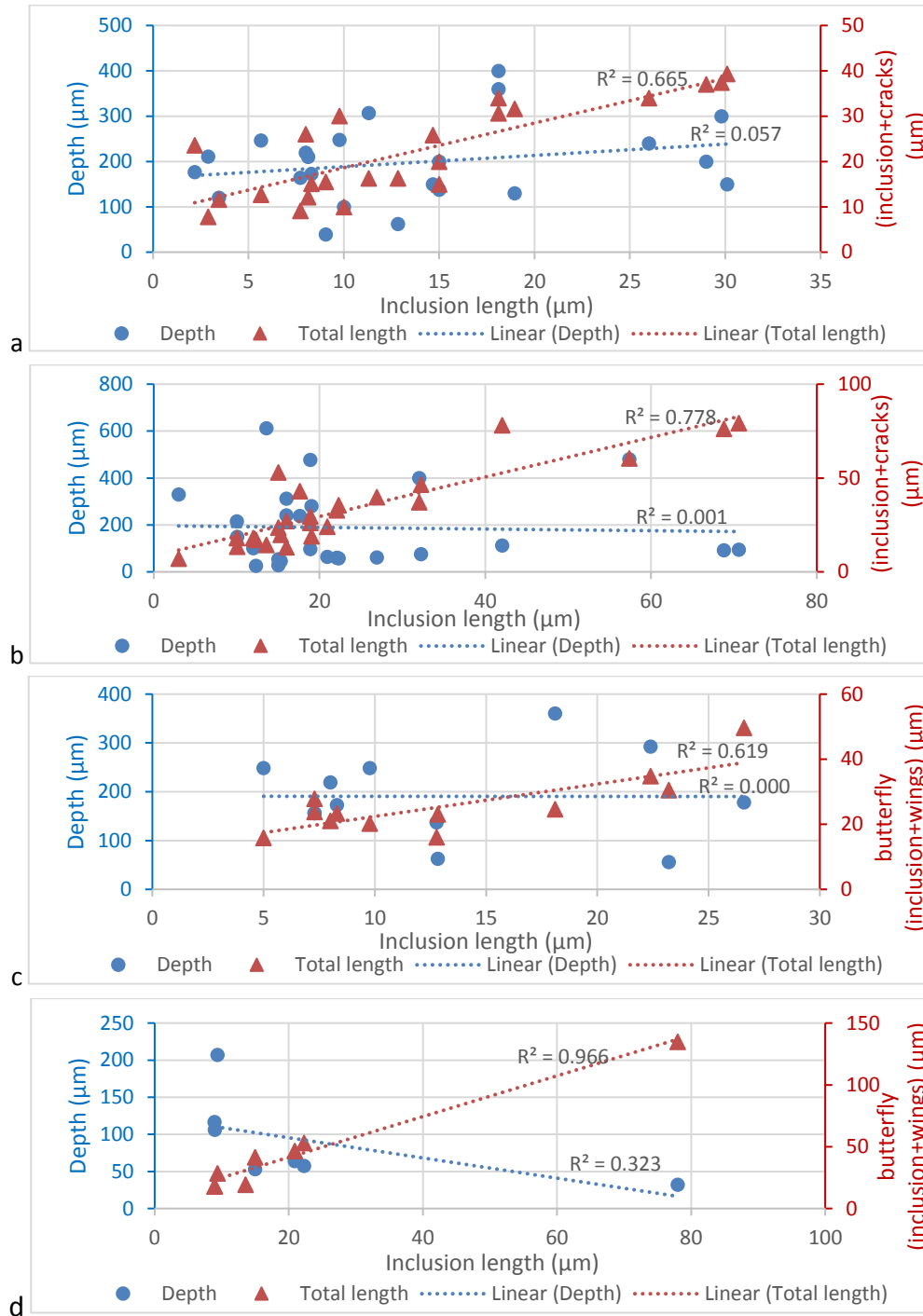


**Figure 5.2.5: Inclusion length vs total length with the depth of inclusions (a) cracks initiated from inclusion in circumferential sections (b) cracks initiated from inclusion in axial sections (c) butterflies in circumferential sections (d) butterflies in axial sections**

### 5.3 Discussion of Surface Traction Effect on Subsurface Initiated Damage

Despite the discussion and analysis of subsurface initiated damage based on the characterization of the initiating inclusions, the depth of inclusions may have a major role in the initiation of subsurface damage. This is because it is related to the subsurface stress distribution, which, along with the stress risers (inclusions and voids) could be determinate in the initiation of subsurface damage. In rolling contact, the Hertzian contact pressure is used to calculate subsurface shear stress distribution,  $\tau_1$  and its location is  $z=0.78b$  under normal load at  $x=0$  as discussed in section 2.4.4. This depth changes with the introduction of a traction force on the surface. In this section, the depth of subsurface damage – mainly considering inclusion initiated cracks and butterflies – is compared with the calculated distribution of  $\tau_1$  for the examined uncoated bearing.

The load history of the examined uncoated bearing is unknown. However, the recommended maximum contact pressure  $p_{max}$  for a wind turbine planetary bearing is 1500 MPa according to the standards BS EN 61400-4:2013 [85] or IEC 61400-4 [86] and this was assumed for the subsurface stress calculations. Since the bearing had failed prematurely, an even greater value for the  $p_{max}$  could be expected. Calculations were also made on the subsurface stress distribution at higher contact pressure up to 2100 MPa, which could be reached at transient loads, as discussed in Chapter 8. The calculations were carried out using the equations presented in Section 2.4.4. The depth of the maximum subsurface shear stress  $\tau_{1(max)}$  under  $p_{max}=1500$  MPa was found to be 370  $\mu\text{m}$ , which becomes deeper if under higher contact pressure. Figure 5.3.1 shows the depth of the micro-cracks initiated by inclusion and butterflies. The average depth for both of these types of damage in both axial and circumferential sections was closer to the surface than the depth of the calculated  $\tau_{1(max)}$ . However, there was a wide deviation from the mean value of the depth of inclusion initiated micro-cracks. Therefore, Figure 5.3.2 was created to show the percentage, frequency, of micro-cracks observed at each bin size of 50  $\mu\text{m}$  of depth in this histogram. This figure shows that the occurrence of inclusion initiated micro-cracks at a range of dominant depths, which is closer to the surface than the depth of  $\tau_{1(max)}$  at various levels of contact pressure of 1500, 1700, 1800 and 2100 MPa. It is known that the location of the shear stress will be shifted towards the surface when surface traction occurs. If the maximum shear stress is considered to be the trigger for subsurface damage, Figures 5.3.1 and 5.3.2 show the observed damage initiated from inclusions at shallower depths that may have been affected by the occurrence of high surface traction. This figure also shows how the butterflies are closer to the surface than micro-cracks initiated by inclusion which could further indicate that it is affected by surface traction. Figure 5.3.1 also shows a shallower depth for the micro cracks initiated by inclusions in the axial sections than that in the circumferential sections. This could be caused by the effect of the inclusions' inclination on the observation direction in the axial and circumferential sections. Section 8.1 presents curves of  $\tau_1$  under a range of COT at  $x=0$  and  $x=0.9b$  which provided information on the initiation of subsurface damage at the edge of the contact

width under high surface traction. Furthermore, the range of angles for micro-cracks and butterfly wings in Figures 5.2.3 and 5.2.4 was lower than  $45^\circ$ , which is the angle of  $\tau_{1(max)}$  caused by normal loading under the point where  $x=0$ . When there is traction force on the surface, the subsurface stress distribution is affected and the angle of  $\tau_{1(max)}$  is changed. It is reported before that the subsurface micro-cracks and butterfly inclined at  $45^\circ$  because it is caused by  $\tau_{1(max)}$  and follow its angle [18][116]. Accordingly, the range of angles for micro-cracks and butterfly wings in the examined bearing could be explained as an effect of the surface traction.

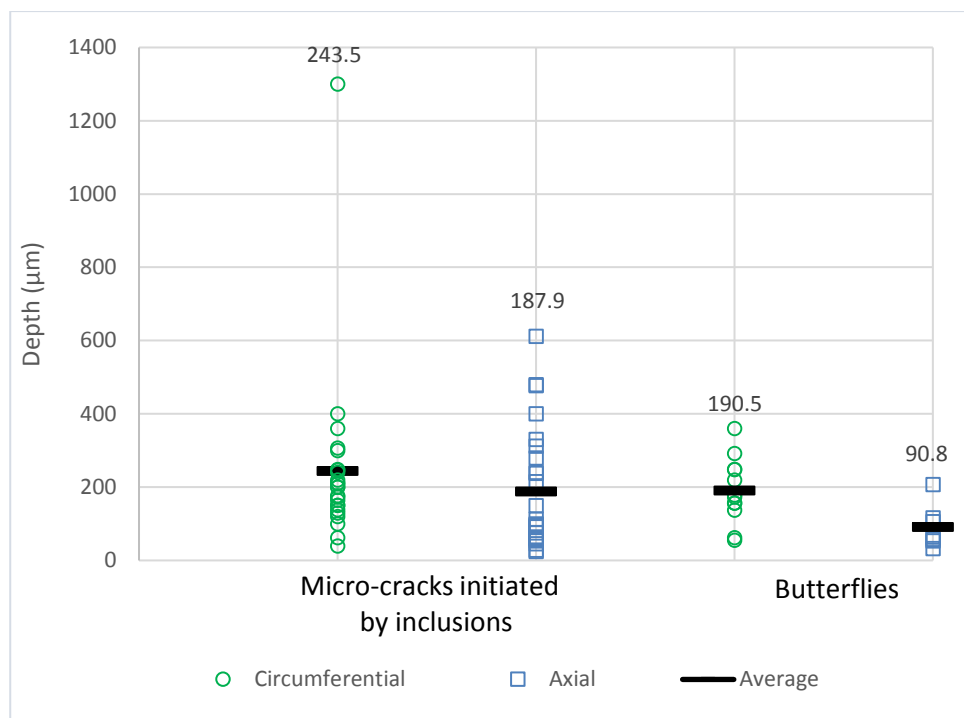


**Figure 5.3.1: Depth of inclusions initiating micro-cracks and butterflies in axial and circumferential sections (the number above each characteristic refers to the average value)**

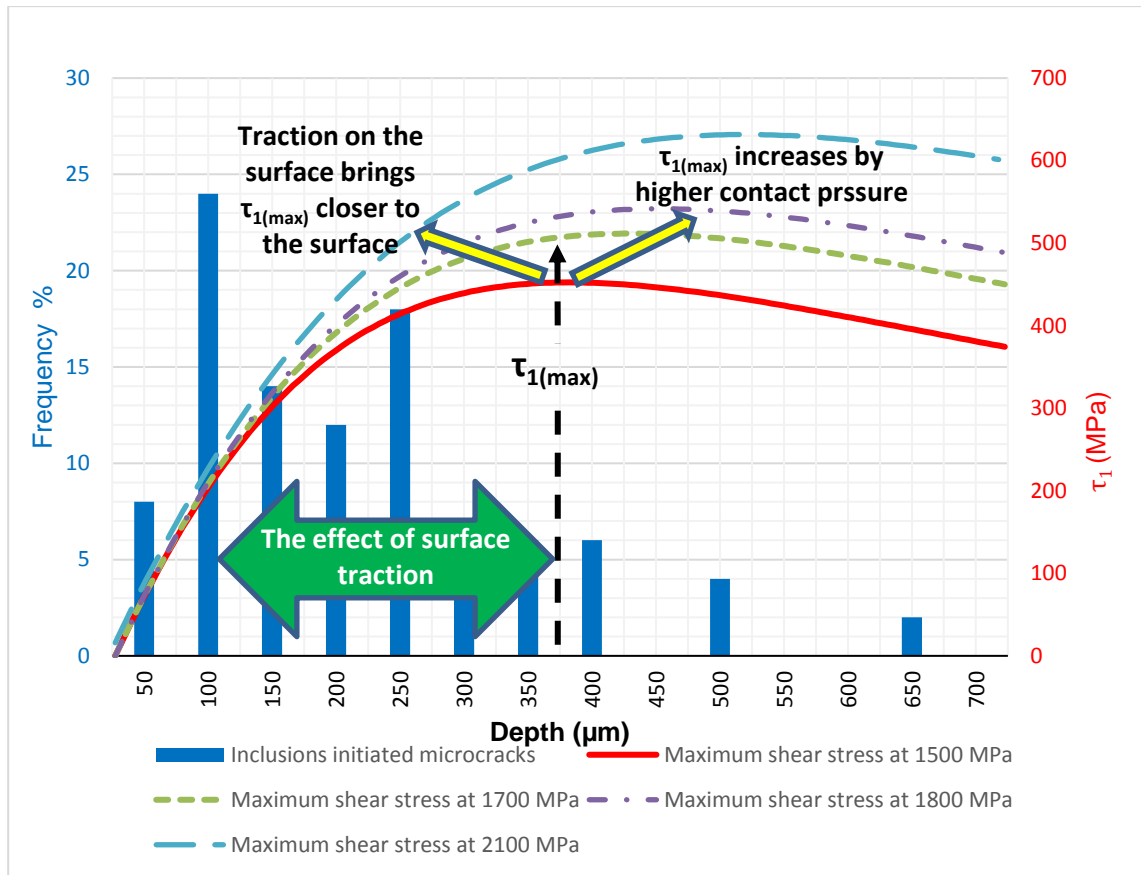


**Figure 5.3.2: Depth of micro-cracks in axial and circumferential sections compared with the depth of subsurface maximum shear stress  $\tau_{1(max)}$  at various levels of contact pressure**

Another investigation was conducted to determine the depth of the subsurface material that was most affected by the surface loading. The subsurface hardness variation was measured by the method described in Section 3.3.2. The variation in hardness could reflect hardening due to a higher load exceeding the yield limit, and this could also be an indication for the location of subsurface initiated damage. Measurements of this were carried out on a sample from the transfer region between the loaded and unloaded zones of the uncoated bearing, as shown in Figure 3.1.3. The average values and the standard deviation from three measurements at each depth are shown in Figure 5.3.3. In this figure, the loaded zone is under the raceway surface showing damage, and the unloaded zone is under the raceway surface that does not show damage, but is at the entrance to the loaded zone. Although both curves showed high hardness closer to the surface, the hardness for the loaded zone is higher at this depth close to the surface. If there was no surface traction the maximum hardness would be expected to be located around the depth of  $\tau_{1(max)}$  which is 370  $\mu\text{m}$  at 1500 MPa. Accordingly, this measurement could be another indication for the occurrence of surface traction because the maximum hardness measured is at the range of less than 200  $\mu\text{m}$ . Figure 5.3.3 also shows softening of the bearing steel below a depth of 400  $\mu\text{m}$ .

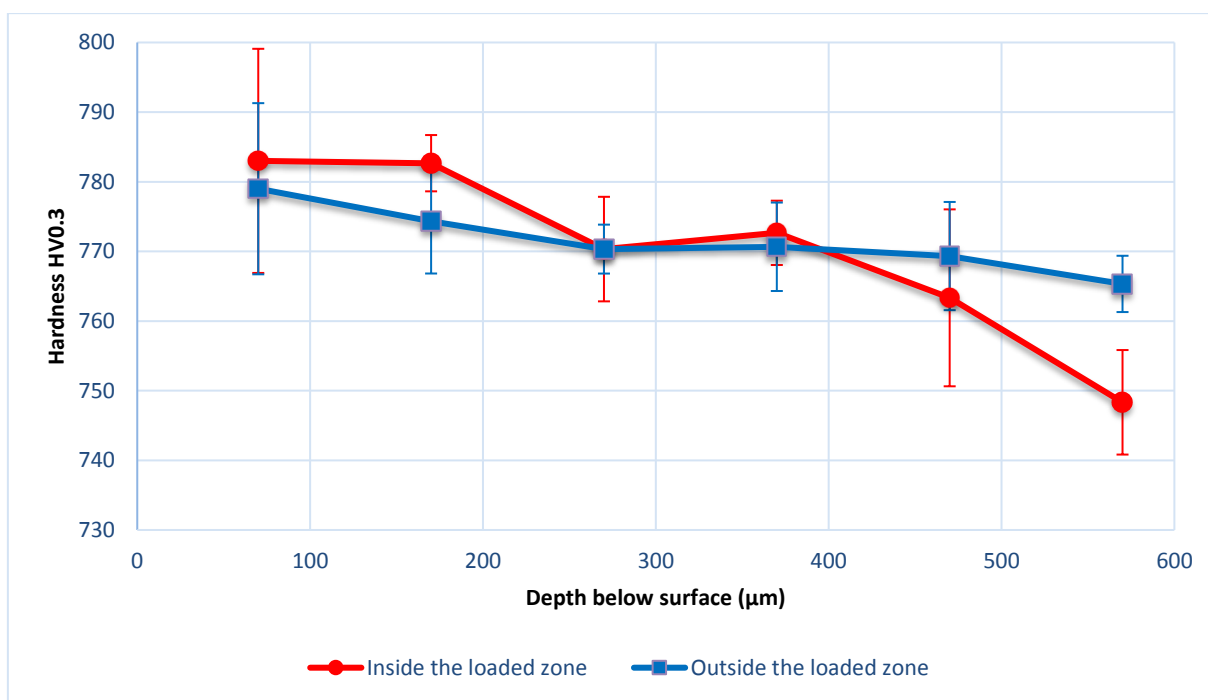


Figure 5.3.3: Hardness variation with depth below the surface for the uncoated bearing

## 5.4 Summary

The focus of this chapter was on identifying and analysing the inclusions that initiated damage. The types of these inclusions include debonded inclusions, cracked inclusions, inclusion initiated micro-cracks, and Butterfly inclusions. The number of examined inclusions was 153 with some of them classified as more than one damage category. Accordingly, the total number of catalogued inclusions analysed is 208 including inclusions that initiated damage and that did not initiate damage. The following is a summary of the results and analysis.

1. Inclusions that initiated damage show greater length and width, and have a slightly shallower angle than that of inclusions that did not initiate damage.
2. Debonding or gaps separate the WEAs from inclusion tips are observed in most of the butterflies found. Almost 60% of the debonded inclusions had cracks, initiated micro-cracks or formed butterflies. 52% of the inclusions that initiated micro-cracks were also debonded and 80% of the inclusions that formed butterflies were also debonded. Furthermore, almost all the cracked inclusions were also debonded. For the cracked inclusions, 21% initiated micro-cracks and 50% resulted in butterflies. These statistics highlights the importance of inclusion debonding in subsurface damage initiation.
3. The WEA was found to be not as dense as the steel matrix according to the AFM scanning and looks like a damaged material. The Nano-indentation results showed lower E and H for the interface between the WEA and steel matrix and this could imply the propagation of most of the observed micro-cracks initiating along the

interface. Butterfly wings were found to be longer and inclined with a higher angle than micro-cracks initiated by inclusions. Butterfly wings and micro-cracks were longer in the axial direction.

4. It was found that the sequence of subsurface initiated damage is not always inclusion internal cracking first then followed by micro-cracks into the steel matrix, then WEA formation as suggested in the literature, since some of the micro-cracks initiated from non-cracked inclusions. Inclusions cracking starts from the interface with the steel matrix, and not all these cracks propagate into the steel matrix.
5. It is concluded that there are different initiation and propagation mechanisms exist for the subsurface initiated cracks, since one of the observations in this study showed a long crack linked to two butterflies, which changed its direction after a certain length to be almost vertical toward the surface.
6. Comparing the depth and inclination angle of the butterflies and the micro-cracks initiated from inclusions with the depth and angle of  $\tau_{1(max)}$  calculated for the examined bearing under a range of contact pressure revealed that high surface traction may have occurred. This conclusion also supported by the measurement of subsurface hardness and the location of maximum hardness comparing to the depth of  $\tau_{1(max)}$ .
7. It was found that total length of an inclusion and the micro-cracks on one or both sides was related directly to the size of inclusion. The same trend was found for the total size of inclusion and butterfly wings. Accordingly, if inclusions, micro-cracks and butterfly wings are assumed to cause the same damaging effect, a bigger inclusion is more detrimental to the lifetime of the bearings.

## 6 Results and Discussion of Investigation of Black Oxide Coated Bearing

The metallurgical examination of this bearing was carried out according to the sectioning and sample preparation methods given in Chapter 3. The observed damage was classified and compared to those from the uncoated bearing to develop a better understanding of premature failure in the bearings using BO-coating. The subsurface damage observed from the metallurgical examination of the BO-coated bearing are butterflies, WECs, subsurface cracks and surface-linked RCF cracks, which are defined in Section 3.4.1.

### 6.1 BO bearing steel cleanliness

The role of the subsurface damage initiators, non-metallic inclusions, was investigated by first examining the cleanliness of the steel. According to the standard ISO-4967 [79], as discussed in Sections 2.1.5 and 3.4.2, five fields were chosen from sections in the axial direction where a bigger length of inclusions was found. This small number of fields was found to be representative of the general cleanliness observed in this bearing. These fields represent the worst cleanliness for each type of inclusion, as shown in Table 6.1.1. The last row in this table is the required cleanliness for through hardened bearing steel, according to ISO 683-17 [82]. By comparison with the cleanliness of worst fields found in this bearing, it is shown that this bearing steel is not clean enough for inclusions Type D, while the cleanliness of all other types, such as Type A, is sufficient according to ISO 683-17. In addition to this cleanliness analysis, the EDX analysis was conducted on a number of inclusions which developed butterfly wing(s). The EDX analysis confirmed the high content of inclusion Type D. As discussed in the following sections in this chapter, not only Type D inclusions were found to initiate subsurface damage but also Type A and combined inclusions that show the chemical compositions of more than one type of inclusion. Although no similar cleanliness analysis was conducted for the uncoated bearing, the general observation showed that inclusion Type A was dominant, which was also confirmed to initiate subsurface damage, as discussed in Chapter 5. Hence, despite the BO coating, which is designed to extend bearing life, the subsurface damage initiators (non-metallic inclusions) still caused a deterioration of the WT bearing's lifespan.

**Table 6.1.1: Cleanliness of BO coated bearing for axial sections (F= Fine and T= Thick)**

Fields	Type of non-metallic inclusions								
	A		B		C		D		Ds
	F	T	F	T	F	T	F	T	
	<b>Total length (<math>\mu\text{m}</math>) (and count number for Type D)</b>								
1	39.746	19.235					10		
2	8.275	63.71					32		
3			84.34				12		
4							18	3	
5	45.962				61.749		29	1	
	<b>Index</b>								
1	0.5	0.5					1.5		
2	0.5	0.5					2.5		
3			1				1.5		
4							2.0	0.5	
5	0.5				0.5		2.5	0.5	
Average cleanliness	<b>0.3</b>	<b>0.2</b>	<b>0.2</b>		<b>0.1</b>		<b>2.0</b>	<b>0.2</b>	
Worst cleanliness	<b>0.5</b>	<b>0.5</b>	<b>1</b>		<b>0.5</b>		<b>2.5</b>	<b>0.5</b>	
Required cleanliness [82]	<b>2.5</b>	<b>1.5</b>	<b>2</b>	<b>1</b>	<b>0.5</b>	<b>0.5</b>	<b>1</b>	<b>1</b>	<b>2</b>

## 6.2 Butterflies

In this bearing, the inclusions associated with butterflies were mostly Type D, at 65%, with inclusion cracking being more difficult to identify than the cracking of the dominant MnS inclusions as observed in the uncoated bearing. As a result, a similar analysis of the inclusions initiated damage was not feasible. The total number of butterflies observed in the circumferential and axial directions was 28 with single and double wings. The characteristics for these butterflies and their inclusions are shown in Figure 6.2.1 and 6.2.2, using the same definitions as that given in Figure 3.4.4.

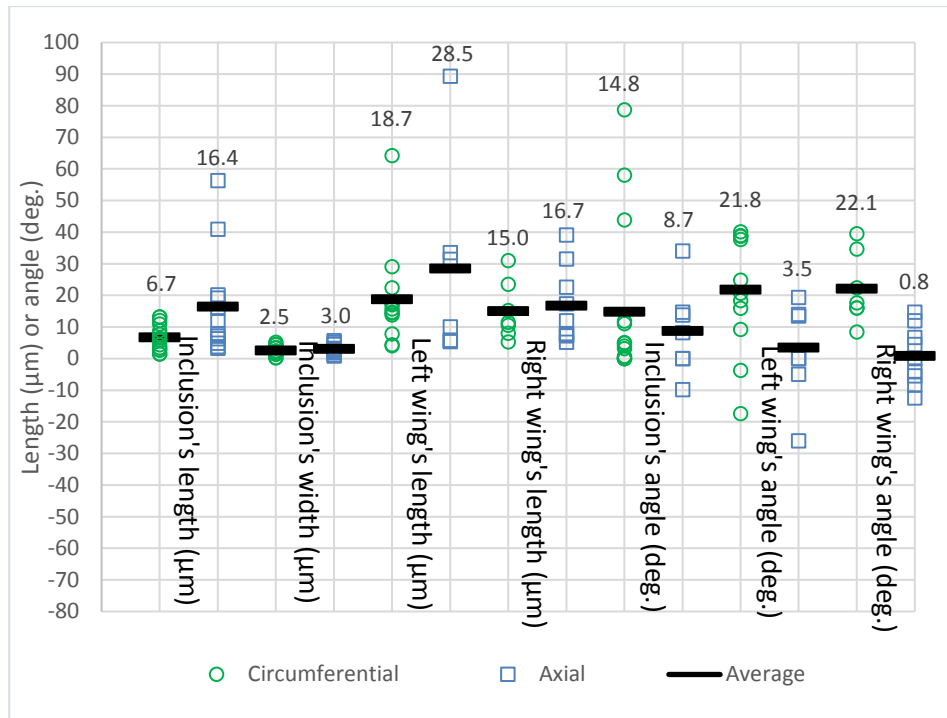


Figure 6.2.1: Characteristics for butterfly wings and their initiating inclusions (the number above each characteristic refers to the average value)

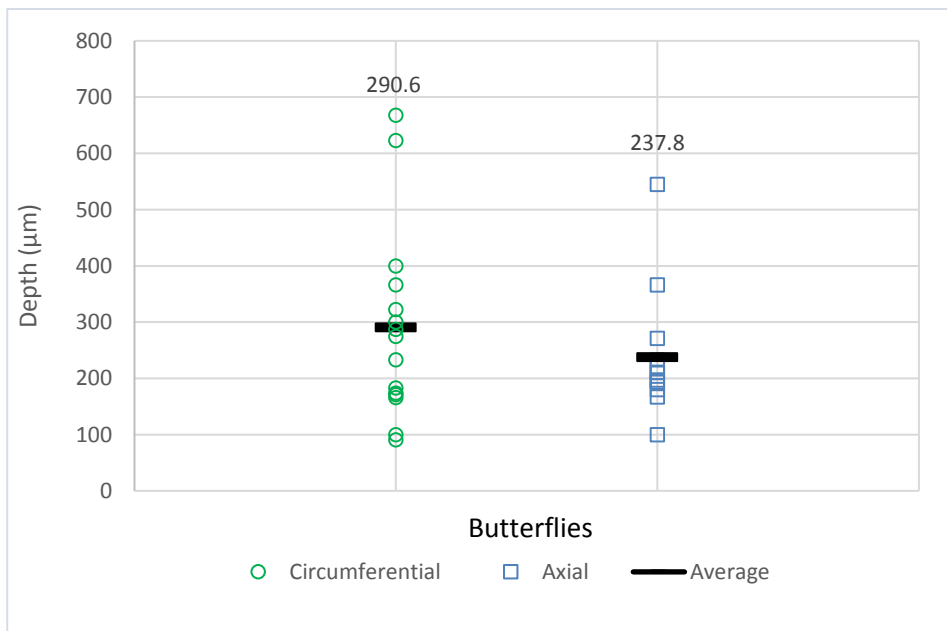
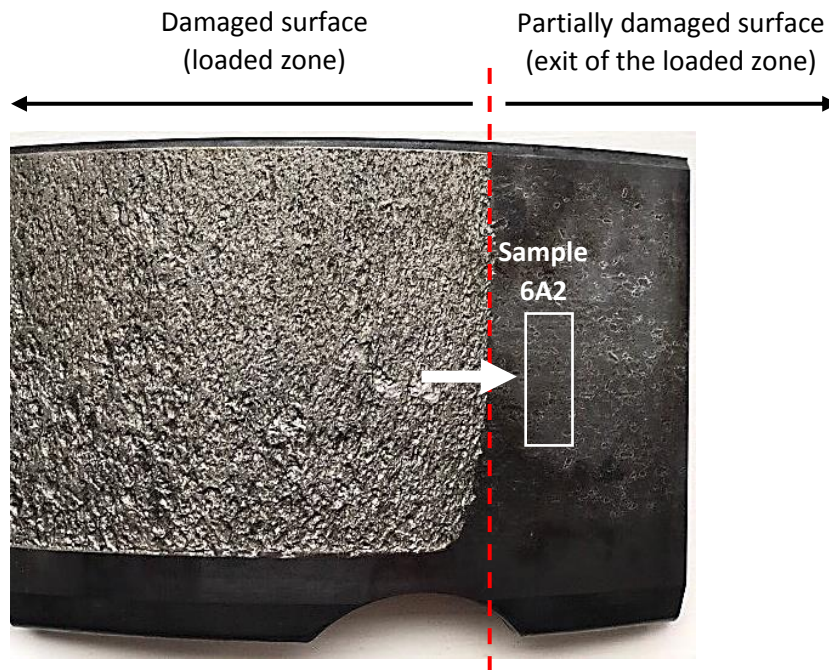


Figure 6.2.2: Depth of butterflies (the number above each characteristic refers to the average value)

Similar to the uncoated bearing, the inclusions have their maximum length in the axial direction, which could be due to the extrusion process as the main part of forming the inner raceway and higher angle in circumferential direction, which could be the result of the rolling process during manufacturing. Also, the circumferential sections show butterflies

with longer left wings. The angle of less than  $45^\circ$  for the butterfly wings in the circumferential direction could be due to the acting direction of  $\tau_{1(max)}$  at the centre or the edge of the contact under high surface traction. In the axial sections, the average butterfly wing angle is much smaller than in the circumferential sections with higher standard deviation. It was also found that butterflies in axial sections were closer to the surface than those in circumferential sections. These characteristics are in line with the findings from the uncoated bearing in Chapter 5. However, in this bearing, the depth of the butterflies was higher than that for the uncoated bearing which could be due to the higher load in the multi-Megawatt WT. Another difference between the uncoated bearing and this bearing is the length of the inclusions initiated butterflies. It was found that these inclusions were smaller in the BO coated bearing which is due to the dominant globular Type D inclusions, which are generally smaller than the MnS inclusions, Type A, the dominant in the uncoated bearing.

One of the most interesting observations is the high number of butterflies observed in Sample 6A2, shown in Figure 6.2.3, and it is the left vertical sample in region 6 in Figure 3.2.2, which is at the exit from the loaded zone. This sample has subsurface deep micro-cracks propagated from inclusions without WEA (butterflies), as shown in Figure 6.2.4 (a). Images (b) to (f) in Figure 6.2.4 show all the butterflies observed in this sample with the butterfly in Image (e) is the longest among all other butterflies in the axial sections. In this sample, the layer of the black oxide coating was not completely removed but the surface showed a high number of big size indents (more than 3 mm maximum dimension). The indented surface can be recognized by the metallurgical examination as a concave surface without any cracks linked to it, which is not the case for another sample from inside the loaded zone.



**Figure 6.2.3: Sample 6A2 at exit to loaded zone with white arrow represents the observation direction**

The EDX analysis confirmed the chemical composition of Type D inclusions for most of the inclusions that developed butterflies. However, some of the inclusions showed either a debonding around the inclusion or a soft inclusion Type A adjacent to a hard inclusion Type D, as shown in Figure 6.2.5. This butterfly was the longest in the circumferential sections and the only one found to have this combination of inclusions. This butterfly was found in a sample taken from the edge of the raceway on the flange side, the lower horizontal sample in region 4 in Figure 3.2.2. To show the distribution of chemical elements among the inclusion, EDX mapping was conducted as shown in Figure 6.2.6. Most of the elements were commonly identified to form one of the four types of inclusions [68]. However, the Magnesium (Mg) was observed in some inclusions, as in Figure 6.2.6, which could form the inclusion of Mg-Al-O. This inclusion is found to affect the geometry and the nucleation of the carbide [144]. Thus, this inclusion contributes to the formation of the WEA, since this microstructure alteration is characterised by the dissolution of carbide.

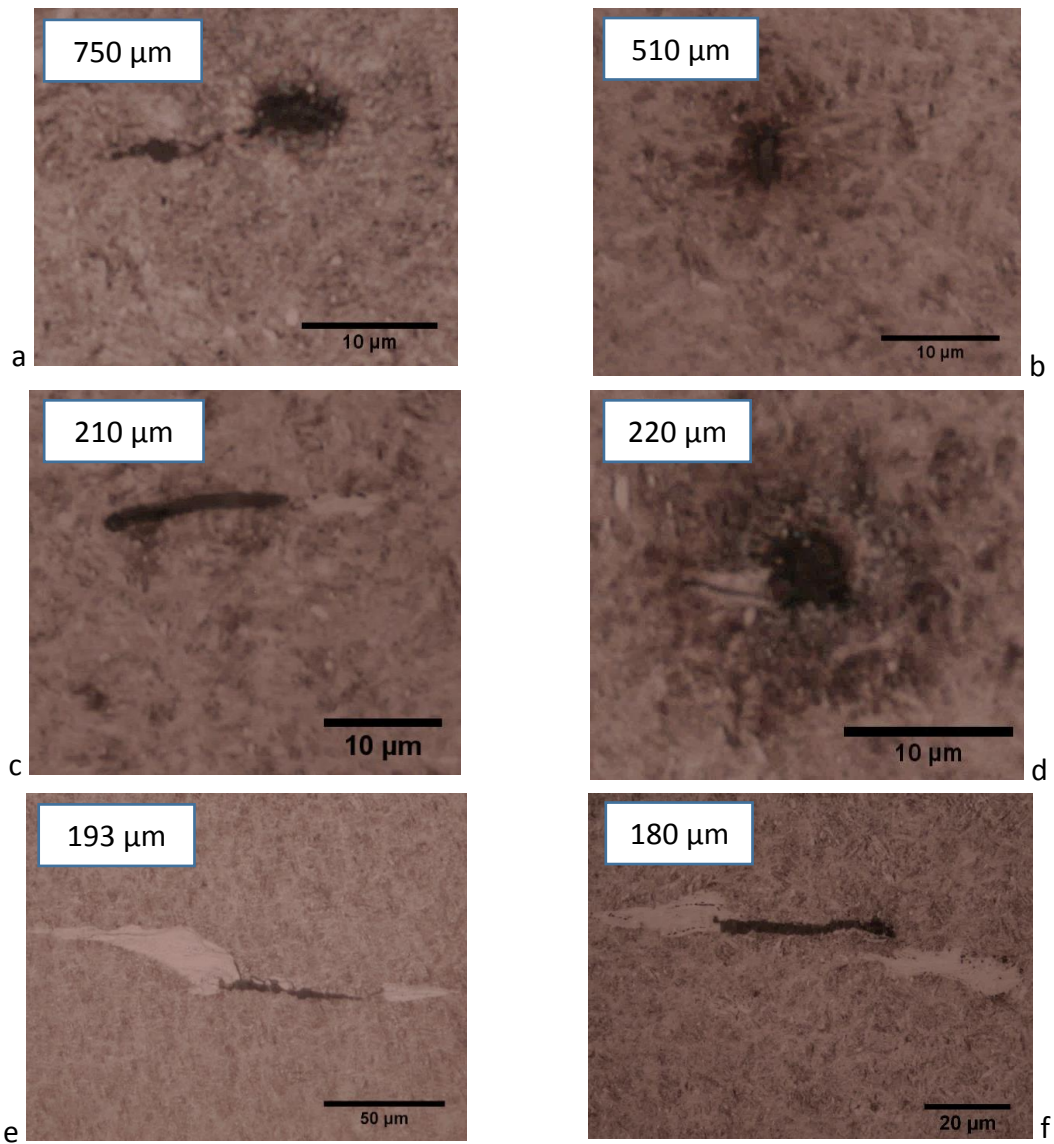
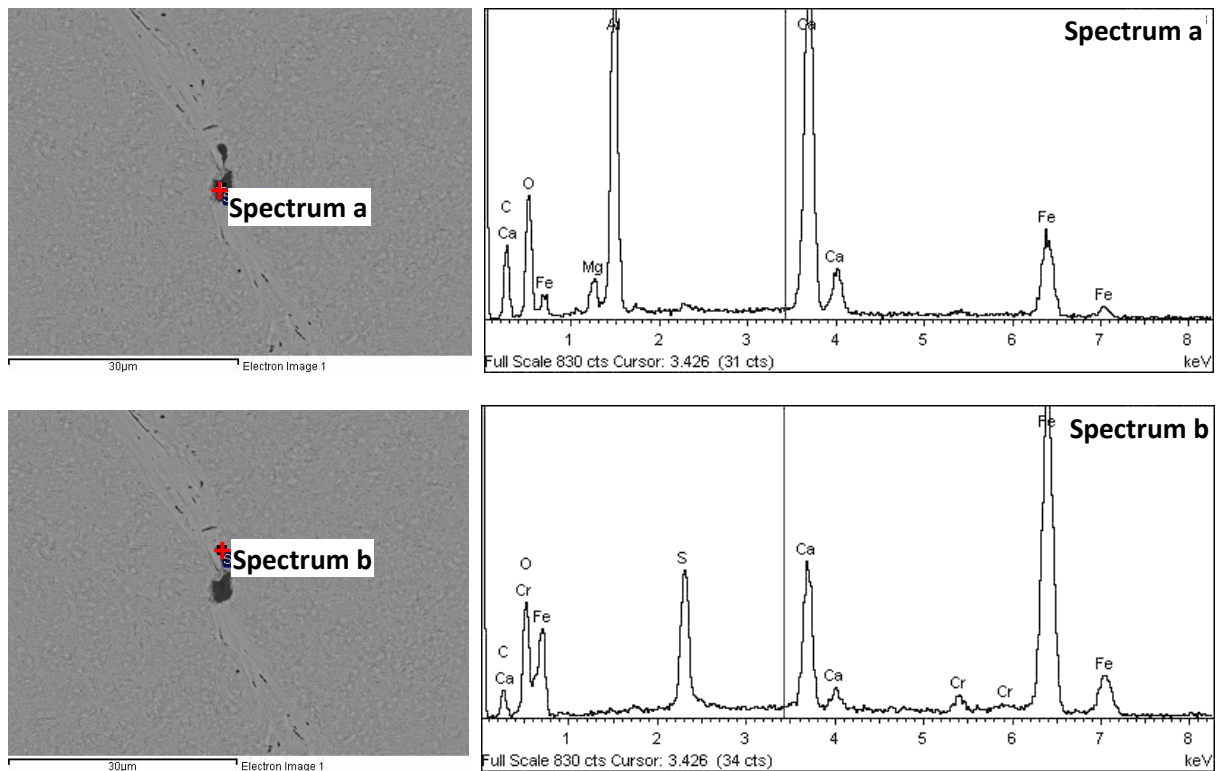


Figure 6.2.4: Observations from axial sample 6A2 (Depth is shown in the upper left corner)



**Figure 6.2.5: EDX analysis of the inclusion which initiated the longest butterfly in circumferential direction**

Figure 6.2.7 (a) shows a direct relationship between butterfly length (inclusion and butterfly wings) and inclusion length in axial sections which is similar trend to that observed for the uncoated bearing and as discussed in Section 5.2. However, in circumferential sections, the relation could not be confirmed, which may be because of the different inclusion types in this bearing that have various geometries compared to the dominant elongated Sulphide inclusions in the examined uncoated bearing. The depth of butterflies still did not show a correlation with the length of the initiating inclusions. Also, no confident conclusions could be made about the effect of depth on the total length of butterfly. However, it is clear that more butterflies formed in the first 300 µm depth close to the surface in both sectioning directions.

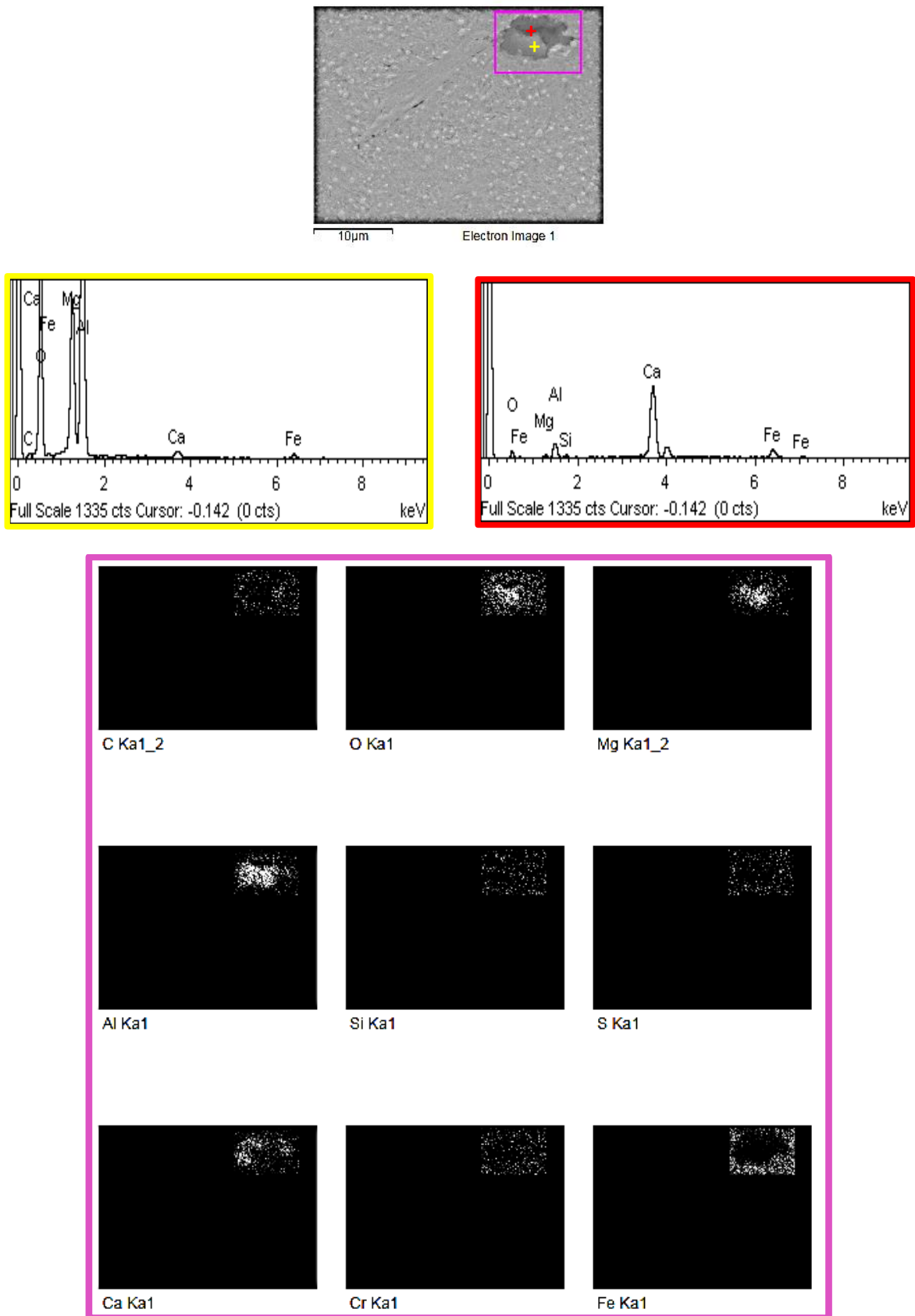
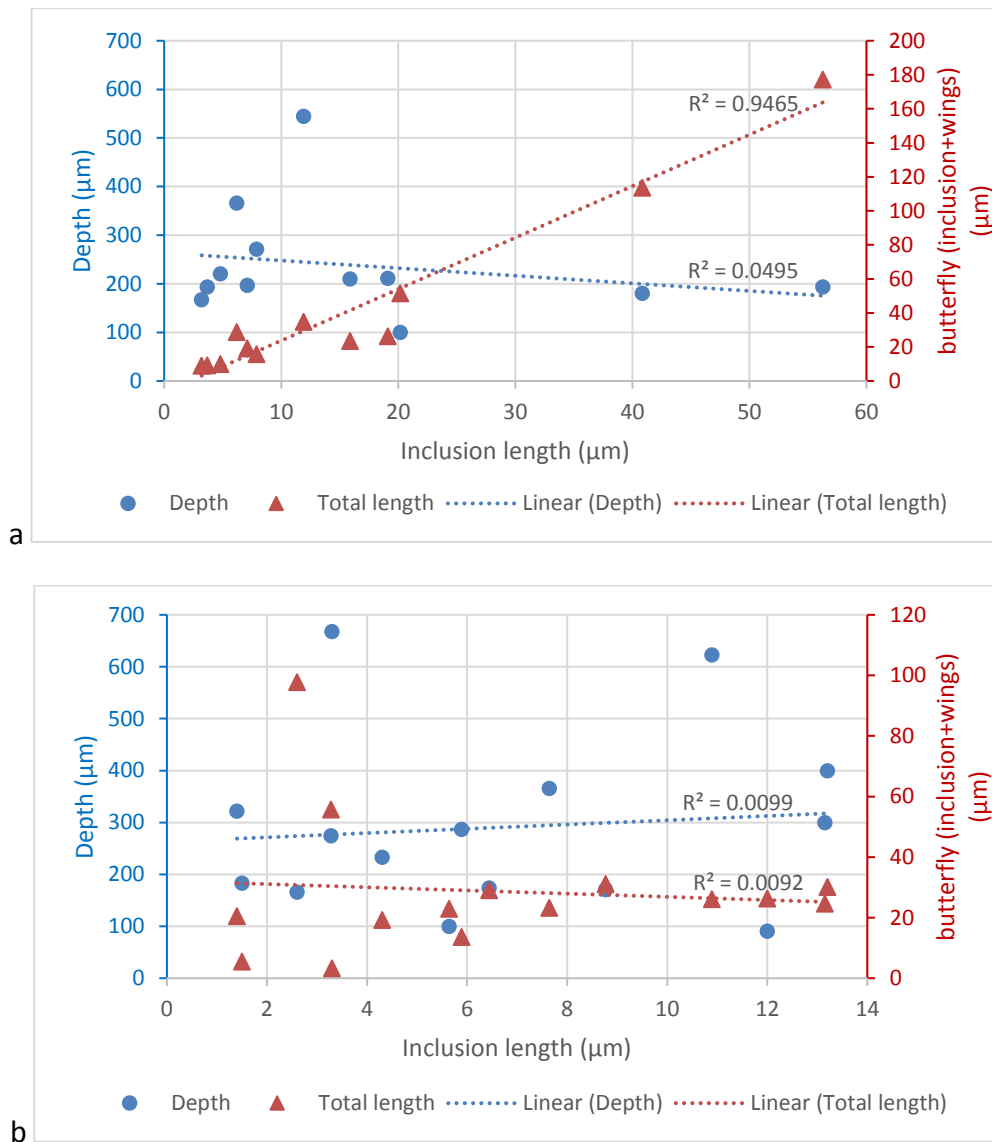


Figure 6.2.6: Mg-Al-O inclusion



**Figure 6.2.7: Inclusion length vs total length with the depth of inclusions (a) butterflies in axial sections; and (b) butterflies in circumferential sections**

### 6.3 Subsurface cracks

Some of the observed cracks in the axial and circumferential directions were not linked to the surface. In both directions, they could be single cracks or a network of cracks, but they show different characteristics in each direction, which has been investigated.

In the circumferential direction, the subsurface cracks can have very irregular shapes, as in Figure 6.3.1, under spalls or severe surface damage. One subsurface crack network was found attached to an inclusion with almost vertical cracks, as shown in Figure 6.3.2. Some of the cracks of different sizes have been found attached to inclusions which could be the initiation point for them, such as the inclusion in Figure 6.3.2. Although the depth of this inclusion can be far from the depth of the expected maximum subsurface shear stress  $\tau_{1(max)}$ , it is still expected for the crack to be initiated from this inclusion or another inclusion, since the crack is completely under the surface and the only stress concentration

point found along the crack was this inclusion. There might be another inclusion where the crack started from, and this inclusion was removed during the sample preparation process, or it was under the examined surface. Also, the inclusion is the only stress concentration that was found along the cracks in Figure 6.3.2. This might initiate the crack then it propagated toward the maximum subsurface stress or propagated due to the hoop stress. The EDX analysis of this inclusion in Figure 6.3.3 showed that it was a MnS inclusion, despite the domination of Type D inclusions in this bearing, as discussed in Section 6.1. This inclusion does not show a gap, as it is observed in the uncoated bearing. However, the non-perfect bonding between this inclusion and the matrix is clear. Although, for some of the cracks, the depth and the angle are not clearly recognizable due to their non-uniform tomography, it is recognized that subsurface cracks which are clearly linked to one inclusion show almost a vertical angle, as shown in Figure 6.3.2 and Figure 5.1.7.

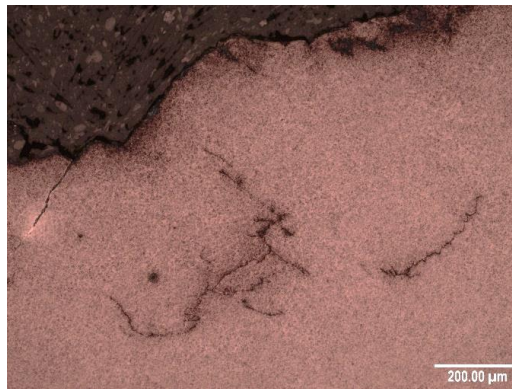


**Figure 6.3.1: Irregular subsurface crack network in circumferential section**

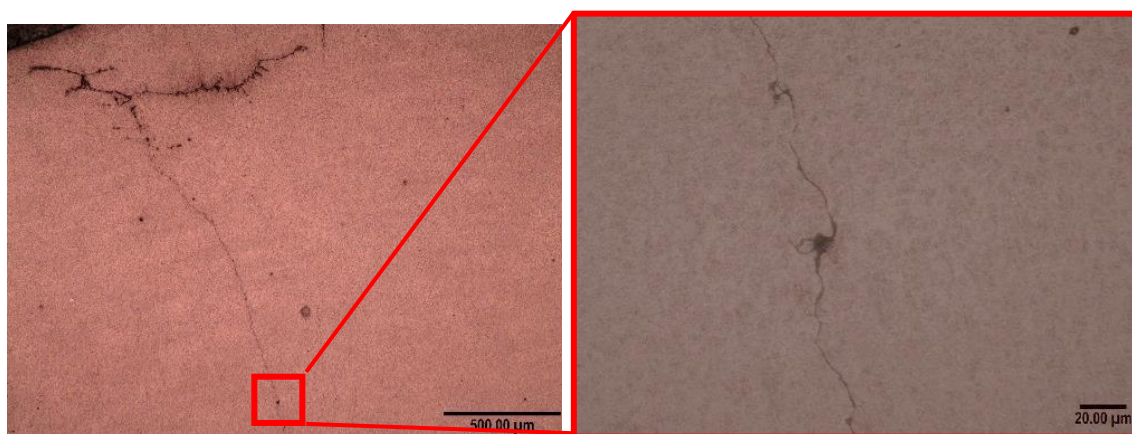


**Figure 6.3.2: Subsurface crack network initiated from deep inclusion at more than 1500 μm in circumferential section**

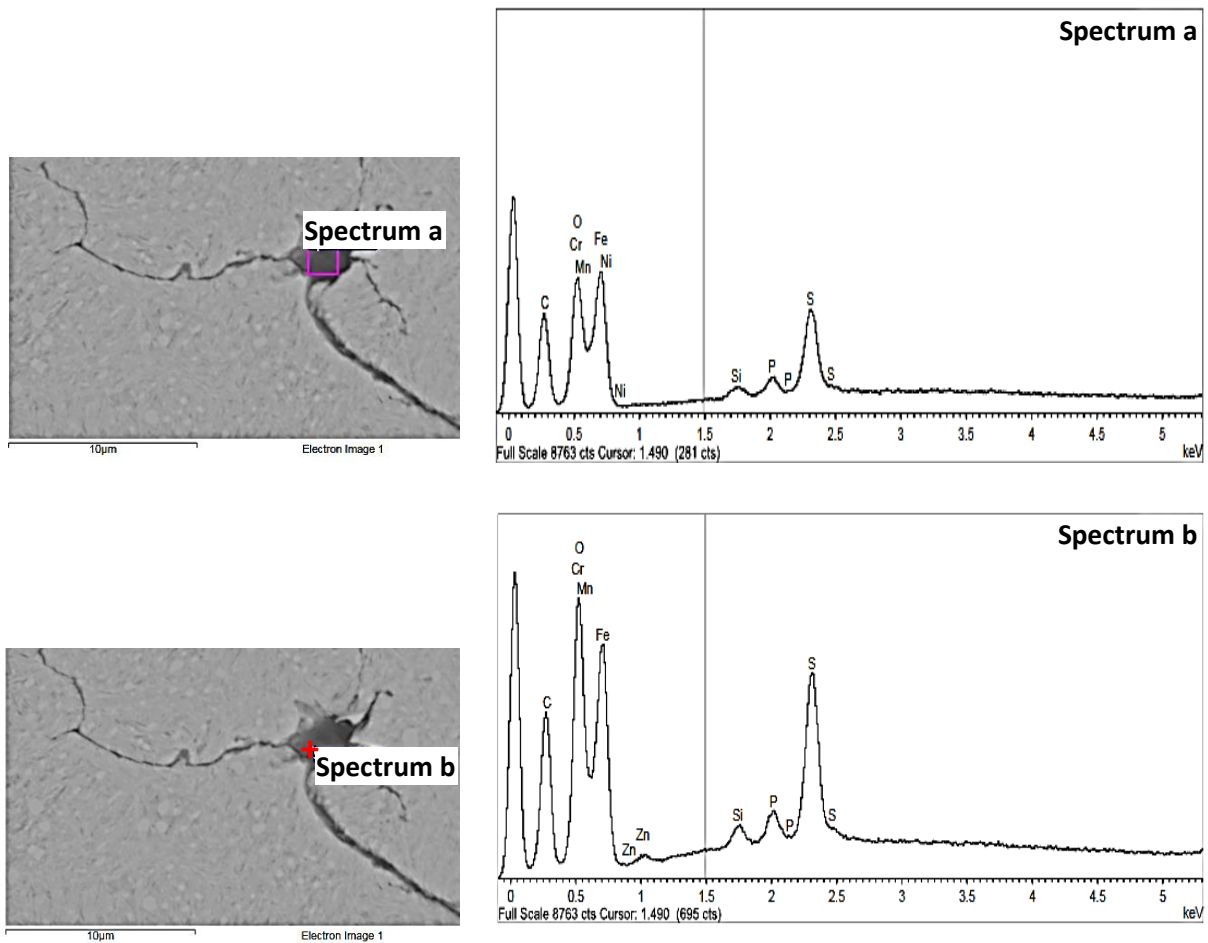


**Figure 6.3.3: EDX analysis of highlighted inclusion in Figure 6.3.2**

The subsurface cracks in the axial direction showed consistent features, which made the analysis of their characteristics feasible. They were mostly flat, parallel to the surface, with some inclined at a specific angle at one or both of their ends. Figure 6.3.4 shows the characteristics of the analysed cracks where the angle was measured from the positive x-axis, which is the horizontal axis toward the right parallel to the surface. It was found that the inclination angle is shallow and about  $15^\circ$  with the horizontal axis. It is expected that these cracks propagate toward the surface and form the subsurface initiated spalls. The depth in axial direction is close to that of butterflies in Figure 6.2.2, while for uncoated bearings the difference is more considerable, as can be seen in Figure 5.3.1. However, the subsurface cracks observed in this bearing are more advanced and some do not show the initiation stage from inclusions.

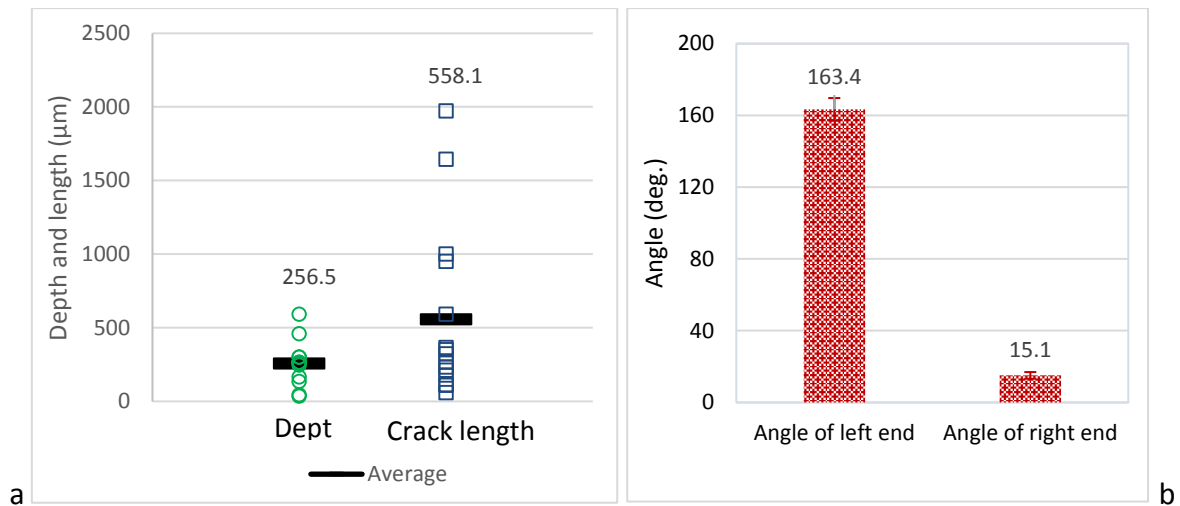


**Figure 6.3.4: Characteristics of subsurface cracks in axial sections (a) depth and length (the number above each characteristic refers to the average value) (b) angle (average values with the error bars show  $\pm$  one standard deviation)**

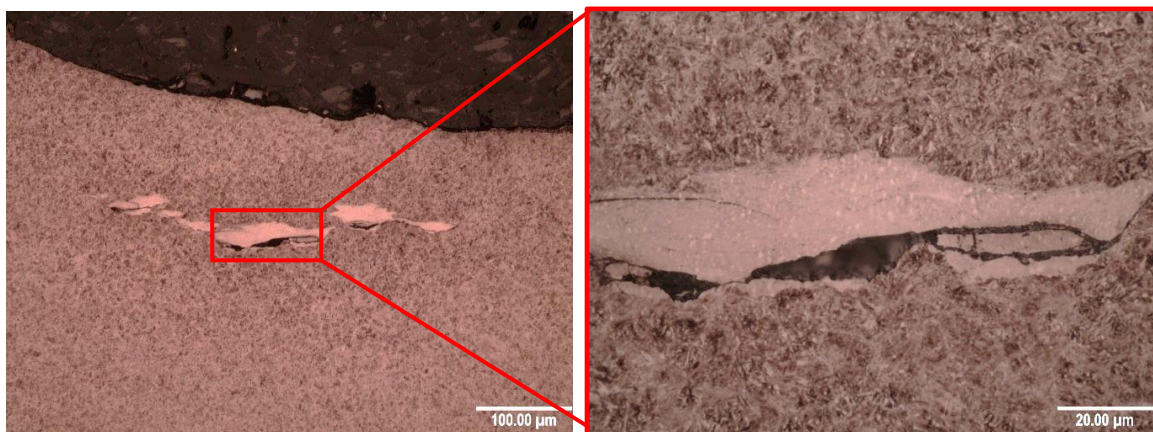


**Figure 6.3.5: Subsurface WECs in axial section**

The depth of these subsurface cracks and butterflies could be in the range of the maximum subsurface stresses. However, without the full dimensions of the bearing and the range of the operating load, this cannot be confirmed. Furthermore, the depth for some of the WECs, such as Figure 6.3.5, is quite in line with the average depth of the butterflies which could mean that these cracks are related to butterflies. Using the procedure in Section 3.3.2, the hardness under the surface of the BO coated bearing was measured. This procedure is similar to the subsurface hardness measurement conducted for the uncoated bearing, as shown in Figure 5.3.3. Figure 6.3.6 shows the variation of hardness in the BO coated bearing under damaged surface in the loaded zone and undamaged surface at the entrance to the loaded zone. No comparison with the depth of  $\tau_{1(max)}$  was possible due to the missing dimensions of roller and loading history, but this figure shows higher hardness close to the surface under the damaged surface, which could be an indication of the effect of surface traction.

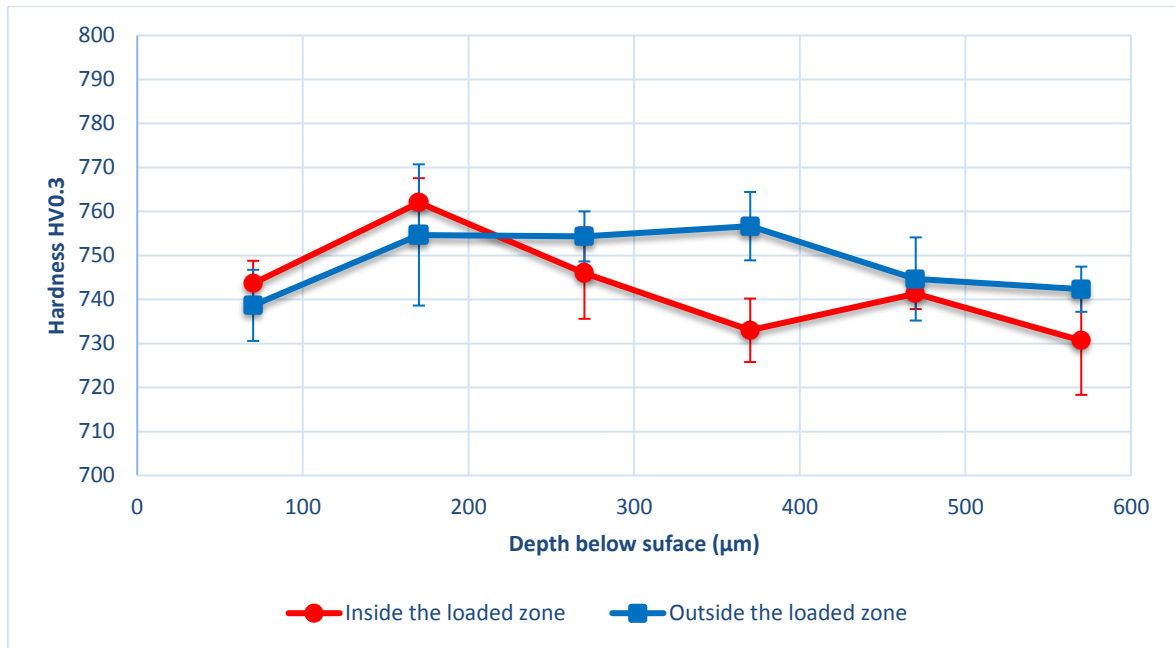
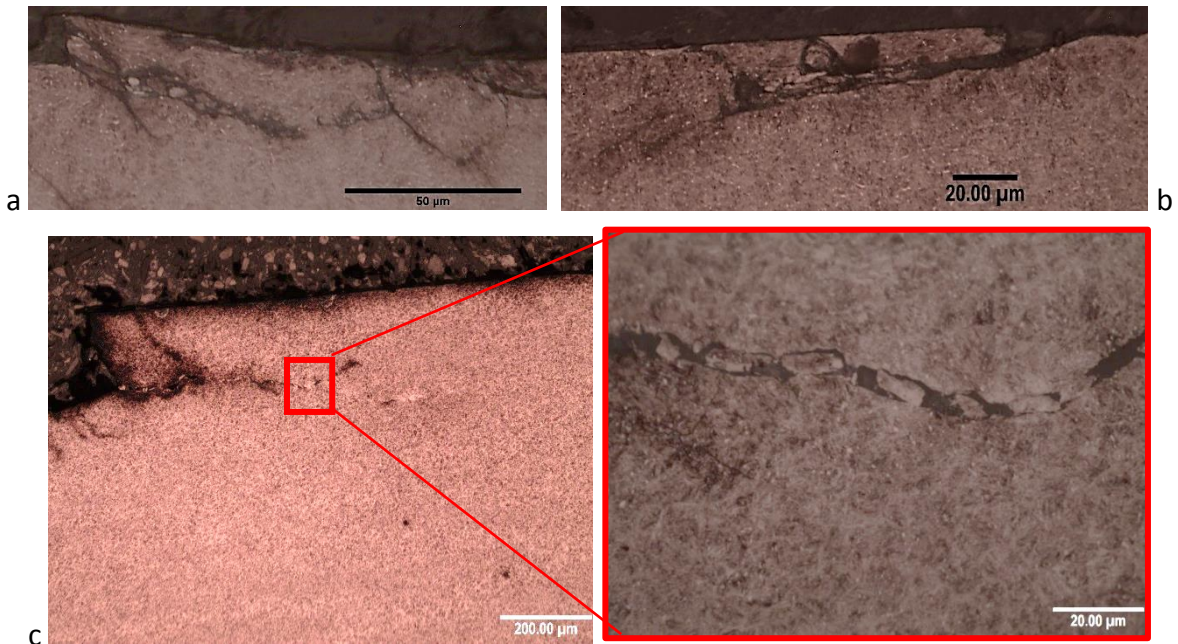


Figure 6.3.6: Hardness variation with depth below the surface for BO coated bearing

#### 6.4 Cracks linked to surface

It was observed that some of cracks linked to the surface show specific characteristics represented by their similar inclination and features, which are defined as surface-linked RCF cracks in Table 3.4.1. In some of these cracks, fragments of steel particles are confined between the two sides of the crack, as shown in Figure 6.4.1. Sometimes the colour of these particles appeared to be similar to the conventional WEA attached to the WECs, especially when they expanded deeper under the surface, as shown in Figure 6.4.2 (a) which can be compared with the WEC in Figure 6.4.2 (b). The appearance of these surface-linked RCF is only different than the WECs in term of uniformity, since in the WECs, the WEA distributes irregularly around a single crack, as shown in Figure 6.3.5. According to this similarity, they could be generated by the same mechanism. The opening of these cracks could be due to fracture mode II, where the double cracks represent a segment of the material that has been sheared, and the shearing deformation flow of the material between them could support this assumption. The results from the tests on the SUROS machine, given in Chapter 7, show similar cracks, which provides an understanding of ways of generating this damage in controlled tests.



**Figure 6.4.1: Surface-linked RCF cracks (a) and (c) in circumferential sections and (b) in axial section**

The characteristics of 18 surface-linked RCF cracks observed in the axial and circumferential directions are shown in Figure 6.4.3, where the angle was measured from the ORD in circumferential sections and from the positive x-axis toward the spacer in the axial sections. In circumferential sections, most of the cracks propagated in the direction of the ORD while, in axial sections there were almost even numbers of cracks propagated toward the flange and the spacer. The angles in the axial sections were close to those of the subsurface cracks, as shown in Figure 6.3.4. Hence, the cracks propagated at almost the same angle in the axial direction regardless of the initiation location, either on the surface or under the surface.

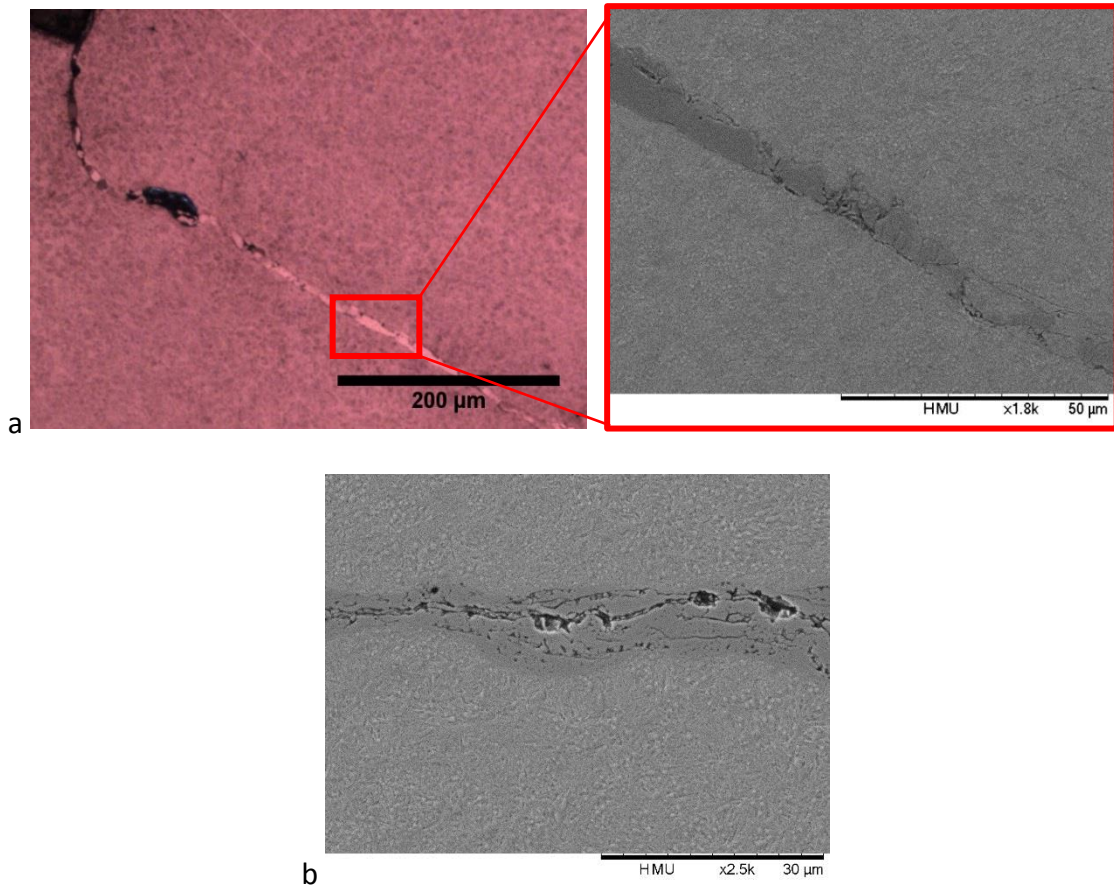


Figure 6.4.2: Surface-linked RCF cracks appears similar to WECs (a) from circumferential section and (b) WEC from axial section

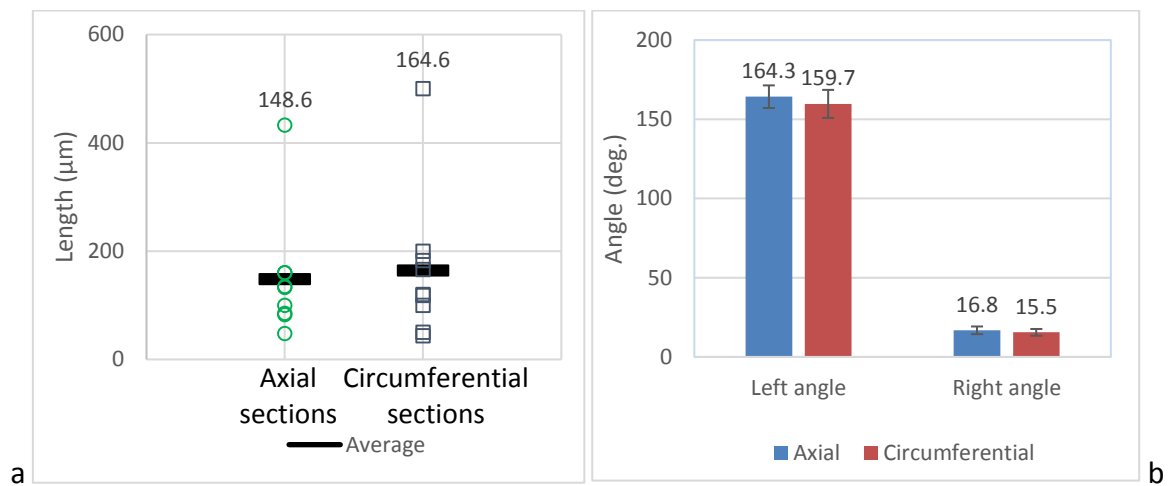


Figure 6.4.3: Characteristics of surface-linked RCF cracks (a) length (the number above each characteristic refers to the average value) (b) angle (average values with the error bars show  $\pm$  one standard deviation)

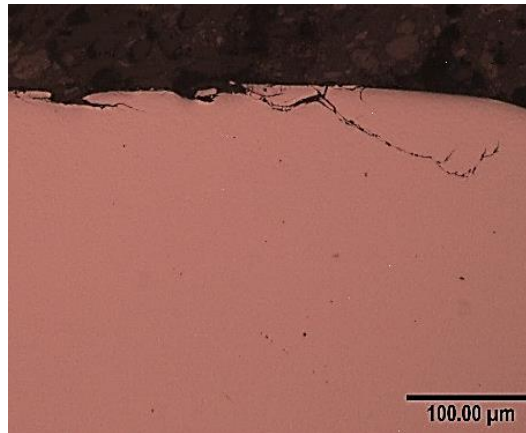


Figure 6.4.4: Surface cracks change direction toward the surface

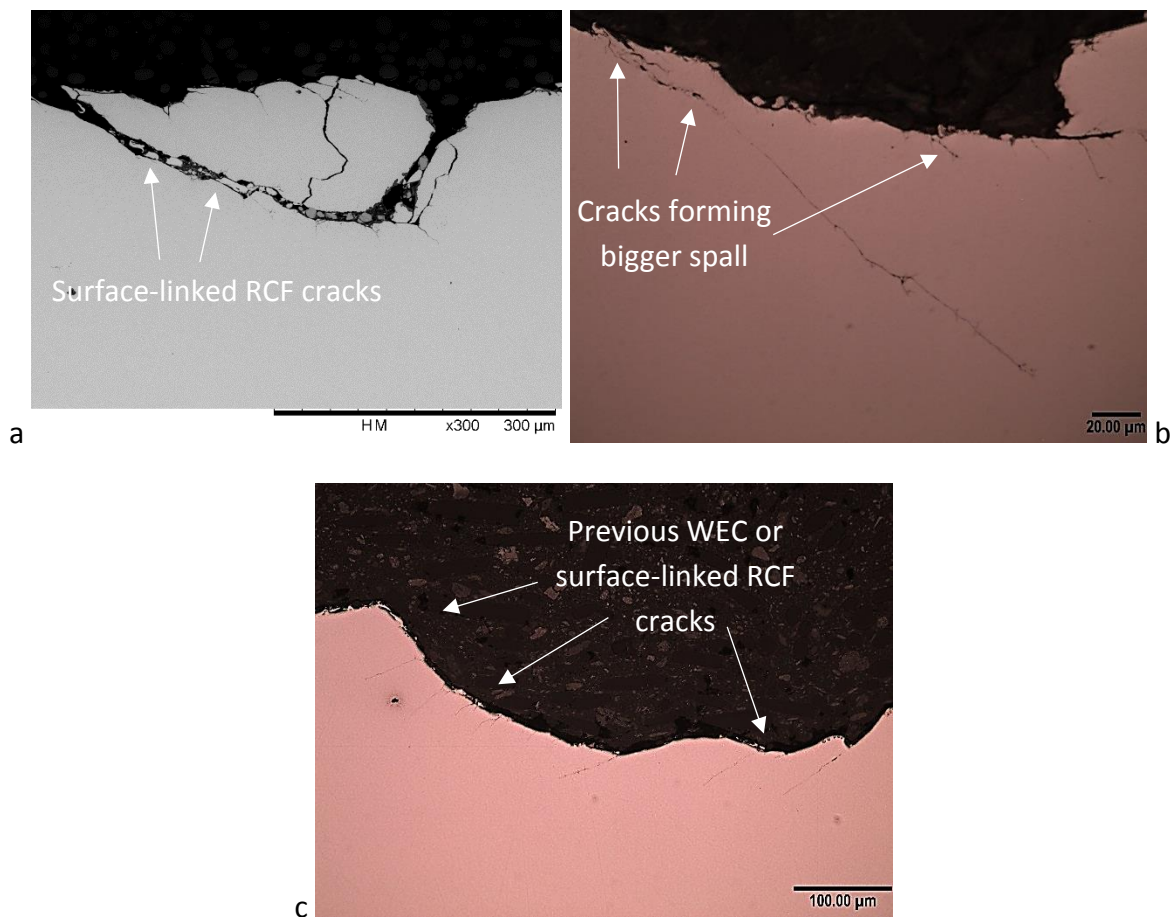
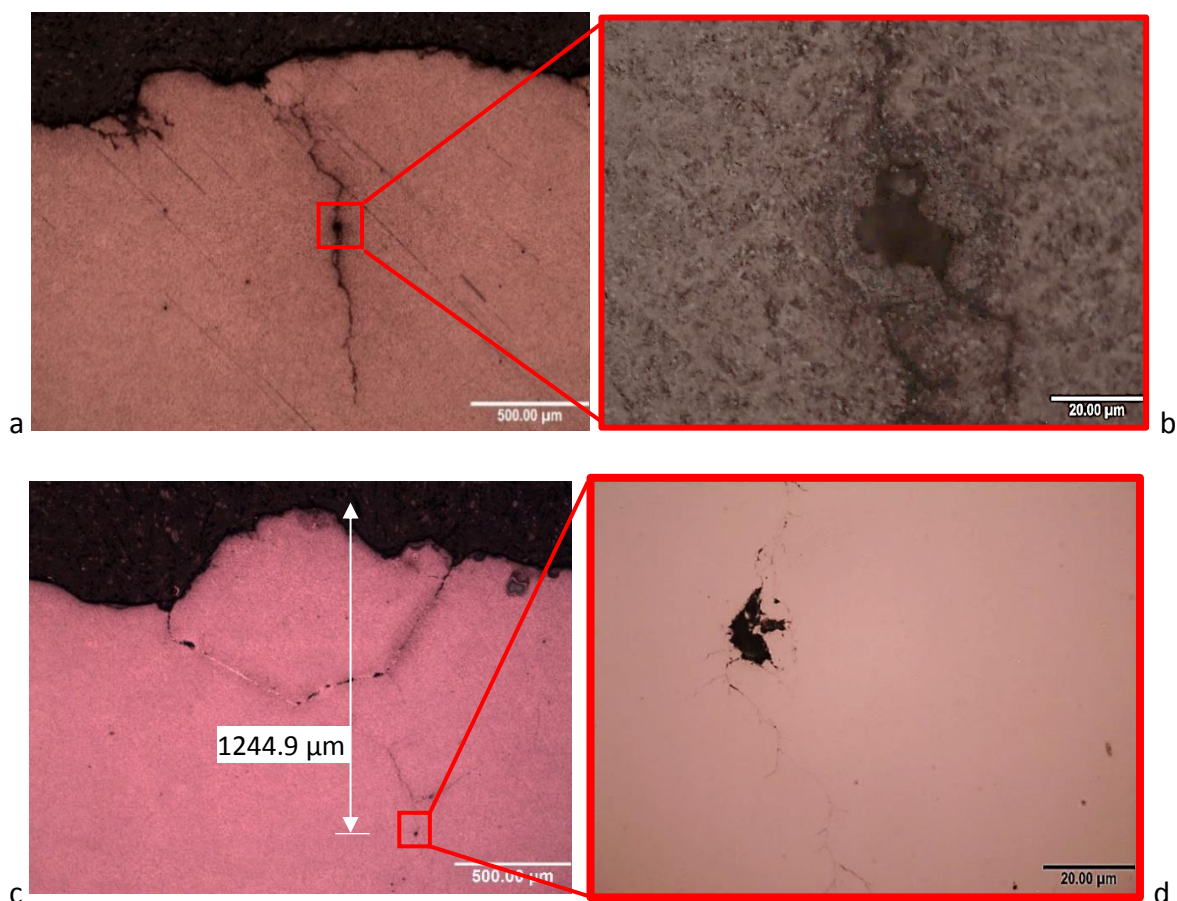


Figure 6.4.5: Spall created by surface-linked RCF cracks in circumferential sections (ORD from left to right)

The surface-linked RCF cracks that initiated from the surface and propagated downward were found to change their propagation direction toward the surface after a certain length, which is a form of generating spalling or micropitting, as shown in Figure 6.4.4. Figure 6.4.3 shows that the average crack length is less than that for subsurface cracks. This reveals that

surface cracks generate pitting at a shorter length, with smaller spalls, than the subsurface cracks, which can cause greater damage if they propagate to the surface. The observations show relatively small spalls/ pits formed by surface-linked RCF cracks, then other cracks starting from these spalls propagate toward the depth and forming bigger spalls, as shown in Figure 6.4.5. These observations show that surface initiated cracks can be one of the deterioration mechanisms of WTGBs. In addition to the surface initiated cracks of specific inclination due to surface traction, vertical or very steep cracks are also observed, passing through inclusion(s), as shown in Figure 6.4.6. For the first crack in this figure, Image (a) and (b), it is not clear whether the crack initiated under the subsurface at the inclusion and propagated to the surface, or that the opposite happened. However, it is more likely for this crack to be initiated due to the stress concentration caused by the inclusion. Thus, this crack could be a more developed subsurface initiated crack similar to the one in Figure 6.3.2. On the other hand, it is found that the crack in Image (c) and (d) in Figure 6.4.6 is linked to one of the cracks that propagated from a spall caused by surface-linked RCF cracks, making it a surface initiated crack.



**Figure 6.4.6: Vertical surface cracks passing through an inclusion**

## 6.5 Analysis of Black Oxide Coating

It is essential to investigate the damage in the BO layer in order to assess the loading condition on the contact surface. The variation of this layer inside and outside the loaded zone can be an indication of damage. To the author's knowledge, the characteristics of the BO layer used for bearings are not revealed by the manufacturer, and no previous study has been conducted for this purpose. Accordingly, this investigation was conducted in this research. The first objective was to find out whether this layer was softer or harder than bearing steel, since the iron oxide can have a range of hardness according to its chemical composition. The second objective was to find the thickness of this layer on damaged and undamaged surfaces to evaluate the variation of this layer due to loading in WT planetary bearings.

The chemical composition of this layer was found by EDX analysis, as shown in Figure 6.5.1 (a). The analysis was conducted on the undamaged region of the BO layer, at the side of the raceway, as shown in Figure 6.5.2. Because the x-ray can penetrate the very thin BO layer, the analysis shows main peaks of iron oxide and others observed in the bearing steel. In Figure 6.5.1 (b), dark dots appear in the SEM image of this layer, which have a similar spectrum of chemical elements as the rest of the BO layer. Accordingly, these dark dots can indicate the porosity of the oxide.

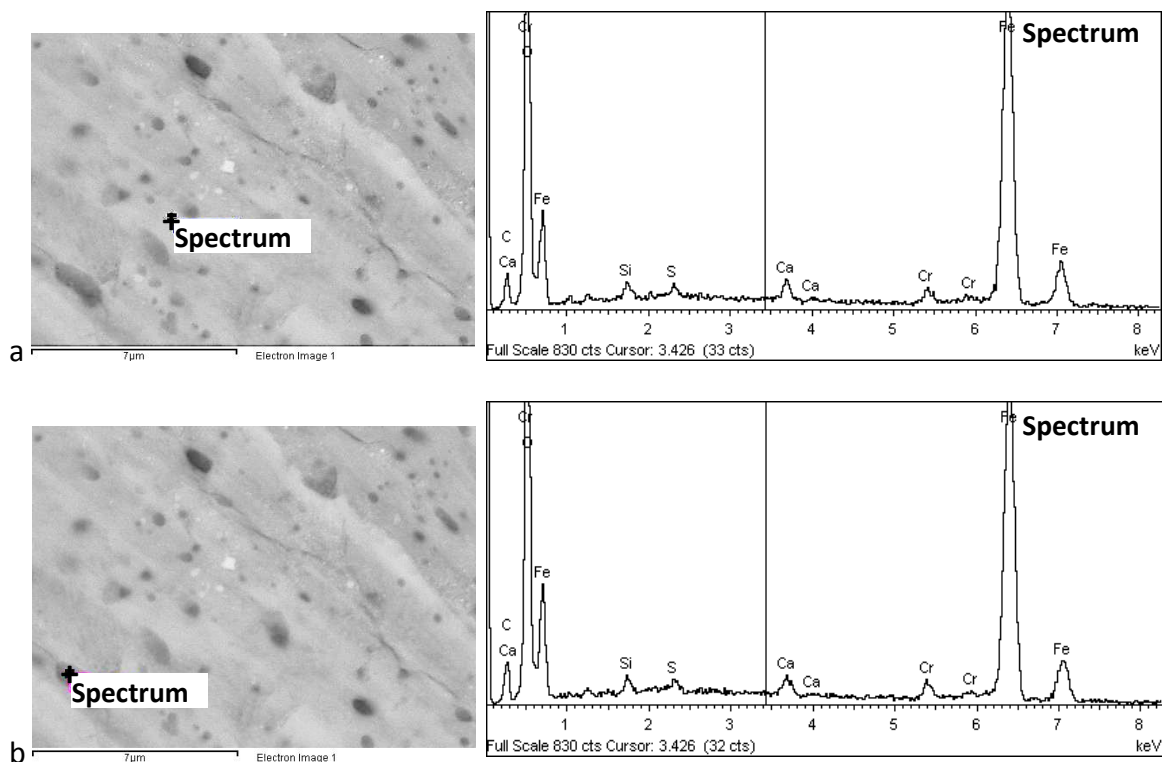


Figure 6.5.1: EDX analysis of the BO layer

The hardness of the iron oxide varies with the chemical formulation, as investigated by Takeda et al. [145], which is not revealed by the EDX analysis. Therefore, Nano-indentation

was used to measure the hardness of this layer. The first measurement was conducted using a Nano-indentation system, Hysitron Triboscope, described in Section 3.3.2. Two regions were chosen for the hardness measurements, which are the entrance to the loaded zone where the layer is partially removed and the edge of the raceway far from the wear track where the layer was intact, as shown in Figure 6.5.2. The methodology for loading /partial unloading described in Section 3.3.2 is adopted for the measurements at both regions, where the maximum load of 10000  $\mu\text{N}$  was applied in 25 steps. The indentation pattern used was a 3 $\times$ 3 matrix, as the AFM image shows in Figure 6.5.3. The results from the entrance region, the damaged BO layer, showed a very thin BO layer, as revealed by the depth in Figures 6.5.4 and 6.5.5. In these curves the hardness and modulus of elasticity of the steel matrix are reached by the end of these curves, which indicates the end of the BO layer thickness. However, the results from the undamaged BO region did not show the total thickness of the BO layer, since the curves in Figure 6.5.4 and 6.5.5 show an ascending trend, until the maximum load was applied.

Sample of undamaged BO coating



Figure 6.5.2: BO regions used for EDX and Nano-indentation analyses

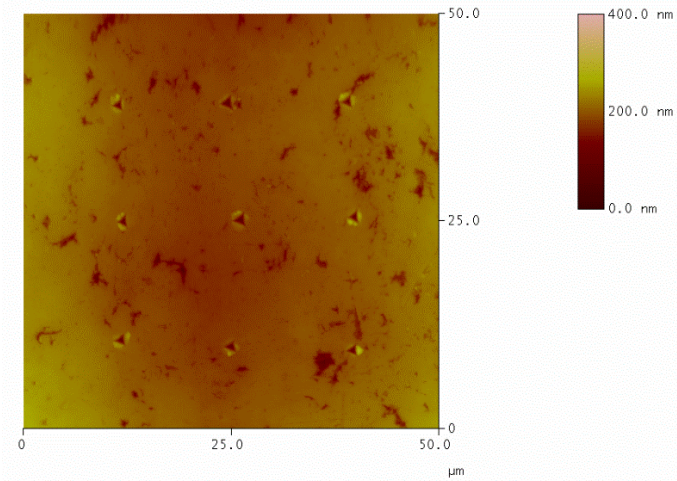


Figure 6.5.3: AFM image of partially removed BO layer shows the adopted pattern off the Nano-indentation measurements using Hysitron Triboscope

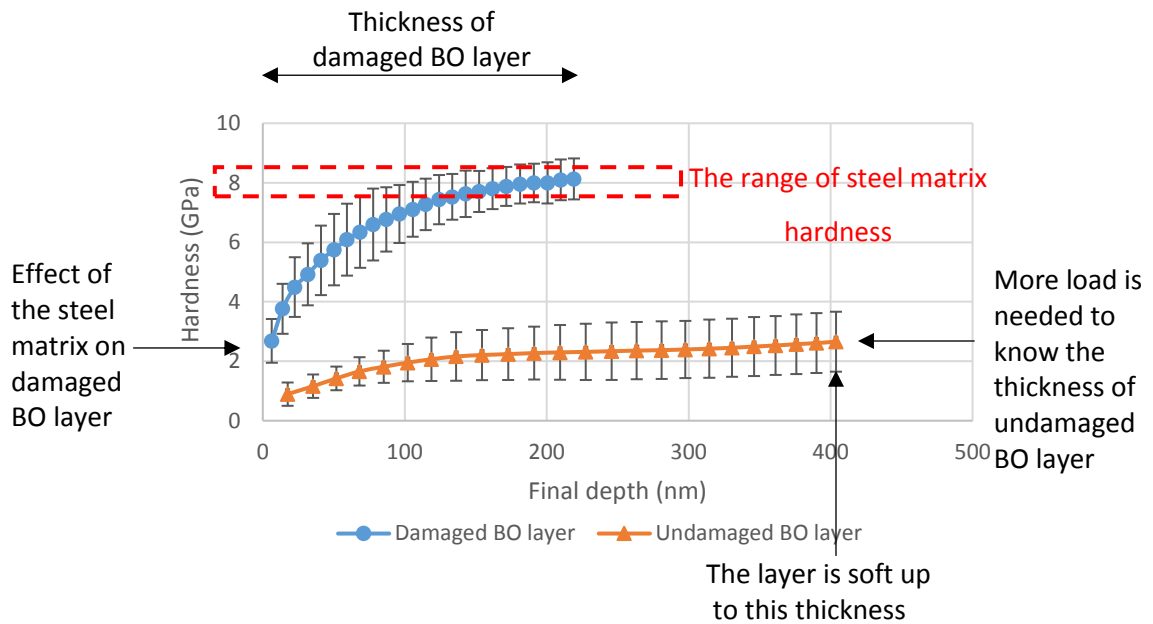
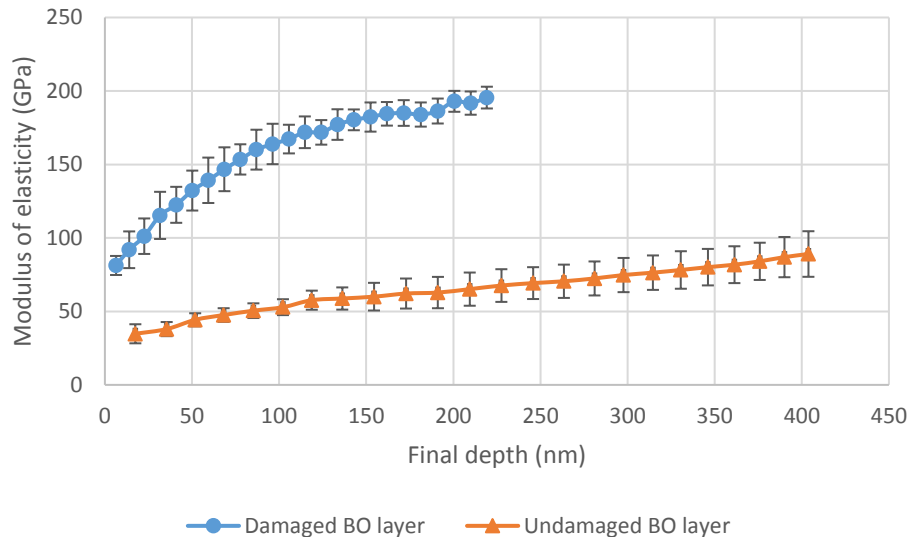
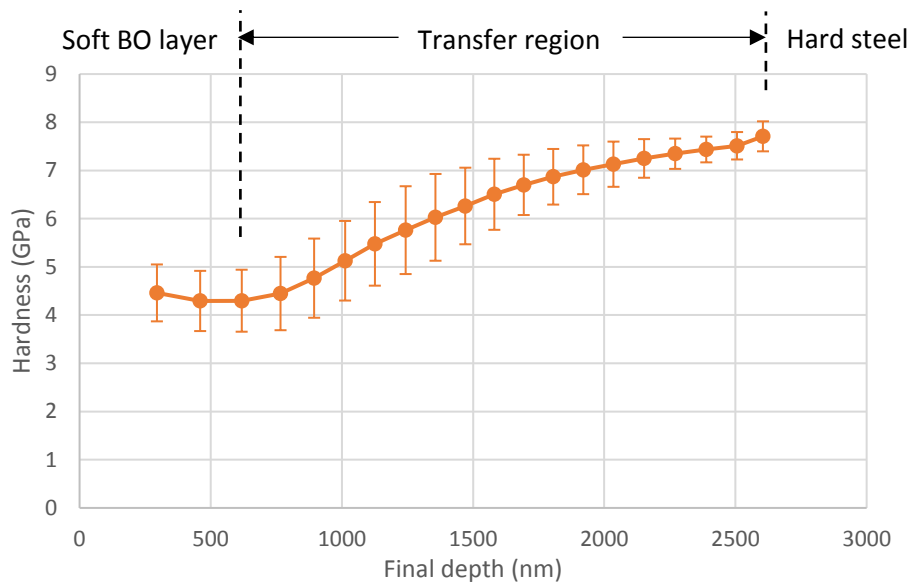


Figure 6.5.4: Nano-indentation hardness of partially removed and undamaged BO layer using Hysitron Triboscope



**Figure 6.5.5: Modulus of elasticity of partially removed and undamaged BO layer using Hysitron Triboscope**

It is clear that the BO layer is softer than the steel matrix and it is significantly removed at the region of the entrance to the loaded zone. However, for a complete measurement of the intact BO layer, a higher load should be applied, which was conducted using the Nano-indentation system Hysitron TI Premier, as described in Section 3.3.2. This system covers a wider range of load than the Hysitron Triboscope. In this test, four indents were made using maximum load of 1000 mN, divided into 20 steps of loading / partial unloading. The pattern of indents was a 2×2 matrix, with 120 μm between the centres of adjacent indents. The measured Nano-hardness and modulus of elasticity for the undamaged BO layer at each load step are shown in Figures 6.5.6 and 6.5.7. The curve in Figures 6.5.6 show clearly the transfer of the soft BO layer to the hard bearing steel and the total thickness of this layer. However, no similar recognition is shown in Figure 6.5.7, where the E of bearing steel is not reached which could be due to measuring the modulus of elasticity of two substances of different modulus of elasticity that forms a compliance of two springs in series. Also, it was found that the E of bearing steel can be reached after penetrating a very shallow thickness for the partially removed BO layer, as shown in Figure 6.5.5. The thickness of the undamaged BO layer can be found from Figure 6.5.6 to be around 2.2 μm. The first 0.5 μm in this figure shows a soft layer with average hardness of  $4.35 \pm 0.1$  GPa, then the hardness gradually increases to the bearing steel hardness. Figures 6.5.6 and 6.5.7 describe the variation of the H and E across the thickness of the BO layer, however, for a simplified description for the properties of this layer, the average values for H and E are found to be 6.1 GPa and 161.8 GPa respectively.



**Figure 6.5.6: Nano-indentation hardness of undamaged BO layer using Hysitron TI Premier**

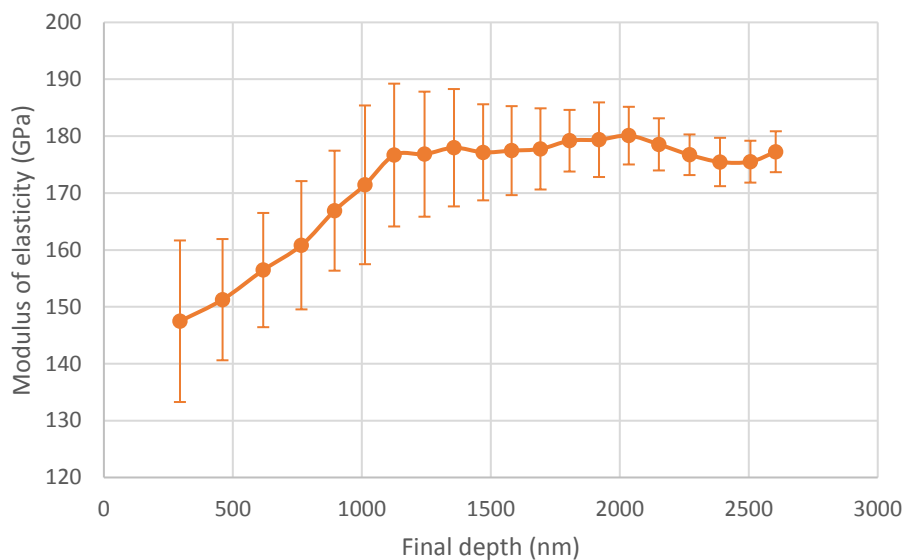


**Figure 6.5.7: Modulus of elasticity of undamaged BO layer using Hysitron TI Premier**

## 6.6 Summary

The main damage types found from the examination of the BO coated bearing include butterflies, WECs, subsurface cracks, surface-linked RCF cracks and different stages of formation of surface spalls.

1. The cleanliness and the EDX analysis showed that this bearing steel is not very clean in Type D inclusions, where 65% of the observed butterflies were associated with this type. Although the cleanliness of other types, such as Type A, was very sufficient, it is evident that they can still be the initiation point for subsurface cracks.
2. In general, the butterflies show similar length and inclination as those found in uncoated bearings. In the axial direction, the longest butterfly was found at the exit

of the loaded zone of sample 6A2, where high local stress concentration can be caused by debris. While in the circumferential direction, the longest butterfly was found at the edge of the raceway and started from a combined inclusion. Similar to the uncoated bearing, a direct relation between butterfly length (inclusion and butterfly wings) and inclusion length in axial sections was found. However, no relation could be found in circumferential sections.

3. Magnesium Mg was observed in some inclusions which may contribute to the formation of the WEA due to its effect on the geometry and the nucleation of carbide.
4. Subsurface cracks were found at similar range of depth, as that of the butterflies. In axial sections, it was found that the inclination angle is similar for cracks linked to the surface and those under the surface, which could be due to a similar propagation mechanism. Some relatively long subsurface cracks linked to inclusions propagated at almost a vertical angle.
5. Some of the surface-linked RCF cracks that show fragmented pieces of material confined by two cracks could be related to the WECs, since they have similar features, especially far from surface. The particles inside these cracks are sheared, which could be a sign of fracture mode II.
6. More butterflies formed in the first 300  $\mu\text{m}$  depth, close to the surface, which is expected to be less than the depth of  $\tau_{1(max)}$  and hence shows the effect of surface traction. Also, a higher hardness close to the surface under the damaged surface can be an indication of this effect.
7. The size of surface pits and spalls was found to be affected by the initiating cracks. The average length of a surface-linked RCF is less than that of subsurface cracks, and therefore the surface-linked RCF propagates to form smaller pits. However, it was found that these small pits were initiating more surface initiated cracks that propagate to form bigger spalls.
8. The specifications of the BO layer were measured. The thickness of the partially removed BO layer at the entrance to the loaded zone was around 0.2  $\mu\text{m}$ . For the undamaged BO layer, the thickness is measured by the variation of hardness and was found to be around 2.2  $\mu\text{m}$ . The first 0.5  $\mu\text{m}$  is softer,  $H = 4.35 \pm 0.1$  GPa, then the hardness gradually increases to the bearing steel hardness. The variation of the H and E across the thickness of the BO layer was found with the overall average of 6.1 GPa and 161.8 GPa, respectively. According to the surface and subsurface damages observed, the BO layer is not effective against WECs, butterflies, surface initiated cracks and cracks initiating from inclusions.

## 7 Results and Discussion of the Experimental Investigation Using the Twin Disc Machine

This chapter presents the RSTs conducted to investigate the variables causing damage on the surface and subsurface of bearings, as observed from the examined failed bearings in Chapters 5 and 6. The tests were conducted using the twin disc machine SUROS described in Chapter 4. The variables investigated were contact pressure, slipping ratio, speed, viscosity and load sequence, with each of them varying between two values. In contrast to previous studies that used twin disc machine, in this research a low speed was used to simulate the actual tribological conditions in the wind turbine planetary bearings. The first step was to investigate the coefficient of traction at different testing condition, then a set of RSTs was conducted. As described in Section 7.1 (Table 7.1.2), except for the first test, each of the RSTs consisted of two steps with different testing variables were used for each step, in order to simulate different surface traction conditions. Another aim of this research is to investigate the effect of varying the sequence of different testing conditions on damage initiation, which has not been the focus of other studies. The comparison between different tests was based on observing the surface and subsurface of the specimens to identify damage initiation. Despite the uncertainty due to conducting each RST only once, the results could be a base for further investigation in the future, when more time and resources are available.

### 7.1 Experimental Design of RSTs

In the RSTs, two discs, crowned on a non-crowned, were rolling over each other under five controlled variables: rotational speed of lower disc, contact pressure, slip ratio, lubricant viscosity and number of cycles. Since the surface traction effect, which is determined by the COT, is one of the main factors to be investigated, a set of tests were conducted to gain an insight into the possible values of the COT under different operation conditions as shown in Table 7.1.1. For these tests, specimens C1 and F1S were used where C1 was the upper specimen and F1 was the lower specimen. Figure 7.1.1 shows the illustration of the testing specimens, the directions of surface traction and tangential velocity. The effect of these variables on surface and subsurface damage initiation will be discussed in this Chapter. Specimens C1 and F1S were used throughout all the tests for measuring the COT, which does not consider the variation of surface roughness. However, it was found that after a running in of 2000 cycles in a lubricated condition before the first measurement, the surface became very smooth and this reduces the effect of surface roughness. Nevertheless, for a dry contact test, the variation of surface roughness and topology is significant, and that is why this test was conducted after the end of the lubricated tests. Although the lubricated test was conducted without lubricant, there may be some oil additives bonded to the surface of the specimens after the lubricated tests and they were not completely removed with the Acetone in the ultrasonic bath. A further analysis on changes in roughness will be discussed in Section 7.3.

**Table 7.1.1: The settings for the COT measurement tests**

Test	Lubrication	Load (kN)	$P_{\max}$ (MPa)	Speed (rpm)	Slip %
COT1	Sp 68	4.6	3052	20	-1
COT2	Sp 68	6.5	3425	400	-10
COT3	Dry	3.5	2786	400	-1

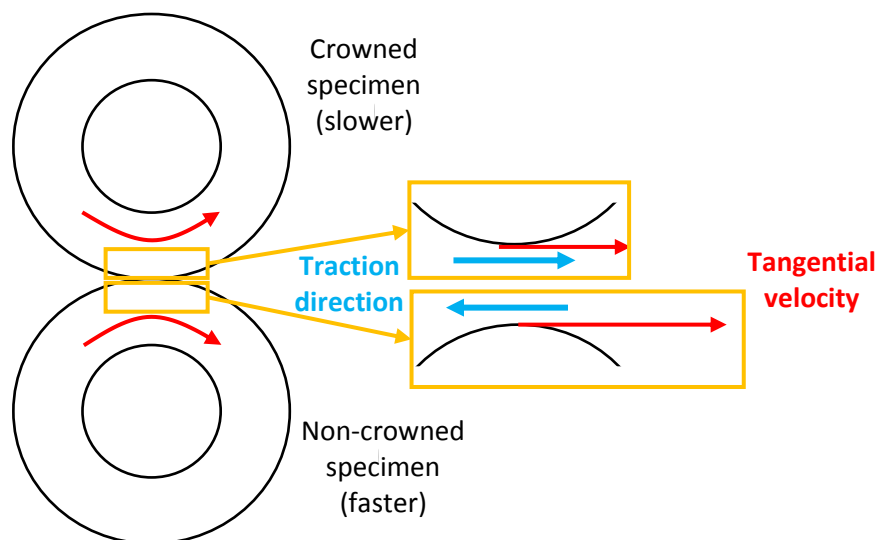


**Figure 7.1.1: Illustration of surface traction direction relative to the rolling direction and tangential velocity. This configuration was used for tests COT1 to COT3 (in Table 7.1.1) and RSTs 2 to 8 (in Table 7.1.2)**

To investigate the effect of different tribological conditions on surface and sub-surface initiated damage, nine RSTs were performed. The first test consisted of three steps, while each of the other eight tests consisted of two steps with different settings of operating variables, as shown in Table 7.1.2. The first test ran longer than the other test, and it was the only test with a step of reversed rotation, which was designated by the (–) sign of speed in Table 7.1.2. The illustration of the tangential velocity and surface traction of specimens used in this test is shown in Figure 7.1.2. In test steps 1a and 1c, the surface traction on the non-crowned specimen is in the same direction as the tangential velocity, which is not the case for all other tests steps. For the other eight tests, the tangential velocity and surface traction are illustrated in Figure 7.1.1. In these tests, with the exception of the number of cycles, the variation of all variables was investigated as well as a change in the sequence of test steps. In each of the eight tests, there was a step which is called the *high speed step* where the testing variables were set to be rotation speed of 400 rpm, maximum contact pressure of 3425 MPa, 250,000 cycles, -10% slip and using SP 68 lubrication oil. The other

step was called *low speed step* where the number of cycles was 50,000 and other investigated variables varied between two values. The selected values were chosen to simulate extreme tribological conditions but also based on the limitations of the machine such as the difficulties to achieve high number of cycles because the machine should be observed during testing and the maximum speed is 400 rpm. However at 87 rpm, the  $h_{\min}$  is very close to that in the planetary bearing of the NREL 750 kW wind turbine considering the applied loads, the lubricants' viscosities and the operation temperatures in the RSTs and in this WT. Table 7.1.2 shows the set of the conducted tests with the two values for each of the investigated variables. In this table, slip ratio is defined in Equation 4.1.1, speed is for the lower specimen, and viscosity is for the utilised lubricant SP 46 and SP 68 in Table 4.2.3. Also, in Table 7.1.2, *sequence 1* is when the first step, step (a), is the low speed step and the second step, step (b), is the high speed step. *Sequence 2* is when the first step, step (a), is the high speed step and the second step, step (b), is the low speed step.

The aim here was to initiate the damage with the low speed step, and propagate the damage with the high speed step. Four non-crowned specimens were used as the lower specimen with two test on each specimen as explained in Section 4.2. The crowned specimen C1 was used for the COT measurement tests and it was also used for the RSTs. For the RSTs, C1 was used for whole steps with low speed and C3 was used for whole steps with high speed. Using the same crowned specimens for several tests was both for economical reason and to achieve high number of cycles on these specimens, two million cycles on C3 at 400 rpm and more than 400,000 cycles on C1 at various speed (mainly 87 rpm). Although the roughness of these specimens might vary during the tests, it was found that surface roughness has a limited effect, during lubricated contact, on the COT and the surface damage of the non-crowned specimens. The tests in table 7.1.2 were designed to investigate the effect of each of the studied variables by comparing certain tests with each other as shown in Table 7.1.3. The characters used to evaluate the effect of the investigated variables were the variation of surface roughness, the hardness under the surface, weight loss, inclusions damage, and the characteristics of surface and subsurface cracks as explained in Section 4.3.

Table 7.1.2: Specifications of RSTs

RSTs	Crowned specimen	Flat specimen	Test step	Speed (rpm)	Slip %	Oil type SP	Sequence	Load (kN)	P <sub>max</sub> (GPa)	Cycles	The radii of the elliptical contact area (mm)
1	C2	F1F	1a	400	-10	68	-	6.5	3.42	900000	1.43 and 0.63
	C2	F1F	1b	-20	0	68	-	1.5-3.5	2.1-2.78	36	(0.88 and 0.39) to (1.16 and 0.52)
	C2	F1F	1c	400	-10	68		6.5	3.42	100000	1.43 and 0.63
2	C3	F2S	2a	400	-10	68	2	6.5	3.42	250000	1.43 and 0.63
	C1	F2S	2b	87	-10	68	2	6.5	3.42	50000	1.43 and 0.63
3	C1	F2F	3a	87	-10	68	1	6.5	3.42	50000	1.43 and 0.63
	C3	F2F	3b	400	-10	68	1	6.5	3.42	250000	1.43 and 0.63
4	C1	F3S	4a	87	-20	46	1	6.5	3.42	50000	1.43 and 0.63
	C3	F3S	4b	400	-10	68	1	6.5	3.42	250000	1.43 and 0.63
5	C1	F3F	5a	48	-10	46	1	6.5	3.42	50000	1.43 and 0.63
	C3	F4F	5b	400	-10	68	1	6.5	3.42	250000	1.43 and 0.63
6	C1	F4S	6a	48	-20	68	1	6.5	3.42	50000	1.43 and 0.63
	C3	F4S	6b	400	-10	68	1	6.5	3.42	250000	1.43 and 0.63
7	C1	F4F	7a	87	-20	68	1	6.5	3.42	50000	1.43 and 0.63
	C3	F4F	7b	400	-10	68	1	6.5	3.42	250000	1.43 and 0.63
8	C3	F5F	8a	400	-10	68	2	6.5	3.42	250000	1.43 and 0.63
	C1	F5F	8b	87	-20	68	2	9.75	3.92	50000	1.63 and 0.73
9	C3	F5S	9a	400	-10	68	2	6.5	3.42	250000	1.43 and 0.63
	C1	F5S	9b	87	-20	68	2	6.5	3.42	50000	1.43 and 0.63

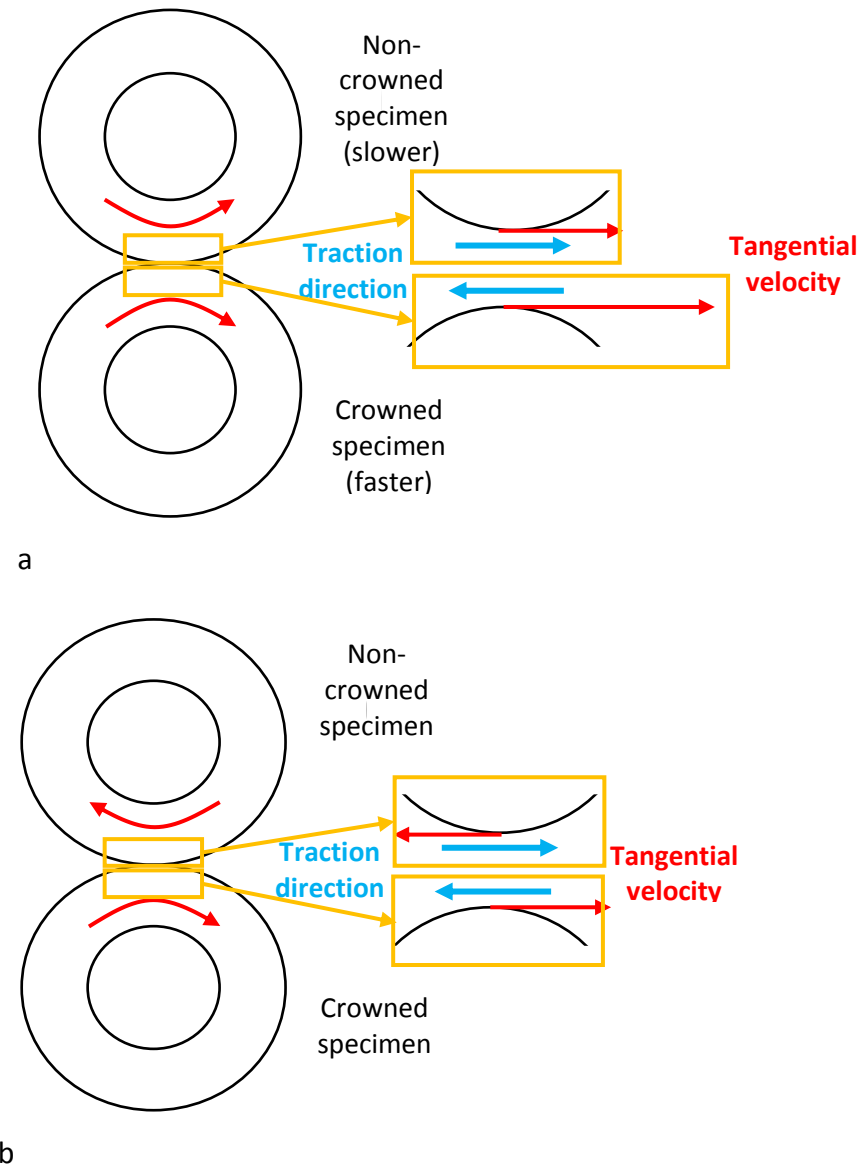


Figure 7.1.2: Illustration of rotation directions used for the RST1 in Table 7.1.2 (a) for RST 1a and 1c and (b) for RST 1b

Table 7.1.3: Investigated variables by RSTs

Tests to be compared		Variable to be changed	Values of variation
7	3	Slip ratio	-20% $\rightarrow$ -10%
4	7	Viscosity	SP46 $\rightarrow$ SP68
6	7	Speed	48 rpm $\rightarrow$ 87 rpm
8	9	Load	3.92 GPa $\rightarrow$ 3.42 GPa
7	9	Sequence	1 $\rightarrow$ 2

## 7.2 Coefficient of Friction at Different Testing Conditions

This section presents the obtained values of COT under various load, speed and slipping ratios. The tests were conducted according to the sequence and testing variables in Table 7.1.1. It was found that, for a lubricated test under certain testing conditions, the COT does not vary significantly after a specific number of cycles, as shown in Figure 7.2.1 (a) and (b). However, for dry contact, the COT reaches a very high value as shown in Figure 7.2.2 (a). Figure 7.2.2 (b) shows that the applied load was varying around the value of 3.5 kN, while the slip ratio in Figure 7.2.2 (c) shows unstable value for the first 350 cycles and thus the COT may be affected within this range of cycles. Although dry contact may not be expected in the WTGBs, it shows the possible COT values during metal on metal contact. In this test, the highest speed, 400 rpm, was used to simulate an instant dry contact. It is found that low slip ratio, -1%, caused a rapid increase in the COT and considerable surface damage. The heat generated could be the main reason for the adhesive surface damage and the increase in COT. However, the accumulation of heat after a number of cycles and increasing the flash temperature reduce the COT due to the oxide formations.

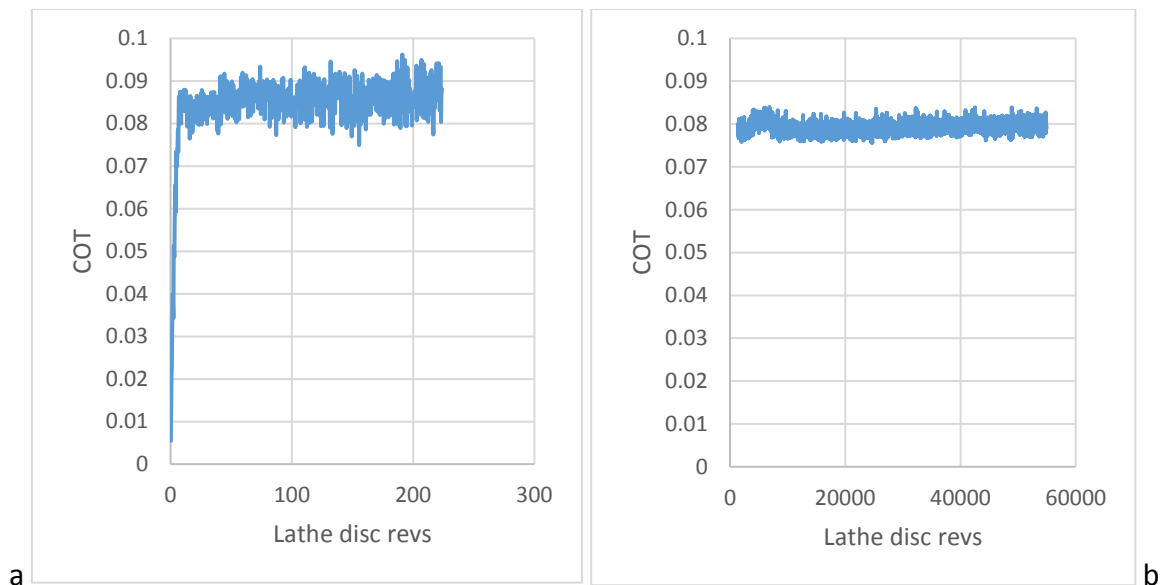
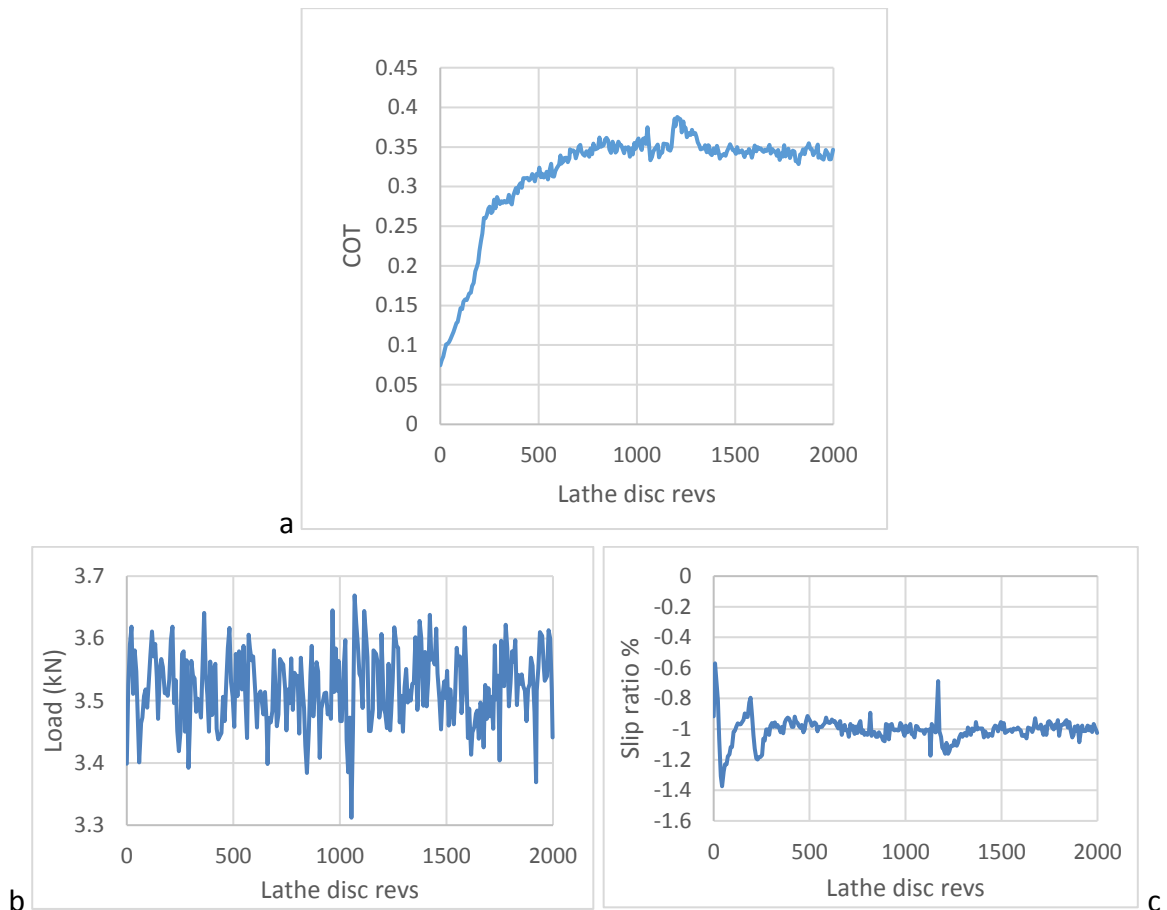


Figure 7.2.1: COT variation with number of cycles according to Table 7.1.1 (a) COT1 (b) COT2



**Figure 7.2.2: (a) COT variation with number of cycles for dry contact (COT3) according to Table 7.1.1 (b) applied load (c) slip ratio**

After the COT measurement tests, the surfaces examination of specimens used for lubricated tests showed a very mild wear track which only reduced the roughness of the surface, as shown in Figure 7.2.3 (a), while after the dry test, the surfaces were highly damaged, as shown in Figure 7.2.3 (b) and (c).

To investigate the effect of reversed rotation on the COT, Test 1 (b), as specified in Table 7.1.2, was conducted for a few minutes only at low speed and a relatively low load, as shown in Figure 7.2.4. This variation of the COT shows that not only dry contact, such as in Figure 7.2.2, can cause a high COT but a very well lubricated contact surfaces can do so as well when the reversed rotation occurs for a brief time. In this figure, the COT jumped to a higher value after the maximum contact pressure reaches  $2.78 \text{ GPa} = 3.5 \text{ kN}$  as shown by the dashed line in Figure 7.2.4, although the load was being gradually increased. Accordingly, the instant reversed rotation under this level of contact pressure can cause high COT. Reversed contact can simulate the torque reversal when roller reversed rotation direction. The accelerated damage observed on the surface and under the surface, as shown in Section 7.3 and 7.4, could explain the premature failure of wind turbine bearings, which can be caused by changes in the direction of rotation. Due to safety regulations related to using the SUROS machine, reversed rotation was not repeated in any other test in this research.

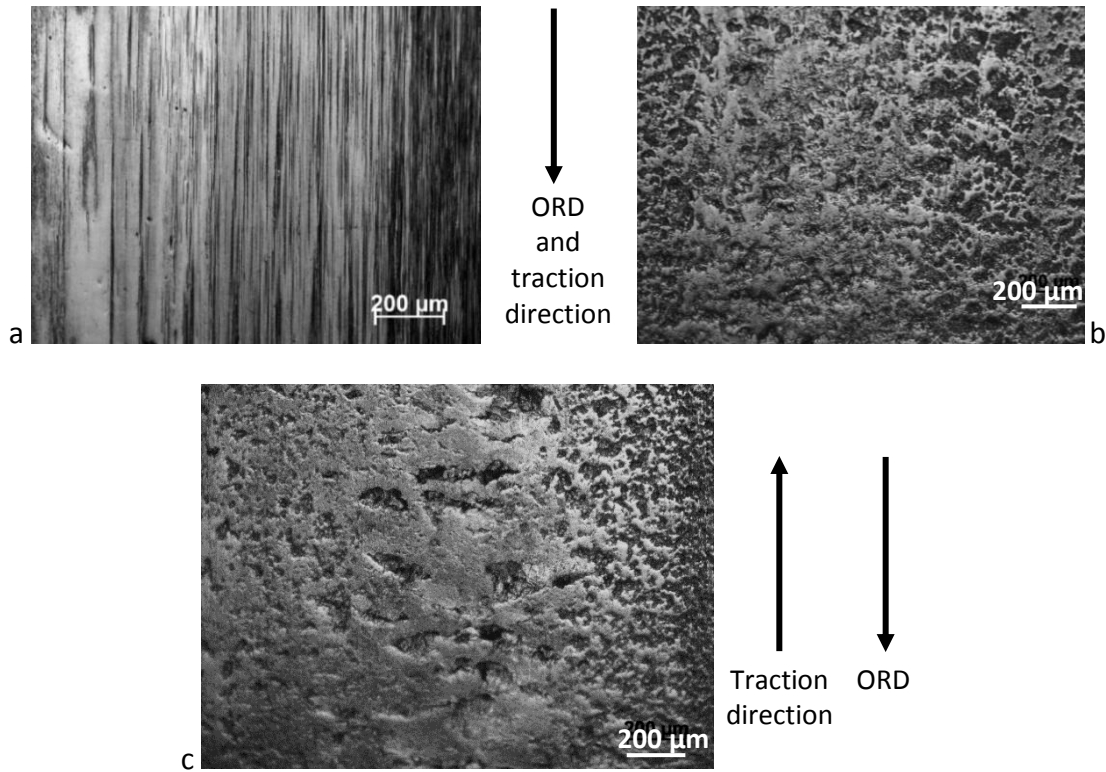


**Figure 7.2.3:** The surface after the COT measurement tests in Figures 7.2.1 and 7.2.2 (a) F1S after lubricated tests; (b) F1S after high speed dry test; and (c) C1 after high speed dry test.

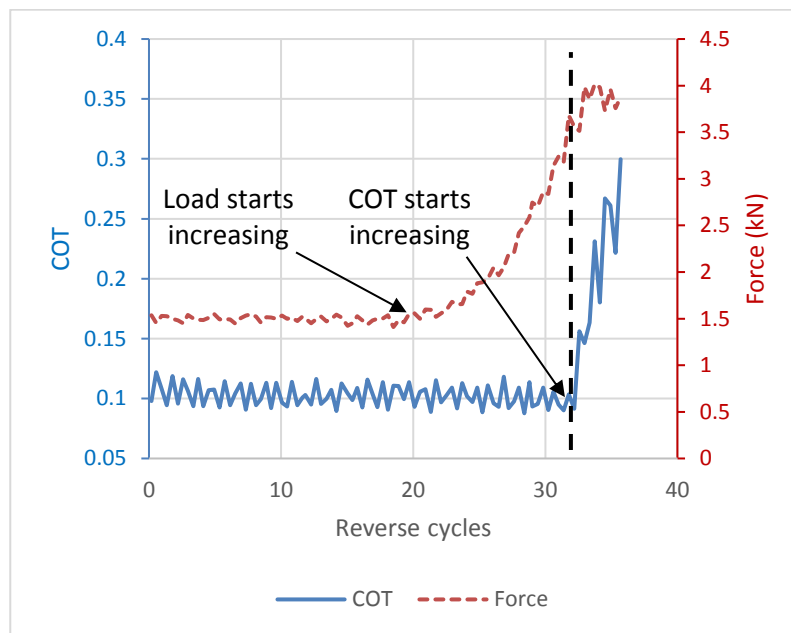


**Figure 7.2.4:** COT during reversed rotation according to testing conditions in Table 7.1.2.

The recording of COT was logged during the specified RSTs in Table 7.1.2 and the data was analysed to calculate the average and standard deviation of the COT for each test, as shown in Figure 7.2.5. As expected the COT during the low speed step of each test is higher than that during the high-speed step for each test, the same observation was found for the overall average shown in Figure 7.2.6. This indicates that the tests were running in the

mixed lubrication regime where higher speed produces a thicker lubricant film and less COT. This has also been confirmed by the calculation of the lambda ratio ( $\lambda$ ) in Section 7.3. Accordingly, the greater surface damage was observed from the low speed step test as a result of more asperities in contact. Because the low speed chosen in this research is within the range of the real tangential speed of wind turbine planetary bearings, the measured COT under the investigated testing conditions could be representative for the COT of planetary bearings in a WTG.

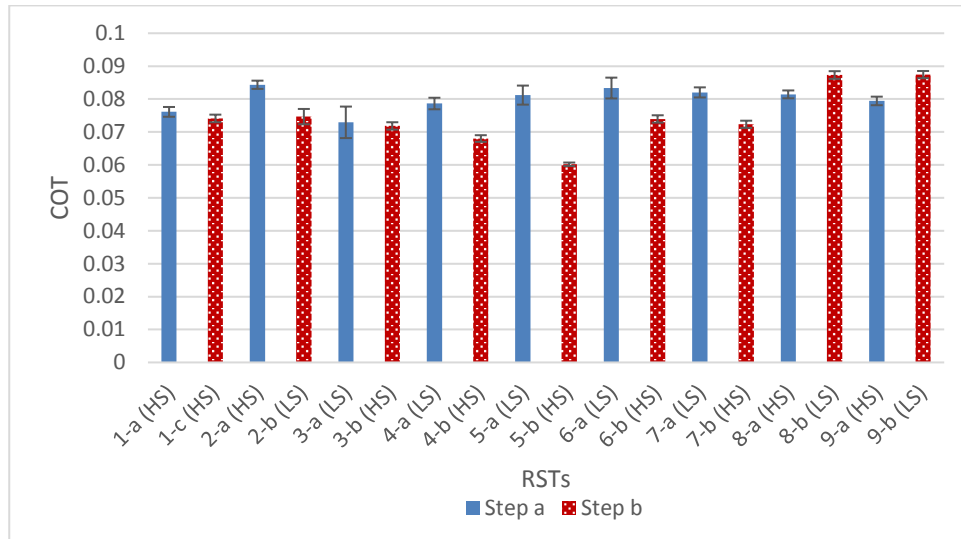


Figure 7.2.5: COT of RSTs 1 to 9 at High Speed (HS) and Low Speed (LS) steps

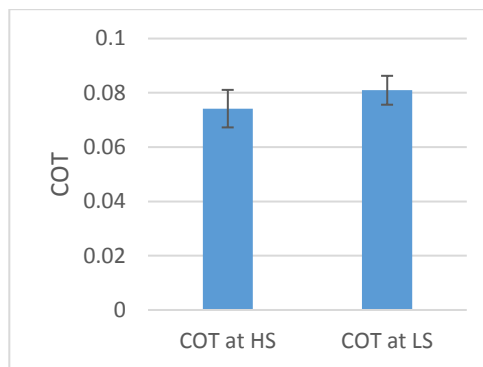
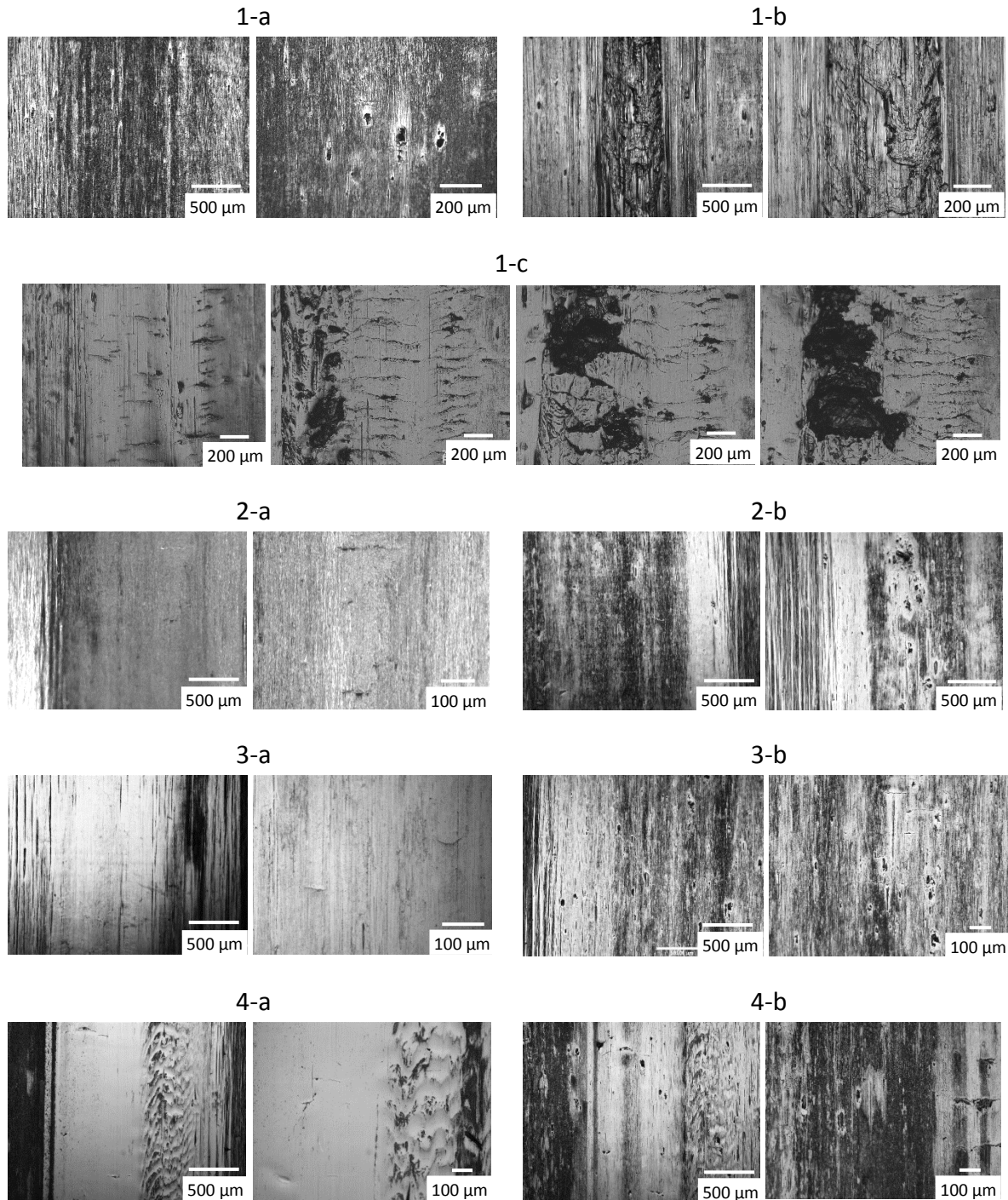


Figure 7.2.6: Overall average for RSTs at High Speed (HS) and Low Speed (LS) steps

### 7.3 Effects of Tested variables on Surface Damage and Wear

After conducting the nine RSTs specified in Table 7.1.2, the surfaces of the specimens were examined to compare the observations between the tests, and to highlight the most important variables affecting damage. The tests were designed to investigate the effect of each tested variables individually. The characters compared were the maximum size of cracks and pits on the surface; surface roughness; wear rate; and lambda ratio between  $h_{\min}$  and the composite surface roughness. The optical microscope was used to take images from selected regions on the surface, as shown in Figure 7.3.1. Because the minimum

magnification of 50 times cannot cover the whole width of a specimen, a number of images from the surface of each specimen were stitched together (montaged) to form the images in Figure 7.3.2. In this figure, images (a) to (e) show two wear scars on each of the flat specimens and images (f) and (g) show one wear scar on the crowned specimens. These images illustrate the variation of surface topography across the contact width. In this figure, it was found that the blue colour in Image (f) and (g) is changing with the light source and no thermal effect is expected to cause this colour.



**Figure 7.3.1: Non-crowned specimen surfaces at the middle of the contact width after each step of RSTs 1 to 9 (continue to the next page)**

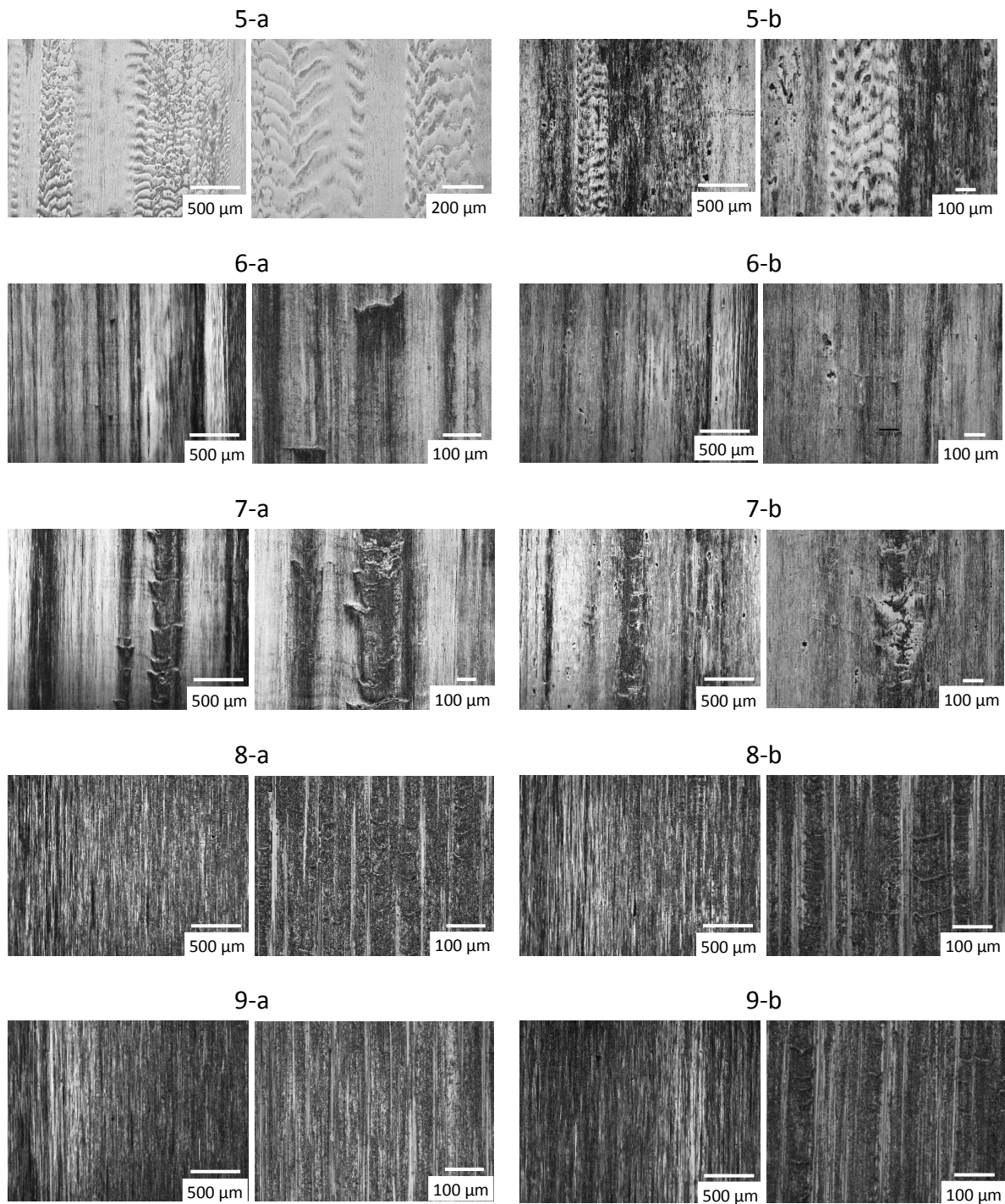


**Figure 7.3.1: Non-crowned specimen surfaces at the middle of the contact width after each step of RSTs 1 to 9 (continue from previous page)**

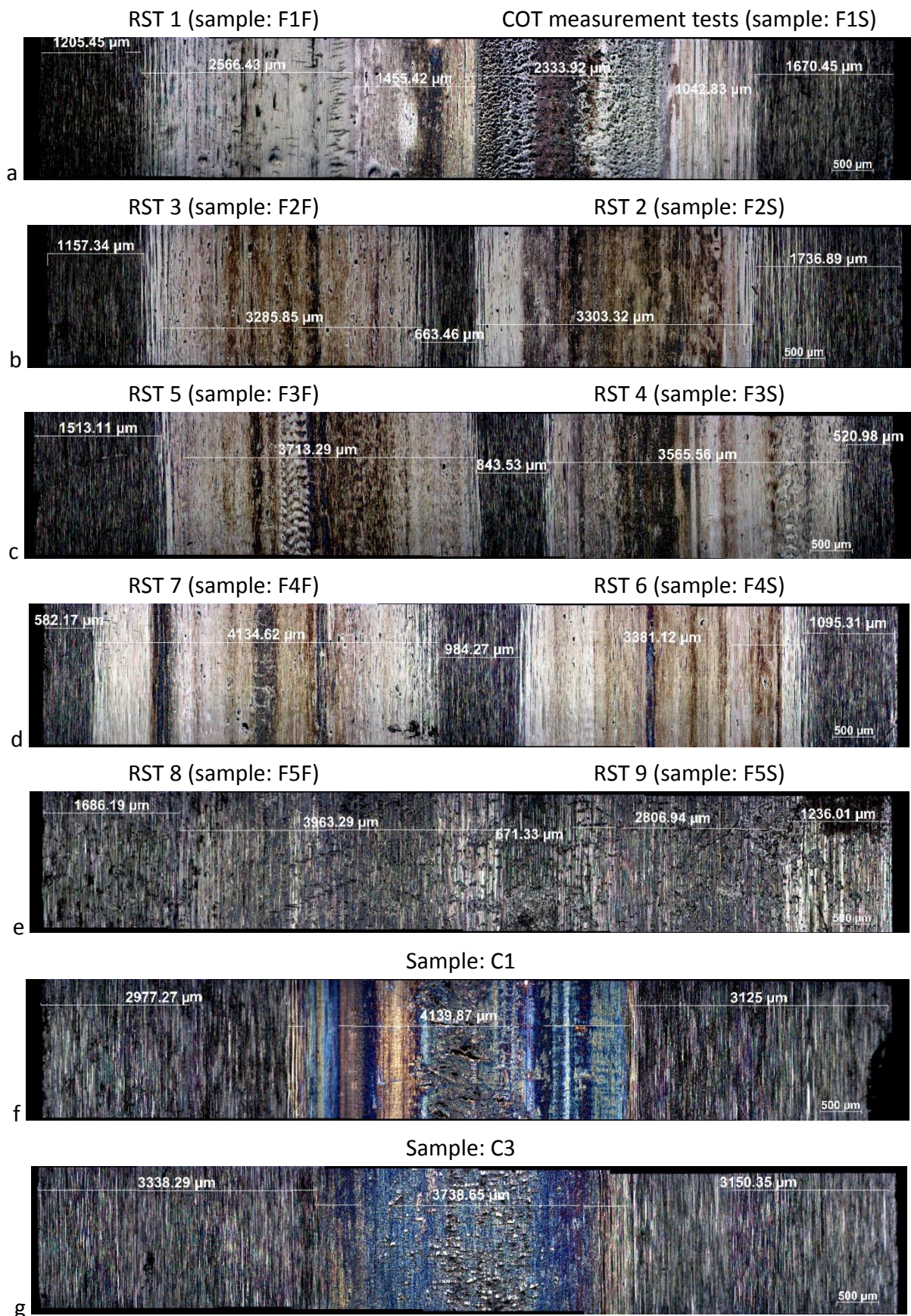


Figure 7.3.2: Specimen surfaces after RSTs and COT measurement tests

The maximum size of cracks and pits on the surface, as defined in Figure 7.3.3, were measured for each wear scar by using the optical microscope. The surface across the width of the specimen was scanned at four equidistant regions around the circumference. Although this method could reflect the local development of surface damage, it neglects the density and distribution of this damage. However, based on observing a number of images of the surface around the circumference, general description of the surface after each test was made and used for the analysis. The results shown in Figure 7.3.4 reveal a maximum crack and pit size on the surface of specimen F1F, which occurred after RST 1 (c). However, not the whole circumference of specimen F1F shows big spalls/pits, which are the development of the observed damage after RST 1 (b), where some regions show only axial cracks, as can be seen from Figure 7.3.2 (a). Apart from RST 1, RST 7 shows the maximum size of cracks and pits on surface. By comparing this test with RST 9, the roll of sequence 1 will be clear where a high slip ratio was applied in the first step of RST 7. Although the surface damage mode observed from RSTs 4 and 5 was not similar to that found from the failed bearings, they showed relatively large-sized cracks ( $\sim 400\text{-}500\ \mu\text{m}$ ) on surface at the centre of the contact width. For all the tests that developed pits, it was found that pits are developed by axial surface cracks that are close to each other.

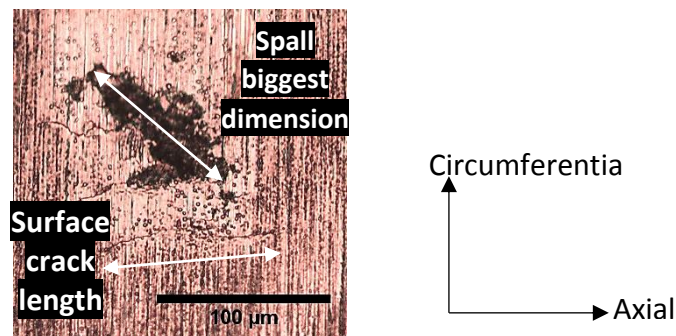


Figure 7.3.3: Surface damages measurement

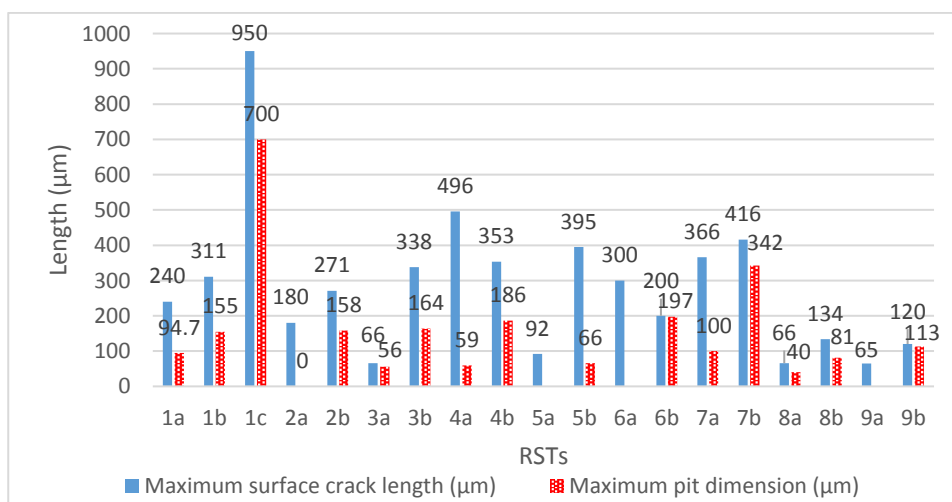
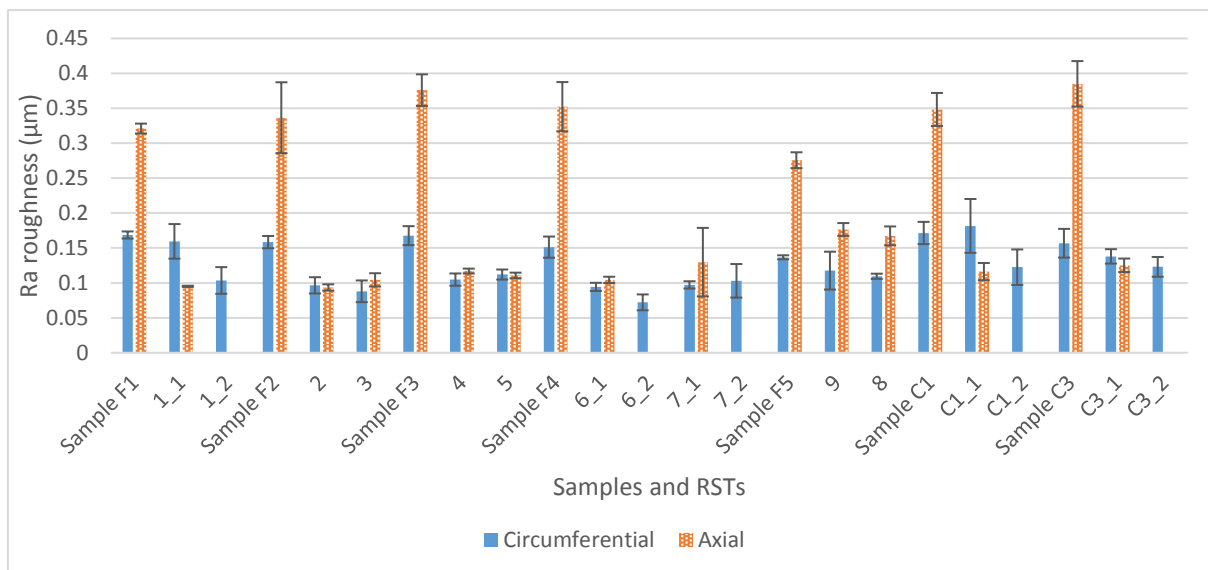


Figure 7.3.4: Maximum size of surface cracks and pits after each step of RSTs 1 to 9

According to the procedure described in Section 4.3, the surface roughness for the specimens used for the RSTs was measured, as shown in Figure 7.3.5. Some wear scars show a central band of different roughness. Accordingly, in Figure 7.3.5, the under-scroll sign 1 refers to the measurement inside the central band and 2 for outside of this band. Using the non-contact Infrared thermocouple, as described in Section 4.1, it was found that the temperature increased rapidly during the first 30-60 minutes of the RSTs, and became more stable after this period of time. For the RSTs steps conducted at low speed (48 and 87 rpm), the average temperature was around 32 °c, and for those at 400 rpm the average temperature was around 50 °c. Sometimes when a test at 400 rpm was running for many hours continuously, the temperature exceeded 60 °c; however, in such a case the test was stopped until the temperature drops. Considering the oil viscosity at 32 °c and 50 °c, the minimum lubricant film thickness  $h_{min}$  is calculated according to the EHL formulas in Chapter 2. The  $h_{min}$  is compared to the composite roughness  $R_{eq}$  to find the lambda ratio ( $\lambda$ ) in Figure 7.3.6, where  $R_{eq}$  is calculated from the final roughness of the flat and the crowned specimens using Equation 2.4.3.2. The circumferential roughness in Figure 7.3.5 was used when considering the higher value, when there is a central band of the wear scar. For all test steps conducted with 400 rpm,  $\lambda$  values were almost one, which makes the asperities on the surfaces almost separated, While at low speeds, 48 and 87, the  $\lambda$  values reveal  $h_{min}$  considerably less than  $R_{eq}$ , and thus a boundary lubrication regime and partial contact between the surfaces are expected. However, no severe damage was observed on the surface, as optical images and the variation of the roughness imply. The reason could be extreme pressure additives, which prevent direct metal on metal contact at low surface roughness. However, the damage occurred during the reverse rotation, confirming the incapability of these additives to protect the surface in such circumstances.



**Figure 7.3.5: Surface roughness of specimens before and after RSTs 1 to 9. The under-scroll sign 1 and 2 refer to the measurement inside the central band of the wear scar or outside it, respectively**

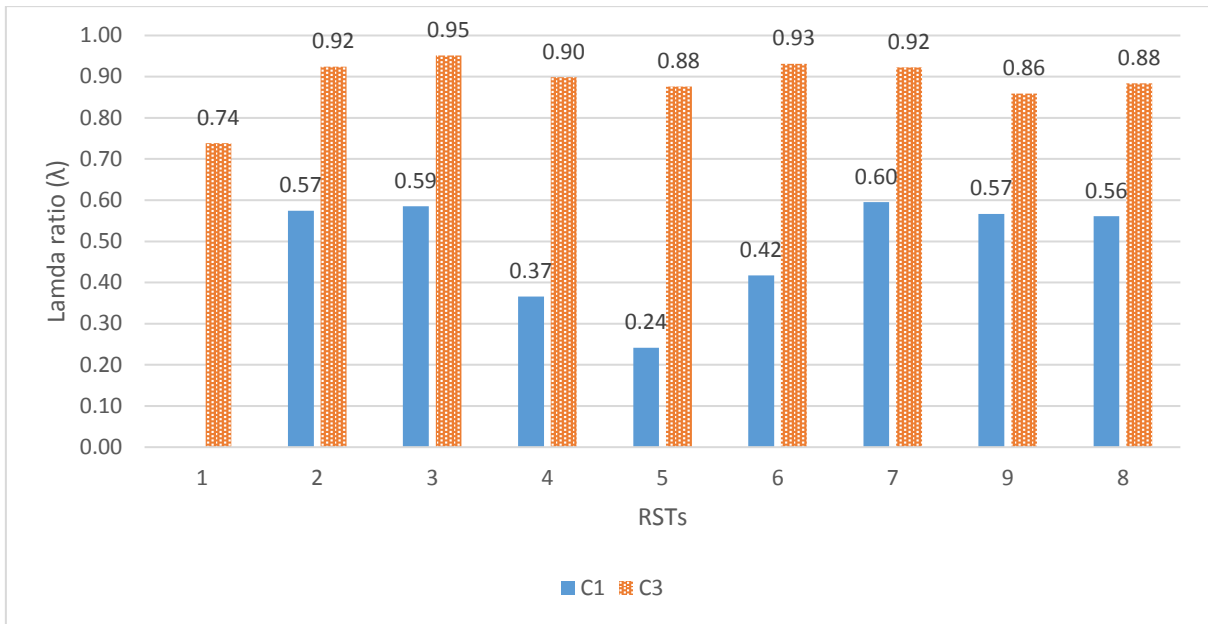


Figure 7.3.6: Lambda ratio (λ) after RSTs 1 to 9

Figure 7.3.5 shows that the initial roughness varies from one specimen to another; therefore the percentage change in roughness relative to the original roughness of each specimen was calculated, as shown in Figure 7.3.7. The first observation from this figure for all the specimens, except C1, is the smoothing of the surfaces after the RSTs, which designates mild wear and a low level of surface damage. Another observation is the clear difference between the change in axial and circumferential direction. These observations imply that the calculation of the lambda ratio should not be based on the initial surface roughness, which varies/reduces quickly after the running in time.

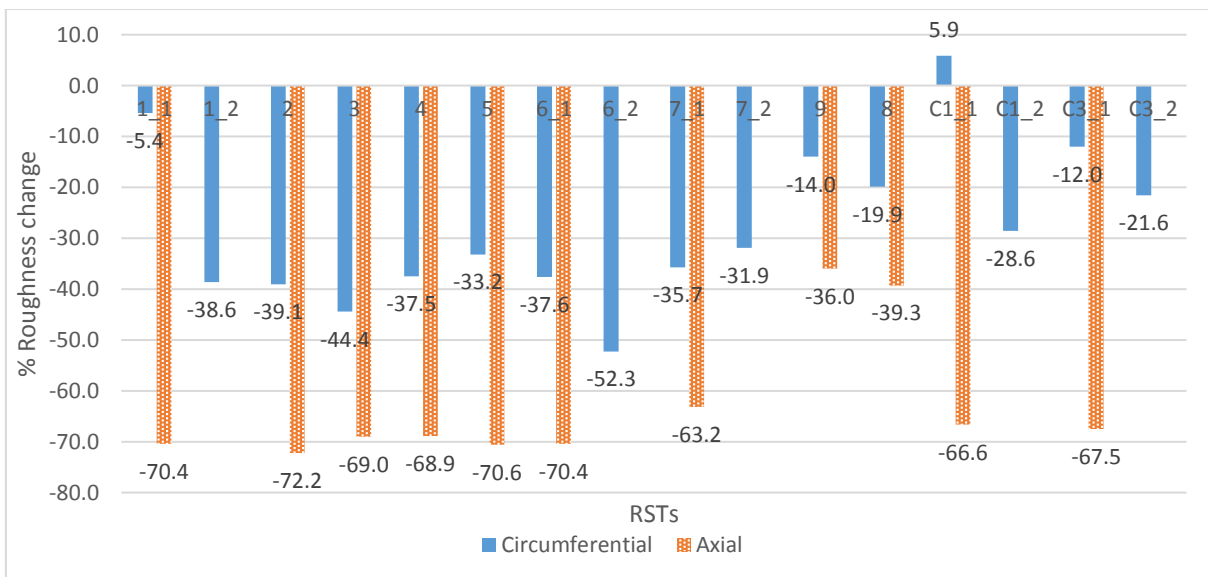
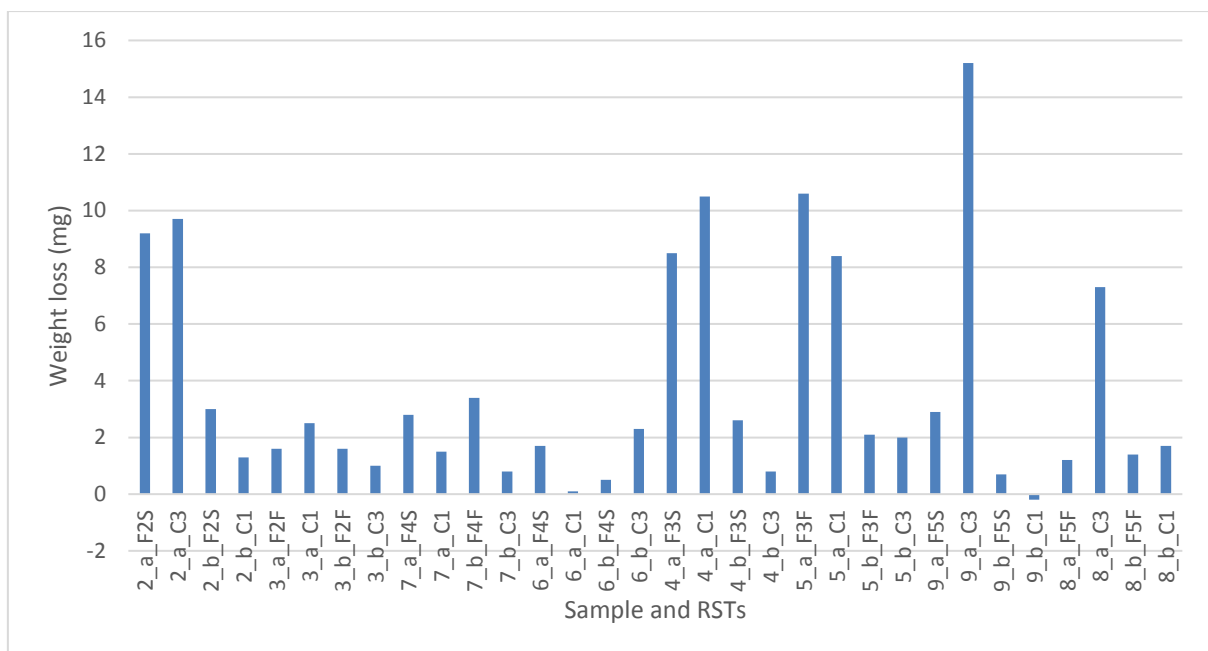


Figure 7.3.7: Percentage change of surface roughness after RSTs 1 to 9

The wear rate was measured by the weight loss from the flat and the crowned specimen after each step of the RSTs, as shown in Figure 7.3.8. In this figure, each of the labels of the x-axis refers to a test's number, steps and the specimen used for the test separated by under-scroll. The labels were sorted according to the sequence in which the tests were conducted. In general, the wear rate is very limited and within the range of milligrams. However, the wear rate for some tests can be considerably higher, compared to other tests. The relatively high wear rate during the first step of RST 2 could be caused by the initial roughness of C3, which was being used for the first time in this test step. The effect of low viscosity on wear rate is shown by the weight loss of Tests 4 and 5 in Figure 7.3.8, where these tests were conducted using the oil of least viscosity. For the crowned specimen C3, the weight loss increased significantly during Tests 9 and 8 because of the initiation of surface pitting, after being used for 1.5 million cycles during Tests 2 to 7.



**Figure 7.3.8: Specimen weight loss after each step of the RSTs 1 to 9 (each of the labels of the x-axis refers to the test number, steps and specimen used for the test separated by an under-scroll)**

To sum up the effect of each of the investigated variables on the observed surface damage, Table 7.3.1 was developed. In this table, each pair of tests was referred to as Test A and Test B. This pair has similar testing conditions, except that only one investigated parameter that varied in Test B. The observations from Test B were compared to that in test A, based on the measurement and analysis in the figures aforementioned in this section, 7.3. This table shows some variables which can increase surface damage, such as increasing the slip ratio and contact pressure (normal load), and other variables that can mitigate this damage, such as reducing the speed and changing the sequence of load steps to high speed first. As the  $\lambda$  calculations show, the tests were running in the boundary lubrication regime at low speeds. This makes a higher slipping ratio causing more relative sliding between the

contacted bodies and more surface strain that accumulates to fatigue the surface and start cracking under mode II. Higher speed within the boundary lubrication regime was found to increase the temperature and the surface damage, which could be due to the higher strain rate at a higher speed. Although damage accumulation theories, such as the Miner rule, neglect the effect of load sequence, this research has found that the sequence has an effect on the surface damage during the RSTs. The results show that the propagation of surface damage was accelerated even under less severe conditions when the surface damage initiates first under the low speed testing. This highlights the importance of avoiding severe tribological conditions or loading at the beginning of a bearings life.

**Table 7.3.1: Effects of investigated variables on surface observations from RSTs 1 to 9 where LS and HS are the low and high speed steps, respectively**

Test A	Test B	The different Parameter in Test B	% Change of Roughness	Maximum surface Crack length	Maximum pit size	Wear rate
3	7	Slip ratio was increased in RST 7 at sequence 1	Reduced	Increased	Increased	Increased
7	4	Viscosity was decreased in RST 4	Increased	Increased (LS) Reduced (HS)	Reduced (LS) Reduced (HS)	Increased (LS) Reduced (HS)
7	6	Speed was decreased in Test 6	Increased	Reduced	Reduced	Reduced
9	8	Load was increased in RST 8	Increased	Increase (HS) Increase (LS)	Increase (HS) Reduced (LS)	Reduced (HS) Increase (LS)
7	9	Sequence was changed from 1 to 2 in RST 9 at -20% slip	Reduced	Reduced	Reduced	Reduced
3	2	Sequence was changed from 1 to 2 in RST 2 at -10% slip	Circumferential: reduced Axial: increased	Reduced	Reduced	Increased

#### 7.4 Effects of Tested Variables on Subsurface Damage and Hardness

The metallurgical investigation of the RST specimens and the crowned specimens C1 and C3 used with the RSTs was conducted using the methods described in Chapters 3 and 4. For each test, samples in axial and circumferential directions were prepared and examined using optical and scanning electron microscopes. For the tests with non-uniform surface damage distribution, such as Test 1, more than four samples were prepared and examined. The first metallurgical observation was of the elongated MnS inclusions, which are almost parallel to the surface in axial sections and have an almost circular shape in circumferential sections. On the other hand, the samples prepared from the uncoated failed bearing show a more elliptical shape to the MnS inclusions, with a clear inclination angle relative to the surface in axial and circumferential sections. The observations of different types of damage from these specimens are surface-linked RCF cracks, micro-cracks initiated by inclusion, cracked inclusion, debonded inclusion, possible butterfly wings, pits and spalls, as shown in Figure 7.4.1.

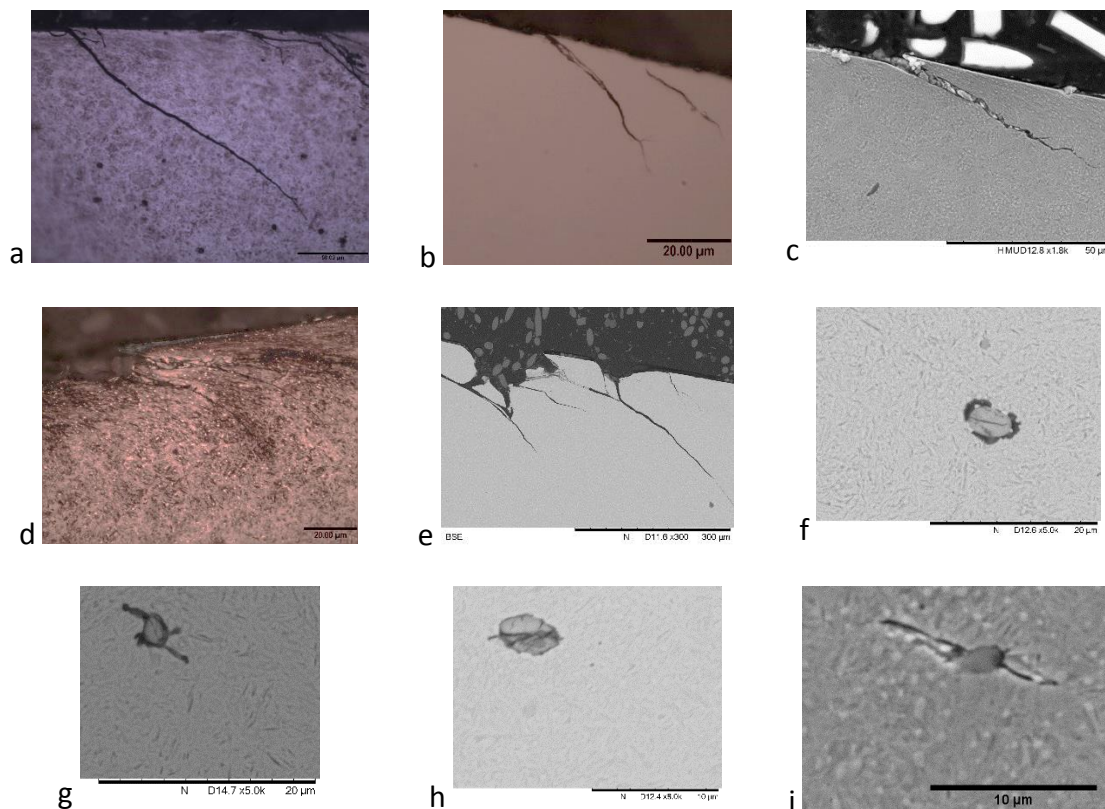


**Figure 7.4.1: Observations from metallurgical examination of RSTs specimens: (a) - (c) Surface-linked RCF cracks, (d) and (e) Pits and spalls (f) Debonded and cracked inclusion (g) and (h) Cracked inclusions initiated micro crack and (i) Possible butterfly**

To evaluate and compare the subsurface damage from each test, statistics analysis was conducted, as shown in Figures 7.4.2 and 7.4.3, with the angle being measured relative to the ORD. These analyses help identify the types of damage that occur due to the investigated variables and quantify their damage characteristics and severity.

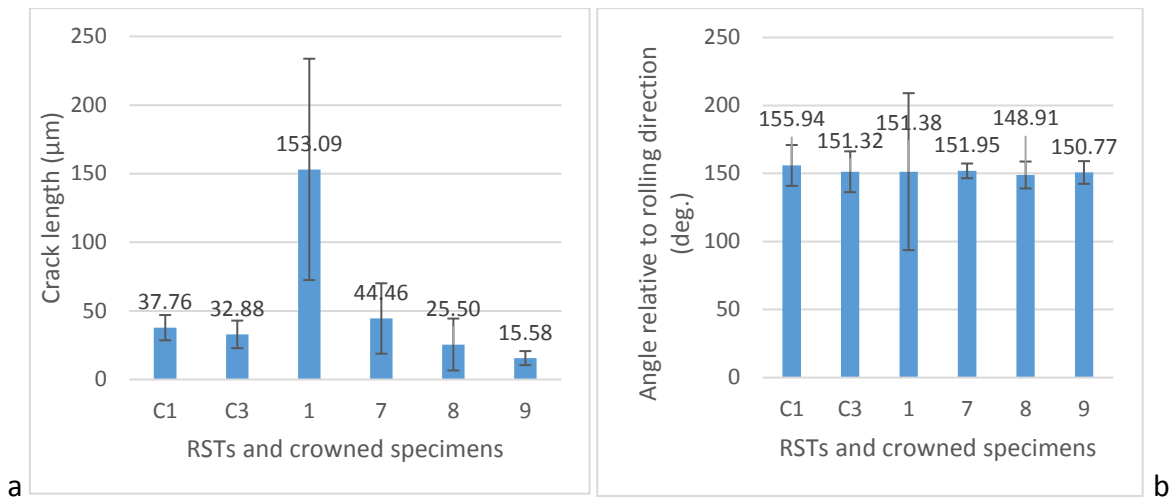


Figure 7.4.2: Surface-linked RCF cracks in circumferential direction: (a) Length and (b) Angle

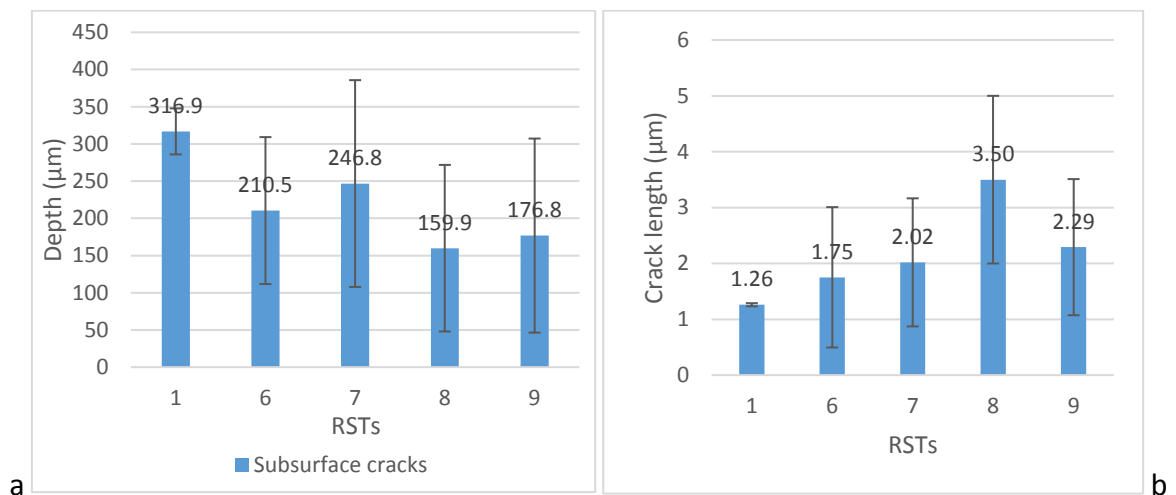
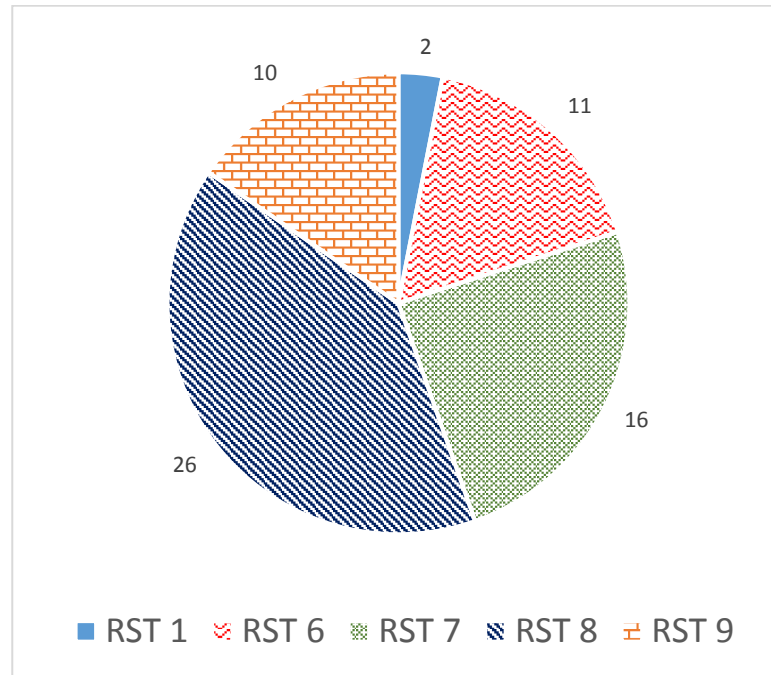


Figure 7.4.3: Micro-cracks initiated by inclusions: (a) Depth in axial and circumferential direction (b) Length in circumferential direction

The results of the analysis are based on damage observed on the subsurface. However, it is not necessarily a complete reflection of all the existing damage, because they were only at the initiation stage and hard to be detected. In addition, the destructive sample preparation technique could remove some of the damage during the preparation. For example, none of the catalogued damage was found in the specimens of RST 4 and 5, despite the cracks observed on the surface. Although these cracks should be observed by the subsurface examination, they might be very shallow in depth and only a few of them exist, which make their detection more difficult. Other tests show only one case of damage, such as RST 2, which shows only one surface-linked RCF crack, and RST 3, which shows one inclusion-initiated micro-crack. These cases cannot be considered to be representative of these tests; accordingly, they were excluded from Figures 7.4.2 and 7.4.3. Although RST 1 shows only two inclusion initiated micro-cracks, they are considered in Figure 7.4.3. However, they are cautiously taken into account, without considering this result being

conclusive. The total number of inclusions that initiated subsurface cracks is shown in Figure 7.4.4.



**Figure 7.4.4: Number of inclusion initiated micro-cracks in axial and circumferential sections**

The tests are compared based on the characteristics of surface and subsurface damage, as shown in Figures 7.4.2 and 7.4.3. The conclusions drawn from these figures are:

1. High instant surface traction results in dominant surface-linked RCF, as shown by the result of RST 1 in Figure 7.4.2 (a).
2. Higher load results in longer and more inclusion-initiated micro-cracks, as shown by the results of RSTs 8 and 9 in Figures 7.4.3 (b) and 7.4.4;
3. The variables investigated have no clear effect on the average angles of the surface-linked RCF, as shown in Figure 7.4.2 (b);
4. From the results of RSTs 7 and 9 shown in Figures 7.4.2 (a) and 7.4.3 (b), sequence 1 (low speed step then high speed step) results in bigger surface-linked cracks, while sequence 2 (high speed step then low speed step) results in bigger subsurface cracks;
5. The lower speed in RST 6 compared to higher speed in RST 7 causes inclusion initiated micro-cracks that are closer to the surface, as shown in Figure 7.4.3 (a). Lower speed should produce smaller  $h_{\min}$  and consequently higher surface traction in the boundary lubrication regime and bring  $\tau_{1(\max)}$  closer to the surface.

The conclusions from the subsurface observations can be summarised in Table 7.4.1. In this table, each pair of tests have the same testing conditions, except for one variable being different which varies in Test B with no subsurface damage observed for RSTs 2, 3 and 4.

**Table 7.4.1: Effects of investigated variables on subsurface observations from RSTs 1 to 9**

Test A	Test B	The different Parameter in Test B	Length of surface-linked RCF cracks	Length of micro-cracks initiated by inclusions	Maximum hardness distance from surface
3	7	Slip ratio was increased in RST 7 at sequence 1	Increased 0 → 44.5 μm	Increased 0 → 2 μm	Closer 370 → 270 μm
2	9	Slip ratio was increased in RST 9 at sequence 2	Increased 0 → 15.6 μm	Increased 0 → 2.3 μm	Closer 570 → 270 μm
7	4	Viscosity was decreased in RST 4	Reduced 44.5 → 0 μm	Reduced 2 → 0 μm	Deeper 270 → 470 μm
7	6	Speed was decreased in RST 6	Reduced 44.5 → 0 μm	Reduced 2 → 1.8 μm	Closer 270 → 70 μm
9	8	Load was increased in RST 8	Increased 15.6 → 25.5 μm	Increased 2.3 → 3.5 μm	Deeper 270 → 370 μm
7	9	Sequence was changed from 1 to 2 in RST 9 at -20% slip	Reduced 44.5 → 15.6 μm	Increased 2 → 2.3 μm	Similar 270 μm

Another comparison between the test results was carried out by measuring the hardness variation under surface, as described in Section 3.3.2. The objective of these measurements was to investigate the effect of the tested variables on hardness under the surface and thus the subsurface damage. Figure 7.4.5 shows the average and standard deviation values for subsurface hardness measured from the specimens of RSTs and the crowned specimens C1 and C3. Although the variation of hardness is not very clear, which is probably mainly due to the limited number of cycles, it can still give an indication of the testing condition and show the effect of the variables investigated on the hardness at different depth. Despite the relatively big distance between the indents, which could conceal the exact location of maximum hardness, it is found that the depth of maximum

hardness can indicate the depth of subsurface damage for some of the RSTs, such as 1 and 7 in Figure 7.4.3 (a). Other RSTs, such as 8 and 9, show a deeper location of maximum hardness than the depth of subsurface damage. Although in RST 1 only two subsurface cracks were found, their depth in F1F seems to be representative of the location of maximum hardness, which is also close to the location of  $\tau_{1(\max)}$ . Except for the reversed rotation of a few cycles, the F1F specimen was exposed to surface traction acting in the same direction as the tangential velocity, or negative slip, as shown in Figure 7.1.2 (a), at more than one million cycles. The C3 that also runs for two million cycles under similar conditions for surface traction and tangential velocity, as shown in Figure 7.1.1, shows subsurface hardness trend almost similar to that of F1F. The sequence of the RSTs steps shows an effect on the subsurface hardness. This can be shown by comparing the location of maximum hardness for RST 7 and 9. It can be concluded that sequence 1 (low speed step then high speed step) shows the effect of surface traction by bringing the maximum hardness closer to the surface. One of the uncertainties in the measurement of hardness could be the offset from the central line under the point of the maximum contact pressure. Overall, the maximum hardness is closer to the surface than the location of  $\tau_{1(\max)}$  for all the RSTs that show subsurface damage. In addition, inconclusively, the average depth of the subsurface damage matches the location of maximum hardness for RSTs with sequence 1 rather than those with sequence 2.

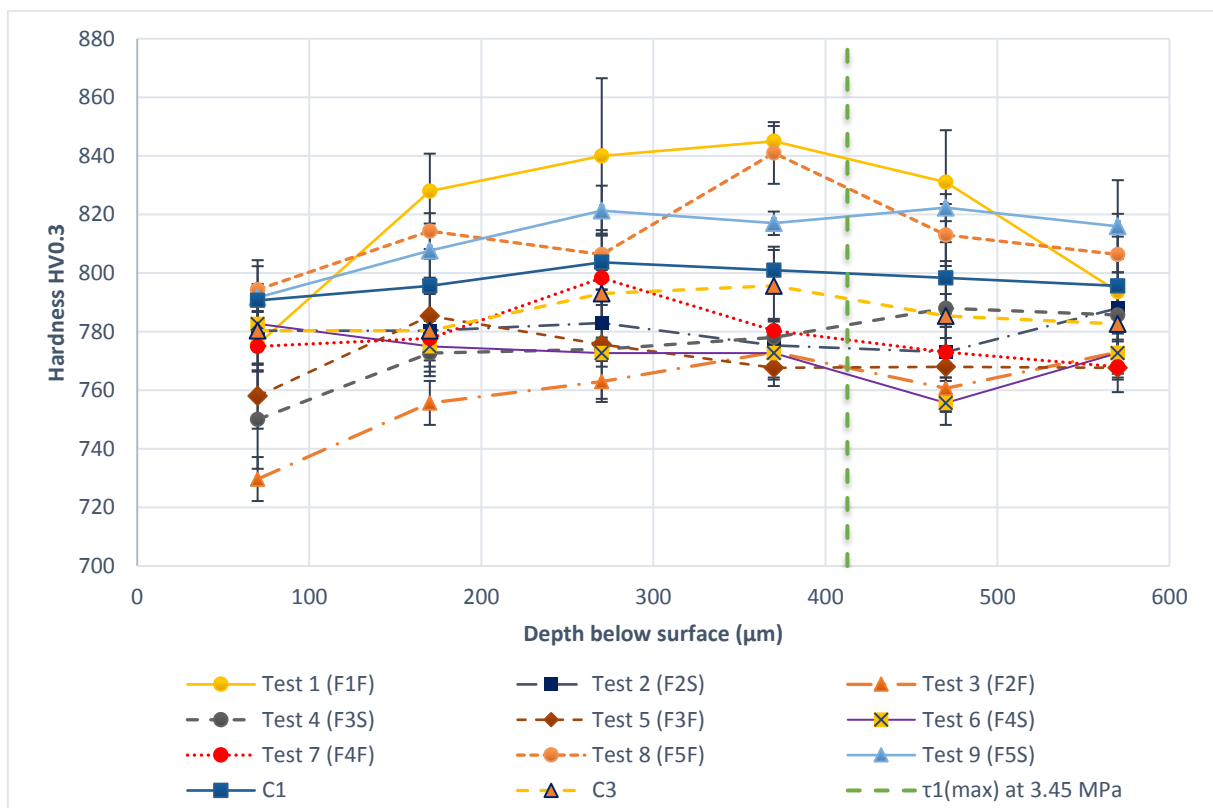
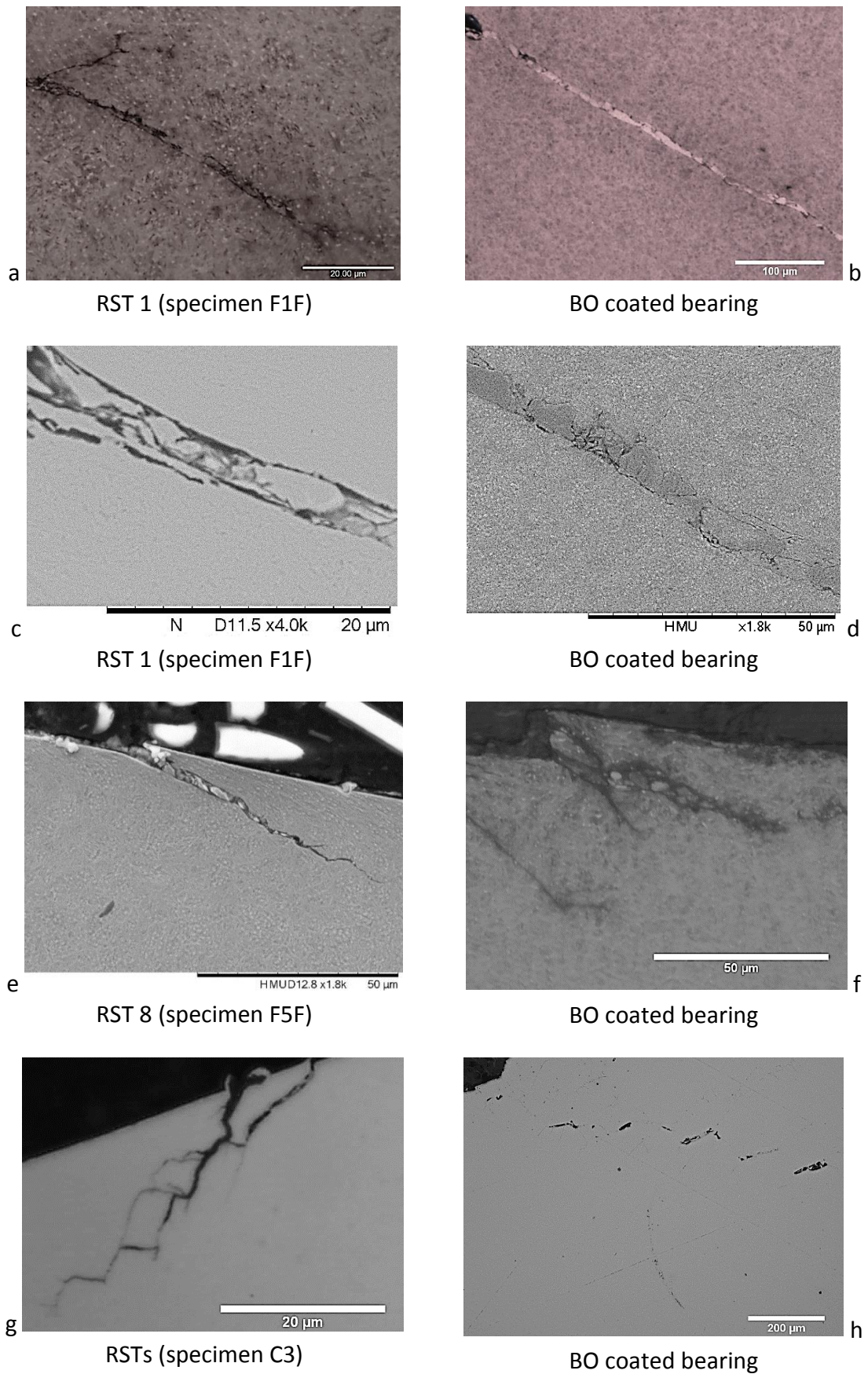


Figure 7.4.5: Variation in subsurface hardness after RSTs

## 7.5 Comparing Damage between Specimens and Failed Bearings

The comparison between some of the subsurface damage observed in the examined bearings and that from the specimens of RSTs improves the understanding of the initiation mechanisms of surface and subsurface damage. A selected number of images from the metallurgical examination of subsurface damage were chosen to show the visual similarity between the surface-linked RCF cracks that occurred in some of the RSTs and that in the examined bearings as shown in Figure 7.5.1. Additionally, the four types of subsurface damage initiated from inclusions, including possible butterflies, were found in the RST specimens and compared to those from the failed bearings, as shown in Figures 7.5.2 to 7.5.4. The characteristics, such as crack length and angle, of the similar observations can be compared using the statistics in Figures 6.4.3 and 7.4.2.

The contact geometry for the RSTs is only an approximation of the actual contact between rollers and raceways in planetary bearings. Although the characteristics and distributions for non-metallic inclusions inside the RSTs specimens may not be the same as that found in the bearings, the inclusions still debonded which was the main effect. The examinations of the RSTs specimens exhibited surface and subsurface initiated damage that show clear similarities to the observations from the failed bearings, in terms of appearance and inclination angle. These results confirm subsurface damage initiation from inclusions. However, the limited test cycles of the specimens, comparing to the millions cycles of real bearing's life, did not produce the subsurface damage to the level of severity as that observed in the failed bearings; it could be the reason for not being able to find clear microstructure alterations in the form of WEA and WECs. Some of the surface-linked RCF cracks appeared as a stair of linked cracks that are similar to the observations from the examined bearings as shown in Figure 7.5.1 (g) and (h). These types of cracks have been explained in previous study to be caused by impact loading [66], however, this explanation is not in line with the finding from this thesis since these cracks have been observed without impact loading in the RSTs.



**Figure 7.5.1: Surface-linked RCF cracks in circumferential sections (a), (b), (c) and (d) cracks start from surface spall; (e) and (f) cracks start from the surface; and (g) and (h) stair-like cracks**

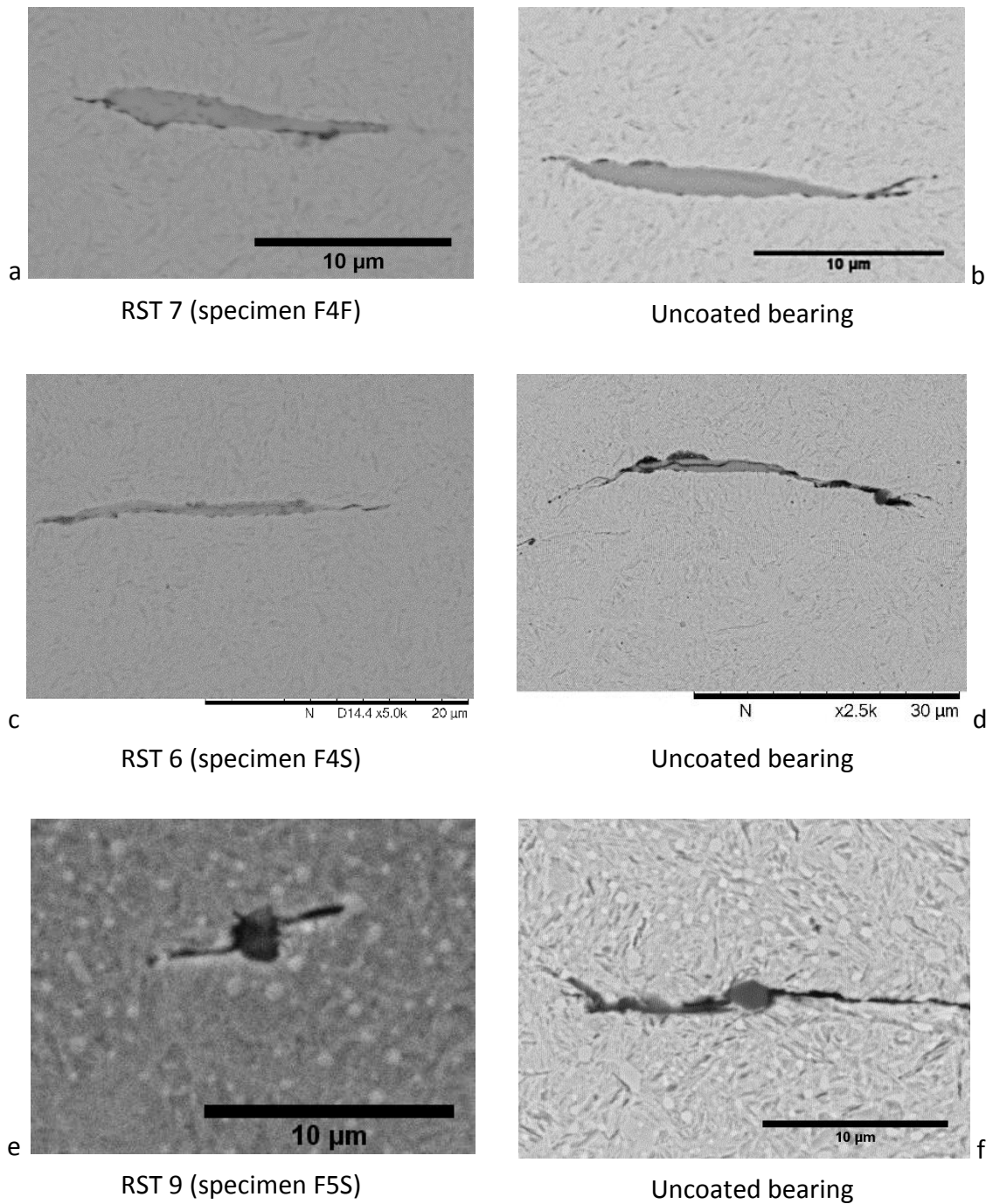


**Figure 7.5.2: Inclusion initiated micro-crack (a) and (b) debonded inclusions in axial sections; (c) cracked inclusion in axial section; (d) cracked and debonded inclusion in axial section; and (e) and (f) undamaged inclusions in circumferential section**

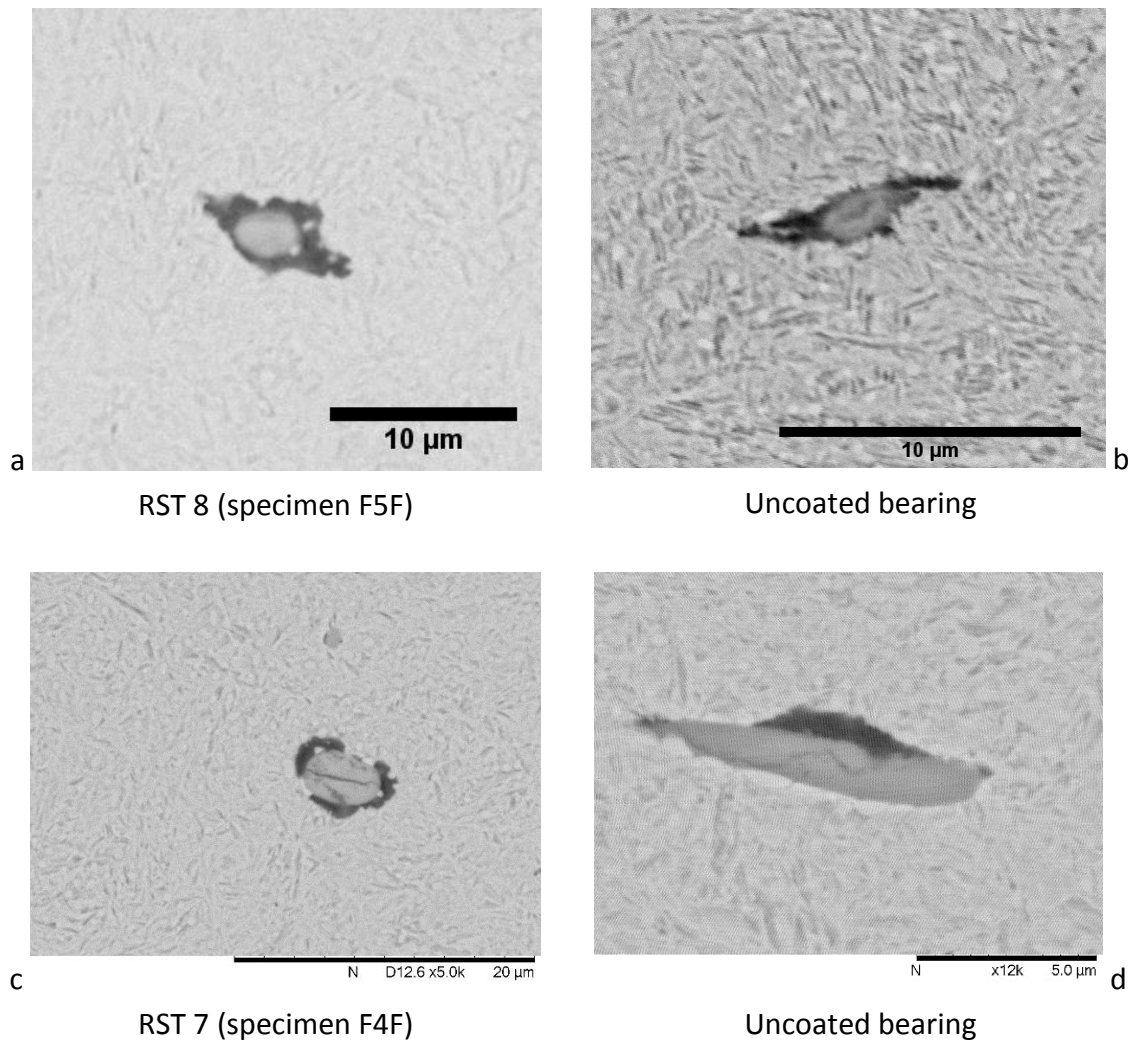


**Figure 7.5.3: Debonded inclusion (a) and (b) debonding expanded to micro cracks in circumferential section; and (c) and (d) debonded and cracked inclusions in circumferential and axial sections, respectively**

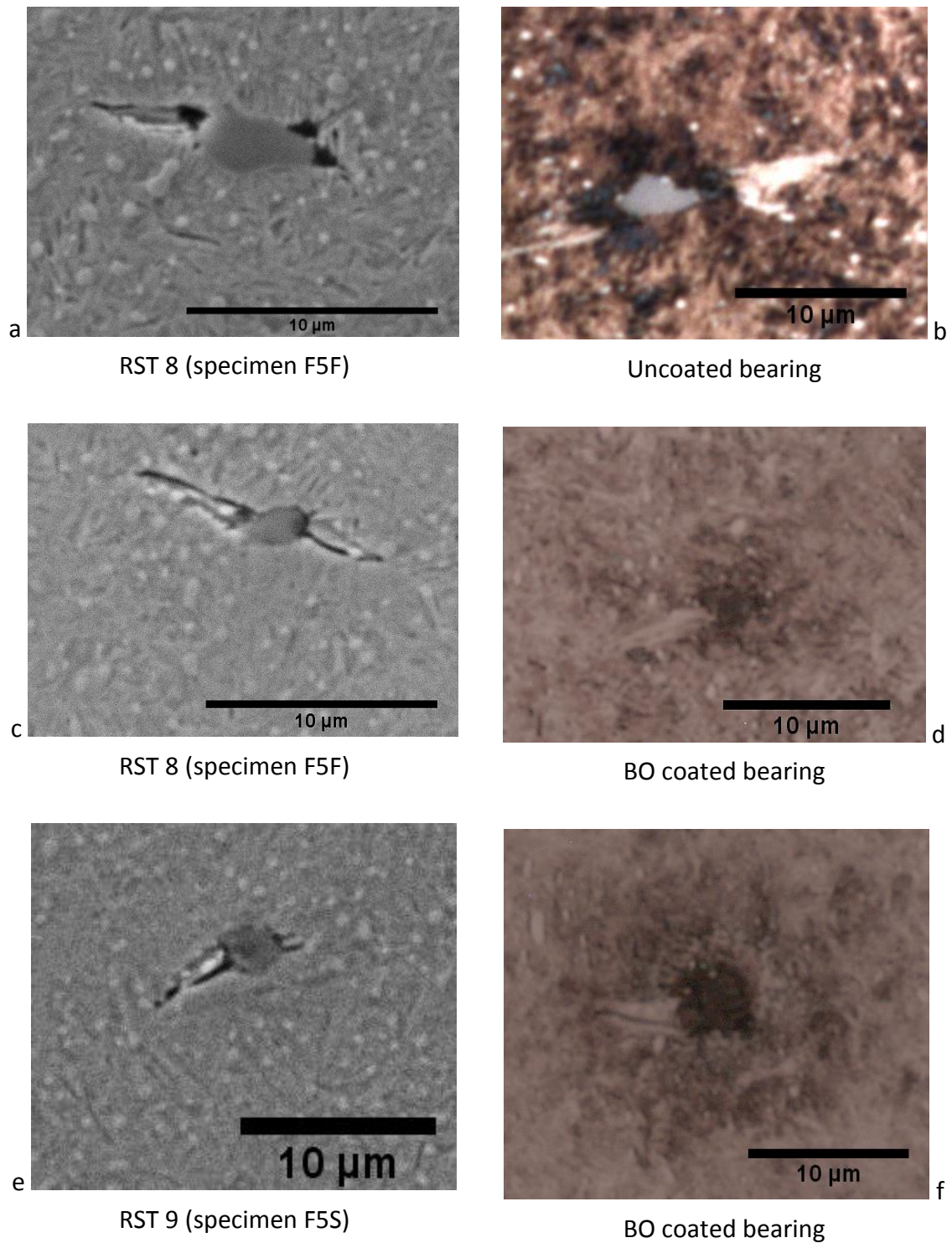


**Figure 7.5.4: Possible WEA and butterfly wings in circumferential sections (a) and (b) debonded inclusions and butterfly wings; and (c), (d), (e) and (f) butterfly wings and micro-cracks.**

## 7.6 The Development of Surface and Subsurface Initiated Damage

The surface-linked RCF cracks can be explained by the effect of surface traction, as shown in Figure 7.6.1. The maximum contact pressure might not lead to the yield limit of the bearing steel being exceeded. However, when this normal load is combined by traction on the surface, the maximum contact pressure required to onset the strain accumulation is reduced according to the shakedown diagram, as discussed in Section 2.1.3. When the shear yield limit is exceeded, a plastic flow accumulates with the repeated cycles. This increases the strength of the material according to the shakedown phenomenon. However, the material fails after the accumulation of plastic deformation exceeds the Ratchetting threshold. It is expected that, when the surface traction causes the maximum shear stress close to the surface, the exhausted material initiates surface-linked RCF cracks after the plastic deformation and the ratchetting. The parallel cracks, or double cracks, are a feature of the sheared material under fracture mode II that causes smashing of the material confined between the cracks. In more advanced cases, it is not easy to recognise the material segment between the parallel cracks and only very small particles that appear white under optical microscopy can be observed. This could explain the WECs that have a similar appearance in the failed bearings and support the surface initiation mechanism.

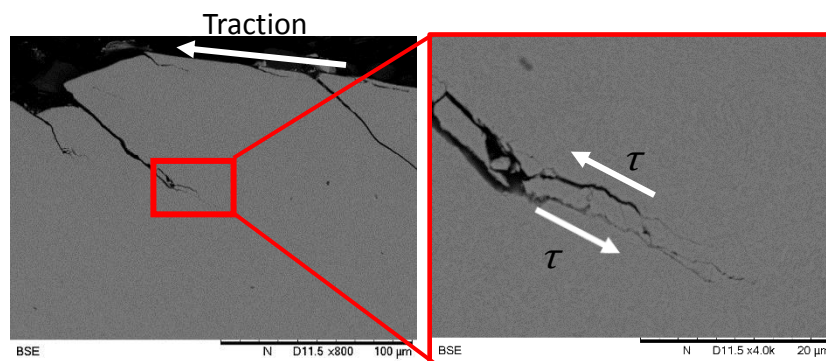


**Figure 7.6.1: Development of surface-linked RCF cracks (specimen F1F for RST 1 with higher magnification to show propagation of crack)**

The surface initiated damage that propagates to form big spall and network of cracks has been observed in the examined wind turbine bearing, as discussed in Section 6.4. The C1, C3 and the specimens of RSTs 1, 7 and 8 show double cracks, which are found to be at the first stage of developing surface pitting. However, only C3 and F1F, which were exposed to negative slip, show the full steps of developing surface spalling, as shown in Figure 7.6.2. It was found that surface-linked RCF cracks, or double cracks, propagate from the surface downward at certain angle, then they change direction to be almost horizontal and meet other cracks to form spalling. It is found that more cracks are initiated from the initial pit or spall and propagated to form bigger spalls, as shown in Figure 7.6.2 (c) and (d), and (e) in axial section.

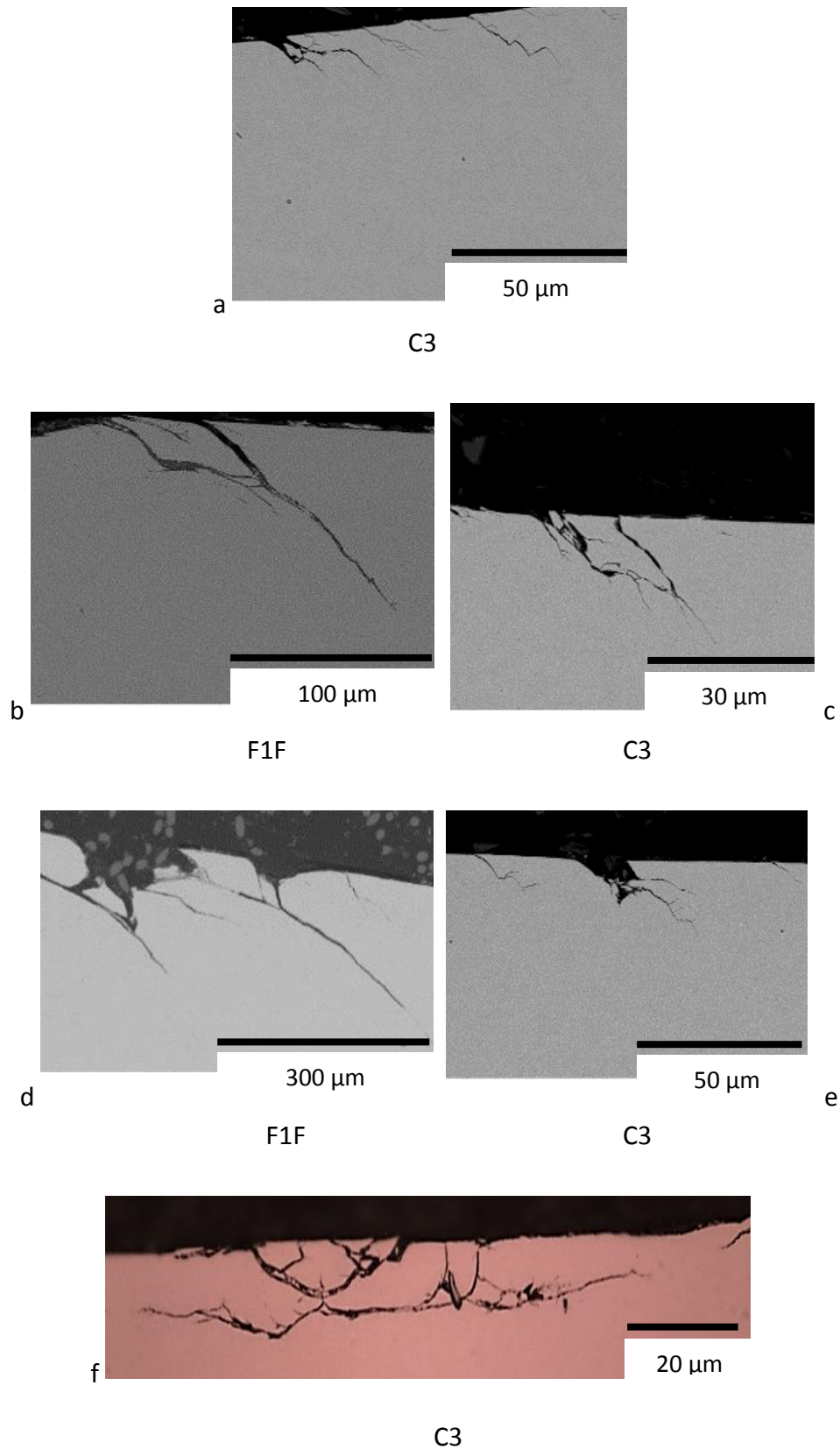


**Figure 7.6.2: Pits and spalls formation in circumferential sections (a) surface-linked RCF cracks propagate close to each other; (b) and (c) surface-linked RCF cracks interact to form a spall; (d) and (e) spall with cracks extending to form bigger spalls; and (f) crack network in axial section**

The subsurface damage initiated by non-metallic inclusions is confirmed by the RSTs, although the dominant damage is the surface initiated. A number of the observed micro-cracks, in the RSTs specimens, initiate from cracked and/or debonded inclusions. Figure 7.6.3 shows the percentage of these inclusions in the total number of inclusions that initiated micro-cracks. It was found that, in RSTs 7 and 9, all the subsurface micro-cracks initiated from debonded inclusions. The high load applied in RST 8 resulted in more subsurface cracks, as shown in Figure 7.4.4, from less number of debonded inclusions, as shown in Figure 7.6.3. Accordingly, at the same slip ratio, such as in RST 8 and 9, a higher load causes more and longer micro-cracks to initiate, mostly from non-debonded inclusions, without causing a high percentage of cracked inclusions, while at lower loads micro-cracks initiate from debonded inclusions and cause a considerable percentage of cracked inclusions.

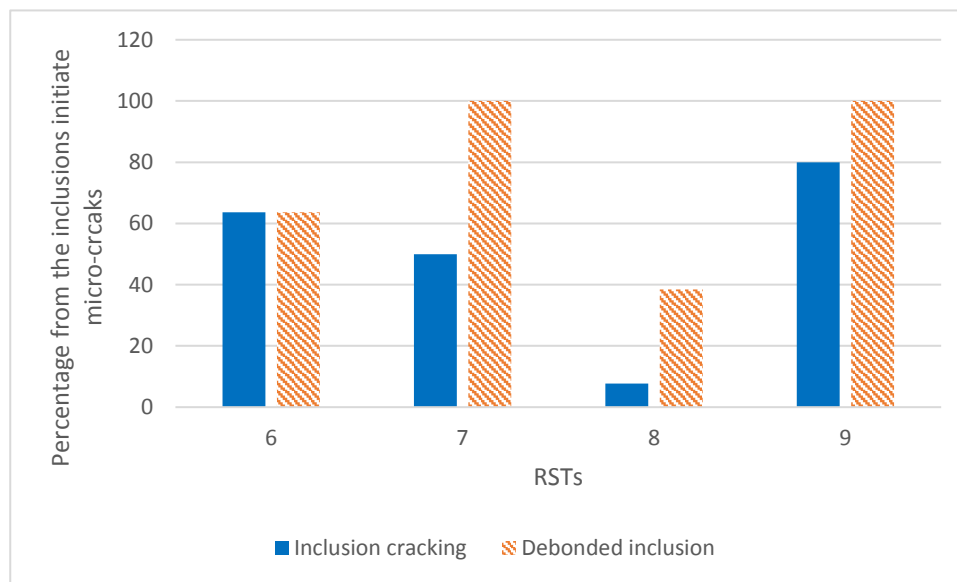


**Figure 7.6.3: Percentage of cracked and debonded inclusions in inclusions that initiated micro-cracks**

## 7.7 Summary

To investigate the effects on surface and subsurface damage, COT measurement tests and RSTs were conducted at different contact pressure, slipping ratio, rotational speed, lubricant viscosity and load sequence. The characters of surface and subsurface damage used for comparison between the RSTs are the maximum size of cracks and pits on the surface, surface roughness, wear rate, the lambda ratio, surface-linked RCF cracks, inclusion initiated micro-cracks, cracked inclusions, debonded inclusions, and possible butterfly wings. The following is a summary of the results and analysis:

1. The COT did not vary significantly after a specific number of cycles for lubricated tests. However, for dry contact or reversed rotation tests, the COT reached a very high value within a short time or a few cycles. Although  $\lambda$  was less than one for all the RSTs, no severe damage was observed on the surface, which could be due to

the extreme pressure additives. The damage that occurred during reversed rotation confirmed the incapability of these additives to protect the surface in such circumstances. The initial surface roughness was reduced significantly after the running in cycles. This makes the calculation of lambda ratio based on the initial surface roughness inaccurate and the assumption of boundary lubrication made by many studies invalid.

2. It was found that cracks and spalls on the surface, the surface-linked RCF cracks, and micro-cracks initiated by inclusions are affected by sequence 1 (low speed step then high speed step), higher slip ratio, higher contact pressure and higher speed within the boundary lubrication regime. However, sequence 1 causes higher surface damage and sequence 2 causes higher subsurface damage.
3. Surface traction was found to affect the subsurface and surface initiated cracks. This was shown by the locations of subsurface initiated micro-cracks and maximum hardness, which were closer to the surface than the location of  $\tau_{1(\max)}$  for all the RSTs. It was also found that high instant surface traction results in dominant surface-linked cracks. The plastic shear for the material could be the reason for the features of the double cracks and WECs. The surface traction reduces the normal load required for yielding, and thus ratchetting could occur and accumulate plastic deformation, resulting in the higher hardness of the WEA. Eventually, cracking by fracture mode II can occur.
4. Debonded inclusions were found to be the initiation for almost all the subsurface micro-cracks observed in some of the RST specimens. However, at high loads the micro-cracks initiated from non-debonded inclusions. Cracked inclusions initiated less micro-cracks than debonded inclusions, making the sequence of debonded inclusion cracks, then initiate micro-crack is not the only mechanism for subsurface damage initiation.
5. The surface and subsurface initiated damage showed clear similarities with the observations of the failed bearings in term of the appearance and inclination angle. These results confirm the subsurface damage initiation from inclusions. However, no clear microstructure alterations in the form of WEA and WECs could be found and the reason could be the limited test cycles, which did not produce the subsurface damage to the level of severity as that observed in the failed bearings.
6. Pits were developed from axial surface cracks that were close to each other. The significant increase in the weight loss of some of the specimens that were used for more than one million cycles was due to the initiation of surface pitting. These specimens were exposed to negative slip, and show the full steps involved in developing surface spalling. It was found that surface-linked RCF cracks propagate from the surface and meet other cracks to form spalling, then more cracks were initiated from the initial pit or spall and propagated to form bigger spalls. It was found that the investigated factors have no clear effect on the average angles of the surface-linked RCF cracks.

## 8 Results and Discussion of Load Calculation and Stress Analysis

This chapter includes calculations of loads on planetary bearings of a WTG, as well as the stresses and strains around an inclusion in the inner raceway. A case study, the NREL 750 kW WTG, was considered, due to the availability of the load spectrum during different operational conditions. The effect of normal and tangential loads on the damage accumulated at the location of maximum subsurface stress was investigated. The second part of this chapter is a FE modelling for an inclusion in the inner raceway of the planetary bearing. The results from load calculation and FE simulation were correlated with the metallurgical examinations presented in Chapters 5 and 6 to understand the effect of surface traction on subsurface damage initiation.

### 8.1 Results and Discussion of Surface and Subsurface Stress Analysis

The maximum load for the rolling element on the inner raceway was calculated from the torque applied on the low speed shaft, using the equations in Chapter 2. The subsurface stresses due to normal and tangential load under the surface of contact at different locations of the contact region were calculated. This section investigates the effect of surface traction on  $\tau_{1(\max)}$  and  $\sigma_{v(\max)}$ , and consequently the subsurface accumulated damage.

#### 8.1.1 Validation of load calculation

Normally, the load on gearbox components is calculated from a full dynamic model of WT drivetrain, considering a range of variables and interactions between the components. After this, the model is optimized by tuning its results with the experimental results. The NREL combined the results of different dynamic models of WT drivetrain as a part of the GRC project [40]. In this chapter the study is based on the GRC 750 kW wind turbine drivetrain with the dimensions shown in Table 8.1.1 for planetary gears [30] and a rated input torque of 325 kN.m and speed of 22 rpm [30][40]. The GRC report shows the results obtained from different dynamic models developed by their academic and industrial partners. The GRC modelling results under a steadily transmitted load between planets and sun gears and the results obtained by this research (based on the calculation procedure in Chapter 2) are shown in Table 8.1.2. Many effects, such as dynamics, bearing and gear contact stiffness, and interactions with other gearbox components, were not considered in this study: therefore, a deviation from the results of the GRC models is expected. The simplicity of the proposed calculation method and a relatively small percentage error demonstrate a good compromise, which makes this calculation method acceptable for this study.

**Table 8.1.1: Gear dimensions of NREL 750 kW WT planetary stage [30]**

Parameter	Annulus Gear	Planet Gear	Sun Gear
Pitch diameter (mm)	990	390	210
Pressure angle (deg)	20	20	20
Helix angle (deg)	7.5	7.5	7.5

**Table 8.1.2: Comparison of steadily transmitted load in planetary stage of NREL 750 kW WT**

	Loads (kN)		
	Circumferential	Radial	Axial
This study	180.6	66.3	23.8
Average of GRC results	175	70	23
Approximate percentage error	3.2%	5.3%	3.4%

### 8.1.2 Contact Pressure and Lubricant Film Thickness

The 750 kW NREL WT was used as a case study to calculate the maximum contact pressure  $p_{max}$  on the inner raceway of planetary bearings and the minimum lubricant film thickness  $h_{min}$  between rollers and inner raceway. Two transient events were considered in addition to the normal operation to show the effect of a transient high load and torque reversal on the life of planetary bearing. The procedure described in Section 2.4 was used to calculate  $p_{max}$  and  $h_{min}$  between the rollers and the inner raceway at the point of maximum load in the upwind planetary bearing. The torque spectra shown in Figure 8.1.1, which was measured on LSS by NREL, were used for the calculations. The results are shown in Figures 8.1.2 and 8.1.3, where the lubricant properties provided for this wind turbine were density  $\rho = 860.7 \text{ kg/m}^3$ , viscosity  $\eta = 0.09887 \text{ Pa s}$  and the pressure viscosity coefficient  $\alpha = 1.385 \cdot 10^{-8} \text{ Pa}^{-1}$  at the input temperature of  $65^\circ\text{C}$  were used for the calculation of  $h_{min}$ . These results show  $p_{max}$  reaches the values of 1700 MPa and 2100 MPa at some points during the shutdown and start-up, which exceeds the limit of 1500 MPa recommended in the design standards [146] and [85]. However, this contact pressure does not cause subsurface yielding of the through hardened bearing steel if the effect of subsurface stress risers, such as inclusions and gaps, is neglected. The spikes of high  $h_{min}$  in Figure 8.1.3 occur when there are torque reversals. The calculations for  $h_{min}$  in Section 2.4 neglect the moment of reversing the torque from positive to negative and treat them as an absolute value. Because the negative torque during start-up and shutdown has small absolute value, high  $h_{min}$  spikes occur at this torque point, as in point A in Figures 8.1.2 and 8.1.3. On the other hand, the positive spikes of the torque during start-up and shutdown cause low  $h_{min}$ .

such as point B in Figures 8.1.2 and 8.1.3. Using Equation 2.4.3.7, it was found that the  $\lambda$  ratio is less than one if the composite roughness of brand new bearing is considered to be 0.18 [49]. This  $\lambda$  ratio shows mixed lubrication, since  $\lambda$  greater than 3 is recommended for roller bearings [49]. However, the  $\lambda$  ratio could reach more than one if the smoothing of the surfaces after the running in is considered. Whatever the value of  $\lambda$ , if the reverse in torque direction is followed by instant reverse in the direction of tangential velocity, a lubricant film failure should be expected, as the entrant speed becomes zero when switching happens from one direction to another. This could cause a high coefficient of friction, as the results showed in Chapter 7, and consequently a high surface traction because of the high normal load.

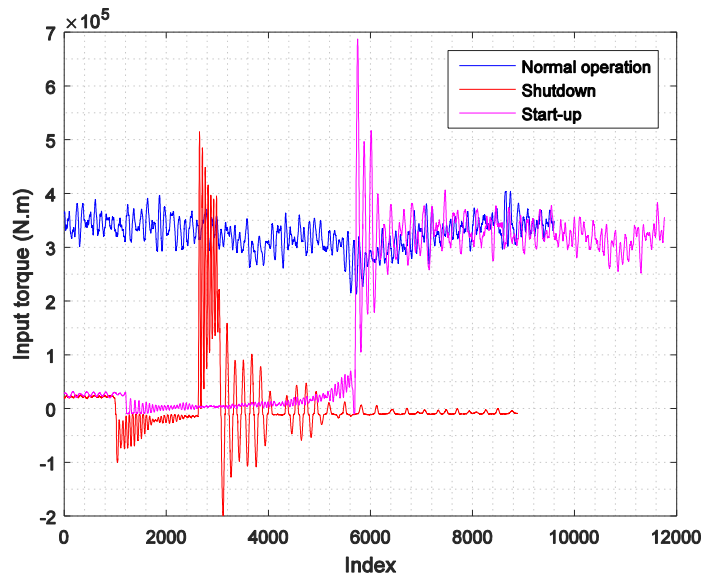


Figure 8.1.1: Torque on LSS for NREL 750 kW WTG

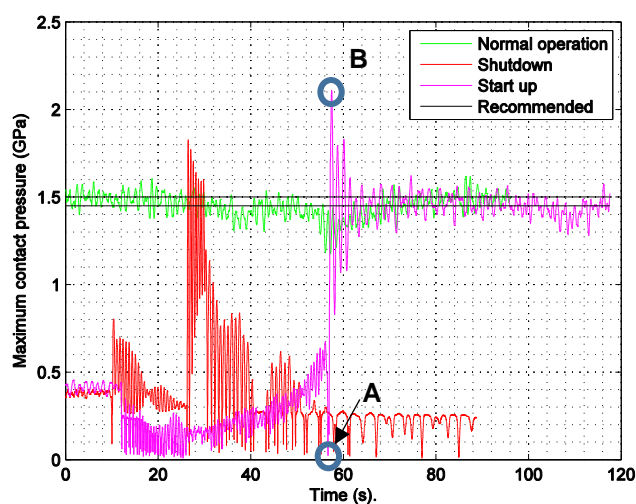
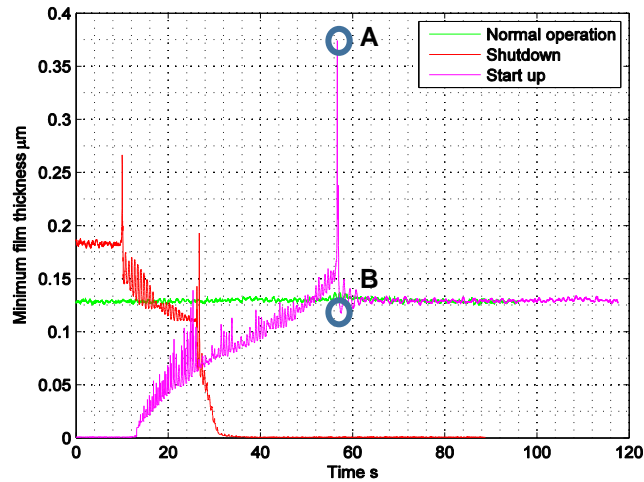
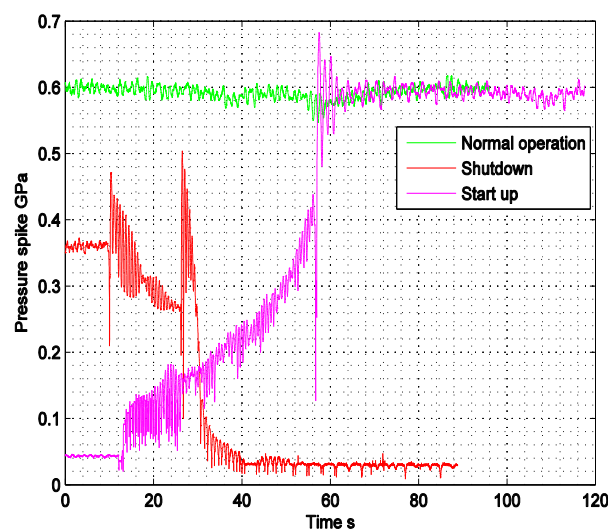


Figure 8.1.2: Maximum contact pressure at inner ring of upwind planetary bearing (points 1 and 2 are the minimum and maximum point during torque reversal)



**Figure 8.1.3: Minimum lubricant film thickness between rollers and inner race of upwind planetary bearing (points 1 and 2 are the equivalent to those in Figure 8.1.2)**

As discussed in Section 2.4.3, according to the EHL theory, a sudden increase in contact pressure, caused by the constriction at the outlet edge of the contact area due to elastic deformation of the contacted surfaces results in a pressure spike  $p_s$ . The  $p_s$  could be higher than the maximum Hertzian contact pressure  $p_{max}$  at certain conditions of load, speed and viscosity. According to previous study [66], the pressure spike due to the EHL theory could be the source for impact loading and the formation of WECs as an adiabatic shear band. In this thesis, the pressure spike  $p_s$  was calculated at different operation conditions to check the values of this pressure compared to  $p_{max}$ . Figure 8.1.4 shows  $p_s$  for the considered operation events and it reveals  $p_s$  of values lower than  $p_{max}$ . This shows that operating parameters of load, speed and viscosity for planetary bearings of the wind turbine under consideration do not cause a significant pressure spike at the outlet edge of the contact area, and thus no impact-like loading is expected.



**Figure 8.1.4: Pressure spike  $p_s$  at inner ring of upwind planetary bearing**

### 8.1.3 Surface Traction Effect on Subsurface Stresses

In this section, an illustration of the effect of surface traction is presented. The dimensions of the 750 kW WT were used to investigate the subsurface stress under different traction forces. As discussed in Section 2.4.3, McEwen provides a solution for calculating the subsurface stress at different depth  $z$  and distance  $x$  from the centre of the contact. This solution also includes the effect of surface traction  $q$  due to the consideration of coefficient of friction  $\mu$ , which is the COT for rolling bearings. This method was used in this research to investigate the variations of the principle shear stress  $\tau_1$  and von Mises stress  $\sigma_v$  under the surface at  $x=0$  and  $x=0.9b$ , where  $b$  is the half width of contact and the maximum orthogonal shear stress  $\tau_{xz,p}$  occurs at  $x=0.9b$  and  $z=0.5b$ . The superposition of the normal load and surface traction was used to calculate the total subsurface stress components  $\sigma_x$ ,  $\sigma_z$  and  $\tau_{xz}$  which were used to calculate the total  $\tau_1$  and  $\sigma_v$ .

To identify the effect of surface traction, COT=0.3 was assumed to calculate  $\tau_1$  and  $\sigma_v$ . This assumption is based on the observations from the failed bearing, which shows a considerable difference between the location of  $\tau_{1(max)}$  and that for the subsurface damage, indicating high surface traction. Also, the COT measured from RST 1 (b) during the reverse rotation supports the occurrence of high COT under reverse rotation. Figure 8.1.5 and 8.1.6 show the stress distributions,  $\tau_1$  and  $\sigma_v$ , under the surface at  $x=0$  and  $x=0.9b$  for  $p_{max}=1700$  MPa. At  $x=0.9b$  the magnitude and depth of maximum stresses are affected by the surface traction more than that at  $x=0$ . It was also shown that at  $x=0.9b$  the maximum  $\tau_{1(max)}$  is higher than that at the centre of the contact  $x=0$  when the surface traction is considered. This is due to the edge effect where the sliding level is the highest. Under COT=0.3, however, the maximum  $\sigma_v$  reaches the surface at  $x=0$ , while it is always under the surface of the contact at  $x=0.9b$ . Thus, under high surface traction, it is more likely for surface damage to occur at  $x=0$  and subsurface damage to occur at  $x=0.9b$ . In addition to the surface traction effect, the stress concentration around inclusions and voids could be significant to form for observing subsurface WEA and micro-cracks, as discussed in Section 8.2.

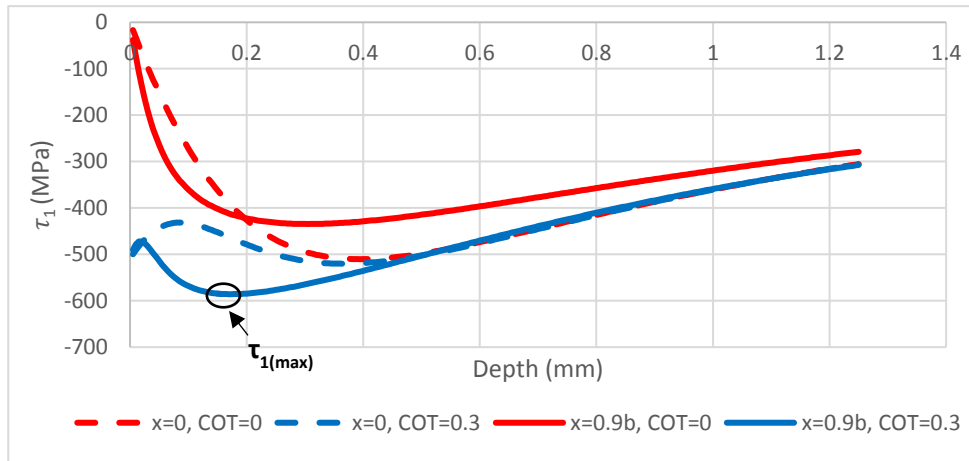


Figure 8.1.5: Subsurface  $\tau_1$  at different COT under  $x=0$  and  $x=0.9b$  at  $p_{\max}=1700$  MPa

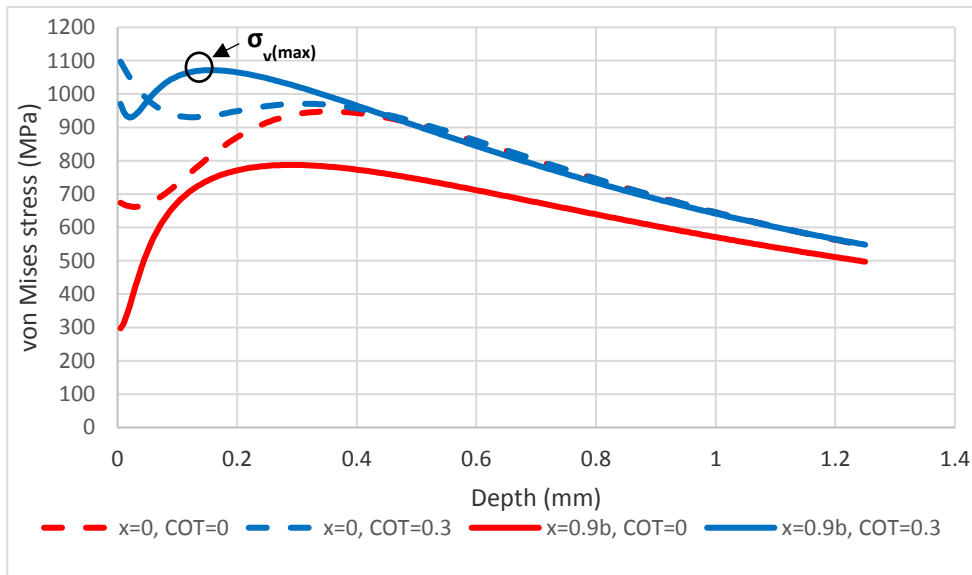


Figure 8.1.6: Subsurface  $\sigma_v$  at different COT under  $x=0$  and  $x=0.9b$  at  $p_{\max}=1700$  MPa

#### 8.1.4 Surface Traction Effect on Damage Accumulation

To study the effect of surface traction on damage accumulation, a moderate value of  $COT=0.08$  was considered for the planetary bearing of NREL 750 kW WT. This value is widely accepted for roller bearing applications. However, the possible high COT, which can occur during torque reversal, as discussed in Section 8.1.2, was not considered.

The torque on LSS for the NREL 750 kW WT at normal operation, shutdown and start-up was used to calculate the maximum subsurface stresses,  $\tau_{1(\max)}$  and  $\sigma_{v(\max)}$  at point 1 ( $x=0, z=0.78$ ) and point 2 ( $x=0.9b, z=0.5$ ) and the results are shown in Figure 8.1.7. In this figure, the x-axis is an index for the number of data points which is equivalent to the time series data points in Figures 8.1.1, 8.1.2, 8.1.3 and 8.1.4. It was used to make the comparison using data label easier. Although in figure 8.1.7  $\tau_{1(\max)}$  and  $\sigma_{v(\max)}$  are higher

at point 1, for higher COT the maximum stresses are at point 2 as shown in Figures 8.1.5 and 8.1.6. Figure 8.1.7 also shows that surface traction affects the stresses at point 2 more than that at point 1.

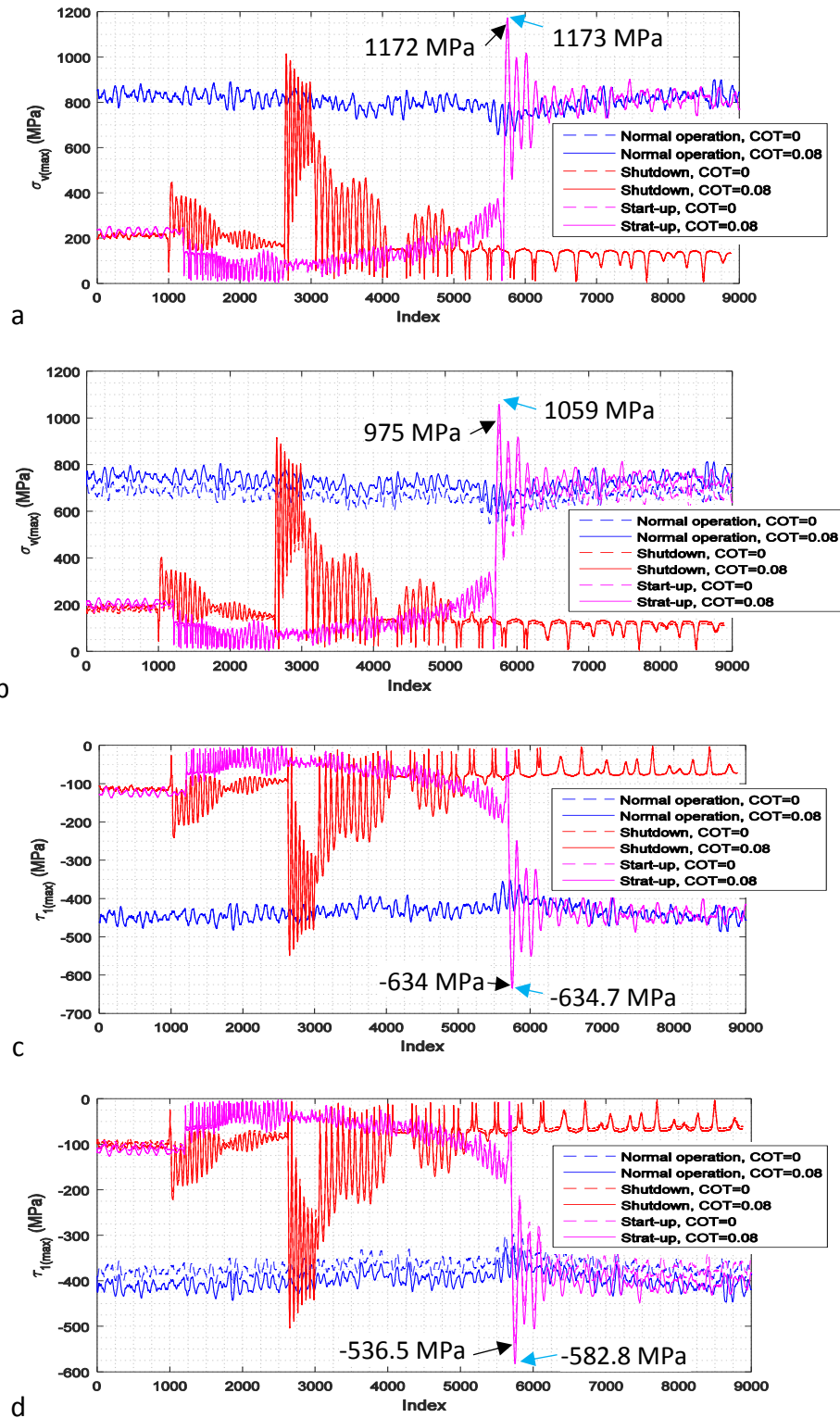


Figure 8.1.7:  $\tau_{1(max)}$  and  $\sigma_{v(max)}$  with and without surface traction at different operation conditions (a) and (c) are for point 1 ( $x=0, z=0.78$ ); and (b) and (d) are for point 2 ( $x=0.9b, z=0.5$ )). Blue and black arrows show maximum value with and without surface traction.

To quantify the effect of surface traction on the life of planetary bearing, the accumulation of fatigue damage was investigated. The damage accumulation can be evaluated using different approaches that could account for the load sequence, however, these approaches need further coefficients that are obtained from dynamic tests comparing to the Palmgren-Miner rule that is based on the parameters of the S-N curve. Although the Palmgren-Miner rule neglects the effect of load sequence, it was used in this thesis to evaluate the effect of surface traction on damage accumulation since the same sequence of the load spectrum was used for each operation condition with and without surface traction. Accordingly, Equation 8.1.4.1 was utilised to calculate the accumulated damage [147]. In this equation,  $N_{i=1,2,3,\dots}$  is the applied number of cycles at specific stress and  $N_{fi=1,2,3,\dots}$  is the number of cycles to failure at the same stress. In this study, a Matlab code was developed to analyse the load spectrum of each operation condition to cycles of a variable amplitude  $\sigma_a$  and mean  $\sigma_m$ . Then damage  $D_{i=1,2,3,\dots}$  was calculated due to maximum subsurface von Mises stress,  $\sigma_{v(\max)}$ , as shown in Figure 8.1.7 (a) and (b). As the considered load has a variable amplitude  $\sigma_a$  and mean  $\sigma_m$ , they both need to be deployed as shown in Equation 8.1.4.2 to find the equivalent completely reversed stress amplitude  $\sigma_{eq}$  [147]. To find  $N_{fi}$  at each stress value, Equation 8.1.4.3 is used where  $\sigma_f' = 2620$  MPa and  $B = -0.0926$  are the fatigue strength coefficient and exponent for bearing steel [148].

To investigate the effect of surface traction, the damage caused by stress due to normal load only and that caused by the total stress calculated from the superimposing of normal load and surface traction were compared. The accumulated damage at each operational event in Figure 8.1.7 (a) and (b) was calculated and compared. In addition, the damage due to the subsurface stress at point 1 was compared to the damage due to the subsurface stress at point 2, as shown in Figure 8.1.8. It can be seen that surface traction has a very limited effect at point 1. However, this is not the point of maximum subsurface stress at high surface traction or COT, as is shown in Figures 8.1.5 and 8.1.6. Figure 8.1.8 also shows that, considering a moderate level of surface traction due to COT=0.08 causes considerable increase in damage accumulation at point 2. At this value of COT, higher damage occurs at point 1. However, if a higher value of COT is considered greater damage accumulates at point 2. Further studies could be carried out to determine the shortening in the total life of bearings due to high traction during torque reversals among all events. Accordingly, the bearing life calculation method could be modified.

$$\frac{N_1}{N_{f1}} + \frac{N_2}{N_{f2}} + \frac{N_3}{N_{f3}} + \dots = D_1 + D_2 + D_3 + \dots = 1 \quad 8.1.4.1$$

$$\sigma_{eq} = \frac{\sigma_a}{1 - \frac{\sigma_m}{\sigma_f'}} \quad 8.1.4.2$$

$$N_f = \frac{1}{2} \left( \frac{\sigma_{eq}}{\sigma'_f} \right)^{\frac{1}{B}} \quad 8.1.4.3$$

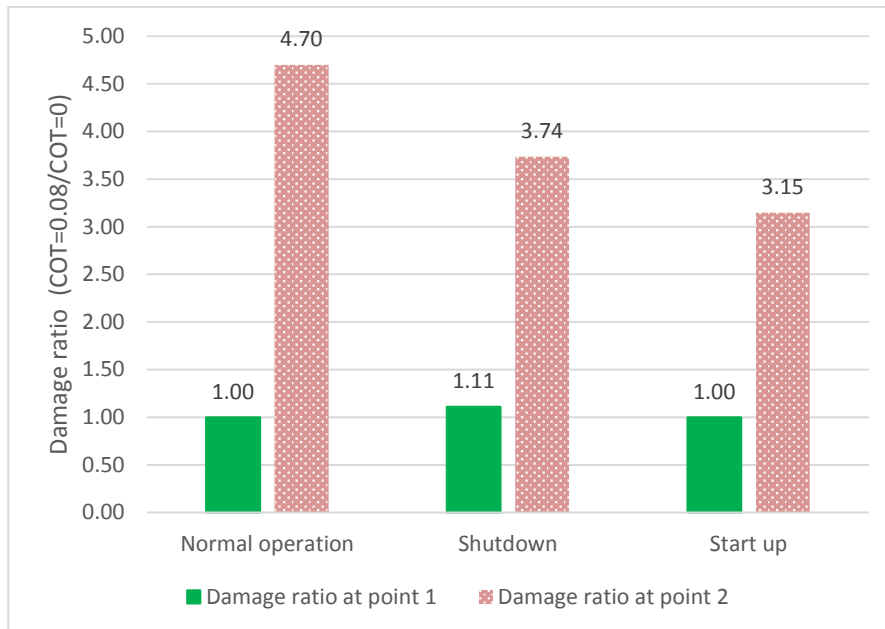


**Figure 8.1.8: Damage accumulation ratio at different operation events with and without surface traction (COT=0.08)**

## 8.2 Results and Discussion of FE Modelling

The FE modelling is presented in this chapter to bring insight regarding the stress state around a MnS inclusion for different loading cases, which could help us to understand the mechanism of subsurface initiated damage, WEA and micro-cracks, for non-metallic inclusions. However, the numerical results do not necessarily represent the realistic values due to the simplifications adopted in the modelling.

### 8.2.1 General description

#### Models description:

This section describes the FE models used to analyse the stress around inclusions in bearing steel under the effect of normal and tangential loads on the surface of contact between the roller and inner raceway of a bearing. Due to the availability of the dimensions of the NREL 750 kW WT planetary bearings and load spectrum for this machine, the development of the FE models was based on this bearing. The models were mainly the plain strain Two Dimensional (2D) cross section in the circumferential direction, with an ellipse inclusion of a certain dimension, depth and inclusion-steel matrix interaction properties. However, a couple of Three Dimensional (3D) models were used to compare with the 2D models, but with an ellipsoidal gap instead of the inclusion. The first type of 2D models (M1-2D) represents a section of the inner raceway with Hertzian pressure distribution on the

surface to represent contact with the roller of maximum rolling element load  $Q_0$ , as discussed in Section 2.4.2. In addition to the normal contact pressure, surface traction with Hertzian distribution was also applied to some of these models, as shown in Figure 8.2.1. Another type of 2D model (M2-2D) was developed. The M2-2D represents sections of the roller, inner raceway and outer raceway, as shown in Figure 8.2.2. Figures 8.2.1 and 8.2.2 show the boundary conditions adopted for all the M1-2D and M2-2D models. The thickness of the inner and the outer raceways in these models are identical to the thickness in the actual bearing and the angle of the sector in these models equals  $360^\circ / \text{number of rollers}$ . The results from the M1-2D and M2-2D models were compared to that from the analytical solution to validate their results. Another validation considering the surface tangential traction of Hertzian distribution was conducted against the stress distribution calculated from the equations in Section 2.4.2. This validation was applied to the subsurface stresses at  $x=0$  and  $x=0.9b$ . Three dimensional models (M1-3D), as shown in Figure 8.2.3, were also developed. Each M1-3D is an extension of the M1-2D to three dimensions but with spherical or ellipsoidal gaps instead of inclusions. The properties of the bearing steel used in the models are:  $\nu=0.3$ ,  $E=210$  GPa, and the elastic plastic data is shown in Figure 8.2.4 [149]. The results from these models were used to show the validity of using 2D models for inclusions.

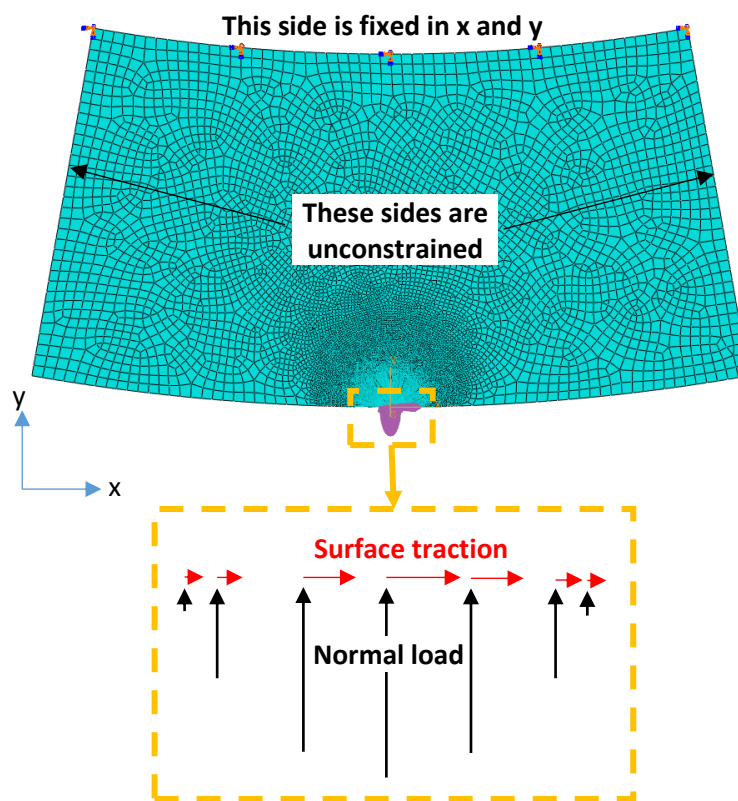


Figure 8.2.1: Illustration of M1-2D models

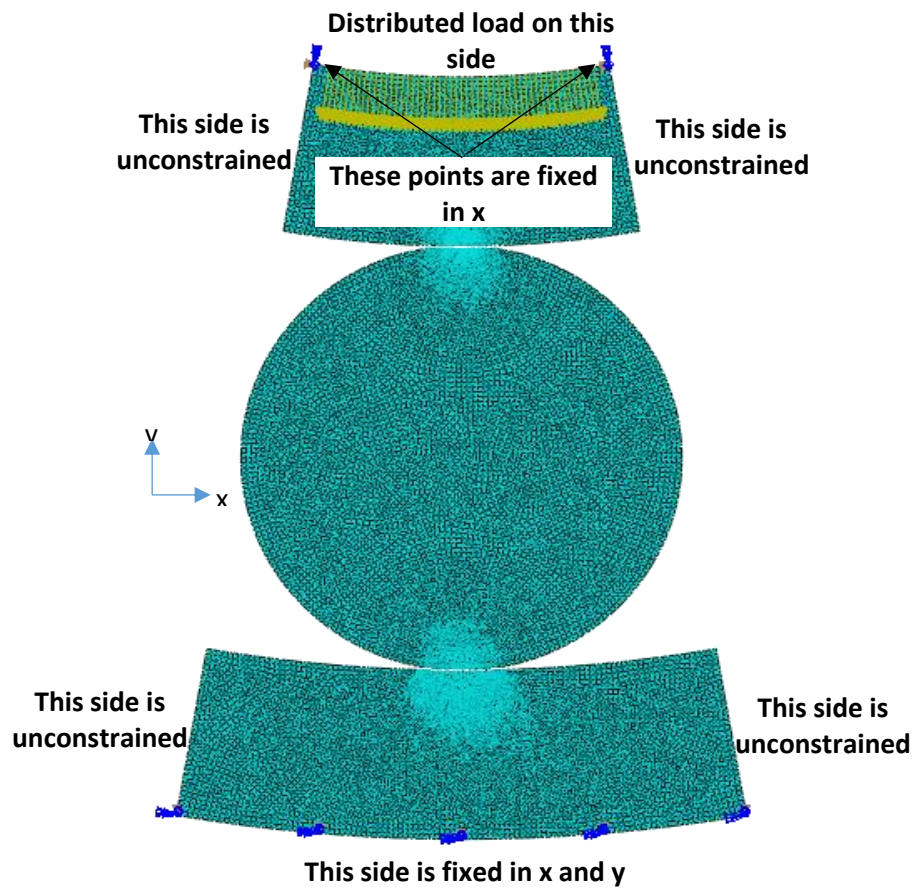


Figure 8.2.2: Illustration of M2-2D models

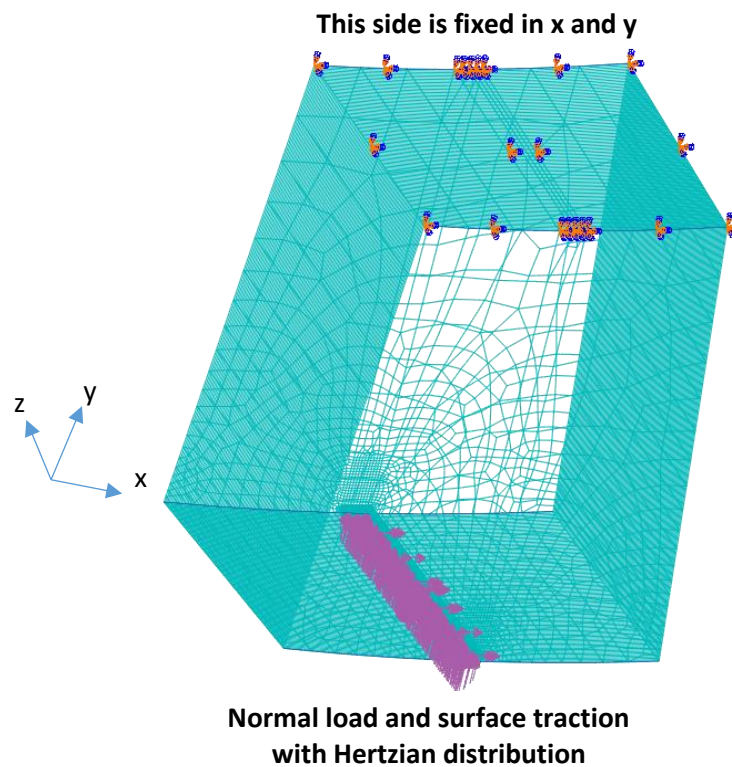
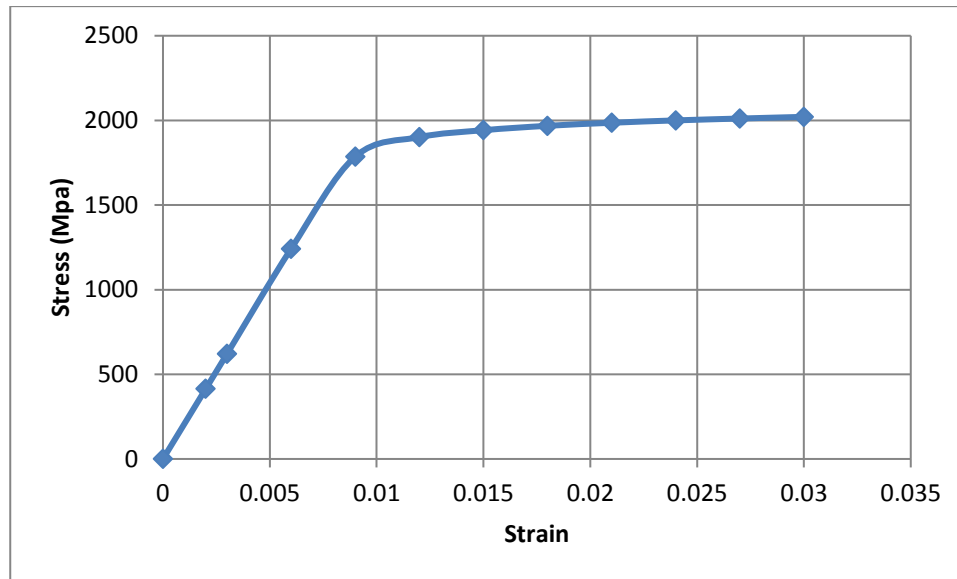


Figure 8.2.3: Illustration of M1-3D models (all the sides are unconstrained)



**Figure 8.2.4: True stress-strain curve for bearing steel [149]**

Inclusion description:

The M1-2D models with Hertzian pressure distribution on the surface were adopted to investigate the stress value and distribution in the inner raceway around inclusions. The inclusion was modelled as a Type A (MnS) by an elliptical shape inclined by  $45^\circ$  with the ORD. Its dimensions were semi-minor and semi-major radii of  $28 \mu\text{m}$  and  $9.6 \mu\text{m}$ , respectively. The centre of this inclusion was  $80 \mu\text{m}$  from the surface and it is exactly under the centre of the contact width  $x=0$ . The properties of this inclusion used in the models were  $\nu=0.25$  and  $E=108\text{GPa}$  as the average for 69-147 MPa in Table 2.1.5.1. These specifications are meant to be generic and do not necessarily match the characteristics of the MnS inclusions observed in the uncoated bearing in Chapters 5 or 6. Also, smaller inclusion means more difficult to create a structural FE mesh. Inclined elongated inclusion was chosen to investigate the effect of surface traction direction, as discussed in Section 8.2.5. Two types of models were utilized to simulate inclusion-steel matrix interaction. In the first type, the inclusion was a partition of different material properties perfectly bonded to the steel matrix with no separation is allowed between the contacted bodies. The inclusion in the second type was modelled as a separate body with contact interaction between the inclusion and the steel matrix with separation is allowed between the contacted bodies. The interaction properties were frictionless and hard contact, to allow separation after contact but no penetration. Although these specifications may not be exactly representative for the interaction between inclusion and matrix, they can provide an insight into the stress state around a non-perfect bonded or separated inclusion, as observed from the examination of the uncoated and BO coated bearings in Chapter 5 and 6. The trials for developing a 3D model for an inclusion as a separated body contacting the 3D gap in the inner raceway were not successful. However, the results from the M1-3D models for an ellipsoidal gap can be compared with that from M1-2D models of ellipse gap, as discussed in the next section.

### 8.2.2 Validation

The models of different complexity were compared to each other as well as to the analytical solution, in order to decide the developed model to be used for investigating the subsurface initiated damage.

#### M1-2D and M2-2D models:

The subsurface stress distributions that had been calculated numerically using models from the two types, M1-2D and M2-2D, were compared to that analytically calculated in Section 8.1.3. The models were developed using similarly structured mesh and without embedded inclusions. The elements for these models were quadratic with the very fine mesh with the same element size in the supposed location of the inclusion and the contact area. The size of the mesh at this location was varied and the variations in the results were recorded. For the M1-2D models without inclusion, it was found that increasing element size from 0.5  $\mu\text{m}$  up to 10  $\mu\text{m}$  does not change the match between the FE solution and the analytical solution. For the M2-2D models without inclusion, a better matching with the analytical solution can be obtained by using bigger elements, such as 10  $\mu\text{m}$ . To compare the two models, they both meshed with the same-sized elements of 0.5  $\mu\text{m}$  in the assumed location of the inclusion. This size was found to be sufficient to represent the elliptical shape of the inclusion and its gap with the steel matrix. Figure 8.2.5 (a) shows a comparison between the two types of models and the analytical solutions under a contact load of 55 kN that results in  $p_{\text{max}}=1466$  MPa and a half width of contact  $b_L=0.434$  mm, according to the Hertzian contact theory. This  $p_{\text{max}}$  value was selected because it is close to the recommended maximum stress limit for WT planetary bearings [85][146]. It can be seen from this figure that the results from M1-2D are better than that of M2-2D, in term of matching the analytical solution. Better matching between the results of M2-2D and the analytical solution can be achieved when a larger size of inclusion is used, but this size makes the geometry of the inclusion not a perfect ellipse. Accordingly, the M1-2D models were adopted for the analysis of inclusion and surface traction effects after showing very accurate results compared to the analytical solution within the elastic limit as shown in Figure 8.2.5 (b).

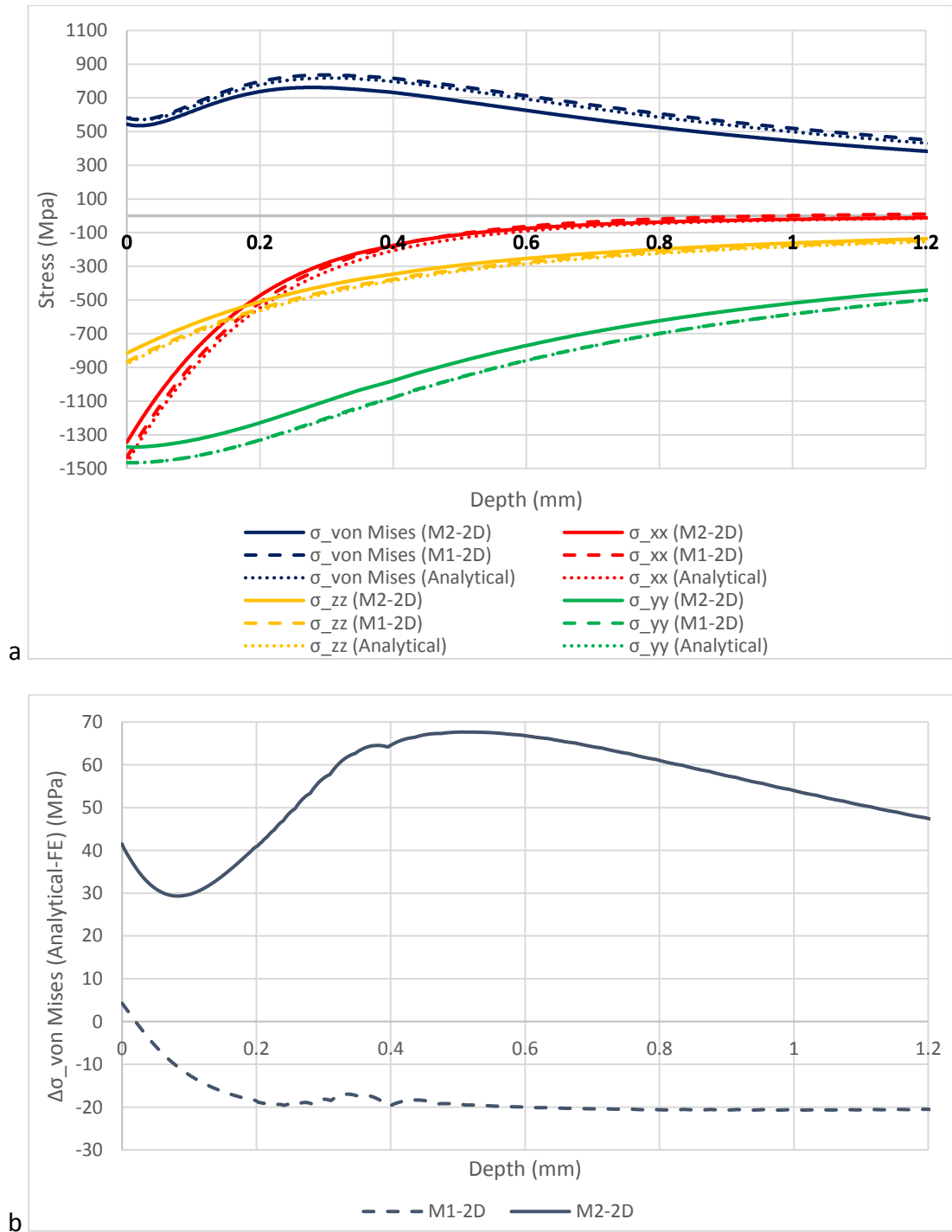


**Figure 8.2.5: (a) Comparison of subsurface stresses at  $x=0$  under  $p_{max}=1466$  MPa and no surface traction using FE models M1-2D and M2-2D, and analytical solution (Figure 8.2.3 shows the axes) (b) the uncertainty of M1-2D and M2-2D**

Normal load and surface traction:

Another comparison was conducted, considering surface traction due to various COTs, as shown in Figure 8.2.6. In this figure, the subsurface stresses from M1-2D were found at the centre of the contact width,  $x=0$ , and at the edge of the contact,  $x=0.9b$ . For this comparison,  $p_{max}=1700$  MPa was applied, since this value is close to the maximum contact

pressure with torque reversal during shutdown. Although higher contact pressure occurs during start up, the  $p_{\max}=1700$  MPa is closer to the maximum contact pressure during normal operation, which makes the results more generic. The fair matching in this figure between the M1-2D models and the analytical results validates the use of these models to investigate the effect of surface traction.

#### Stress concentration:

The stress concentration factor for inclusions perfectly bonded to the steel matrix can be used to validate the modelling of inclusions. The stress concentration factors for elliptical inclusions perfectly bonded to the matrix is provided by L.H. Donnell [150] and [76]. However, these factors are for inclusions in plates under tension and compression loading, which is not applicable for the M1-2D models. Accordingly, a special model of a plate under tension and compression was developed just to confirm the validity of the meshing and the bonding used for the embedded inclusion in the M1-2D. The stress concentration caused by MnS inclusion with  $E_{\text{inclusion}}/E_{\text{matrix}}=0.65$  were used to compare to the one which had been calculated from the FE model. Figure 8.2.7 (a) shows the geometry and dimensions of the inclusion and the applied load adopted in the FE model utilized for comparison. The FE model is a plain strain rectangle of 6×24 mm under tension and compression of  $\pm 500$  MPa. At the centre of the rectangle a vertical elliptical inclusion of 10  $\mu\text{m}$  semi-minor and 20  $\mu\text{m}$  semi-major radii was placed with perfect bonding and aligned with the load direction, as shown in Figure 8.2.7 (a). The bar chart in Figure 8.2.7 (b) reveals an agreement between the results of the FE model and the analytical solution, which validates the stress increase at the inclusion, using the size and geometry of elements defined in the M1-2D models.

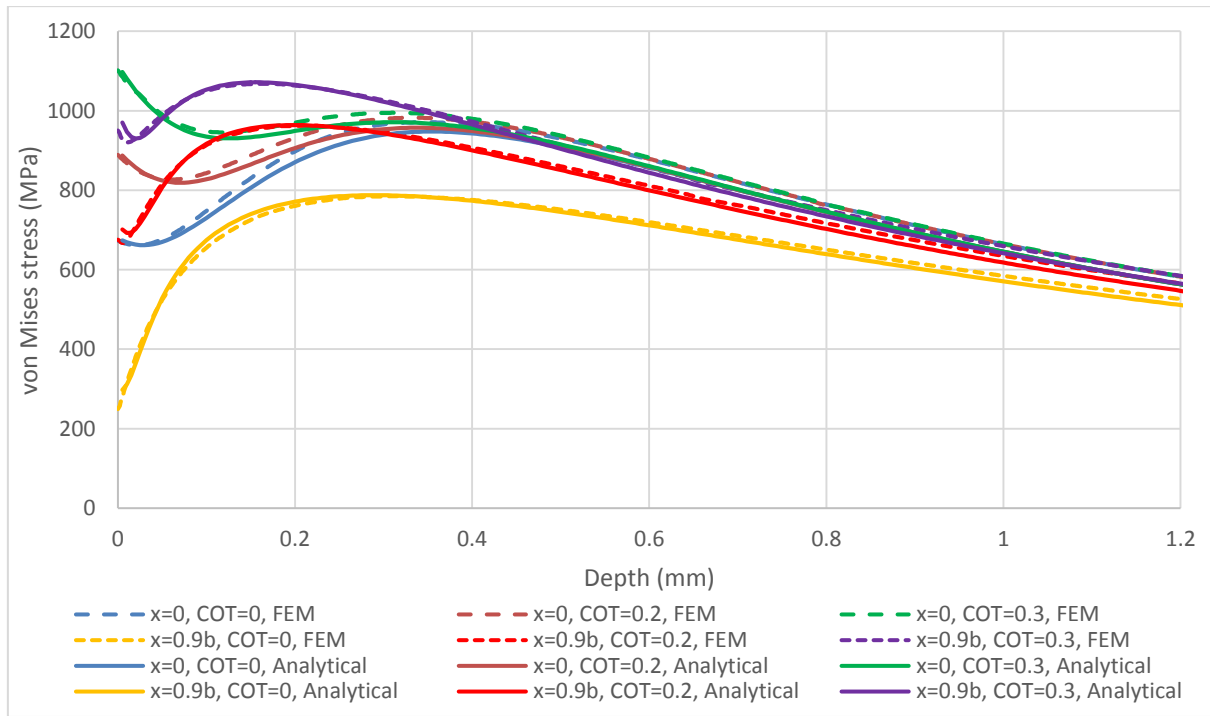


**Figure 8.2.6: Validating results of M1-2D models at different values of surface traction and under  $p_{max}=1700$  MPa**

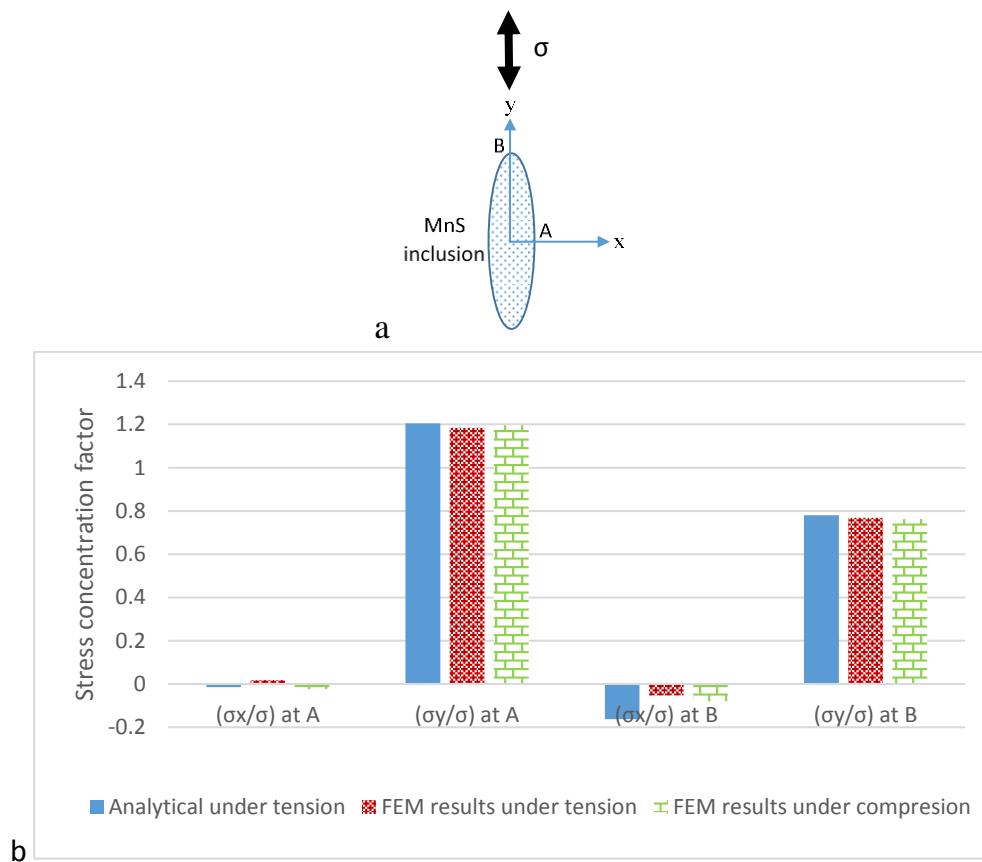


**Figure 8.2.7: Validating results of 2D FE modelling with MnS inclusion (a) schematic illustrates the inclusion and points A and B are where the stress concentration calculated (b) comparing the stress concentration calculated analytically with that from FE modelling**

### Three-dimensional models:

The M1-2D models may not exactly reflect the stress state around the inclusion, due to the simplicity of assuming a three dimensional inclusion or a gap as a 2D plain strain. Accordingly, three-dimensional models, M1-3D, were used to check the how accurate or practical are the results obtained from the M1-2D models. However, no 3D models with inclusions could be developed due to convergence difficulties. The first comparison was between two pilot / elementary models, which are a M1-2D model with a circular gap and a M1-3D model with a spherical gap, with a  $2\mu\text{m}$  radius for both. The boundary conditions for these models are similar to those shown in Figures 8.2.1 and 8.2.3. The load on both of these models is Hertzian pressure distribution of  $p_{\text{max}}=1700$  MPa on the contact surface. The equivalent von Mises stress and the orthogonal shear stress for these models are shown in Figure 8.2.8. For the M1-3D model, at some of the free meshing elements that are not close to the spherical gap, there were some stress concentrations, which are highlighted in the legends of Figure 8.2.8. However, the results in Figure 8.2.8 show the close results between the two models and the similar stress distribution around the gap. These results indicate the fairly accepted approximation for the M1-2D models for spherical gap and separated inclusions since they both cause material discontinuity. The second comparison was between two other M1-2D and M1-3D models with elliptical and ellipsoidal gaps, respectively. In these models, the loads on the surface were normal and tangential, with Hertzian distribution, as shown in Figures 8.2.1 and 8.2.3. The maximum contact pressure and surface traction were  $p_{\text{max}}=1700$  MPa and  $q_{\text{max}}=600$  MPa, respectively. In these models, the magnitude of the load varies from zero at the beginning of the loading step to maximum at the middle of the step and ends up with zero at the end of the step. This kind of loading/unloading was used in this research to investigate the residual stress; and it represents a robust method to validate the 2D models. The results from these two models are presented in Figure 8.2.9 with the stress concentration highlighted in the legends are not related to the stress distribution around the ellipsoidal gap. The stress at maximum load and the residual stress at unloading show close values in both models. Although the equivalent plastic strain is over estimated in the 2D model, this strain in both models exceeds that at the yield and it is expected that modelling longer inclusion in the 3D model may result closer equivalent plastic strain to that results from the 2D model. Overall, the tensile residual stress is proved to occur even for the 3D gap. This tensile stress occurs when the maximum loading results in local yielding (plastic zone) around the inclusion or inclusion tips. When the load is removed, the unyielded material around the plastic zone attempt to recover the elastic deformation which results in tensile stress on the yielded material. This tensile stress may be the main crack opening stress under subsequent loading cycles. The development of the residual tensile stress under loading cycles will be discussed in Section 8.2.4. The 3D model also shows that the stress concentration around the inclusion could be surrounding the whole gap and not just the tips, which could be correlated to the three dimensions of the butterfly, since the wings are observed in axial and circumferential sections.

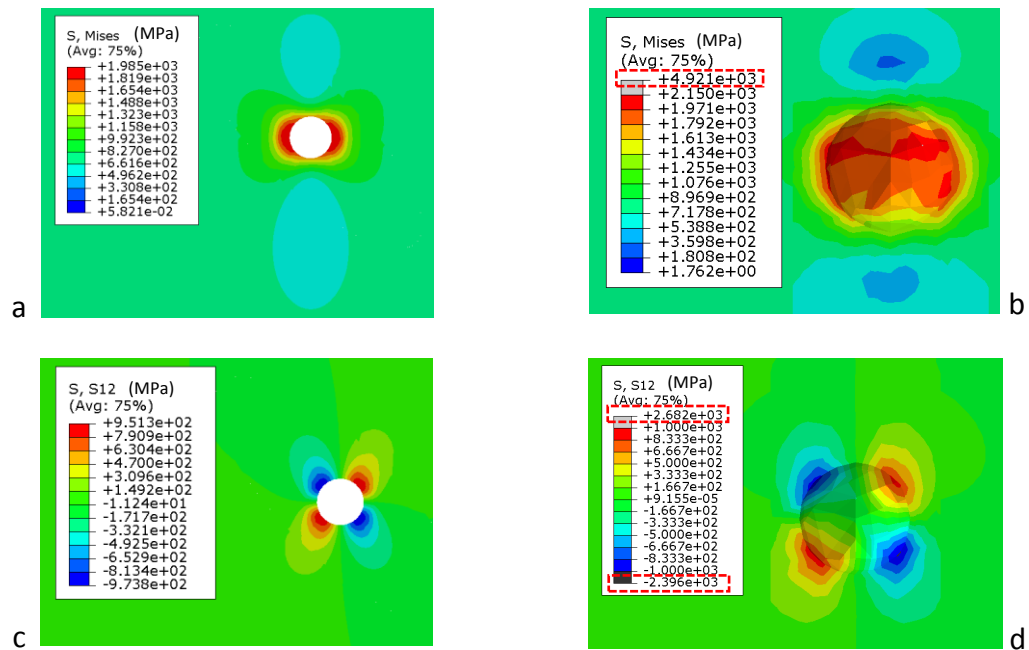


**Figure 8.2.8: Comparison between results from 2D model with circular gap and 3D model with spherical gap (a) and (c) M1-2D model, and (b) and (d) M1-3D model (the highlighted values are not related to the stress around the gap)**

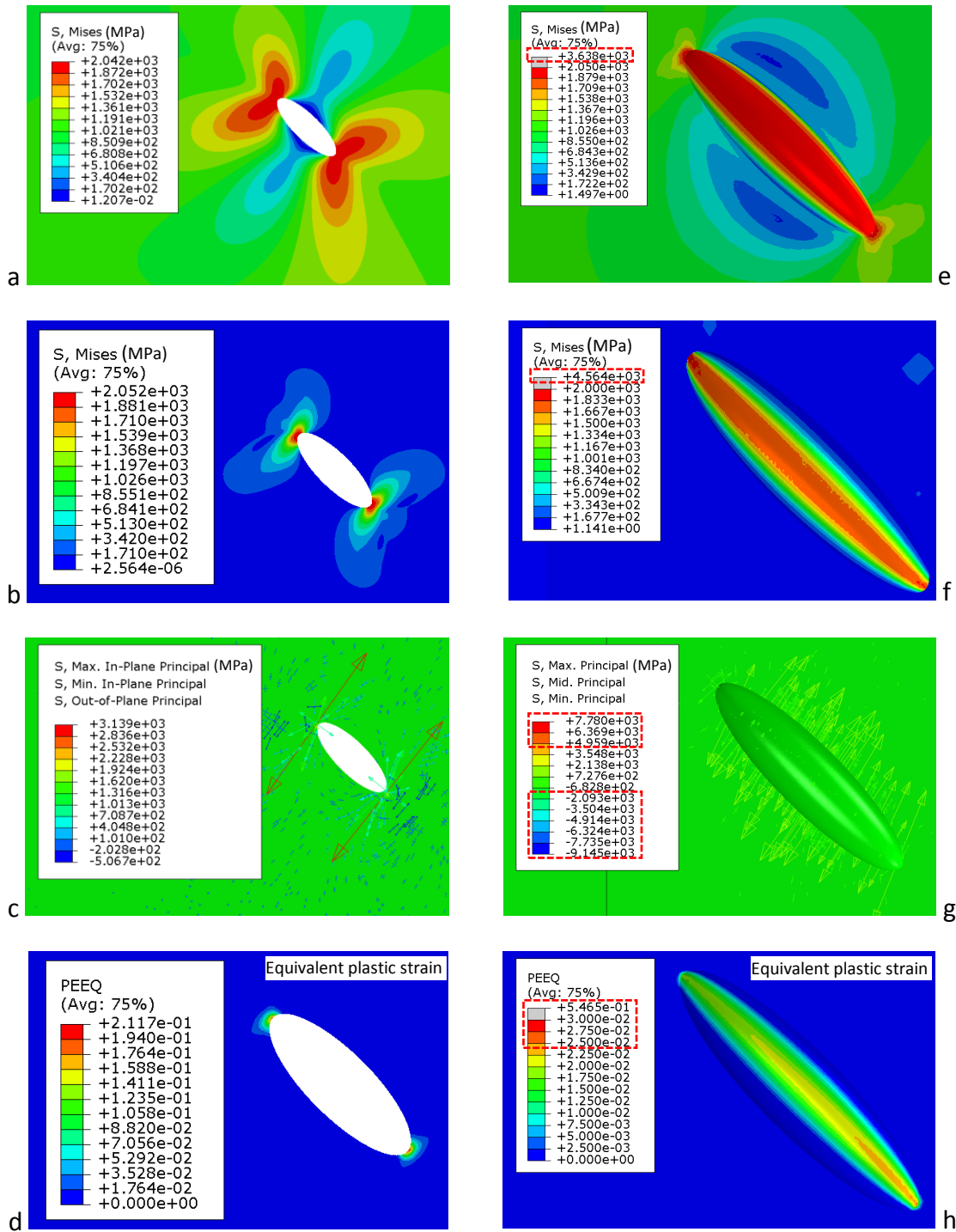


**Figure 8.2.9: Comparison between results from 2D model (on left) and from 3D model (on right), the load at (a) and (e) is maximum and all others are at unloading (the highlighted values are not related to the stress around the gap)**

### 8.2.3 Local Effect of Inclusion for different steel matrix bonding

The local effect of inclusions on subsurface stress concentration was investigated. Two M1-2D models were utilized, one with embedded inclusion and the other without. As described in Section 8.2.1, one elongated MnS inclusion was embedded in a circumferential section of the inner raceway of NREL 750 kW WT planetary bearing. A normal load of  $p_{max} = 1700$

MPa was used for both modes, with and without inclusion. For the model with inclusion, the interface between the inclusion and the steel matrix was modelled in two ways. Firstly, the inclusion was modelled as perfectly bonded to the steel matrix; secondly, it was modelled as another body confined inside the steel matrix with contact interaction. Stress variation was found across the inclusion and at its tip along lines (a) and (b) in Figure 8.2.10. The results are shown in Figure 8.2.11 and they clearly reveal local stress concentration around the inclusion, without changing the stress distribution far from the inclusion. This local stress concentration shows that even malleable inclusions such as MnS can still cause high stress concentrations and initiate damage. Although, in reality, the interaction between the inclusion and steel matrix may not be represented by frictionless contact, this interaction may represent the separation observed for some inclusions in the failed bearings. Accordingly, the effect of inclusion bonding is very clear, showing that the separation may have a significant effect on the stress concentration level.

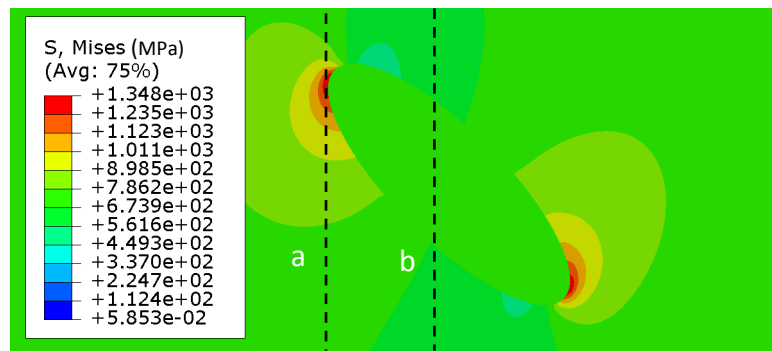


**Figure 8.2.10: Lines measuring variation of  $\sigma_v$  at  $p_{\max}=1700$  MPa (a) across inclusion, and (b) at tip of inclusion (contact surface being  $80 \mu m$  below inclusion)**

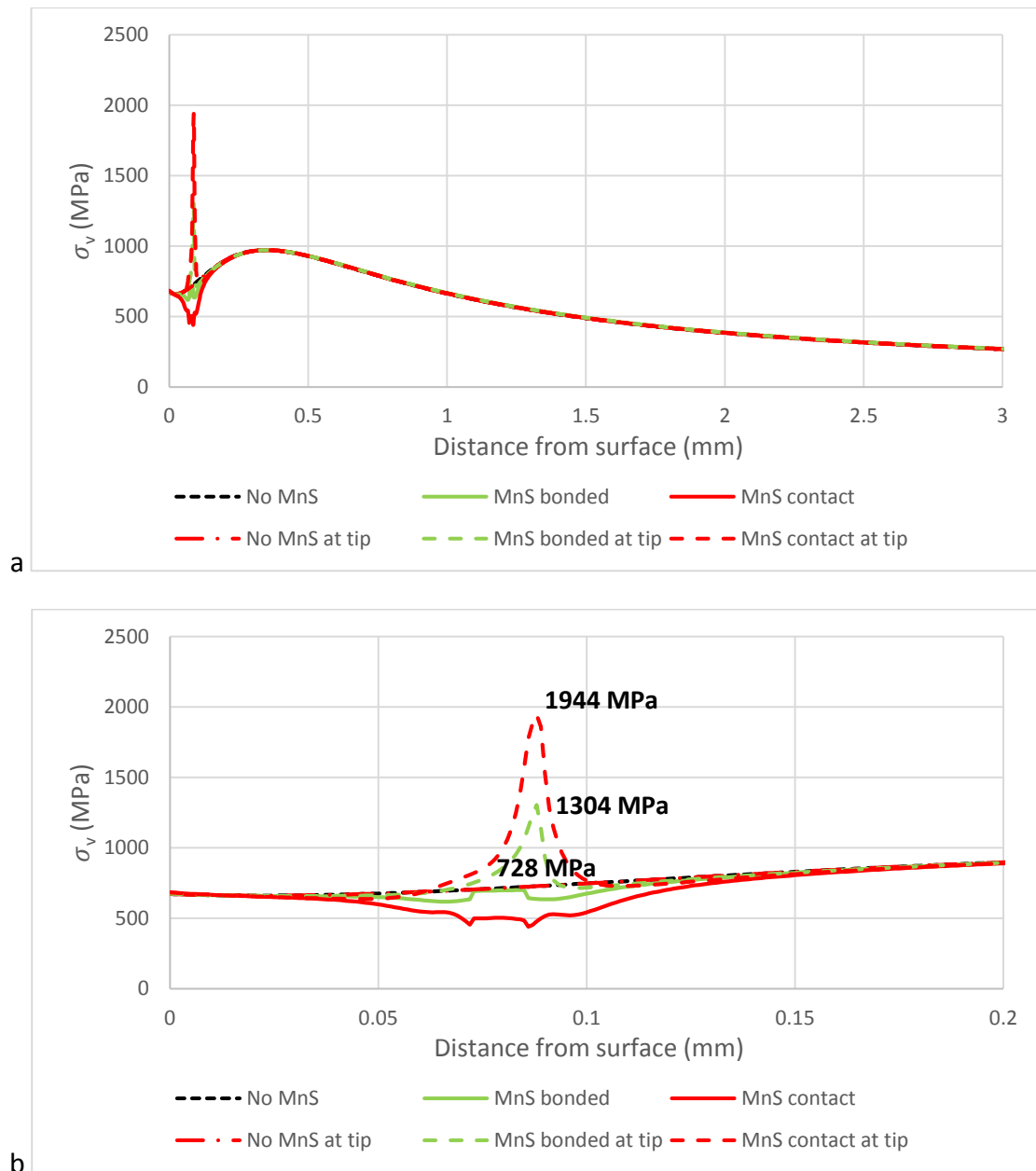


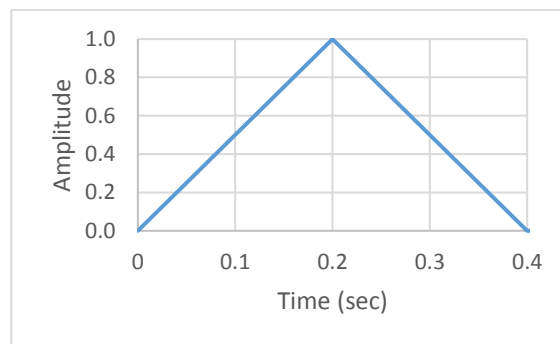
**Figure 8.2.11: Local effect of inclusion on the variation of  $\sigma_v$  under  $p_{\max}=1700$  MPa**

It can be seen that, even for the perfectly bonded MnS inclusion, the stress almost doubled at the tip, which emphasises the importance of considering the inclusions for subsurface stress and damage calculations. The stress increase at the inclusion tip due to separation from the steel matrix could make the yielding or stress induced transformation more feasible at lower contact pressure than that expected if inclusion effect is neglected. It is also observed that the stress inside the separated inclusion was less than that in the adjacent steel matrix, due to the deformability of the MnS inclusion. The local stress concentration around the tips of MnS inclusions could be correlated to the local microstructure alteration, such as WEA. However, this stress may not cause an observable microstructure alteration but residual stress, which is expected to be a beneficial

compression stress under loading. Nevertheless, during the unloading the residual stress needs to be investigated, as discussed in Section 8.2.4 below.

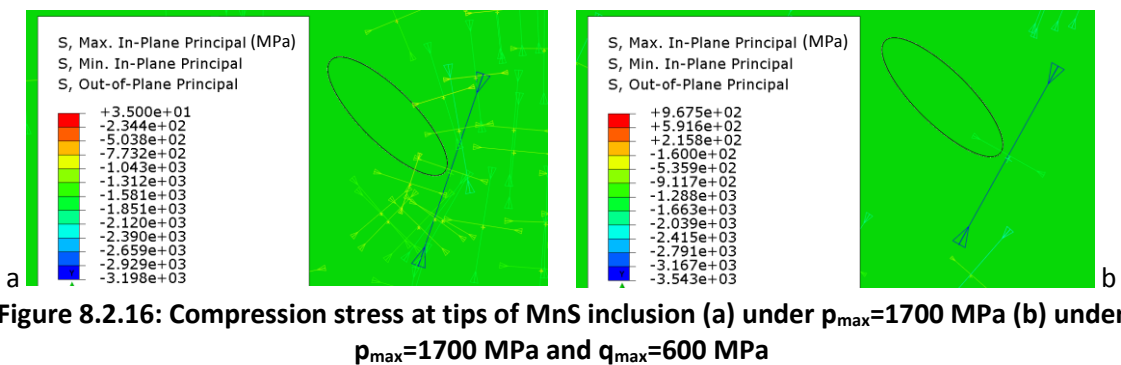
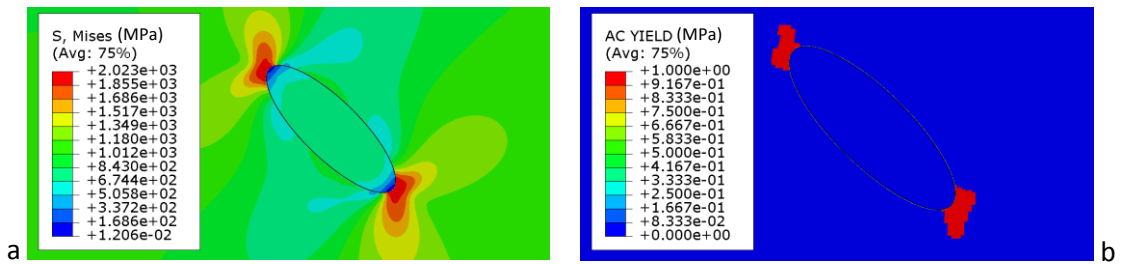
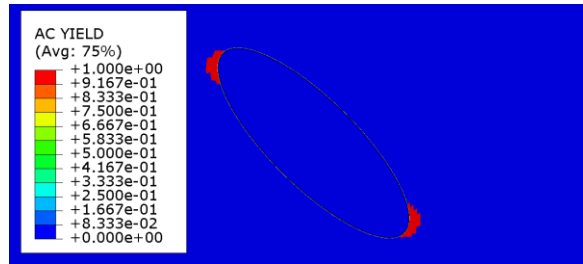
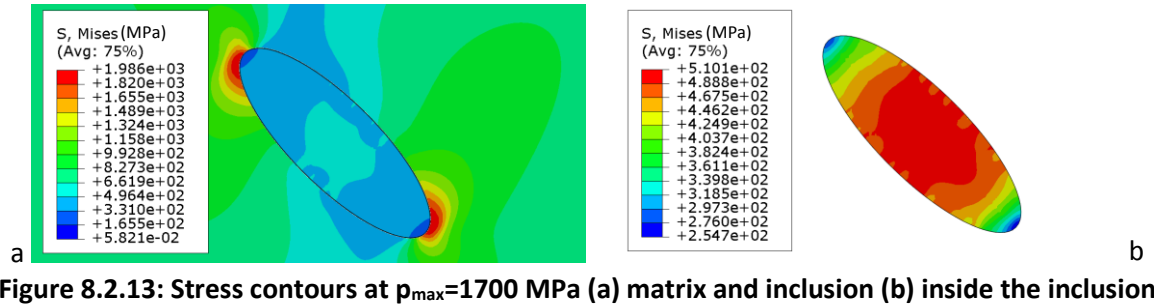
#### 8.2.4 Effect of normal and tangential loading-unloading on residual stress

The load on each point on the raceways alternates between loading and unloading during the pass of each roller. A FE model with contact interaction between MnS inclusion and the steel matrix was utilized to show the effect of loading-unloading with and without surface traction on the residual stress around inclusion tips. This kind of loading was modelled by a Hertzian pressure distribution that changes between zero and maximum, as shown in Figure 8.2.12 which is a simplification for the roller moving over the point of maximum load on the raceway. Probably, this rate of loading-unloading is not exactly similar to the passing frequency of the rollers. However, it was found that the stress values and distribution were not affected by the load rate when it was changed from 0.2 to 0.02 seconds.



**Figure 8.2.12: Load amplitude representing loading/unloading on bearing raceways**

A similarity between the stress distribution around the inclusion and the butterfly configuration was observed during the variation of surface loading. At  $p_{\max}=1700$  MPa, the stress around the inclusion and inside it at maximum load is shown in Figure 8.2.13. At the maximum loading, the stress exceeded the average yield limit for bearing steel of 1800 MPa [68], as shown in Figure 8.2.14. The contour of equivalent stress and the yielded elements show similarity with the topography of the butterflies wings observed from the examination of the failed bearings. However, better matching is observed when a surface traction  $q_{\max}=600$  MPa is applied, as shown in Figure 8.2.15. Nevertheless, no crack opening could be expected under loading, since the principle stresses show compressing, as shown in Figure 8.2.16. On the other hand, the high value of residual stress after removing the load shows tension at the inclusion tip, as shown in Figure 8.2.17, which could derive crack opening.



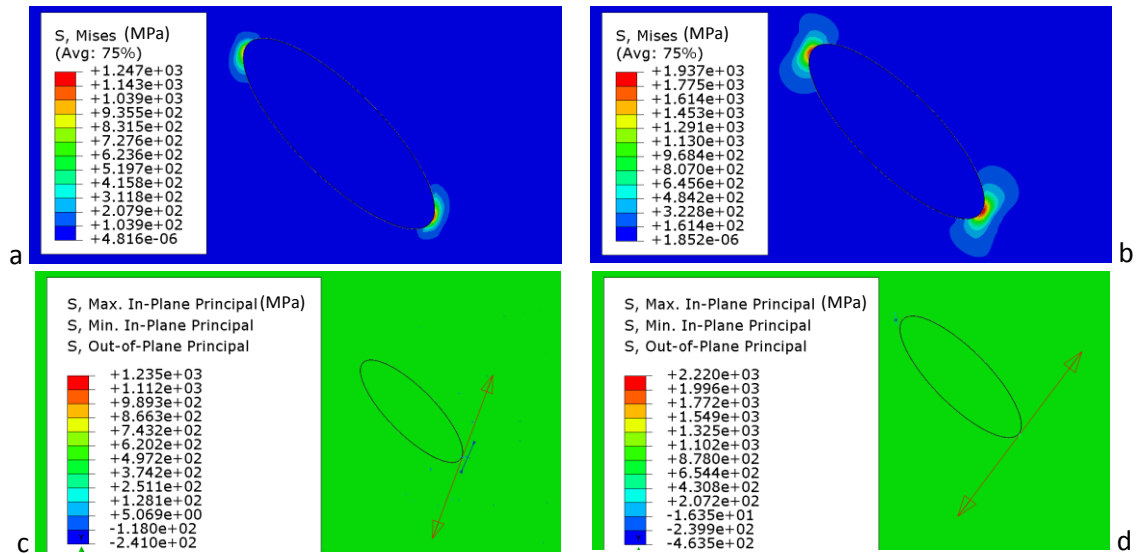


**Figure 8.2.17: Residual tensile stresses (a) and (c) after  $p_{\max}=1700$  MPa; and (b) and (d) after  $p_{\max}=1700$  MPa and  $q_{\max}=600$  MPa**

The effect of the inclusion-steel matrix interaction and the value of  $p_{\max}$  and  $q_{\max}$  on residual stress around inclusion tips were investigated. It is observed that no residual stress is developed when the inclusion is modelled with perfect bonding to the steel matrix. This highlights the role of the separation between inclusion and steel matrix, as a non-perfect bonding or a gap attached to the inclusion, as observed from the examination of the failed bearings. The effect of surface traction on the value of residual stress is very clear, as shown in Figure 8.2.17. To compare the effect of high surface traction and high normal load, another model with a normal load only of Hertzian distribution with  $p_{\max}=3000$  MPa was developed to investigate the effect on the residual stress. The results of this model, as shown in Figure 8.2.18, was almost the same residual tensile stresses as from  $p_{\max}=1700$  MPa and  $q_{\max}=600$  MPa in Figure 8.2.17. This result supports the occurrence of subsurface damage due to high surface traction rather than high normal load, since the results from Section 8.1 did not show contact pressure reaching a very high value, such as 3000 MPa, while surface traction is confirmed from the metallurgical examinations in Chapter 5 and 6. Additionally, in the following sections in this chapter, a comparison between the observed butterfly wings and the inclination of the stress concentrations around the inclusion supports the occurrence of surface traction.

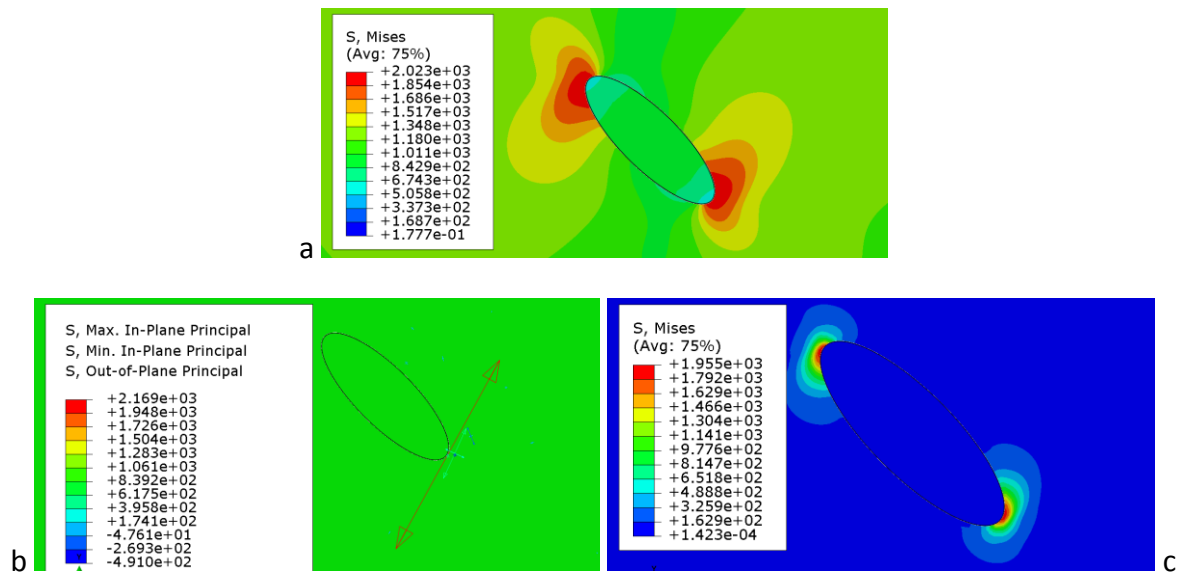


**Figure 8.2.18: Stresses resulting from  $p_{max}=3000$  MPa (a) equivalent stress at maximum loading; and (b) and (c) residual tensile stresses**

In addition, the evolution of maximum equivalent stress, residual stress and equivalent plastic strain under a number of loading-unloading cycles was investigated. Repeating the loading/unloading for a number of cycles was applied in a model with  $p_{max}=1700$  MPa and  $q_{max}=320$  MPa, which is equivalent to  $COT=0.188$ . This value of  $COT$  is not extremely high and keeps the maximum stress under the surface. The amplitude of normal and tangential load was varied between zero and maximum during ten identical cycles, as shown in Figure 8.2.19, where the  $p_{max}$  and  $q_{max}$  at any time was  $1700 \cdot \text{Amplitude}$  and  $320 \cdot \text{Amplitude}$ , respectively. The letters in this figure are utilized to discuss the variation of maximum  $\sigma_v$  and the residual stress in Figures 8.2.20, and the equivalent plastic strain in Figure 8.2.21. It was found that  $\sigma_v$  at maximum load decreases while the residual stress increases with increasing the number of cycles, as shown in Figure 8.2.20. Also, the effect of this loading on the equivalent plastic strain was investigated and it was found that at this normal and tangential load the increasing is very clear according to the ratchetting mechanism, as shown in Figure 8.2.21.

To show the effect of surface traction during cyclic loading, the results in Figures 8.2.20 and 8.2.4.21 were compared with that from another model, where only a normal load was applied. The same amplitude shown in Figure 8.2.19 was used with  $p_{max}=1700$  MPa. The results of equivalent stress  $\sigma_v$  and equivalent plastic strain are shown in Figure 8.2.22 and 8.2.4.12. The trend of these results is similar to those in Figures 8.2.4.20 and 8.2.21, in term of decreasing the maximum equivalent stress and increasing the residual stress by increasing the number of cycles. However, the values and the variation of residual stress and the equivalent plastic strain are much higher when there are normal and tangential forces on the surface. Accordingly, any stress or strain induced microstructure alteration, such as WEA, will be much faster if surface traction occurs. Also, the higher tensile residual stress makes crack opening more expected.

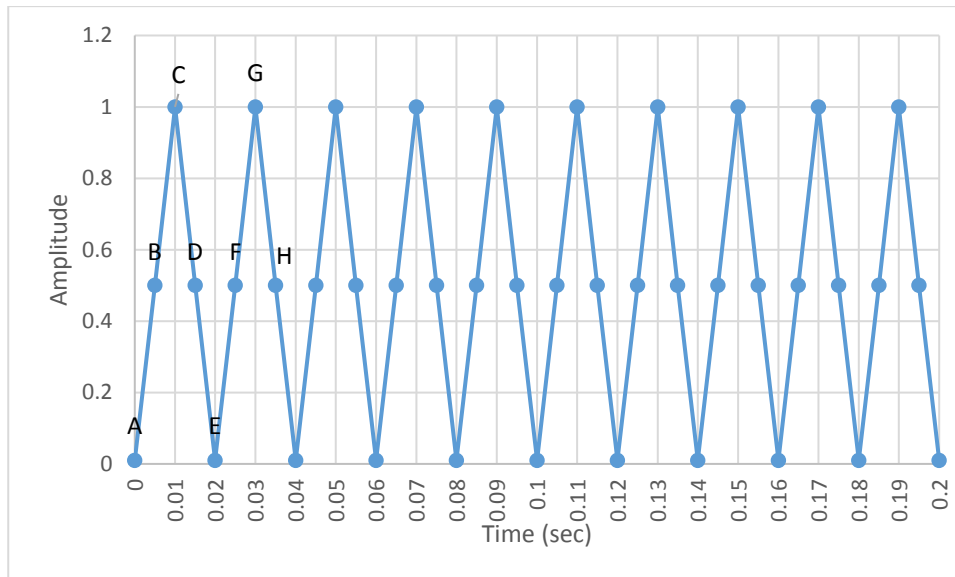


Figure 8.2.19: Cyclic amplitude of normal and tangential load, representing cyclic loading on bearing raceways

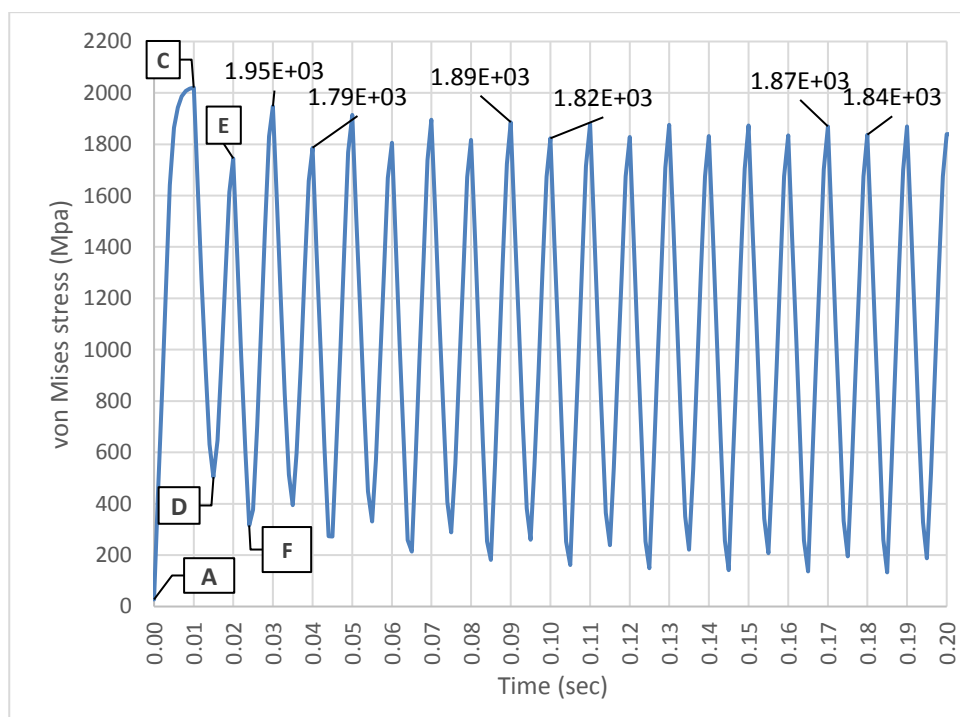
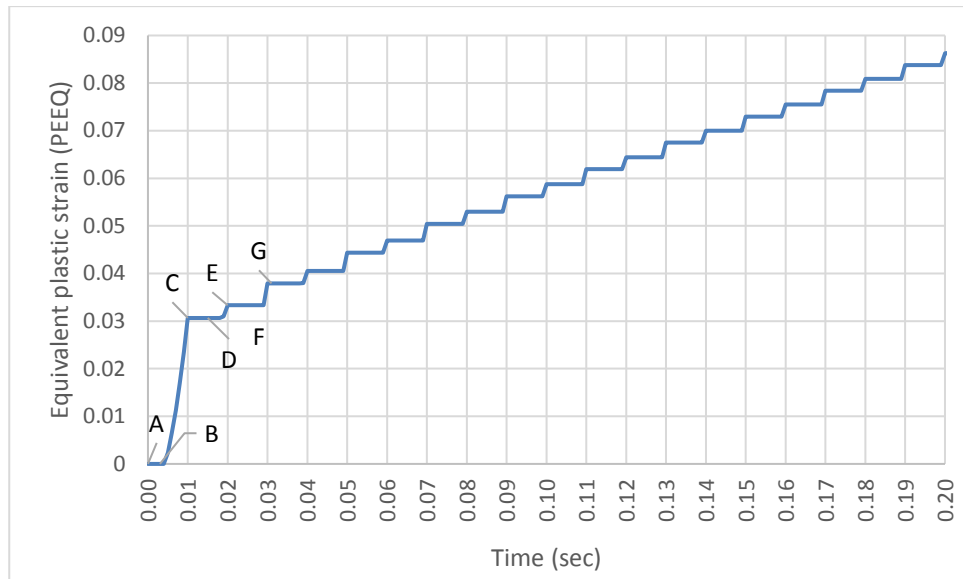
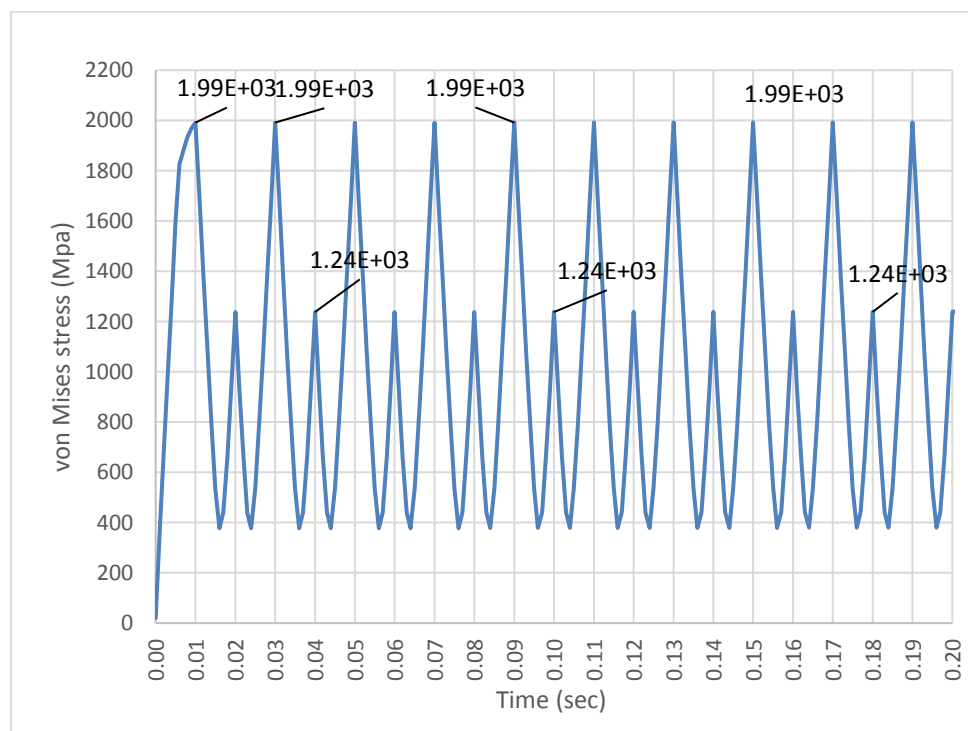


Figure 8.2.20: Stress variation at inclusion tip due to load amplitude variation shown in Figure 8.2.19 with  $p_{\max}=1700$  MPa and  $q_{\max}=340$  MPa. A: No load and no residual stress; C: Maximum load and maximum equivalent stress; D:  $(p_{\max}/2)$  Start of build-up of residual stress in this cycle; E: No load and maximum residual stress in this cycle; and F:  $(p_{\max}/2)$  overcoming the residual stress from previous cycles and starting the compression stress



**Figure 8.2.21: Equivalent plastic strain at inclusion tip due to the load amplitude variation shown in Figure 8.2.19 with normal load of  $p_{\max}=1700$  MPa and surface traction of  $q_{\max}=340$  MPa (letters have similar representation in Figure 8.2.20)**



**Figure 8.2.22: Stress variation at inclusion tip during cyclic loading with the peaks and valleys have similar representation as in Figure 8.2.20 (the load amplitude applied is shown in Figure 8.2.19 and  $p_{\max}=1700$  MPa)**

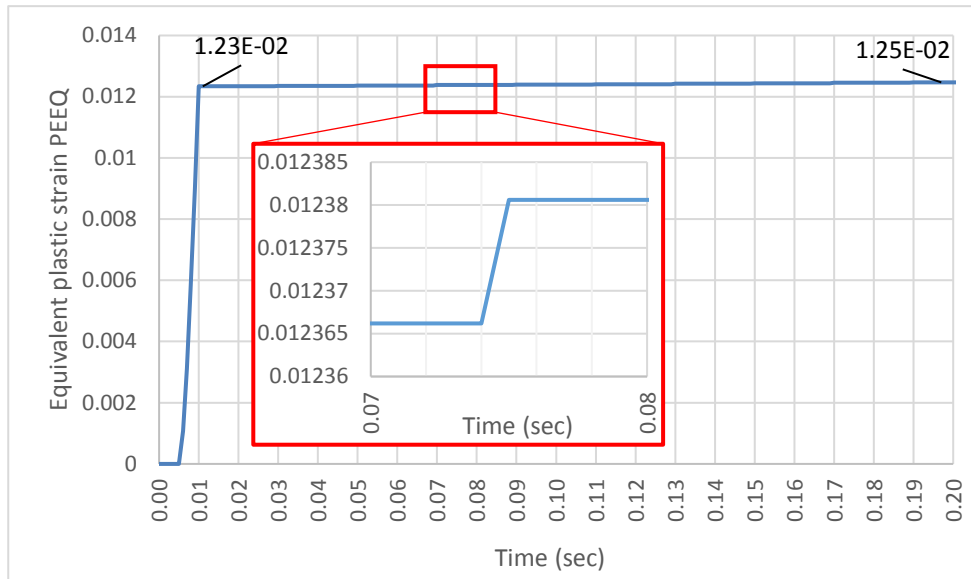


**Figure 8.2.23: Equivalent plastic strain at inclusion tip without surface traction during cyclic loading with highlighting the stepwise increase of the PEEQ as in Figure 8.2.21 but with smaller rate (the load amplitude applied is shown in Figure 8.2.19 and  $p_{\max}=1700$  MPa)**

### 8.2.5 Effect of Surface Traction Direction

The surface traction was shown in the previous section to have a significant effect on the stress and strain around the inclusion. The possible cause of surface traction in WTGBs was investigated by correlating the direction of surface traction to the inclination direction of the observed butterfly wings in the failed bearings. Two models were developed with a Hertzian distribution of normal contact pressure and a tangential surface traction of  $p_{\max}=1700$  MPa and  $q_{\max}=600$  MPa. Each of these models has embedded MnS inclusion with contact interaction between this inclusion and the steel matrix. These models are identical, except for the direction of surface traction, as shown in Figure 8.2.24. The load amplitude shown in Figure 8.2.12 was used in both models to simulate the loading/unloading on the raceway. At maximum load (time=0.2 sec), the stress around inclusions is shown in Figure 8.2.25; and at the unloading (time=0.4 sec), the residual stress and equivalent plastic strain are shown in Figure 8.2.26. These results show clearly the significant effect of traction direction on residual stress and equivalent plastic strain, if elongated inclusion with a certain angle is considered. To demonstrate the stress distribution around a perfectly rounded stress riser, two similar models were developed but the inclusions were replaced by a circular gap of 2 microns radius. The results of these models illustrate identical symmetry around the diagonal axis regardless of the surface traction direction, as shown in Figure 8.2.27, which is not the case for the elliptical inclined inclusion. Accordingly, this property can be used to predict the direction of the surface traction in WT planetary bearings and hence the occurrence of sliding or reverse rotation.

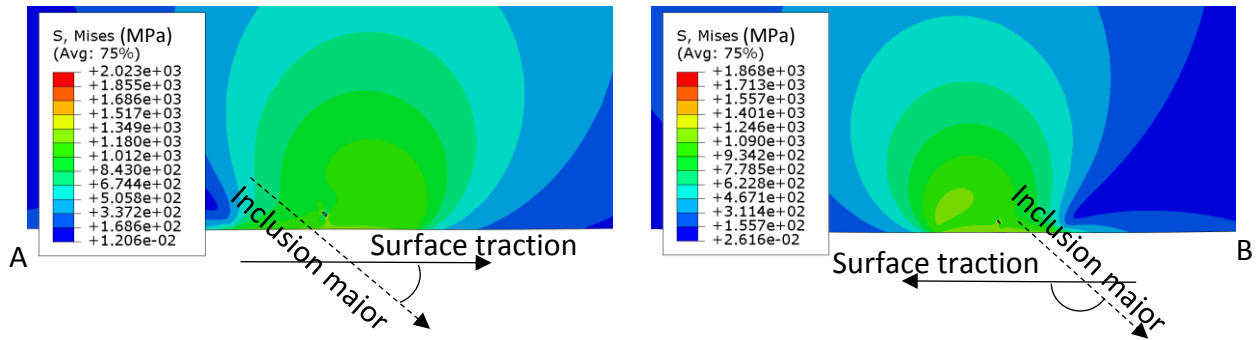


Figure 8.2.24: Models (A and B) used to investigate effect of surface traction direction on stress and strain at inclusion tips

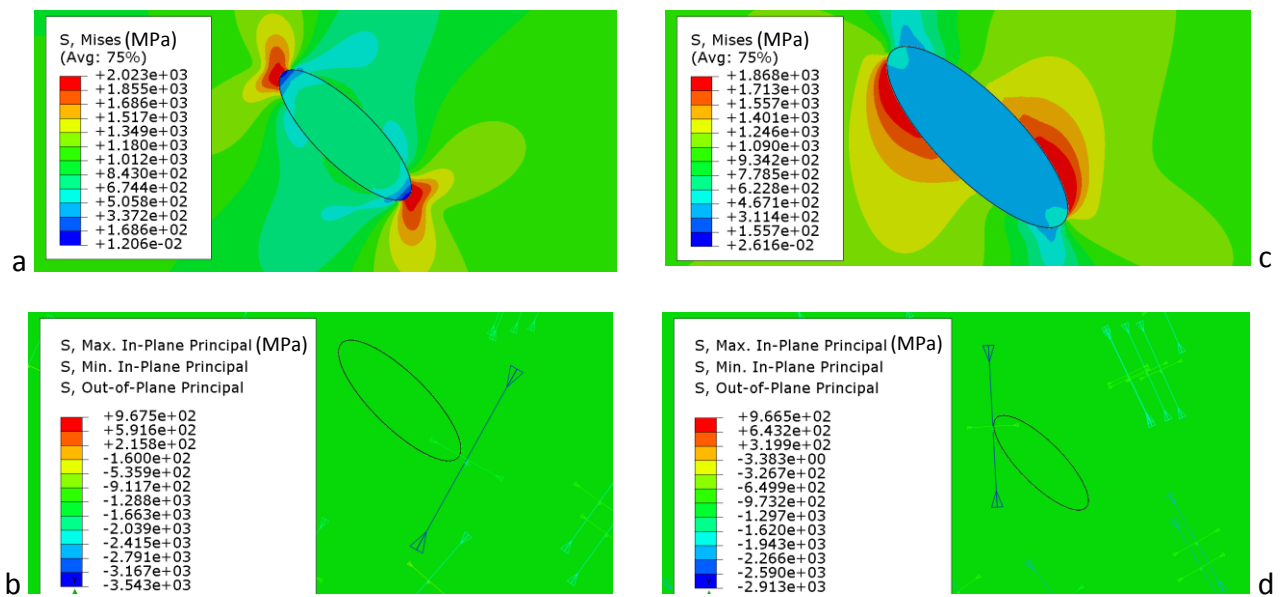
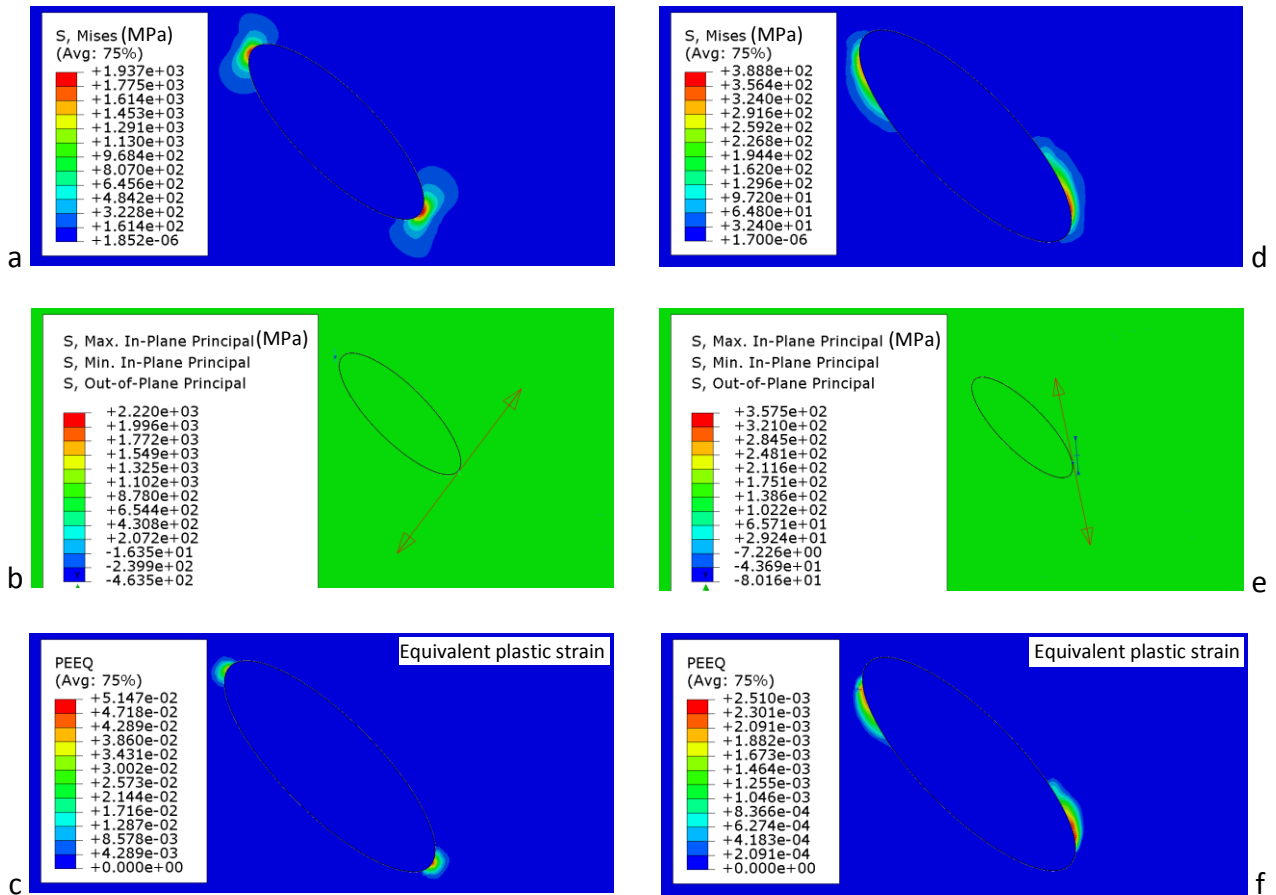
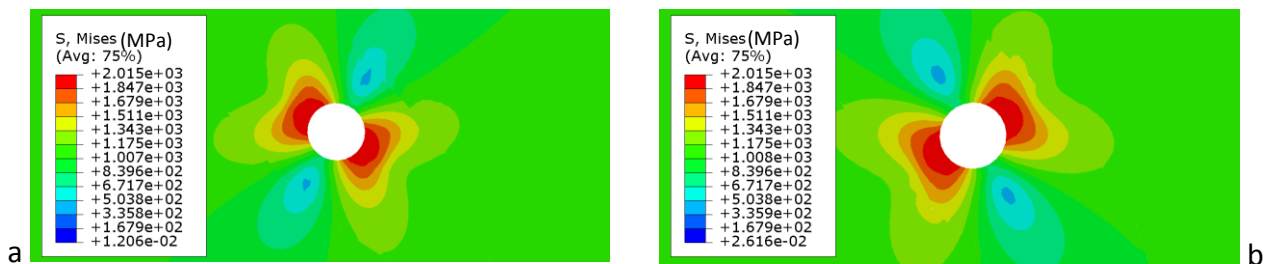


Figure 8.2.25: Stress at maximum load (time=0.2 sec) from models in Figure 8.2.24 ((a) and (b) for model (A) and (c) and (d) for model (B))



**Figure 8.2.26: Residual stress and equivalent plastic strain at unloading (time=0.4 sec) from models in Figure 8.2.24 ((a) to (c) for model A and (d) to (f) for model B)**



**Figure 8.2.27: Illustrations of stress around 2 μm circular gap under different directions of surface traction, shown in Figure 8.2.24 ((a) corresponding to model A; and (b) corresponding to model B)**

Different surface traction directions can make either an acute or an obtuse angle with the inclusion’s major axis, the line that links the initiation points of butterfly wings, as shown in Figure 8.2.24. When this angle is acute, as in Figures 8.2.25 (a) and (b) and Figure 8.2.26 (a) to (c), the stress concentration around inclusion tips matches the feature of butterflies better, specifically the inclination angle of the butterfly wings. Figure 8.2.28 shows some of the observed butterflies and the ORD in the uncoated and BO coated bearings. If no sliding is assumed between rollers and races, the direction of surface traction should be

complementary/opposite to the rolling direction. However, it was found that this pure rolling results in an obtuse angle between this surface traction and the line that links the initiation points of the butterfly wings, as shown in Figure 8.2.28. On the other hand, the surface traction due to sliding or reverse rotation makes an acute angle with the inclusion's major axis. This finding emphasises the occurrence of high surface traction in WT planetary bearings, which could be due to sliding or reverse rotation.

Since the direction of surface traction relative to the inclination direction of inclusion has a significant effect on the subsurface initiated damage, one measure for this damage could be to modify either of these directions: in other words, changing the configuration in Figure 8.2.24 from (A) to (B). However, changing the surface traction direction means changing the rotation direction of the rotor and the whole drive train, which is not feasible. Accordingly, the inclination direction of inclusions inside the inner raceway may be changed. To achieve this, the manufacturing process of this part should be modified. Because the rolling process during the forming of the final size of the ring determines the inclination direction of elongated inclusions, changing the direction of rolling should change the inclination direction of the elongated inclusions.

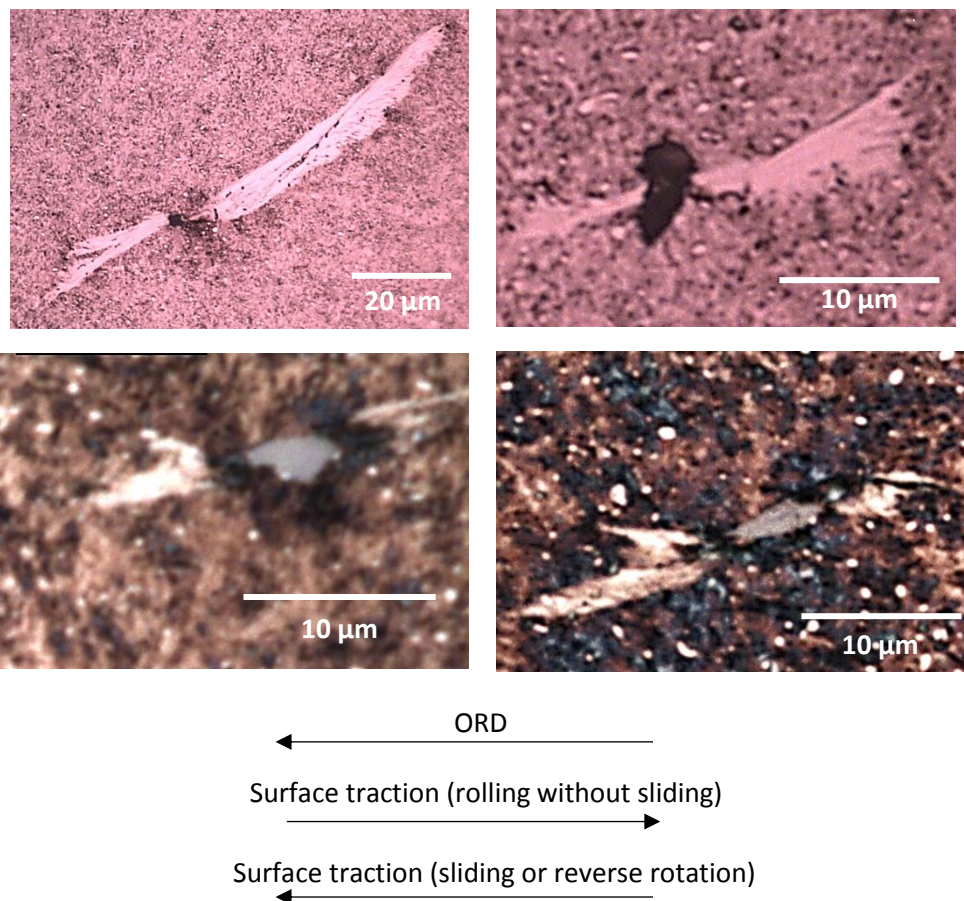


**Figure 8.2.28: Butterfly wing angle relative to rolling direction (surface of contact is below the butterflies and rolling direction from left to right)**

### 8.3 Summary

The first part of this chapter considered the measured torque spectra of the NREL 750 kW WT, in order to investigate the effect of normal and tangential load on subsurface stress, the values and locations, and the accumulated damage. In the second part, the damage initiation at MnS inclusion was investigated using FE modelling, correlating the results with the observations from the failed bearings. The following summarise the findings in this chapter.

1. It was found that during transient events the recommended maximum contact pressure may be exceeded. However, no subsurface yielding should be expected if only a normal load is considered. Also, no impact effect was found due to the occurrence of a pressure spike, according to the EHL theory.
2. Correlating the results of FE modelling and the butterflies' inclination suggests the occurrence of reverse rotation or sliding in the ORD. Also, the calculations of  $\lambda$  shows mixed lubrication and a possible lubricant film failure during torque reversals, which could cause high COT.
3. Surface traction affects the value and location of maximum subsurface stress where it is more likely that surface damage will occur at  $x=0$  and subsurface damage at  $x=0.9b$  and since the raceway is exposed to all the values of  $x$ , surface and subsurface damage could be observed at the same location. It was also found that even moderate surface traction can cause a considerable increase in damage accumulation. Accordingly, the effect of surface traction on the total life of bearings should be investigated in future studies.
4. The stress concentrations around the tips of the modelled inclusion were found to have only a local effect, without changing the stress distribution elsewhere, thus stress contours and yielded elements around the inclusion resemble the distribution of butterflies. Also, matching was observed between the WEA in the butterflies and the stress distribution at inclusion tips when a surface traction was applied in the ORD, which can occur due to reverse rotation or sliding.
5. In the model of MnS inclusion, the separation between the inclusion and the steel matrix shows a significant effect on the stress concentration. However, even the perfectly bonded MnS inclusion almost doubles the stress at the tips, which emphasises the importance of considering the inclusions for subsurface stress calculations.
6. It was found that tensile residual stress and equivalent plastic strain were generated around the tips of the inclusion modelled to involve contact interaction with the steel matrix, while no residual stress was developed when the inclusion was modelled as perfectly bonded with the steel matrix. The tensile residual stress increases significantly with introducing cyclic loading and surface traction, making an acute angle with the inclusion's major axis. Accordingly, the surface traction

accelerates crack opening and any stress or strain induced microstructure alteration, such as WEA.

7. One suggestion to alleviate the effect of surface traction is to change the rolling direction during the manufacturing of WT bearings raceways, in order to reverse the inclination direction of elongated inclusions.

## 9 Conclusions and Future Work

This chapter firstly summarises the key findings from each of the results chapters 5 to 8, and then presents a number of ideas and recommendations for future research work based on these conclusions.

The findings from each of the results chapters are considered together to draw the main conclusions, and present new contributions to knowledge on the investigation of the root causes contributing to the premature bearing failures in WT GB.

### 9.1 Conclusions

According to the reviewed studies in Chapter 2, the premature failure of WTGBs is dominated by WECs with the subsurface initiation from non-metallic inclusions as reported as one of the damage theories. This study investigated the factors affecting the initiation of this failure mainly in the WT planetary bearings. The research consisted of destructive examination of two failed bearings with and without surface coating (Chapters 5 and 6); conducting a set of rolling and sliding tests (Chapter 7); and FE modelling of a MnS inclusion (Chapter 8). This research produced characterisation of the observed surface and subsurface damage and identified the key factors affecting the damage. The experimental observations were also correlated to the modelling results to understand the effect of surface traction on the initiation of damage at non-metallic inclusions with a non-perfect bonding with the steel matrix. In addition to the result summaries at the end of each chapter, the following points are the main findings and conclusions drawn from this research representing a new contribution to the knowledge in this field.

1. **Observed types of damage:** The subsurface initiated cracks and WEA from non-metallic inclusions were confirmed by examinations of the WT failed bearings and the RSTs, which were in line with the previous studies [19][61]. However, in this research two different types of bearings were examined, new observations were made and seven types of damage were categorized and analysed. In addition to the subsurface initiation, surface initiation was confirmed by surface-linked RCF cracks that showed shearing of the material. These cracks were found to be involved in different stages of spall formation. The procedures developed in this research in terms of damage identification and analysis could be more widely adopted as a systematic method of damage examination and diagnosis.
2. **The size of inclusions, cracks and butterflies:** Previous studies reported that more damage could arise from shorter length inclusions [61]. This could not be verified in this study. However, it was found that butterflies were longer than micro-cracks initiated by inclusion although the initiation inclusions themselves were smaller in size. It was also observed that at the same depth, the inclusions initiated damages were bigger than inclusions that were not related to damage. Also, the total length of the inclusions and butterfly wings or micro-cracks was found to be directly

proportional to the size of the inclusion which led to greater damage. It was found that the butterfly wings were longer than micro-cracks initiated from inclusions, which didn't agree with the rubbing theory [151] that the WEA formed on the sides of the crack did not exceed the crack length.

3. **Inclusion debonding and order of damage initiation:** The debonding, that separated the WEA and inclusion tips observed in most of the butterflies, was found to be a material defect rather than a result from loading. The dimensions of debondings in a butterfly were studied using AFM scanning. The statistical analysis of the catalogued damage observed in the failed bearings highlighted the role of inclusion debonding in subsurface damage initiation. This was also confirmed by the results of the RSTs and the stress concentration around debonded inclusions shown in the FE models. It was found that these debonded inclusions could cause more damage than self-cracked inclusions. However, under high loads the micro-cracks could be initiated by non-debonded inclusions. It was observed that the order of the subsurface initiated damage was not always starting from the cracking of the inclusion, followed by micro-crack into the steel matrix and then the development of WEA along the micro-crack, as suggested in previous studies such as [18].
4. **Characteristics of WEA** were correlated to stress concentration: A new feature for the WEA was observed using the AFM scanning. It was found that the WEA was a torn material which was not as dense as the steel matrix with lower E and H values at the interface between WEA and steel matrix. This observation supports the fracture initiation by mode I which was also correlated to the tensile stress concentration around the inclusion based on the FE modelling results. The FE results showed the generation of tensile stress beyond the material initial yielding limit and an equivalent plastic strain around the tips of a debonded inclusion after each loading-unloading cycle. The results of the FE modelling also showed that surface traction significantly increased these stress and strain levels at the inclusion. It can be concluded that surface traction accelerates sub-surface initiated cracks as well as any stress or strain induced microstructure alteration, such as WEA.
5. **Initiation and propagation of cracks:** This study confirmed both the surface and subsurface damage initiation theories. The results from Chapter 6 showed that surface initiated spalling started from surface-linked RCF cracks to form micro-pitting which propagated the surface-linked RCF cracks further to form spalling. The RSTs showed that the severity of spalling correlated to the level of surface traction. On the other hand, the subsurface initiated spalling started from micro-cracks initiated by inclusion that propagated in a direction to be almost vertical to the rolling surface before forming a network of cracks and causing surface spalling. It was found that both surface and subsurface initiated cracks propagated at almost the same angle ( $\approx 15^\circ$ ) in the axial direction. This could explain the difficulty in

recognising the various initiation mechanisms when reaching the advanced stages of damage, which has been the subject of debate in the published literature.

6. **High surface traction:** The occurrence of high slipping ratios in WT bearings had been reported before, however the effect of varying levels of surface traction/ COT had not been investigated. In this study, it was found that a high slip ratio did not necessarily correlate to high surface traction/COT under full lubrication. A comparison between the observations of the butterfly from the failed bearings and the results of the FEM revealed that it was sliding or reverse rotation to cause high COT under full lubrication. In addition, the depth of butterflies and micro-cracks initiated from inclusions and the location of the maximum subsurface hardness measured were found to be closer to the surface than the zone of  $\tau_{1(max)}$  which indicated the occurrence of high surface traction.
7. **BO coated bearing characterization** (steel cleanliness and coating properties): This study investigated a failed WT BO coated bearing by assessing the steel cleanliness and the BO layer characteristics. The cleanliness analysis showed a high content of inclusions Type D which exceeded the maximum allowable limit according to the ISO standard 683-17 [82]. It was found that 65% of the observed butterflies were associated with this type of inclusion. Although the cleanliness of other defined Types such as Type A was satisfactory, it was shown that they could become the initiation point for subsurface cracks. Many other inclusions that initiated cracks or butterflies were combinations of more than one defined Type according to EDX analysis. The thickness measurement of the undamaged BO layer was found to be around 2.2  $\mu\text{m}$ . This layer had been completely removed within the load zone, and reduced significantly at the entrance to the loaded zone where the thickness was measured at around 0.2  $\mu\text{m}$ . The first 0.5  $\mu\text{m}$  of the BO layer had a hardness  $H=4.35\pm 0.1$  GPa, it was then gradually increased in value to the bearing steel hardness where the average H and E values for the BO layer were found to be 6.1 GPa and 161.8 GPa respectively. According to the surface and subsurface damage observed, the BO layer was not effective against WECs, butterflies, surface initiated cracks and cracks started from inclusions.
8. **Factors affecting damage initiation:** The results from the RSTs showed clear similarities to the observations from the failed bearings. The RSTs confirmed subsurface damage initiated from inclusions. However, the limited duration of these tests did not allow the damage to develop to the level observed in the failed bearings. It was found that higher levels of the compressive load and surface traction caused more surface and subsurface damage. In addition, the order of conducting test steps with varied speed conditions was found to affect the damage initiation, causing higher surface damage starting from low speed step followed by high speed step and higher subsurface damage at the opposite order of the speed steps.

9. **Formation of WEA and WECs:** A hypothesis for the formation of WEA in the butterflies and the WECs was proposed based on investigations of this study. It is suggested that surface traction plays a major role by reducing the normal load required for reaching the material initial yielding limit as shown by the results of the FE modelling and strain hardening due to plastic deformation accumulation through Ratchetting under repeated fatigue cycles. This process is more prevalent at inclusion tips or debondings where the stress concentration is at the highest. However, when the maximum shear stress reaches the surface or very close to it, the surface-linked RCF cracks with steel particles confined between the two sides of the crack will appear. The trapped particles inside these cracks showed evidence of the influence of the shear stress and surface traction. The similarity between these cracks, such as in RST 1 and the WECs in the BO coated bearing, suggests a similar damage formation mechanism.

## 9.2 Future work

The investigation of this study led to a number of findings and conclusions that clarified important issues relating to the premature failure of WT GB bearings. Future research in some of these areas would contribute to an in-depth understanding in the field. The following ideas are suggested for future studies.

- Further work is required to classify the debonding of the inclusion from the steel matrix and identify those which could be caused by loading such as the impact-like loading during transient events of WTG.
- To gain more confidence in the results from the RSTs, each test should be repeated several times under identical conditions. Also, studies with a larger number of cycles may be useful to allow the damage to propagate to more advanced stages. This would allow a better comparison to be made with the observations in the failed bearings. It is also important to develop tests to investigate the propagation of subsurface initiated damage to reach the surface, and to cause spalling.
- One of the recently emerging non-destructive techniques that can be used for metals, such as x-ray scanning, should be considered to investigate the development of subsurface initiated cracks or WEA in the RSTs specimens. This would reveal the propagation rate due to the factors that cause damage such as surface traction and high loading.
- More advance FE modelling for the inner raceway could be developed by considering a three dimensional model, more realistic loading, more accurate interaction between the inclusion and steel matrix, and higher number of load cycles. Such a model would provide more accurate results and may determine thresholds for normal and tangential loads required to initiate the damage at inclusions.

- The rapid occurrence of damage during reverse rotation highlights the need for further tests to be conducted using reverse rotation under different loading conditions.

## References

- [1] GWEC (Global Wind Energy Council), "Global Wind Report 2016," 2017.
- [2] European Commission, "Energy Strategy and Energy Union," 2017. [Online]. Available: <https://ec.europa.eu/energy/en/topics/energy-strategy-and-energy-union>.
- [3] GWEC (Global Wind Energy Council), "Global Wind Report 2014," 2014.
- [4] IEA (International Energy Agency), "IEA wind TCP 2015 Annual Report," 2015.
- [5] AWEA, "The Cost of Wind Energy in the U.S.," 2017. [Online]. Available: <https://www.awea.org/falling-wind-energy-costs#ComparativeCost>.
- [6] WindEurope, "IEA Wind Recommended Practices for Reliability Data," 2017. [Online]. Available: <https://windeurope.org/summit2016/networking/iea-wind-recommended-practices-reliability-data/>.
- [7] S. Faulstich, B. Hahn, H. Jung, and K. Rafik, "Suitable failure statistics as a key for improving availability," in *Proceedings of the European Wind Energy Conference, EWEC, 2009*, p. Online resource.
- [8] S. Faulstich and B. Hahn, "Comparison of different wind turbine concepts due to their effects on reliability," *Contract*, pp. 1–20, 2009.
- [9] J. Ribrant and L. M. Bertling, "Survey of failures in wind power systems with focus on Swedish wind power plants during 1997-2005," *IEEE Trans. Energy Convers.*, vol. 22, no. 1, pp. 167–173, 2007.
- [10] S. K. G, I. D, B. N, C. J, and S. A, "Effects of Extreme and Transient Loads on Wind Turbine Drive Trains," *Proc. 30th ASME Wind Energy Symp.*, pp. 1–24, 2012.
- [11] M.-H. Evans, "White structure flaking (WSF) in wind turbine gearbox bearings: effects of 'butterflies' and white etching cracks (WECs)," *Mater. Sci. Technol.*, vol. 28, no. 1, pp. 3–22, Jan. 2012.
- [12] a. Ruellan, F. Ville, X. Kleber, a. Arnaudon, and D. Girodin, "Understanding white etching cracks in rolling element bearings: The effect of hydrogen charging on the formation mechanisms," *Proc. Inst. Mech. Eng. Part JJ. Eng. Tribol.*, vol. 228, no. 11, pp. 1252–1265, 2014.
- [13] K. Stadler and A. Stubenrauch, "Premature bearing failures in industrial gearboxes," *Annu. Rev. Mater. Sci.*, vol. 9, no. 1, pp. 283–311, 2013.
- [14] B. Gould and A. Greco, "The Influence of Sliding and Contact Severity on the Generation of White Etching Cracks," *Tribol. Lett.*, vol. 60:29, no. 2, pp. 1–13, 2015.
- [15] B. Gould and A. Greco, "Investigating the Process of White Etching Crack Initiation in Bearing Steel," *Tribol. Lett.*, vol. 62:26, no. 2, pp. 1–14, 2016.
- [16] P. Rycerz, A. Olver, and A. Kadiric, "Propagation of surface initiated rolling contact

- fatigue cracks in bearing steel,” *Int. J. Fatigue*, vol. 97, pp. 29–38, 2017.
- [17] B. Gould, A. Greco, K. Stadler, E. Vegter, and X. Xiao, “Using advanced tomography techniques to investigate the development of White Etching Cracks in a prematurely failed field bearing,” *Tribol. Int.*, vol. 116, pp. 362–370, 2017.
- [18] J. Gegner, “Tribological Aspects of Rolling Bearing Failures,” in *In: C.-H. Kuo (ed.), Tribology–Lubricants and Lubrication*, Rijeka, Croatia: InTech, 2011, pp. 33–94.
- [19] T. Bruce, E. Rounding, H. Long, and R. Dwyer-Joyce, “Characterisation of white etching crack damage in wind turbine gear- box bearings,” *Wear*, vol. 338–339, pp. 164–177, 2015.
- [20] A. Greco, “Bearing Reliability-White Etching Cracks (WEC),” in *Gearbox Reliability Collaborative Annual Meeting*, 2014.
- [21] H. Uyama, “The mechanism of white structure flaking in rolling bearings,” *Natl. Renew. energy Lab. Wind turbine*, pp. 1–37, 2011.
- [22] H. Uyama, H. Yamada, H. Hidaka, and N. Mitamura, “The Effects of Hydrogen on Microstructural Change and Surface Originated Flaking in Rolling Contact Fatigue,” *Tribol. Online*, vol. 6, no. 2, pp. 123–132, 2011.
- [23] J. Gegner and W. Nierlich, “Tribology Seminar Wind Turbine A Recap Tribology Seminar,” in *NREL Wind Turbine Tribology Seminar*, 2011.
- [24] “International Organization for Standardization, BS ISO15243: Rolling bearings — Damage and failures — Terms , characteristics and causes,” *BS ISO15243*, 2017.
- [25] S. K. F. Bearings, “Bearing failures and their causes,” 1994.
- [26] R. G. Bayer, *Mechanical Wear Fundamentals and Testing, Revised and Expanded*, 2nd ed. 2004.
- [27] T. A. Harris and M. N. Kotzalas, *Advanced Concepts of Bearing Technology*, 5th ed. CRC Press, 2007.
- [28] “International Organization for Standardization, ISO 281: Rolling bearings — Dynamic load ratings and rating life,” *ISO 281*, 2007.
- [29] P. J. Blau, L. R. Walker, H. Xu, R. Parten, J. Qu, and T. Geer, “Wear Analysis of Wind Turbine Gearbox Bearings,” 2010.
- [30] F. Oyague, “Gearbox reliability collaborative (GRC) description and loading,” *NREL*, no. November, 2011.
- [31] K. Stadler and A. Stubenrauch, “Premature bearing failures in wind gearboxes and white etching cracks (WEC),” *Evolution - the business and technology magazine from SKF*, 2013.
- [32] W. Musial, S. Butterfield, and B. McNiff, “Improving Wind Turbine Gearbox Reliability,” in *European Wind Energy Conference*, 2007, pp. 1–13.

- [33] “International Organization for Standardization, ISO 15243: Rolling bearings — Damage and failures — Terms, characteristics and causes,” *ISO 15243*, 2004.
- [34] M. N. Kotzalas and G. L. Doll, “Tribological advancements for reliable wind turbine performance,” *Philos. Trans. A. Math. Phys. Eng. Sci.*, vol. 368, no. 1929, pp. 4829–4850, 2010.
- [35] P. Eschmann and L. Hasbargen, *Ball and roller bearings: theory, design, and application*. John Wiley & Sons, 1985.
- [36] OLYMPUS, “Inspections of Wind Turbine Gearboxes.” [Online]. Available: <http://www.olympus-ims.com/en/applications/rvi-wind-turbine/>.
- [37] F. Oyague, “Gearbox Modeling and Load Simulation of a Baseline 750-kW Wind Turbine Using State-of-the-Art Simulation Codes,” *Nrel*, no. February, p. 81, 2009.
- [38] R. Wood, “Tribology and corrosion aspects of wind turbines,” in *Challenges for Materials, Mechanics and Surface Science*, 2010.
- [39] K. Scott, “Effects of Transient Loading on Wind Turbine Drivetrains,” University of Strathclyde, 2014.
- [40] H. Link, W. LaCava, J. Van Dam, and B. McNiff, “Gearbox reliability collaborative project report: findings from phase 1 and phase 2 testing,” *NREL*, no. June, 2011.
- [41] T. Bruce, H. Long, and R. S. Dwyer-Joyce, “Dynamic modelling of wind turbine gearbox bearing loading during transient events,” *IET Renew. Power Gener.*, vol. 9, no. 7, pp. 821–830, 2015.
- [42] J. Helsen, Y. Guo, J. Keller, and P. Guillaume, “Experimental investigation of bearing slip in a wind turbine gearbox during a transient grid loss event,” *Wind Energy*, vol. 19, no. 12, pp. 2255–2269, 2016.
- [43] W. LaCava, J. Keller, and B. McNiff, “Gearbox Reliability Collaborative: Test and Model Investigation of Sun Orbit and Planet Load Share in a Wind Turbine Gearbox,” in *53rd Structures, Structural Dynamics and Materials Conference (SDM)*, 2012.
- [44] W. LaCava, Y. Guo, C. Marks, Y. Xing, and T. Moan, “Three-dimensional bearing load share behaviour in the planetary stage of a wind turbine gearbox,” *IET Renew. Power Gener.*, vol. 7, no. 4, pp. 359–369, Jul. 2013.
- [45] Y. Guo, J. Keller, and W. Lacava, “Planetary gear load sharing of wind turbine drivetrains subjected to non-torque loads,” *Wind Energy*, vol. 18, no. 4, pp. 757–768, 2015.
- [46] Z. Jiang, Y. Xing, Y. Guo, T. Moan, and Z. Gao, “Long-term contact fatigue analysis of a planetary bearing in a land-based wind turbine drivetrain,” *Wind Energy*, vol. 18, no. 4, pp. 591–611, 2015.
- [47] Y. Guo, J. K. Nrel, Z. Zhang, R. Insight, D. Lucas, and T. Timken, “Planetary Load Sharing in Three-Point-Mounted Wind Turbine Gearboxes: A Design and Test Comparison,” in *3rd Conference for Wind Power Drives*, 2017.

- [48] S. Jain and H. Hunt, "A dynamic model to predict the occurrence of skidding in wind-turbine bearings," *J. Phys. Conf. Ser.*, vol. 305: 01202, Jul. 2011.
- [49] J. A. Williams, *Engineering Tribology*. Oxford University Press, 1994.
- [50] K. L. Johnson, *Contact mechanics*. Cambridge University Press, 1987.
- [51] F. Sadeghi, B. Jalalahmadi, T. S. Slack, N. Raje, and N. K. Arakere, "A Review of Rolling Contact Fatigue," *ASME. J. Tribol.*, vol. 131, no. 4: 041403-15, 2009.
- [52] D. Nélias *et al.*, "Role of Inclusions, Surface Roughness and Operating Conditions on Rolling Contact Fatigue," *J. Tribol.*, vol. 121, no. 2, pp. 240–251, 1999.
- [53] S. S. Crețu, "Cylindrical roller bearings with profiled contacting surfaces," *IOP Conf. Ser. Mater. Sci. Eng.*, vol. 174: 01200, 2017.
- [54] S. K. Wong and A. Kapoor, "Effect of hard and stiff overlay coatings on the strength of surfaces in repeated sliding," *Tribol. Int.*, vol. 29, no. 8, pp. 695–702, 1996.
- [55] S. K. Wong, A. Kapoor, and J. A. Williams, "Shakedown limits on coated and engineered surfaces," *Wear*, vol. 203–204, no. 96, pp. 162–170, 1997.
- [56] M. Brückner, J. Gegner, A. Grabulov, W. Nierlich, and J. Slycke, "Butterfly formation mechanisms in rolling contact fatigue," in *Proc VHCF-5*, 2011, pp. 101–106.
- [57] K. Stadler, J. Lai, and R. H. Vegter, "A Review: The Dilemma With Premature White Etching Crack (WEC) Bearing Failures," *Bear. Steel Technol. 10th Vol. Adv. Steel Technol. Roll. Bear.*, pp. 1–22, 2014.
- [58] A. M. Diederichs, A. Schwedt, J. Mayer, and T. Dreifert, "Electron microscopy analysis of structural changes within white etching areas," *Mater. Sci. Technol.*, no. 32:16, pp. 1683–1693, 2016.
- [59] J. Gegner and W. Nierlich, "The Bearing Axial Cracks Root Cause Hypothesis of Frictional Surface Crack Initiation and Corrosion Fatigue-Driven Crack Growth," in *NREL Wind Turbine Tribology Seminar*, 2011.
- [60] A. M. Diederichs, S. Barteldes, A. Schwedt, J. Mayer, and W. Holweger, "Study of subsurface initiation mechanism for white etching crack formation," *Mater. Sci. Technol.*, vol. 32, no. 11, pp. 1170–1178, 2016.
- [61] M. H. Evans, A. D. Richardson, L. Wang, and R. J. K. Wood, "Serial sectioning investigation of butterfly and white etching crack (WEC) formation in wind turbine gearbox bearings," *Wear*, vol. 302, no. 1–2, pp. 1573–1582, 2013.
- [62] V. Šmeļova, A. Schwedt, L. Wang, W. Holweger, and J. Mayer, "Microstructural changes in White Etching Cracks (WECs) and their relationship with those in Dark Etching Region (DER) and White Etching Bands (WEBs) due to Rolling Contact Fatigue (RCF)," *Int. J. Fatigue*, vol. 100, no. March, pp. 148–158, 2017.
- [63] J.-H. Kang, R. H. Vegter, and P. E. J. Rivera-Díaz-del-Castillo, "Rolling contact fatigue in martensitic 100Cr6: Subsurface hardening and crack formation," *Mater. Sci. Eng.*

- A, vol. 607, pp. 328–333, 2014.
- [64] A. Warhadpande, F. Sadeghi, M. N. Kotzalas, and G. Doll, “Effects of plasticity on subsurface initiated spalling in rolling contact fatigue,” *Int. J. Fatigue*, vol. 36, no. 1, pp. 80–95, 2012.
- [65] R. Errichello, R. Budny, and R. Eckert, “Investigations of Bearing Failures Associated with White Etching Areas (WEAs) in Wind Turbine Gearboxes,” *Tribol. Trans.*, vol. 56, no. 6, pp. 1069–1076, Nov. 2013.
- [66] J. Luyckx, “White Etching Crack Failure Mode in Roller Bearings: From Observation via Analysis to Understanding and an Industrial Solution,” *Roll. Elem. Bear. STP 1542*, Yoshimi R. Tak. William F. Mandler, Ed., vol. doi:10.152, no. ASTM International, pp. 1–25, 2012.
- [67] B. H. Uyama and H. Yamada, “White Structure Flaking in Rolling Bearings for Wind Turbine Gearboxes,” *Wind Syst. Mag.*, pp. 14–25, 2014.
- [68] H. K. D. H. Bhadeshia, “Steels for bearings,” *Prog. Mater. Sci.*, vol. 57, no. 2, pp. 268–435, 2012.
- [69] R. Wood, J. Basumatary, and M. Evans, “Energy-related tribo-corrosion research at the National Centre for Advanced Tribology at Southampton,” *ASTM STP*, pp. 169–202, 2013.
- [70] R. H. Vegter, J. T. Slycke, J. Beswick, and S. W. Dean, “The Role of Hydrogen on Rolling Contact Fatigue Response of Rolling Element Bearings,” *J. ASTM Int.*, vol. 7: 102543, no. 2, 2010.
- [71] J. Luyckx, “Hammering Wear Impact Fatigue Hypothesis WEC/irWEA failure mode on roller bearings,” *Wind Turbine Tribol. Semin.*, 2011.
- [72] J. Rosinski and D. Smurthwaite, “Troubleshooting wind gearbox problems,” *Gear Solutions*, pp. 22–33, 2010.
- [73] M. H. Evans, “An updated review: white etching cracks (WECs) and axial cracks in wind turbine gearbox bearings,” *Mater. Sci. Technol. (United Kingdom)*, vol. 32, no. 11, pp. 1133–1169, 2016.
- [74] W. Solano-Alvarez and H. K. D. H. Bhadeshia, “White-etching matter in bearing steel. {Part 1}: Controlled-cracking of bearing steel,” *Metall. Mater. Trans. A*, vol. 45, pp. 4907–4915, 2014.
- [75] M. N. K. and Tedric A. Harris, *Essential concepts of bearing technology*, 5th ed. Boca Raton, Fla. ; London: CRC/Taylor & Francis, 2007.
- [76] Y. Murakami, *METAL FATIGUE: EFFECTS OF SMALL DEFECTS AND NONMETALLIC INCLUSIONS*, 1st ed. 2002.
- [77] “Total Materia.” [Online]. Available: <http://www.totalmateria.com/page.aspx?ID=CheckArticle&site=kts&NM=216>. [Accessed: 01-Aug-2017].

- [78] ASTM-E45-13, "Standard Test Methods for Determining the Inclusion Content of Steel," *Am. Soc. Test. Mater.*, pp. 1–19, 2013.
- [79] ISO-4967, "ISO 4967 nonmetallic inclusions — Micrographic method using standard diagrams," 2013.
- [80] ASTM E2283, "Standard Practice for Extreme Value Analysis of Nonmetallic Inclusions in Steel and Other Microstructural Features," *Astm*, vol. 8, no. Reapproved 2014, pp. 1–11, 2015.
- [81] H. Hunter, "Cleanliness Assessment of Bearing Steels," in *Advances in Rolling Bearing Fatigue FESI workshop*, 2014.
- [82] ISO-683-17, "International Standard: Heat-treated steels, alloy steels and free-cutting steels - Part 17: Ball and roller bearing steels," 2014.
- [83] A. Melander, "SIMULATION OF THE BEHAVIOUR OF SHORT CRACKS AT INCLUSIONS UNDER ROLLING CONTACT FATIGUE LOADING - SPECIALLY THE EFFECT OF PLASTICITY," in *Bearing Steels: Into the 21st Century*, ASTM STP 1327, J. J. C. and E. Hoe and W. B. Green, Eds. American Society for Testing and Materials, 1998.
- [84] N. Tsunekage, K. Hashimoto, T. Fujimatsu, K. Hiraoka, J. Beswick, and S. W. Dean, "Initiation Behavior of Crack Originated from Non-Metallic Inclusion in Rolling Contact Fatigue," *J. ASTM Int.*, vol. 7: 102612, no. 2, 2010.
- [85] BS-EN-61400-4, *Wind turbines Part 4: Design requirements for wind turbine gearboxes*. BSI Standards Publication, 2013.
- [86] IEC-61400-4, *WIND TURBINES – Part 4: Design Requirements for Wind Turbine Gearboxes*. International Electrotechnical Commission, 2009.
- [87] "International Organization for Standardization, ISO 16281: Rolling bearings - methods for calculating the modified reference rating life for universally loaded bearings," *ISO 16281*, 2008.
- [88] NREL, "Dynamometer Research Facilities," 2017. [Online]. Available: <https://www.nrel.gov/wind/facilities-dynamometer.html>.
- [89] CATAPULT, "Drive train testing," 2017. [Online]. Available: <https://ore.catapult.org.uk/our-services/test-demonstration-assets/drive-trains/>.
- [90] M. H. Evans, A. D. Richardson, L. Wang, and R. J. K. Wood, "Effect of hydrogen on butterfly and white etching crack (WEC) formation under rolling contact fatigue (RCF)," *Wear*, vol. 306, no. 1–2, pp. 226–241, 2013.
- [91] A. Ruellan, F. Ville, X. Kleber, and B. Liatard, "Understanding white etching cracks in rolling element bearings : State of art and multiple driver transposition on a twin-disc machine," *Proc. Inst. Mech. Eng. Part J J. Eng. Tribol.*, vol. 231, no. 2, pp. 203–220, 2017.
- [92] W. Kruhöffer and J. Loos, "WEC Formation in Rolling Bearings under Mixed Friction : Influences and ' Friction Energy Accumulation ' as Indicator," *Tribol. Trans.*, vol. 60,

- no. 3, pp. 516–529, 2017.
- [93] N. Kino and K. Otani, “The influence of hydrogen on rolling contact fatigue life and its improvement,” *JSAE Rev.*, vol. 24, no. 3, pp. 289–294, 2003.
- [94] A. J. Tarawneh, Constantine, Koester, Lucas W., Fuller and J. A. Wilson, Brent M., and Turner, “Service Life Testing of Components with Defects in the Rolling Contact Fatigue Zone,” in *Bearing Steel: Advances in Rolling Contact Fatigue Strength Testing and Related Substitute Technologies*, ASTM International STP 1548, 2012.
- [95] B. Mahmoudi, G. L. Doll, C. H. Hager, and R. D. Evans, “Influence of a WC/a-C: H tribological coating on micropitting wear of bearing steel,” *Wear*, vol. 350–351, pp. 107–115, 2016.
- [96] R. Evans, C. H. Hager, Y. S. Kang, and G. Doll, “Comparison of black oxide and tungsten carbide reinforced diamond-like carbon(wc/a-c:H) surface treatments for rolling element bearings,” *Tribol. Trans.*, vol. 58, no. 3, pp. 444–453, 2015.
- [97] K. Stadler, B. Han, V. Brizmer, and R. Pasaribu, “Benefits of using black oxidized bearings in wind applications,” *Bearing-news.com*, 2017. [Online]. Available: <http://www.bearing-news.com/benefits-of-using-black-oxidized-bearings-in-wind-applications/>.
- [98] K. Stadler, “HOW BLACK OXIDE-COATED BEARINGS CAN MAKE AN IMPACT ON CUTTING O&M COSTS FOR WIND TURBINES,” 2017. [Online]. Available: <http://evolution.skf.com/how-black-oxide-coated-bearings-can-make-an-impact-on-cutting-om-costs-for-wind-turbines/>.
- [99] J. C. Gregory, “Chemical conversion coatings of metals to resist scuffing and wear,” *Tribol. Int.*, vol. 11, no. 2, pp. 105–112, 1978.
- [100] T. W. Scharf *et al.*, “Atomic-scale structure and composition of tungsten carbide reinforced diamondlike carbon films,” *Appl. Phys. Lett.*, vol. 93: 151909, no. 15, 2008.
- [101] H. Dimigen and H. Hubsch, “Carbon-Containing Sliding Layer,” U.S. Patent No. 4, 525, 417, 1985.
- [102] H. Sjostrom and V. Wikstrom, “Diamond-like carbon coatings in rolling contacts,” in *Proceedings of the Institution of Mechanical Engineers - Part J: Journal of Engineering Tribology*, 2001, vol. 215, pp. 545–561.
- [103] A. R. Nejad, Z. Gao, and T. Moan, “Long-term analysis of gear loads in fixed offshore wind turbines considering ultimate operational loadings,” *Energy Procedia*, vol. 35, no. 1876, pp. 187–197, 2013.
- [104] A. R. Nejad, Z. Gao, and T. Moan, “On long-term fatigue damage and reliability analysis of gears under wind loads in offshore wind turbine drivetrains,” *Int. J. Fatigue*, vol. 61, pp. 116–128, 2014.
- [105] Z. Zhang and A. Crowther, “Validation of RomaxWind Model vs . Dynamometer

- Measurement Campaign for NREL GRC Gearbox 2 Romax Technology," in *Update on Data Analysis Work for Gearbox 2 -Romax*, 2015, pp. 1–38.
- [106] G. E. Morales-Espejel and a. W. Wemekamp, "Ertel-Grubin methods in elasto-hydrodynamic lubrication - a review," *Proc. Inst. Mech. Eng. Part J J. Eng. Tribol.*, vol. 222, no. 1, pp. 15–34, 2008.
- [107] P. M. Lugt and G. E. Morales-Espejel, "A Review of Elasto-Hydrodynamic Lubrication Theory," *Tribol. Trans.*, vol. 54, no. 3, pp. 470–496, 2011.
- [108] B. J. Hamrock and D. Dowson, "Isothermal Elasto-hydrodynamic Lubrication of Point Contacts: Part III—Fully Flooded Results," *J. Lubr. Technol.*, vol. 99, no. 2, pp. 264–275, 1977.
- [109] P. Pan and B. Hamrock, "Simple formulas for performance parameters used in elasto-hydrodynamically lubricated line contacts," *J. Tribol.*, vol. 111, no. 2, pp. 246–251, 1989.
- [110] R. Errichello, "Gear Technology," 2017. [Online]. Available: [http://www.geartechnology.com/articles/0715/Elastohydrodynamic\\_Lubrication\\_\(EHL\):\\_A\\_Review/](http://www.geartechnology.com/articles/0715/Elastohydrodynamic_Lubrication_(EHL):_A_Review/).
- [111] G. W. Stachowiak and A. W. Batchelor, *Engineering Tribology*. Butterworth Heinemann, 2014.
- [112] T. He, D. Zhu, J. Wang, and Q. Jane Wang, "Experimental and Numerical Investigations of the Stribeck Curves for Lubricated Counterformal Contacts," *J. Tribol.*, vol. 139, no. 2, p. 21505, 2016.
- [113] I. Hutchings, *Tribology: Friction and Wear of Engineering Materials*, 1st ed. Butterworth-Heinemann, 1992.
- [114] E. McEwen, "stresses in elastic cylinders in contact along a generatrix," *Philos. Mag.*, vol. 40, no. 454, 1949.
- [115] R. G. Budynas, J. K. Nisbett, and J. E. Shigley, *Mechanical engineering design*, 9th ed. New York: McGraw-Hill, 2011.
- [116] K. Hiraoka, M. Nagao, and T. Isomoto, "Study on flaking process in bearings by white etching area generation," *J. ASTM Int. STP 1465*, vol. 3, no. 5, pp. 234–241, 2006.
- [117] N. Weinzapfel, F. Sadeghi, and V. Bakolas, "An Approach for Modeling Material Grain Structure in Investigations of Hertzian Subsurface Stresses and Rolling Contact Fatigue," *J. Tribol.*, vol. 132: 04140, no. 4, 2010.
- [118] L. A. Mobasher Moghaddam. S, Sadeghi. F, Weinzapfel. N, "A Damage Mechanics Approach to Simulate Butterfly Wing Formation around Non-Metallic Inclusions," *ASME J. Tribol.*, vol. 137: 01140, no. 1, 2014.
- [119] S. M. Moghaddam, F. Sadeghi, K. Paulson, N. Weinzapfel, M. Correns, and M. Dinkel, "A 3D numerical and experimental investigation of microstructural alterations around non-metallic inclusions in bearing steel," *Int. J. Fatigue*, vol. 88, pp. 29–41,

- 2016.
- [120] M. Cerullo, "Sub-surface fatigue crack growth at alumina inclusions in AISI 52100 roller bearings," *Procedia Eng.*, vol. 74, pp. 333–338, 2014.
- [121] M. Cerullo, "Application of Dang Van criterion to rolling contact fatigue in wind turbine roller bearings under elastohydrodynamic lubrication conditions," *Proc. Inst. Mech. Eng. Part C J. Mech. Eng. Sci.*, vol. 228, no. 12, pp. 2079–2089, Dec. 2013.
- [122] "BSI Standards Publication, Coated abrasives — Grain size analysis Part 3 : Determination of grain size distribution of microgrits P240 to P2500," *BS ISO 6344-3*, 2013.
- [123] "Draft International Standard, ISO/DIS 4969: Steel — Etching method for macroscopic examination," *ISO/DIS 4969*, 2014.
- [124] "Veeco Dimension 3100 - Hysitron Triboscope." [Online]. Available: <http://esi.oeaw.ac.at/afm>.
- [125] N. A. Geisse, "AFM and combined optical techniques," *Mater. Today*, vol. 12, no. 7–8, pp. 40–45, 2009.
- [126] G. Binnig and C. F. Quate, "Atomic Force Microscope," *Phys. Rev. Lett.*, vol. 56, no. 9, pp. 930–933, 1986.
- [127] "International Organization for Standardization, BS EN ISO 6507-1: Metallic materials- Vickers hardness test part1: Test method," *BS EN ISO 6507-1*, 2005.
- [128] "Struers Ensuring Certainty." [Online]. Available: <http://www.struers.com/Knowledge/Hardness-testing/Vickers#>.
- [129] Hysitron, "Probe Calibration - Hysitron." [Online]. Available: <https://www.hysitron.com/media/1683/t-003-v30-probe-calibration.pdf>.
- [130] Hysitron, "Nanoindentation." [Online]. Available: <https://www.hysitron.com/resources-support/education-training/nanoindentation>.
- [131] W. C. Oliver and G. M. Pharr, "An improved technique for determining hardness and elastic modulus using load and displacement sensing indentation experiments," *J. Mater. Res.*, vol. 6, pp. 1564–1583, 1992.
- [132] J. E. Garnham and J. H. Beynon, "The early detection of rolling-sliding contact fatigue cracks," *Wear*, vol. 144, no. 1–2, pp. 103–116, 1991.
- [133] D. I. Fletcher and J. H. Beynon, "Development of a Machine for Closely Controlled Rolling Contact Fatigue and Wear Testing," *J. Test. Eval.*, vol. 28, no. 4, pp. 267–275, 2000.
- [134] D. Fletcher, "BEARING FRICTION ASSESSMENT FOR SUROS LEFT HAND DISC SUPPORTING BEARING ( TEST DIF45 ), witten in 1998 and received in 2018."

- [135] “British Standard, BS EN 10027-1: Designation systems for steels Part 2 : Numerical system,” *BS EN 10027-1*, 2016.
- [136] “OVAKO.” [Online]. Available: <http://www.ovako.com/>. [Accessed: 01-Jan-2017].
- [137] Castrol, “Alpha SP Range,” 2015.
- [138] R. Danzl, F. Helml, and S. Scherer, “Focus variation - A robust technology for high resolution optical 3D surface metrology,” *Stroj. Vestnik/Journal Mech. Eng.*, vol. 57, no. 3, pp. 245–256, 2011.
- [139] L. E. Iorio and W. M. Garrison, “Effects of gettering sulfur as CrS or MnS on void generation behavior in ultra-high strength steel,” *Scr. Mater.*, vol. 46, no. 12, pp. 863–868, 2002.
- [140] C. Luo, “Evolution of voids close to an inclusion in hot deformation of metals,” *Comput. Mater. Sci.*, vol. 21, no. 3, pp. 360–374, 2001.
- [141] M. R. Allazadeh, C. I. Garcia, A. J. Deardo, and M. R. Lovell, “Analysis of Stress Concentration around Inclusions due to Thermally Induced Strain to the Steel Matrix,” *STP49153S Quenching Cool. Residual Stress Distortion Control. STP49153S, L. Canale M. Narazaki, Ed., ASTM Int.*, vol. 6, no. 5, pp. 253–268, 2013.
- [142] Y. Murakami, S. Kodama, and S. Konuma, “Quantitative-Evaluation of Effects of Non-Metallic Inclusions on Fatigue-Strength of High-Strength Steels .1: Basic Fatigue Mechanism and Evaluation of Correlation Between the Fatigue Fracture-Stress and the Size and Location of Non-Metallic Inclusions,” *Int. J. Fatigue*, vol. 11, no. 5, pp. 291–298, 1989.
- [143] P. W. D. and D. F. Pilkey, *Peterson’s Stress Concentration Factors*. John Wiley & Sons, 2008.
- [144] K. Hui *et al.*, “The mechanism of intragranular acicular ferrite nucleation induced by Mg-Al-O inclusions,” *Adv. Mater. Sci. Eng.*, vol. 2015: 3786, 2015.
- [145] M. Takeda, T. Onishi, S. Nakakubo, and S. Fujimoto, “Physical Properties of Iron-Oxide Scales on Si-Containing Steels at High Temperature,” *Mater. Trans.*, vol. 50, no. 9, pp. 2242–2246, 2009.
- [146] “American National Standard, ANSI/AGMA/AWEA 6006-A03: standard for design and specification of gearbox of wind turbines,” *ANSI/AGMA/AWEA 6006-A03*, 2004.
- [147] N. E. Dowling, *Mechanical behavior of materials: engineering methods for deformation, fracture, and fatigue*. Prentice hall, 1993.
- [148] Boller, Chr, and T. Seeger, *Materials Data for Cyclic Loading: Low-alloy Steels*. Elsevier, 1987.
- [149] Totalmateria, “Bearing steel.” [Online]. Available: <http://www.totalmateria.com/>.
- [150] R. Peterson, *Stress concentration factors : Charts and relations useful in making strength calculations for machine parts and structural elements*. New York ; London:

Wiley, 1974.

- [151] Y. Kadin and M. Y. Sherif, “Energy dissipation at rubbing crack faces in rolling contact fatigue as the mechanism of white etching area formation,” *Int. J. Fatigue*, vol. 96, pp. 114–126, 2017.